



ULTRAFAST DYNAMICS IN CONDENSED MATTER
UNIVERSITY OF POTSDAM

MASTER THESIS

**Ultrafast Magnetostriction in Dysprosium studied
by Femtosecond X-Ray diffraction**

Author:

Alexander VON REPPERT

First assessor:

Prof. Dr. Matias BARGHEER
University of Potsdam

Supervisor:

Dr. Flavio ZAMPONI
University of Potsdam

Second assessor:

Prof. Dr. Uwe BOVENSIEPEN
University of Duisburg-Essen

Acknowledgements

Reaching the end of this experimental physics project would not have been possible without the support of many people that helped me in the course of my work. The following few lines are intended to thank the persons who provided help in various ways although the space here is in its nature insufficient.

Firstly the enthusiasm and optimism towards a positive outcome with which Prof. Dr. Matias Bargheer followed the development was a very motivating experience. The numerous discussions with him throughout all stages of the work were a great experience.

I am also indebted to Prof. Uwe Bovensiepen who as an external expert in the field of ultrafast lattice dynamics and rare earth metals agreed to correct and comment on this work even though he has no obligations to do so.

In particular I would like to mention Daniel Schick as father of the Plasma X-Ray source setup. In countless hours of his PhD work he has constructed a well thought-out experiment and I profited a lot from his legacy. He has now moved on to synchrotron based science, but his passion for detailed work left his mark on the established routines that are still in use.

I am grateful for my direct supervisor Dr. Flavio Zamponi who, as an experienced post doc, has many duties but nevertheless was always open to discuss my little problems of which there were many. In particular he introduced me to the merits of the open source programming language Python and introduced me to the many little good habits of real scientists.

A special thanks goes to my master colleague Jan Pudell who not only takes care of the good technical infrastructure of our group but also shared the long measurement days in the laboratory with me. A team of Jan and our skilled technician Elko Hannemann is an invaluable help when it comes to developing, designing and implementing improvements of the experiments.

A silent but nonetheless helpful colleague was Dr. Matthias Rössle who has words of advice for many people in our group. His knowledge on ellipsometry measurements and vacuum as well as cryostat technology made otherwise difficult experiments feasible. Together with him I learned the tricks of the trade in ultrafast X-ray diffraction, when we first started measuring Holmium in my introductory project.

Like many people of our group I am indebted to André Bojahr, who in spite of his own workload very often found the time to share his expertise on ultrafast phenomena, and the group internal UDKM1Dsim simulation toolbox with me. Being around him is often fun and I enjoy discussing the manifold aspects of physics with him.

I can only thank the UDKM team as a whole which succeeds in providing a positive and helpful working atmosphere in our group. The possibility to just come and ask each group member in

case of a problem is at the heart of a functioning group and I hope we can keep up or even extend this collaborative mindset in the future.

I do not want to forget to acknowledge the work of Karine Dumesnil from the Université de Lorraine who grew the Dysprosium thin film samples, which turned out to work well in my experiments.

And then there are all my friends and family who admittedly did not see much of me in the last months but nevertheless supported me mentally during the stressful last months. I am thankful for your patience and understanding, when I was absent once more due to my master thesis work. When you read these lines this permanent excuse is over with and better times are to come.

My dearest Levke I do not know how I would have managed without you. You never lost faith that I will eventually finish and helped me wherever you could. Words can not express my gratitude.

I thank all those who I have explicitly mentioned and also the countless people who indirectly contributed to this work especially the open source programming community. A last special mention goes to Lisa, Levke, Jan, Flavio and Daniel who took their time to comment on this work in the very final stage of its preparation, despite having lots of work to do themselves.

”The smallest act of kindness is worth more than the grandest intention.”
Oscar Wilde

Abstract

I use ultrafast X-ray diffraction (UXRD) to study the lattice dynamics of the heavy rare earth Dysprosium after femtosecond laser excitation across a large temperature range of 25 K – 300 K with three different magnetic orderings in the rare earth thin film. The anomalous increase of the lattice constant with decreasing temperatures below the antiferromagnetic ordering temperature T_N shows a strong coupling between magnetism and the lattice already from static measurements. I study this magnetostriction effect at a laser-driven tabletop plasma X-Ray source (PXS) using hard X-ray pulses with a time resolution of approx. 250 fs by following the position of the diffraction peak of Dysprosium in reciprocal space as a function of the pump-probe delay. The dynamics of the atomic lattice strongly depend on the magnetic phase of the rare earth as well as on the applied excitation fluence. I find that a simple and intuitive equilibrium physics approach is not sufficient to predict and explain these experimental results. Early time dynamics in the first 30 ps point to a spatial balancing effect between an expansive stress due to excited incoherent phonons and a compressive magnetic stress due to the removal of the magnetic order which releases the magnetostriction. This data can only be explained by spatially different excitation profiles for the two contributions. In the interpretation of my results I have developed a purely data-based analysis of two temperature model, which indicates that the phonon system and the spin system have not reached a common temperature up to the nanosecond timescale.

Kurzfassung

Ich benutze ultraschnelle Röntgenbeugung um die Gitterdynamik des seltenen Erdelements Dysprosium nach der Anregung durch einen Femtosekunden-Laserpuls zu untersuchen. Dabei habe ich die Dynamik über einen großen Temperaturbereich von 25 K – 300 K betrachtet, in dem verschiedene magnetische Ordnungen in dem dünnen Dysprosiumfilm auftreten. Die anormale lineare Ausdehnung der c-Achsen Gitterkonstante, die auftritt, wenn die Temperatur unterhalb der antiferromagnetischen Ordnungstemperatur gesenkt wird, zeigt die starke Kopplung zwischen Magnetismus und Gitter bereits in statischen Messungen. Ich untersuche diesen Magnetostraktionseffekt zeitaufgelöst mittels harter Röntgenstrahlung, die an einer laborbasierten Laser-getriebenen Plasma-Röntgenquelle erzeugt wird. Mit einer Zeitauflösung von etwa 250 fs messe ich die Position der Beugungsmaxima von Dysprosium im reziproken Raum als Funktion der Zeit nach der Anregung.

Die beobachtete Gitterdynamik hängt stark von der magnetischen Phase des seltenen Erdmetalls und der aufgewendeten Anregungsfluenz ab. Meine Analyse zeigt, dass eine einfache, aber intuitive Gleichgewichtsannahme zwischen dem Phononensystem und dem magnetischen System nicht ausreicht, um die experimentellen Beobachtungen zu erklären. Die Dynamik in den ersten 30 ps deutet auf einen räumlichen Kompensationseffekt zwischen der Wärmeausdehnung und der Kontraktion aufgrund der Abnahme der repulsiven Magnetostruktion hin. Zur Interpretation der Messergebnisse habe ich eine rein datenbasierte Analyse im Rahmen eines Zwei-Temperaturmodells entwickelt, welche ergibt, dass sich selbst auf einer Nanosekunden-Zeitskala keine einheitliche Temperatur zwischen Phononensystem und dem Spinsystem einstellt.

Contents

1	Introduction	9
1.1	Motivation of my work	9
1.2	Structure of the thesis	10
1.3	Overview over relevant literature	11
1.3.1	Properties of the rare earth Dysprosium	11
1.3.2	Electronic orbitals and their associated energy	13
1.3.3	RKKY-interaction and the magnetic phases of Dysprosium	15
1.3.4	Magnetocrystalline anisotropy	18
1.3.5	Magnetostriction	18
1.3.6	The heat capacity of Dysprosium	19
1.3.7	Ultrafast demagnetization upon fs-laser excitation	21
2	Experimental method and static characterization measurements	25
2.1	Sample structure	25
2.2	Crystal Structures and the Principle of X-ray Diffraction	26
2.3	Data acquisition routine	28
2.4	Static Measurements	38
3	Time resolved measurements	43
3.1	Principle of pump-probe experiments	43
3.2	Generation of short X-ray pulses	46
3.3	Experimental setup at the plasma X-ray source	49
3.4	Determination of the temporal overlap	54
3.5	Measurement results	60
3.5.1	Lattice response in the paramagnetic phase	60
3.5.2	Lattice response in the antiferromagnetic phase	63
3.5.3	Lattice response in the ferromagnetic phase	67
3.6	Dynamics in an external magnetic field	69
3.7	Indirect excitation of the Dysprosium layer	74
4	Discussion and interpretation of the results	79
4.1	General Trends	79
4.2	Initial dynamics	85
4.2.1	Speed limit of Magnetostriction	85
4.2.2	Compensation effect in the fast dynamics	88
4.3	Equilibrium Model approach	93

4.4	Spatially resolved Equilibrium Model simulation	97
4.5	Non-Equilibrium data analysis	105
4.5.1	Setup of the model	107
4.5.2	Application and results of the Non-Equilibrium model	109
4.6	Synthesis of the interpretation steps	118
5	Summary	122
	Bibliography	124
6	Appendix	136
6.1	Influence of the inhibited in-plane expansion	136
6.2	Reference Values of Material Properties	142
6.3	Listing of measurements	149

1 Introduction

1.1 Motivation of my work

Finding answers to the questions: "How fast does demagnetization and remagnetization occur?" and "What are the relevant underlying mechanisms of these processes?" is not only of fundamental scientific interest but also strongly motivated by future applications of our information technology that aim at pushing the writing rate in magnetic data storage devices to the ultimate physical limits. The timescales and processes of demagnetization have been investigated extensively since the groundbreaking work of Beaurepaire on the sub-picosecond demagnetization of thin Nickel films¹.

Despite the importance of the lattice system as possible bath of energy, entropy and angular momentum within the sample system, the coupling between magnetism and the lattice is an aspect of the ongoing debate over the processes of ultrafast demagnetization that, to my knowledge, has so far not been systematically investigated. With the tool of ultrafast X-ray diffraction at a laser-driven Plasma X-ray source our group has a method at hand to study the lattice dynamics of crystalline magnetic samples that happen concurrently to the demagnetization upon femtosecond-laser excitation with a subpicosecond time resolution².

A well suited material for these investigations is the element Dysprosium since it exhibits a large response of the lattice constant to the magnetization state^{3,4}. In addition to this spontaneous magnetostriction it has one of the largest magnetic moments per atom of all elements and displays three fundamentally different magnetic ordering states: paramagnetic, antiferromagnetic and ferromagnetic within the temperature range of 15 K – 320 K accessible in our setup⁵. Thus a systematic variation of the initial temperature and excitation energy density allows for studying the relevant energy transfer processes and coupling timescales in the sample.

Understanding the couplings between different physical subsystems is at the very foundation for the design of functional units. For example an ultrafast change in the magnetic system could possibly induce a strain in the lattice of a thin film and thereby be coupled to an adjacent

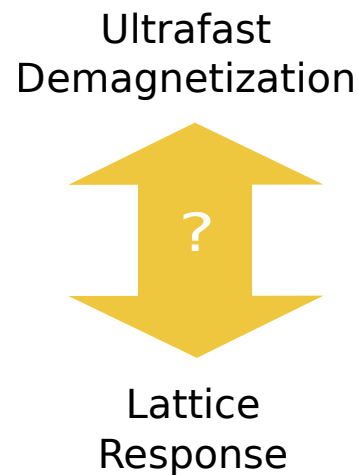


Figure 1.1. Motivation:
Can we learn something about magnetism by studying the lattice response?

nonmagnetic material. If this adjacent layer itself is sensitive to the strain, for example by a change of its polarization, an artificial multiferroic could be constructed⁶. However the focus of this work is on the fundamental physical mechanisms of the coupling between the lattice and magnetic dynamics.

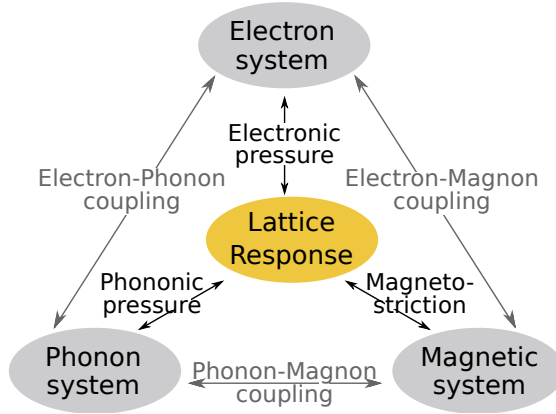


Figure 1.2. Schematic subsystem coupling. Three different subsystems are identified to act on the lattice and this figure schematically depicts their interplay.

The lattice response detected after ultrafast laser excitation in a magnetic sample is a result of the interplay of electronic, magnetic and vibrational (phononic) degrees of freedom. The measured ultrafast lattice response therefore contains information on all of the relevant couplings. Figure 1.2 shows the three main subsystems of electrons, phonons (lattice vibrations), and the magnetic system that can exert a strain on the lattice. Arrows between the systems emphasize that a coupling exists between these defined subsystems in the material.

In order to understand the manifold processes in a material with different active subsystems time resolved studies are a valuable tool because they access the additional intermediate states that often provide crucial pieces of information on the course of events. The maximum information on the process would be obtained by studying each subsystem under comparable conditions but this is often hampered by very different detection setups necessary to access the selected information. The time resolved X-ray diffraction experiments presented here provide the lattice response piece to the puzzle of ultrafast demagnetization.

1.2 Structure of the thesis

To clarify the logical structure and the relations between the chapters into which I subdivided my work I provide here a short overview over the organization of my thesis.

- In this first introductory chapter I motivate my experiments and provide an overview over the existing literature that forms the context of my studies.
- Chapter 2 contains the details about the investigated sample, the data analysis routine and static characterization measurements.
- In Chapter 3 I present the time resolved X-ray diffraction setup as well as the data acquired at the plasma X-ray source which are the main experimental results of my master thesis.

- Chapter 4 is then devoted to the detailed analysis and interpretation of the results that are supported by simulation results using the UDKM1Dsim tool box⁷. In this chapter I develop an experimental solution to a two temperature model for the spin and phonon system that I use to interpret the data.
- Chapter 5 briefly summarizes my findings.
- The Appendix contains reference values, additional calculations and details that would otherwise impair the reading fluency.

1.3 Overview over relevant literature

The physical concepts that are relevant to the studies of magnetostriction on ultrafast timescales of the rare earth materials by ultrafast X-ray diffraction are very diverse and partially even still under discussion within the scientific community. The following section summarizes certain aspects of the large body of literature that I find of particular importance to my project. A comprehensive review of this field lies outside the scope of this thesis so I chose to discuss selected topics of high relevance to my experiments.

At first I provide a brief general introduction especially of the heavy rare earth elements that introduces the magnetic phases, which have been extensively studied by neutron diffraction^{5,8,9,10,11} and resonant magnetic X-ray scattering^{12,13,14,15,16}. Relevant properties for my experiments that have been taken from the existing literature for the element Dysprosium are presented. The concept of the so called "RKKY-mechanism" that is responsible for the magnetic coupling between the localized spins of the rare earth elements is followed by a brief introduction to the theory on magnetostriction. I close the overview over the relevant literature by discussing the established time-resolved aspects that are reported on ultrafast demagnetization in general with a special focus on the work on the rare earth materials. References to the literature of the used time-resolved X-ray diffraction technique and the setup are provided within the description of the setup and data reduction Section in 3.3.

1.3.1 Properties of the rare earth Dysprosium

Dysprosium is part of the so called lanthanide series that contains 15 elements from Lanthanum ($_{57}\text{La}$) to Lutetium ($_{71}\text{Lu}$). Its location in the periodic system is outlined in Figure 1.3. The six elements from Gadolinium to Thulium are often referred to as heavy rare earth elements^{17,18} since they exhibit nearly identical chemical properties but exhibit a variety of different magnetic phases depending on temperature and applied external magnetic fields. The review article by Köhler⁵ (1965) and the books of Elliott¹⁹ (1972), Coqblin¹⁷ (1977) and Jensen and Mackintosh²⁰ (1991) among others provide a general overview over the known properties of rare earth materials.

Dysprosium has nine electrons in the 4f-shell and together with Holmium it exhibits the largest magnetic moment per atom of all elements of approximately $10.64 \mu_B$. The value of $10 \mu_B$ is predicted for the trivalent Dy^{3+} -ion by Hund's rules whereas the remaining $0.6 \mu_B$ are associated

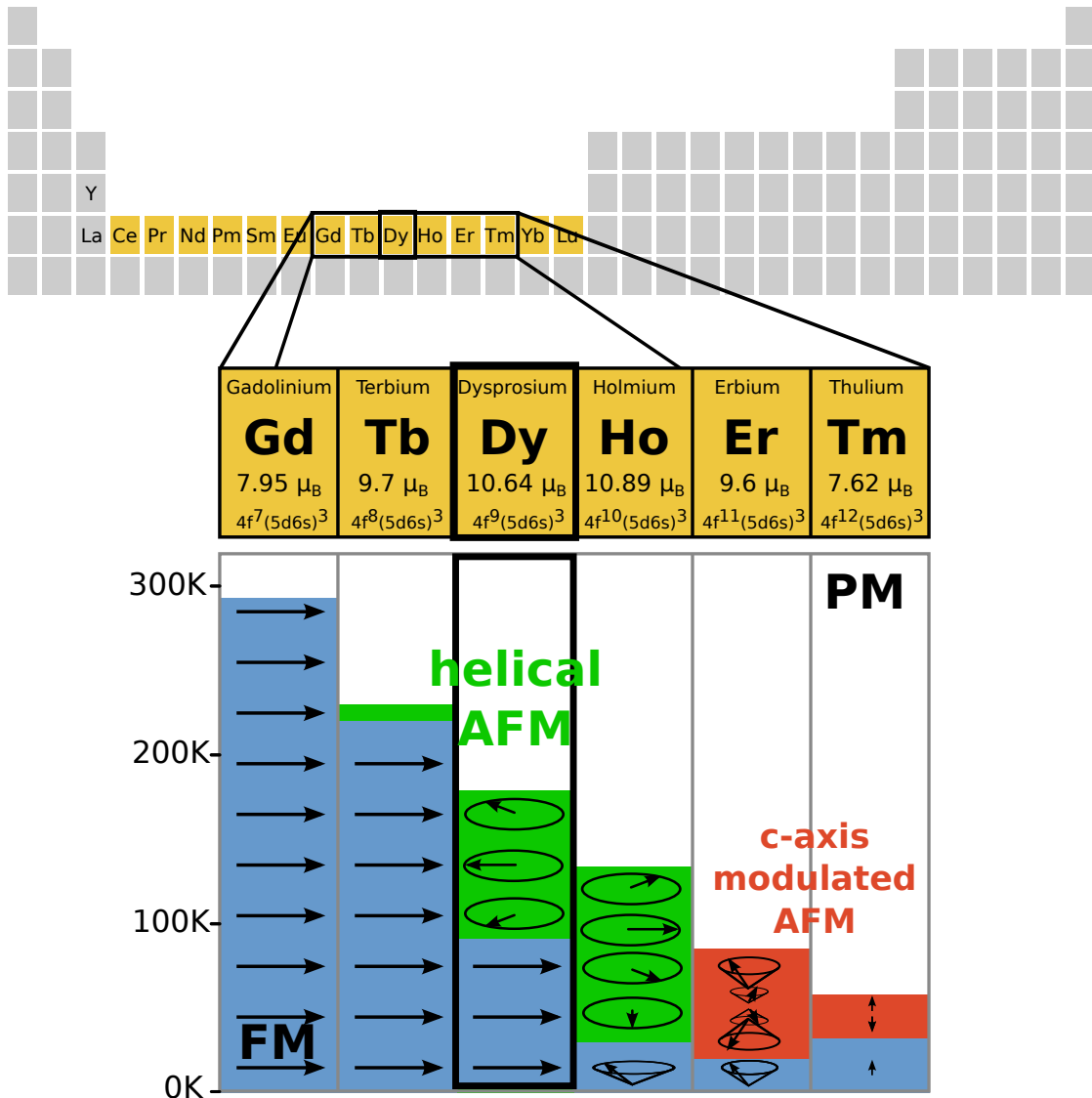
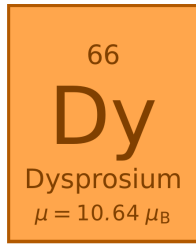


Figure 1.3. Properties of the six heavy rare earth elements. The so-called heavy rare earth metals are part of the second half of the lanthanoid series of the periodic system of elements (marked in yellow). Dysprosium, which is the material of interest for my studies, is part of this group that has very similar chemical properties due to their similar valence band structure but exhibit very different magnetic properties. Dysprosium is a generic example for these materials that with the exception of Gadolinium all exhibit a high temperature paramagnetic phase (PM) that is followed by an intermediate antiferromagnetic (AFM) ordering that transitions into a ferromagnetic ordering at low temperatures. Detailed reviews of the variety of magnetic properties are available in the literature^{5,19,21,20}. This figure is adapted from a similar schematic shown in the thesis of Ott²².

with the spin polarization of the 5d6s conduction band electrons¹⁷. Dysprosium crystallizes in a hexagonally closed packed structure and exhibits three different magnetic phases when no external magnetic field or pressure is applied⁵. At the Néel- temperature $T_N = 179$ K its magnetic state changes from a paramagnetic phase to a helical antiferromagnetic (AFM) phase. Bulk Dysprosium is known to become ferromagnetic below the Curie temperature $T_C = 85$ K. Figure 1.4 summarizes the relevant quantities originating from the electronic band structure and schematically visualizes the magnetic phases of Dysprosium that we observe in our experiments.

(a) Dysprosium properties



[Xe] 4f⁹(5s6d)³

$L = 5$
 $S = 5/2$
 $J = 15/2$
 $g = 5/3$
 $\theta_{Debye} = 183$ K

(b) Magnetic Phases of bulk Dysprosium

Ferromagnetic Antiferromagnetic Paramagnetic

$T_C = 85$ K $T_N = 179$ K

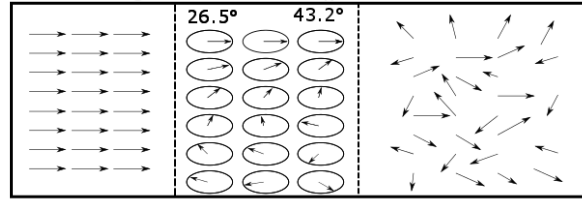


Figure 1.4. Dysprosium properties: a) Electronic structure of this element and the resulting quantum numbers deduced by Hund's rules. b) Schematic of the magnetic phases of bulk Dysprosium with the transition temperatures taken as reported in the review by Koehler⁵ for bulk Dysprosium.

Above $T_N = 180$ K the 4f-spins are disordered whereas a helical antiferromagnetic ordering is attained between $85 \text{ K} \leq T \leq 179 \text{ K}$. This means that the spins order ferromagnetically within the hexagonal plane but the relative orientation of the sublattice magnetization rotates from lattice plane to lattice plane as one goes along the c-axis dimension. Below 85 K the 4f-moments all align ferromagnetically along the a-axis, which is the easy axis of magnetization²³. Figure 1.5 shows a pseudo-three dimensional depiction of the spin orderings in the different magnetic phases. It schematically includes the anomalous lattice expansion as the temperature is lowered below the phase transition^{4,24}. To motivate these findings a brief introduction to the electronic structure and the prevalent RKKY-coupling mechanism is provided in the following.

1.3.2 Electronic orbitals and their associated energy

For historical reasons that date back to the years of their discovery between approximately 1850 and 1900 these elements are often called "rare earth elements", "rare earth metals" or simply "rare earths" because these metals have been found as oxides, which at the time were called "earths". They exhibit similar chemical properties, due to their very similar electronic structure, which usually has the form¹⁷:

$$[\text{Xe}](4f)^n(5d6s)^3 \quad n \in 1, 2, \dots, 14. \quad (1.1)$$

The electronic structure of the rare earth elements contains three valence electrons in a hybridized 5d6s-band and n electrons in the 4f shell with n increasing from $_{57}\text{La}$ ($n = 0$) to $_{71}\text{Lu}$ ($n = 14$) over closed electronic shells of the Xenon noble gas configuration. Exceptions to this rule

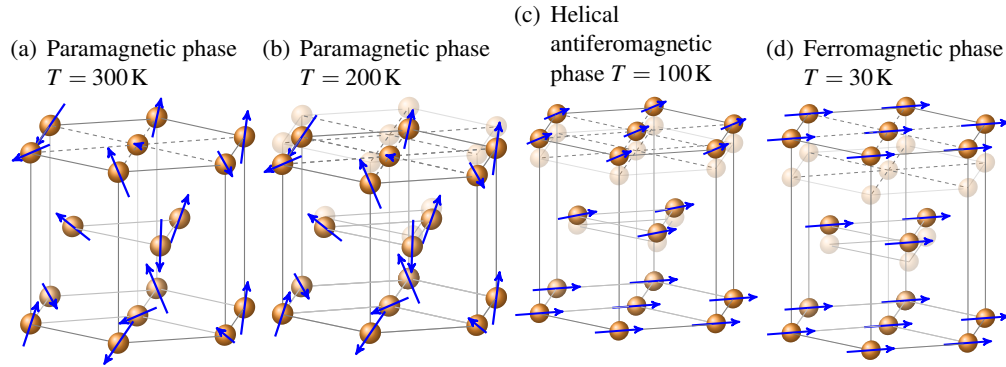


Figure 1.5. Magnetic orderings and magnetostriction: Blue arrows indicate the magnetic moments originating from the coupled 4f-electrons at their location in the conventional unit cell of the hexagonal Dysprosium lattice. The temperature of the sample is lowered from (a) to (d). This sketch schematically combines the 4f-spin ordering in the different magnetic phases described in the text with resulting change in the out-of-plane dimension of the unit cell of Dysprosium as it is cooled. The relative change of this c-axis dimension is exaggerated for clarity as it is on the order of $\%_0^4$.

are Europium (${}_{63}\text{Eu}$ ($n = 6$)) and Ytterbium (${}_{70}\text{Yb}$ ($n = 13$)) that have only two electrons in a 6s-band because an energetically favorable half filled or filled 4f-shell configuration is thereby attained¹⁷.

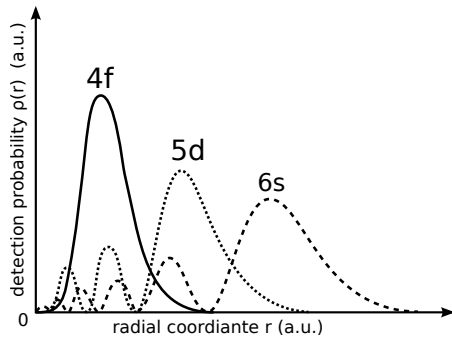


Figure 1.6.

Schematic radial valence band electron distribution:

The detection probability of the 4f-electrons close to the core is much larger as compared to the detection probability of the 5d and 6s electrons. This non-quantitative schematic sketch has been drawn based on results of Hartree-Fock calculations reported for Gadolinium²⁵ and other rare earths²⁰.

The probability density ρ to detect an electron from the 4f shell at a distance r away from the nucleus $\rho(r) = |\psi_{4f}(r)|^2$ is non-vanishing only in close proximity of the nucleus and a correspondingly defined radius of the 4f-orbitals would be ten times smaller than the lattice constant¹⁷. The probability density for the 5d6s-wavefunction extends much further. This has been schematically depicted in Figure 1.6. The strong localization of the 4f-electrons is the reason that their contribution to chemical bonding is screened by the other more delocalized valence states. This leads to the fact that the chemical properties in the lanthanide series are very similar. For example the heavy rare earth materials crystallize all in the hexagonal closed packed structure due to their identical valence state¹⁷. This structure is introduced and displayed in Section 2.2 where I discuss X-ray diffraction from crystal lattice structures. Despite the chemical inertness of the 4f

electrons their influence on the magnetic properties is very large since they carry spin and angular momentum¹⁸. The resulting magnetic moment of the 4f electrons is very well described by Hund's rules^{26,27} to potentially large values that vary drastically among these rare earth elements.

The 4f electrons are localized close to the nucleus and exhibit a larger binding energy than the itinerant 5d6s-electrons in the rare earth materials^{17,28}. The density of states of the electrons in the rare earth materials as a function of binding energy has been studied by X-ray photoelectron spectroscopy reported by Lang et al.²⁸ and the values for Dysprosium are reproduced in Figure 1.7. It can be seen that Dysprosium is a metal since it exhibits a non-zero density of states close to the Fermi-edge. Furthermore it is relevant for my studies to know that an excitation of the electron system with photons of an energy of 1.55 eV can only excite 5d6s-electrons into a previously unoccupied state. A direct excitation of the 4f-states is not possible.

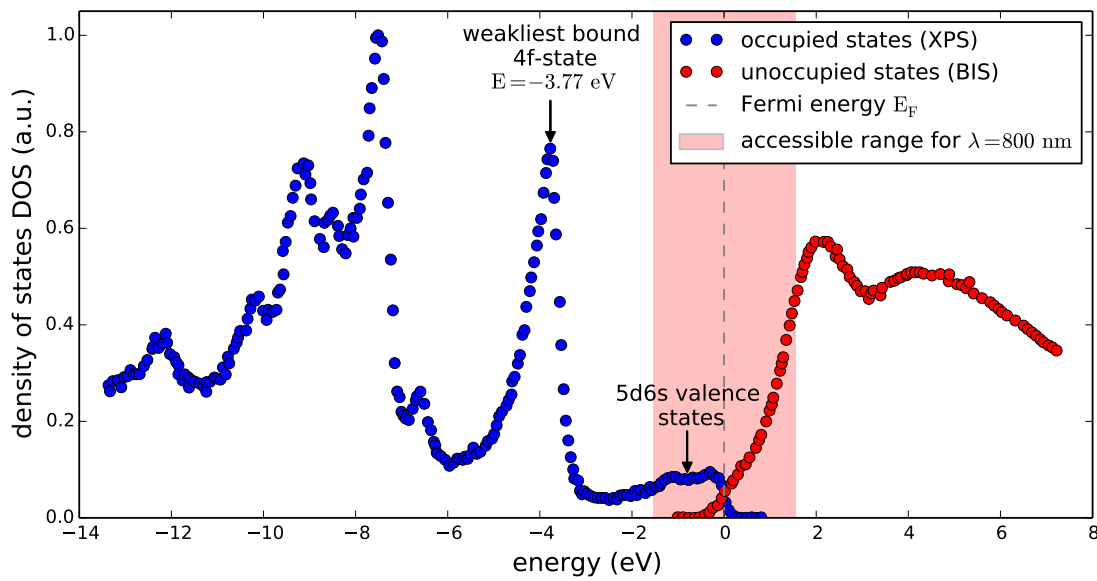


Figure 1.7. Electronic density of states in Dysprosium: The large maxima in the density of states at and below 3.77 eV are associated with the 4f-electrons whereas the relatively low density of states close to the Fermi Energy are associated with the 5d6s electron states. Reproduced here are the results from a comprehensive study of all rare earth elements by Lang et al.²⁸ obtained by X-ray photoelectron spectroscopy (XPS) and bremsstrahlung isochromat spectroscopy (BIS) (see their publication for details). It is important to note that photons with the energy of 1.55 eV ($\lambda = 800$ nm) used in my experiments can only excite the valence states into the conduction band.

1.3.3 RKKY-interaction and the magnetic phases of Dysprosium

As mentioned previously the large magnetic moments of the 4f-electrons are localized in the close vicinity of the nucleus. Under the assumption of Hydrogen-like wavefunctions Coqblin¹⁷ derives an effective Bohr radius for the 4f electrons of 0.35 \AA . Thus there is no considerable direct overlap between the quantum mechanical wavefunctions of the 4f-electrons of adjacent

lattice sites since the in-plane lattice constant $a \approx 3.59 \text{ \AA}$ and the out of plane lattice constant $c \approx 5.65 \text{ \AA}$, are much larger²⁹. This therefore excludes direct coupling mechanisms as cause for magnetism in these elements.

The indirect coupling mechanism that leads to magnetic interaction between the magnetic moments of the distant 4f-electrons in Dysprosium is called Rudderman-Kittel-Kasuya-Yosida^{30,31,32} (RKKY)-interaction after the physicists who have developed the concept. The general idea of the RKKY interaction is that large but localized magnetic moments interact via the spin polarization of itinerant conduction band electrons. Figure 1.8(a) depicts the model situation of two spins at a distance R_{ij} surrounded by a fermi-gas of spin-unpolarized conduction band electrons. The coupling of the localized spins with the electron gas is treated as a perturbation to the Hamiltonian of the free electron system. The second order perturbation calculation is carried out in the book by Nolting and Ramakanth³³ and it yields the following results:

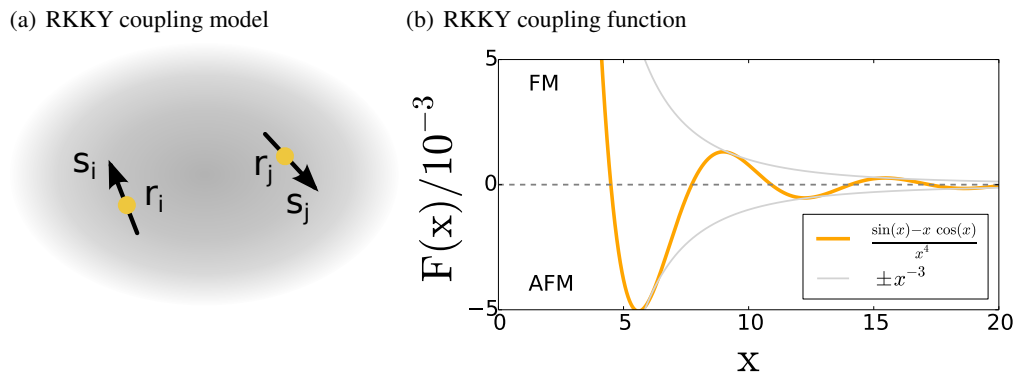


Figure 1.8. RKKY interaction model and result: (a) Model system of localized spins s_i and s_j in a "sea" spin unpolarized free electrons at a distance $R_{ij} = r_i - r_j$. (b) The quantum mechanical treatment of this situation, where the interaction of the localized spins are introduced as perturbation to the free electron system, yields an effective Heisenberg-type coupling between the spins s_i and s_j via an induced spin-polarization of the free electrons³³. The spatial variation of the effective coupling constant J_{ij}^{RKKY} derived from this model is described by the function $F(x)$. This function decays with distance as r^{-3} and oscillates between positive and negative values, which corresponds to ferromagnetic and antiferromagnetic coupling respectively.³³

The magnetic coupling between the localized spins which is mediated by the electron gas can be effectively described by a Heisenberg Hamiltonian of the type:

$$H = - \sum_{i,j} J_{i,j}^{\text{RKKY}} \vec{s}_j \vec{s}_i \quad (1.2)$$

with an effective coupling constant

$$J_{ij}^{\text{RKKY}} = \frac{J^2 k_F^6}{E_F} \frac{h^2 V^2}{N^2 (2\pi)^3} F(2k_F R_{ij}). \quad (1.3)$$

This formula contains the assumed intraatomic coupling constant J between the localized spins and the spins in of the free electron gas electrons, the Fermi energy of the free electron gas E_F ,

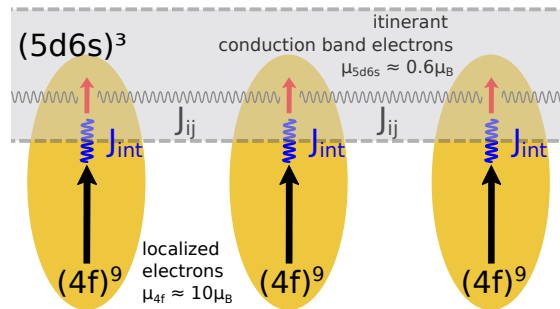
their Fermi vector k_F , the volume of the system V and the number of electrons in the system N , which are all constants. The important part in this result is the function F that determines the amplitude of the magnetic coupling constant as a function of the distance between the spins R_{ij} . This function

$$F(x) = \frac{\sin(x) - x\cos(x)}{x^4} \quad (1.4)$$

is depicted in Figure 1.8(b). It decays with x^{-3} , and thus extends further than the exponentially decaying direct interaction³³. It is important to stress that it oscillates as function of distance, between positive and negative values which leads to ferromagnetic or antiferromagnetic coupling between the localized magnetic moments, depending on their distance. A handwaving argument to make this behavior plausible is given by Nolting³³: The localized spin polarizes the adjacent conduction band spins ferromagnetically. The Pauli exclusion principle leads to the fact that the immediate neighbors of the spin polarized conduction band electrons whose wavefunctions that have some spatial overlap order antiferromagnetically to the first spin-polarized free electrons. The neighbors of the second spin polarized electrons are then again ordered parallel to the first electrons by again coupling antiferromagnetically. Regions of preferred ferromagnetic and antiferromagnetic alignment thus alternate with the distance. The initially spin-unpolarized electrons between the localized atoms can thus create a coupling between the distant magnetic moments S_i and S_j .

In the case of the Dysprosium the 4f-electrons represent the large but localized magnetic moments and the 5d6s conduction band electrons represent the nearly free electron gas. Another schematic of the coupling mechanism is provided in Figure 1.9. There the large but localized 4f-magnetic moments represented by large black arrows and itinerant 5d6s electrons small red arrows are shown separately. The key that is necessary for the helical antiferromagnetic order is a frustration between preferred ferromagnetic order with the next neighbor and antiferromagnetic coupling with the next-next neighboring spin¹⁷. This can in principle be accounted for via the spatial oscillation of the RKKY coupling constant J_{ij}^{RKKY} .

Figure 1.9. Schematic visualization of the spin system The localized moments of the 4f-electrons that carry a large magnetic moment $10\mu_B$ but their wavefunctions do not overlap directly. Instead they couple to the delocalized 5d6s-electrons that carry a much smaller magnetic moment of $0.6\mu_B$. This sketch has been adapted to Dysprosium based on a drawing from a recent article by Frietsch et al.³⁴. I take the coupling constants reported for Gadolinium $J_{ij} = 5.9\text{meV}$ for the interatomic coupling and $J_{\text{int}} = 130\text{meV}$ for the intraatomic coupling constants as an order of magnitude estimate for the constants in the similar here studied Dysprosium.



The so far discussed RKKY exchange interaction is categorized as a two ion term in the literature³⁵

and it is in its nature isotropic. Due to the variation of the interaction energy with distance this mechanism provides a first coupling between the lattice and the magnetic system of the 4f-electrons termed exchange striction³⁵. For the heavy rare earth materials Europium and Gadolinium that exhibit no spin-orbit coupling, this is the dominant mechanism³⁵. However for Terbium, Dysprosium and Holmium, which exhibit a large spin-orbit coupling the anisotropy energy is another considerable influence on the magnetic orientation. It is briefly discussed in the next section.

1.3.4 Magnetocrystalline anisotropy

The two ion contribution of the RKKY-exchange interaction is not the only mechanism that determines the magnetic order in the heavy rare earths. An additional contribution arises from the crystal field that influences the shape of the electron orbits and via spin orbit coupling indirectly the alignment of the spins. Spin orbit coupling means that the magnetic moment of the spin system has a preferential alignment relative to the strongly anisotropic electron orbitals²⁶. This electron distribution however has the same symmetry as the underlying crystal lattice so that the magnetic moments also adapt a certain order. This crystal-field anisotropy mechanism is a single ion contribution³⁵ and is the reason why the magnetic moments for Tb, Dy and Ho are confined preferentially to the basal plane of the unit cell. The crystal field mechanism of magnetostriction is thus based on the fact that changes in the lattice constant affect the electron density via a change in the effective field of the electrons. Through spin orbit coupling this thus affects the orientation of the magnetic moments of the 4f-electrons. Conversely a change of the magnetic orientation will as a consequence affect the crystal lattice potential.

The interplay between the two ion exchange interaction and the large anisotropy contributions leads to very different magnetic orderings among the heavy rare earth metals that were measured first via inelastic neutron diffraction³⁶ as summarized in the review by Koehler⁵. A third aspect that has been reported to play an important role is the shape of the Fermi surface where the presence of a nesting feature, (parallel planes of unoccupied states in the fermi surface), is found to promote the existence of a helical spin orderings^{37,38,18}.

1.3.5 Magnetostriction

Magnetostriction is the effect that a material changes its shape or dimensions upon a change in magnetization²⁶. It was first discovered by Joule in 1842 in Nickel³⁹ and later on confirmed in a more extensive study on steel bars⁴⁰. Magnetostriction is commonly measured in the relative change of the length or volume of a material as defined in relations (1.5) and (1.6):

$$\text{Linear magnetostriction : } \lambda = \frac{\Delta l(T, B)}{l} \quad (1.5)$$

$$\text{Volume magnetostriction : } \omega = \frac{\Delta V(T, B)}{V} \quad (1.6)$$

Magnetostriction effects can be categorized into two types based on the driving mechanism: It is termed forced magnetostriction when the change in magnetization is due to the application of

an external magnetic field or spontaneous magnetostriction in case the magnetization changes due to a change in the temperature of the material. During my project I mainly focus on effect of spontaneous magnetostriction in Dysprosium resulting from a change in the magnetization as a consequence of a change in temperature which is induced by the deposition of energy by the incident laser pulse.

Magnetostriction in the rare earth materials arises from both the RKKY-exchange interaction and the crystal field interaction³⁵. The atoms in the crystal lattice assume the energetically favorable position that minimizes their free energy which has a contribution of the harmonic elastic energy potential, the potential due to RKKY-exchange striction and the potential due to the crystal field contribution. The details for the theory are summarized in a review by Doerr et al.³⁵ on which I base the arguments presented here.

A giant forced linear magnetostriction of up to 7.5 % along the a-axis of Dysprosium under the application of a B-field of 2.6 T was found by Legvold et al. in 1963³ using a strain gauge method where resistance of a wire changes with the strain. As a comparison the observed magnetostriction in Iron is of the order $7 \cdot 10^{-6}$, approximately three orders of magnitude smaller⁴². The forced magnetostriction results of Dysprosium along c-axis direction, which is accessible in our experiments, is displayed in figure 1.11.

The spontaneous magnetostriction in Dysprosium was investigated in detail by Darnell and Moore on bulk single crystalline Dysprosium using X-ray diffraction in 1963^{4,43}. A previous study by Banister et al.⁴⁴ in 1954 had already shown an anomalous increase of the interatomic c-axis spacing in Dysprosium with decreasing temperature T below T_N although with smaller amount of datapoints. Figure 1.10 displays the experimental results by Darnell and Moore and more recent measurements by Bulatov et al.⁴¹. They are essential for this work because they show a strong coupling between the magnetic phase of the material and the lattice spacing already from static measurements.

1.3.6 The heat capacity of Dysprosium

Exciting an absorbing sample with a short laser pulse deposits energy into the material. After an equilibration time between the accessible degrees of freedom one observes a temperature change $\Delta T = T_{\text{end}} - T_{\text{start}}$ that is related to the deposited energy Q via the integral of the heat capacity C_p of the material according to

$$Q = \int_{T_{\text{start}}}^{T_{\text{end}}} C_p(T) dT. \quad (1.7)$$

Within the analysis and interpretation of my measurements I frequently use the heat capacity of Dysprosium as a function of temperature. An overview over the literature values of the heat capacity of Dysprosium extracted from different publications is presented in figure 1.12. The heat capacity exhibits two distinct maxima in the vicinity of the phase transition temperatures

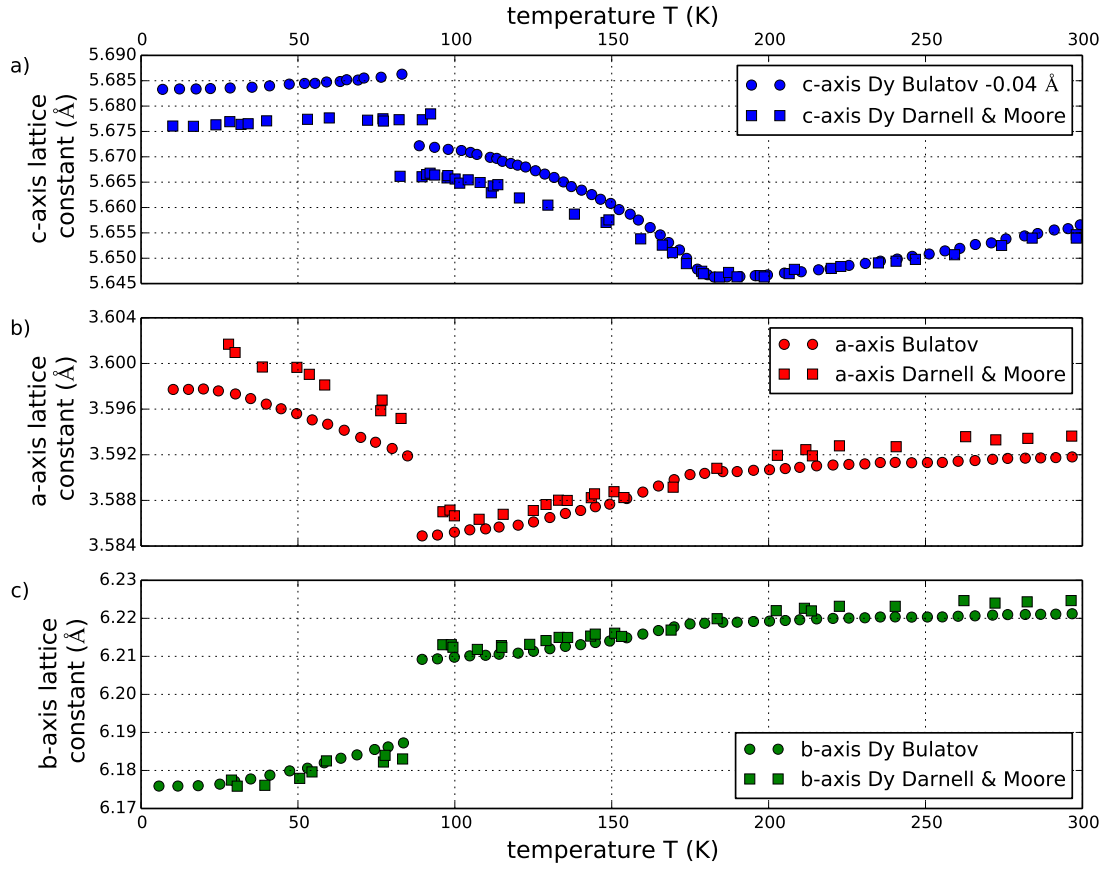


Figure 1.10. Spontaneous magnetostriction: Lattice constant along different directions in the hexagonal lattice of Dysprosium as measured by Darnell and Moore.⁴ as well as Bulatov et al.⁴¹ on bulk Dysprosium. Note the anomalous increase of the c-axis interatomic spacing with decreasing temperature in (a) below $T_N = 179$ K and the discontinuous step at $T_C = 85$ K. Also the in plane lattice constants shown in (b) undergo pronounced changes at the FM-AFM phase transition. These findings show that the magnetic phases of Dysprosium are visible in the lattice spacing, which forms the basis of my time resolved X-ray diffraction experiments.

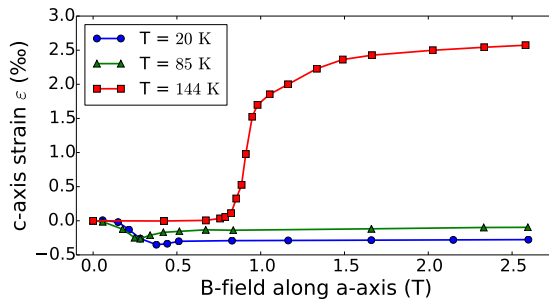


Figure 1.11. Forced magnetostriction: Depicted here is the relative change of the c-axis lattice constant of Dysprosium under the application of an external magnetic field at different temperatures reproduced from a publication by Legvold et al.³. The large increase of the c-axis at 144 K at approximately 0.8 T is indicative of a switching from the antiferromagnetic phase to the ferromagnetic phase which is accompanied by a 2‰ lattice expansion and a change of symmetry from hexagonal to orthorhombic⁴.

$T_N = 179\text{ K}$ and $T_C = 85\text{ K}$. Deviations in the reported data originate from the different sample purities and heating rates. The first measurements of the heat capacity of Dysprosium were carried out by Griffel et al.⁴⁵ but they deviate notably from the other more recent results. The measurement results with the sample of highest purity were reported by Pecharsky et al.⁴⁶. In my data analysis I use these measurement results as reference heat capacity. The heat capacity at the FM-AFM transition is predicted to be infinite $C_P = \frac{\Delta Q}{\Delta T} = \infty$ in the sense that for small amounts of deposited energy very close to the phase transition the temperature change ΔT is found to be zero⁴⁶, which makes the actual heat capacity value at the FM-AFM transition somewhat arbitrary. The enthalpy of transformation however is reported to be $50.7 \pm 1.2\text{ J/mol}$ ⁴⁶.

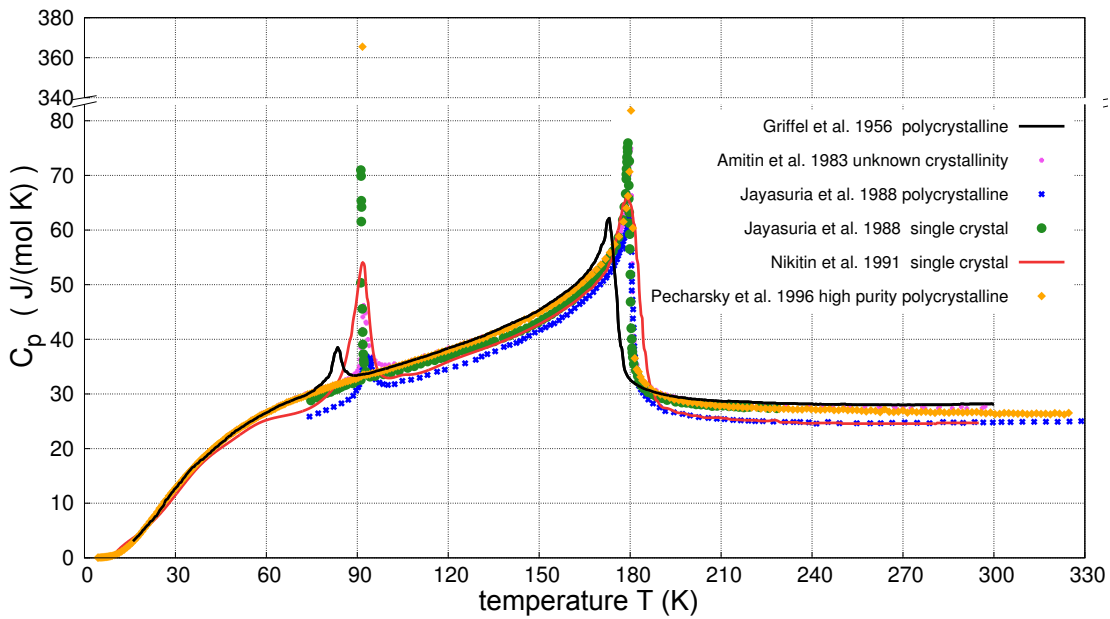


Figure 1.12. Heat capacity of Dysprosium: Summarized here are different reports for the heat capacity of Dysprosium published in the literature^{45,46,47,48,49} which is an important quantity for the interpretation of my data, since it determines the temperature change per deposited energy in thermal equilibrium. The collection is to show the relatively small deviations of the heat capacity reports depending on crystallinity and purity. For my data analysis I used the values provided by Pecharsky et al.⁴⁶.

1.3.7 Ultrafast demagnetization upon fs-laser excitation

In my experiments thin films of magnetic Dysprosium are excited with a femtosecond laser pulse leading to a transient demagnetization. Even though we do not directly probe the time evolution of the magnetization or the magnetic order parameter, the lattice responds to a change in the magnetic order. Therefore I briefly discuss the developments in the field of ultrafast demagnetization which are closely related to the processes I study.

To my knowledge the first experiments on the timescales of ultrafast demagnetization was carried out by Agranat et al. in 1984⁵⁰ on thin Nickel films where no demagnetization was found after a 5 – 20 ps laser pulse has excited the sample in contrast to the demagnetization observed after the irradiation with a 40 ns laser pulse. In the following Vaterlaus et al. conducted spin-resolved photoemission experiments^{51,52,53} mainly on Iron and Gadolinium where it was found that the spin lattice coupling time, that was thought to limit the demagnetization speed, is for Iron in the range between 30 ps and 20 ns and for the ferromagnetic rare earth Gadolinium in the range of 100 ± 80 ps. Consequently it came as a surprise when Beaupaire et al. reported on the ultrafast demagnetization of thin Nickel films on subpicosecond timescales in his seminal paper¹ published in 1996 using the time resolved magneto optical Kerr effect (trMOKE). These findings sparked a large amount of scientific investigations with the goal of understanding the microscopical mechanisms of the demagnetization processes. Two main types of demagnetization mechanisms are found. One of them is the Elliott-Yafet⁵⁴ type spin-flip scattering where the electrons scatter with phonons or impurities into states with opposite angular momentum. A schematic view of this process is shown in Figure 1.13(a). A comprehensive demagnetization model based on this spin-flip scattering that accounts for the largely different demagnetization timescales ranging from few hundred femtoseconds in Nickel to tens of picoseconds effects found in Gadolinium was presented Koopmans et al. in 2009⁵⁵. On the other hand Battiatto et al. found in 2010 another mechanism called superdiffusive spin transport⁵⁶. In this model the majority and minority spin carrying electrons have a different mean free path originating from a different likelihood for their scattering. This idea is depicted in Figure 1.13(b). A higher mean free path for the laser excited hot majority electrons as compared to the minority electrons leads then to a demagnetization upon laser excitation. Experimental evidence for local spin dissipation via spin-flip processes^{57,55,58,59} as well as for the non-local spin diffusion theory^{60,61,56,62} can be found. Recently it has been reported that the both mechanisms are thought to act concurrently where the dominant mechanism depends on the material and sample geometry^{63,64}. In addition to the two main models Zhang et al.⁶⁵ and Bigot et al.⁶⁶ propose a direct interaction between light and the magnetic state of matter as possible way to influence magnetism on the femtosecond timescale. However their findings are mainly based on experiments using thin films of the 3d-band itinerant ferromagnets Nickel, Cobalt and Iron.

The literature on the demagnetization of the heavy rare earth elements focuses mainly on Gadolinium and Terbium as ferromagnetic model systems. A two step demagnetization with a fast component of approximately 0.8 ps and a slower component of 40 ps for Gadolinium and 8 ps for Terbium have been reported using X-ray-Magnetic-Circular-Dichroism experiments (XMCD)^{68,69}. The second demagnetization timescale is attributed to the equilibrium spin lattice coupling timescale that is faster in Terbium due to the larger spin-orbit coupling. This is corroborated by composition-resolved measurements that shows a faster second demagnetization with an increase in the Terbium concentration in $\text{Gd}_x\text{Tb}_{1-x}$ alloys^{70,71,72}. The first fast demagnetization is the same both for Terbium and Gadolinium and it happens in nonequilibrium between phonons and electrons. In the PhD thesis of Trabant⁷³ the antiferromagnetic order of Holmium was studied using resonant time resolved X-ray diffraction experiments at the femtoslicing facility of the BESSY II synchrotron and he found as well two timescales of 0.35 ± 0.08 ps and 22 ± 2 ps during

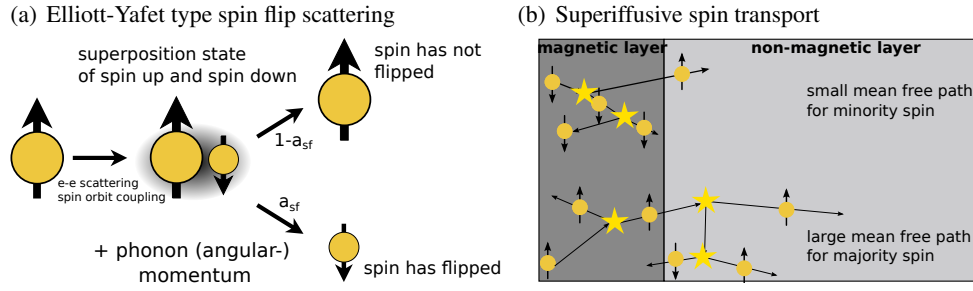


Figure 1.13. Two proposed mechanisms in the literature for ultrafast demagnetization: The Elliott-Yafet type of spin flip depicted in (a) is a local phonon assisted theory that assumes that excited electrons can be scattered into states of a superposition of their two spin orientations. A finite probability a_{sf} exists that the electrons flip their spin by passing their angular momentum to a phonon. The visualization has been adapted from a schematic published in a comment by Münzenberg⁶⁷. (b) The superdiffusive spin transport theory advanced by Battiato et al.⁵⁶ is based on different mean free paths for majority and minority electrons. Their model predicts a smaller inelastic scattering rate for electrons carrying majority spins that thus exit the thin magnetic film faster as compared to minority spins that are more likely to be inelastically scattered.

which the long range antiferromagnetic order is lost. Terbium and Holmium are the left and right neighbors within the lanthanoid series to Dysprosium in the periodic table of elements. I expect them to show very similar magnetization dynamics compared to the here-studied rare earth Dysprosium since their electronic structure only differs by one electron in the 4f-shell. In a private communication about so far unpublished data I was informed that resonant X-ray diffraction measurements on Dysprosium in the antiferromagnetic and the ferromagnetic phase also show a two step demagnetization with a fast time constant of 0.25 ps and a slow time constant of approximately 20 ps⁷⁴.

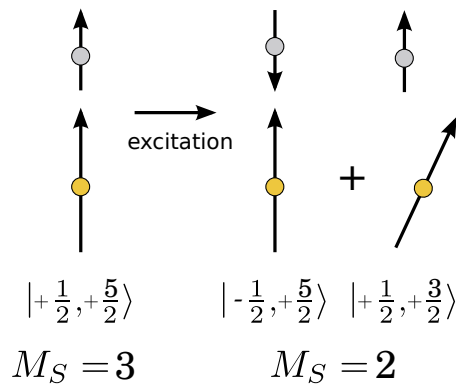


Figure 1.14. Possible demagnetization mechanism for the 4f-spin-system: The laser excitation flips a valence band spin either via phonon assisted spin flip scattering oder superdiffusive spin transport of majority electrons. The intraatomic coupling between the valence electrons and the 4f-electrons then leads to the excitation of the 4f-system. This mechanism is proposed in the PhD thesis of Wietstruck⁶⁸ from which this sketch has been adapted. This view has recently been challenged by the finding of a non-equilibrium dynamics between 5d- and 4f-electrons for many picoseconds reported by Frietsch et al.³⁴, which indicates a weak coupling between these two systems after laser excitation on ultrafast timescales.

Time-resolved studies on transient magnetostriction upon femtosecond laser excitation are to my knowledge scarce. This might be due to the combination of high requirements on the experimental technique. A resolution in the lattice constant on the order of 0.1% in combination with a

temporal resolution on the order of picoseconds or better are desirable to study this effect. Using a very similar Plasma-X-ray source setup as used in my experiments Korff-Schmising et al.⁷⁵ have measured the rise time of the magnetostriction stress component in thin films of SrRuO₃ (SRO) in a SrRuO₃/SrTiO₃ superlattice sample to be in the subpicosecond regime. They observed a decrease of the superlattice oscillation amplitude using Ultrafast X-ray diffraction and concluded that a contractive magnetostrictive stress (σ_m) that only exists in the ferromagnetic phase of the material counteracts the expansive phonon stress (σ_p) in the excited SRO layers. From their measurements they find that the amplitude of the magnetic stress scales as the magnetization M^2 , which has been corroborated by another publication⁷⁶. They conclude that the magnetostriction effect in SRO must be of comparable order of magnitude as the phonon stress and have a similar timescale to account for the observed damping. To my knowledge these two publications are the only other studies of magnetostrictive effects via ultrafast X-ray diffraction where the lattice response is monitored parallel to a demagnetization process.

A theoretical study by Kovalenko et al.⁷⁷ suggests that picosecond sound pulses could be able to nonthermally switch the magnetization in a Terfenol-D (Te_{0.27}Dy_{0.73}Fe₂) film. Terfenol is an alloy that exhibits one of the largest known linear magnetostriction effects and therefore is applied as a magnetic transducer material⁴². An experimental step towards the manipulation of magnetization via lattice strain has already been reported by Kim et al.⁷⁸ who conducted optical pump-probe experiments on Nickel where they generated a sound wave that propagates through the magnetic layer and thus deforms the lattice. They showed that a precession of the magnetization vector can be achieved by the large amplitude strain-waves that modifies the magnetoelastic energy in a the observed Nickel film⁷⁸. The observed precession period of the magnetization vector in Nickel is on the order of hundreds of picoseconds, which is approximately two orders of magnitude larger than the fastest timescale of the experiments reported in this work. However the idea to switch magnetization by sound pulses is complementary to the experiments reported here where I study lattice dynamics triggered by demagnetization.

2 Experimental method and static characterization measurements

The observed effects in the time-resolved measurements are closely linked to the structure and constituent parts of the investigated sample. Measurements of the equilibrium lattice constant of Dysprosium reported in this chapter provide the context for the interpretation of the time-resolved results discussed in the following chapters. At first I introduce the structure of the studied sample. In the second step I briefly introduce the main concept of the X-ray diffraction technique supplemented by a first schematic version of the measurement setup. In a step-by-step description I present the data reduction routine which is used to derive the out-of-plane lattice constants from the photons detected by the X-ray area detector. Finally I report the static results of the temperature dependence of the out-of-plane lattice constants obtained by static X-ray diffraction experiments from using a microfocus X-ray tube.

2.1 Sample structure

The sample that I mainly studied during my thesis consists of thin metal films grown by Molecular Beam Epitaxy (MBE) on a Sapphire substrate. It was supplied by Karine Dumesnil from the University of Lorraine and exhibits the layered structure that Salamon et al.⁷⁹ in 1986 discovered to produce the long range magnetic order within the Dysprosium thin films, which was previously known only for bulk samples.

In the applied growth scheme every layer serves a distinct purpose. The 100nm Niobium layer provides a buffer to avoid reactions between the rare earth metals Dysprosium and Yttrium and the Sapphire substrate⁷⁹. The 10nm Yttrium capping layer is necessary to avoid oxidation of the 100nm Dysprosium thin film that is of main interest of my work. The 10nm Yttrium in between the Niobium buffer layer serves as a seed for the epitactical growth of the Dysprosium film. Epitactical growth is signified by an interface without dislocations between two different materials and in this case it is achieved by very similar in-plane atomic distances between the Dysprosium and Yttrium layers. Dysprosium, Yttrium and Sapphire crystallize in the hexagonally close packed

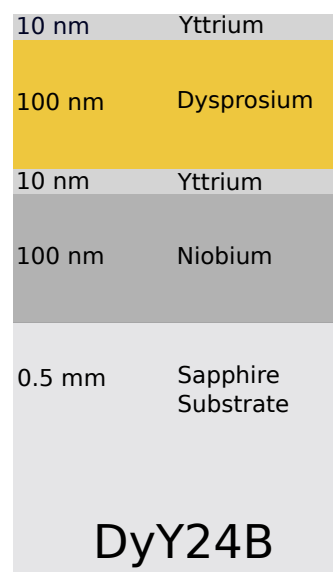


Figure 2.1. Sample structure: Layered structure of the main sample containing a 100nm Dysprosium layer.

crystalline structure and Niobium in the body centered cubic (bcc) phase. The Dysprosium and Yttrium lattice are oriented such that the (0001)-lattice planes are perpendicular to the surface normal. A sketch of the unit cell geometry that schematically depicts the arrangement of atoms in the unit cell for a hcp crystal is provided in Figure 2.2.

The main interest of this work is to study the lattice dynamics within the 100 nm Dysprosium layer. More precisely the conducted experiments detect changes in the inter-planar lattice distance after laser excitation or static temperature change. However the influence of the adjacent Yttrium and Niobium thin films, which are prerequisites for a successful sample growth process need to be taken into account in the analysis and interpretation of the data.

2.2 Crystal Structures and the Principle of X-ray Diffraction

The thin film samples studied in this thesis exhibit a crystalline structure signified by a periodic arrangement of atoms. The conventional unit cell of the hexagonally closed packed Dysprosium is shown in figure 2.2. By translating the unit cell by integer multiples of the indicated basis vectors the entire atomic lattice can be constructed. The crystal unit cell dimensions in Dysprosium are such that the length of the indicated a-axis is approximately $|\vec{a}_i| \approx 3.59 \text{ \AA}$ whereas the out-of-plane lattice plane distance at room temperature is approximately²⁹ $|\vec{c}| \approx 5.65 \text{ \AA}$. The corresponding c/a ratio for Dysprosium is 1.574 which is smaller than the ideal ratio for hexagonal close packing of 1.633. This ratio decreases progressively from Gadolinium ($c/a = 1.596$) to Thulium ($c/a = 1.570$) through the lanthanide series²⁹. This effect is termed "lanthanide contraction" and it has been shown theoretically to have a driving influence on the large variety of magnetic phases observed among the heavy rare earth elements¹⁸.

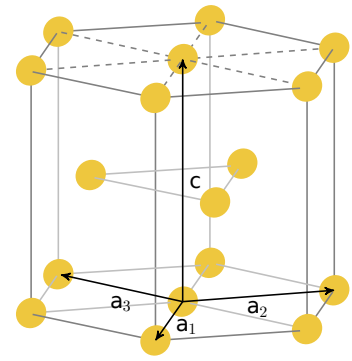


Figure 2.2. HCP unit cell: Conventional unit cell of the hexagonally closed packed (hcp) lattice structure including the used hexagonal unit cell vectors $\vec{a}_1, \vec{a}_2, \vec{a}_3$ and \vec{c} .

One standard method to determine the average distance between atomic lattice planes is to measure the reflection of X-ray radiation from the crystals. The basic case* for the experimental geometry in such an experiment is sketched in Figure 2.3. There the generated X-rays strike the sample at the angle of incidence ω relative to the surface and the X-ray detector monitors the diffraction intensity at an angle θ also relative to the sample surface. Both angles ω and θ can be varied using a goniometer setup that can rotate the sample relative to the incident X-rays and move the detector position on an outer circle.

*Considered here is that the source the surface normal of the sample and the center of the detector lie in the plane of the drawing. In general the detector could be placed at an angle ϕ outside of the plane defined by the source point and surface normal of the sample in order to be sensitive to lattice planes that are not parallel to the sample surface.

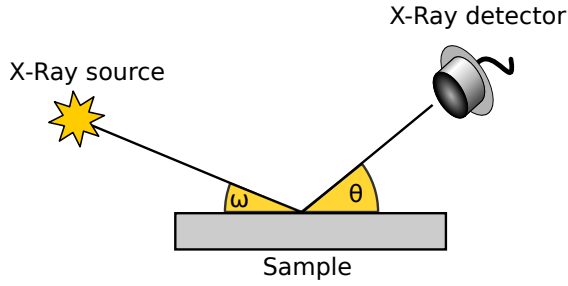


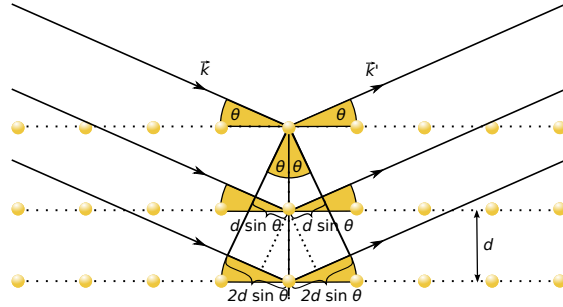
Figure 2.3. Experimental geometry: X-rays impinge on the sample at an angle ω relative to the surface and the diffracted X-ray intensity is detected at an angle θ relative to the surface.

For the special case $\omega = \theta$ H.W Bragg and W.L. Bragg showed for the first time in 1913 that the interplanar spacing d of atoms in crystals can be inferred from the angular position of the reflected intensity using the simple relation:

$$n\lambda = 2d \sin(\theta). \quad (2.1)$$

In this relation λ is the wavelength of the used X-rays and n is the order of the diffraction reflex. A graphical illustration for the derivation of relation (2.1) is shown in Figure 2.4. It shows that the X-ray diffraction intensity is a result of constructive interference of the light scattered elastically from the electron clouds of the periodically arranged atoms. Constructive interference is attained if the optical path length difference between the light scattered in different lattice planes is an integer multiple of the wavelength of the incident light. Under this condition the reflected intensity of the X-rays becomes maximal at this angle θ . One requirement for the diffraction from crystal lattices is thus that the wavelength of the used light is smaller than the lattice constants of the investigated materials which is typically on the order of few Ångström. This requirement is fulfilled by hard X-rays which I define as the part of the electromagnetic wave spectrum have with an energy of 5 keV ($\lambda \approx 2.48 \text{ Å}$) and higher.

Figure 2.4. Bragg relation visualized: The incident and the elastically scattered waves interfere in the far field. At certain angles θ relative to the lattice planes this interference is constructive since the difference in optical path lengths of the incident X-rays is an integer multiple of the used wavelength.



Constructive interference patterns of X-rays were observed prior to the work of Bragg by Friedrich et al. in the group of Laue⁸⁰. They conducted X-ray experiments in transmission geometry and observed defined X-ray maxima to the side of the direct X-ray beam. Their diffraction experiments were clear evidence for the wave nature of the recently discovered X-rays. The detected diffraction maxima were explained based on the so called Laue condition:

$$\vec{k}_{\text{out}} - \vec{k}_{\text{in}} = \vec{Q}. \quad (2.2)$$

It states that constructive interference occurs if the wavevector difference of the incoming X-ray radiation \vec{k}_{in} matches a reciprocal lattice vector \vec{Q} of the crystal one observes constructive interference. The direction of the \vec{k} -vectors is determined by the propagation direction of the light and the direction of the lattice \vec{Q} -vector is oriented perpendicular to the considered crystalline lattice planes. The absolute value of the wave vector is inversely related to the wavelength $|\vec{k}| = \frac{2\pi}{\lambda}$ in the same way as the reciprocal lattice vector is related to the interatomic distance $|\vec{Q}| = \frac{2\pi}{d}$. A schematic sketch of this relation is provided in Figure 2.5.

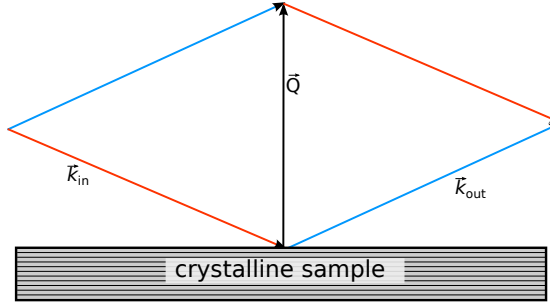


Figure 2.5. Laue condition visualized: The wavevector difference between the outgoing wavevector \vec{k}_{out} and incoming wavevector \vec{k}_{in} needs to match the reciprocal lattice vector \vec{Q} for constructive interference

It can be shown that the Laue condition and the Bragg conditions are equivalent²⁷. In the experiments presented here we study the average out of plane lattice constant d of the sample materials which can be derived from the location of the intensity peaks in reciprocal space q_z by :

$$d = \frac{2\pi n}{q_z} \stackrel{\text{Bragg condition}}{=} \frac{n\lambda}{2\sin(\theta)}. \quad (2.3)$$

In relation (2.3) n is the order of the reflex, λ is the wavelength of the used X-ray radiation[†] and $\theta = \omega$ is the angle of incidence of the X-rays on the sample in the symmetric diffraction geometry. A more detailed theory that makes quantitative predictions on the peak width and the intensity of the observed diffraction intensity maxima is given elsewhere^{26,27}. An introduction to the details of X-ray diffraction especially from thin film samples is provided in the book of Holy et al.⁸². For most of the experiments I report here the so far introduced level of diffraction theory suffices to discuss the observed effects. In the following section I discuss the detailed procedure used to extract the out-of-plane lattice constants from the diffraction intensity.

2.3 Data acquisition routine

In the X-ray diffraction experiments I analyze the average out-of-plane interatomic distance in the materials of the sample, with a focus on the temporal evolution of the Dysprosium lattice constant after laser excitation. The raw data from which this information is inferred consists of the diffracted X-ray photons, which are detected in a certain source-sample-detector geometry over time. In this section I describe the underlying data reduction routine, which is at the heart of my experiments. The general concept of the used data analysis method is described

[†] $\lambda \approx 1.54 \text{ \AA}$ for Cu K_α -radiation used here⁸¹

in the publication "Ultrafast reciprocal-space mapping with a convergent beam" published by Schick et al.⁸³. Based on the existing routine written in the proprietary MATLAB programming environment I implemented a data analysis routine in the open source software Python with some technical adjustments.

Setup for static measurements

Figure 2.6 schematically depicts the geometry between X-ray source, focusing optics, sample and the area X-ray detector that is used in our diffraction measurements. For the static characterization measurements that require no time resolution we employ a continuous wave microfocus X-ray tube containing a copper anode as a source. The micro focus source creates X-rays by accelerating electrons released by thermionic emission from a coiled filament onto a copper anode. The spectrum of the emitted X-rays consists of characteristic emission lines that superimpose a broad background of bremsstrahlung. The characteristic lines match the energy differences between atomic levels in the anode material and originate from the energy release of higher energetic electrons that refill holes created by electron electron collisions in the anode. The broad background originates from the deceleration of the electrons in inelastic collisions, where one possible release channel of the energy is the emission of radiation. The highest obtainable X-ray energy from such a source is set by the accelerating voltage of the electrons. The electrons are focused to a micrometer spot where they emit X-rays into the full solid angle.

A fraction of the isotropically emitted X-rays is collected by the Montel Multilayer X-ray optic^{84,85,86}, which focuses the $\text{Cu K}\alpha$ -part of the emitted spectrum on the sample with a convergence angle of $\Delta\omega \approx 0.3^\circ$ [‡]. X-rays are reflected from the sample at an exit angle θ with respect to the surface, which is determined by the Bragg or Laue condition stated in equations (2.1) and (2.2) respectively.

The diffracted X-rays are measured by an X-ray area detector. For each pixel the detector returns a binary signal that is "1" when it has detected at least one X-ray photon during the last exposure time and "0" otherwise. This single photon counting scheme only works correctly in the low photon flux regime when the probability of more than one X-ray photon impinging on the detection volume of the same pixel during exposure is negligible. This advantage of a very high signal to noise ratio, which is very useful for the operation of the Plasma X-ray source and the X-ray tube where approximately $2 \cdot 10^5 \frac{\text{photons}}{\text{s}}$ are incident on the sample of which only a small fraction in the order of 10^{-3} is diffracted by the thin film layers.

A basic measurement of the reciprocal space of a sample consists then of recording the diffracted photons at different ω - θ angle combinations. In my work I evaluated data from symmetrical scans where the goniometer is moved so that the incident angle of the X-ray photons is symmetrical to the diffraction angle of the photons, which corresponds to scans in reciprocal space along q_z . This is evident from the schematical depiction shown in Figure 2.7.

[‡]A description of the used Montel optic can be found in Section 3.3 where I provide a more detailed account of the setup used for the time resolved experiments.

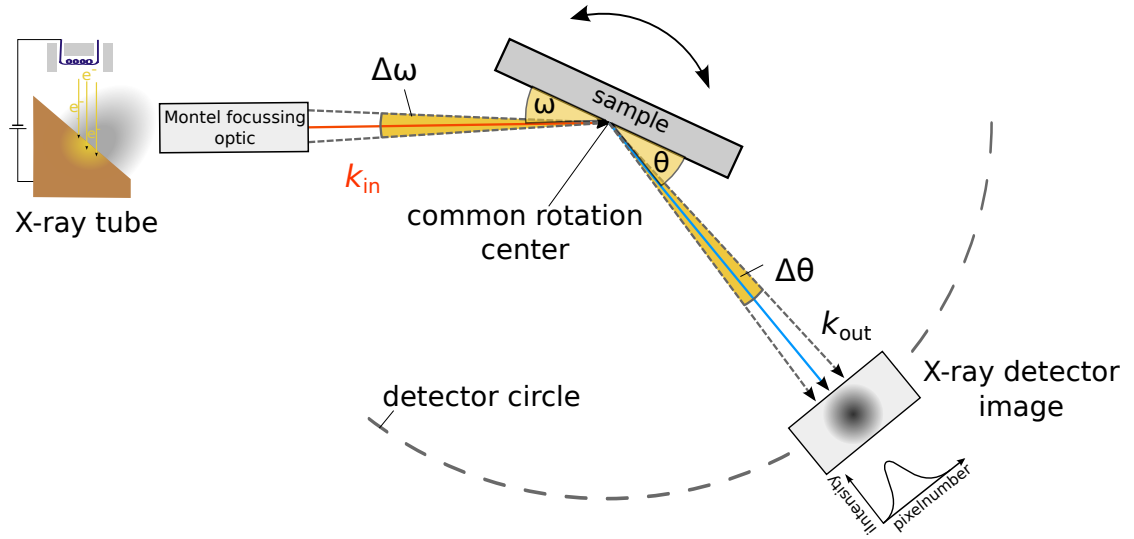


Figure 2.6. Source - sample - detector geometry used in static diffraction experiments: The diverging emission of X-rays that is emitted from a point source of electrons that are accelerated into the copper anode in a microfocus X-ray tube are collected and imaged onto the sample at an angle ω . The Montel optic focuses only the $\text{CuK}\alpha$ -part of the spectrum onto the sample at a convergence of $\Delta\omega = 0.3^\circ$. Diffracted photons are detected using an X-ray area detector at an angle θ . The sample can be rotated relative to the incident X-rays and the detector can be moved on a circle relative to the sample surface.

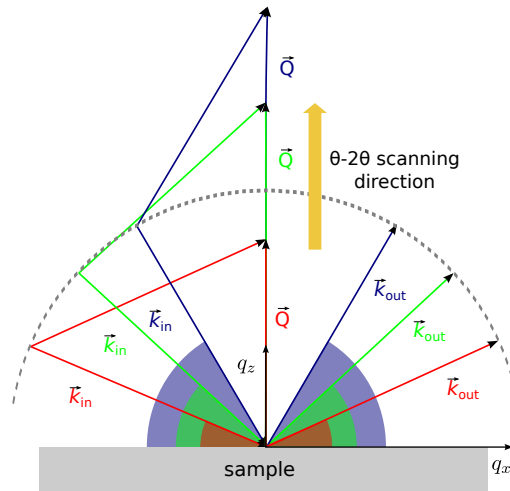


Figure 2.7. Symmetric $\theta - 2\theta$ -scan: The reciprocal spacemaps in this work are acquired by $\theta - 2\theta$ -scans along the q_z -direction in reciprocal space. As shown this corresponds to symmetrically increasing ω and θ . This sketch includes the convention of the orientation of the coordinate system used in this work. A more detailed version of this schematic that takes into account also the nonzero convergence of the incoming X-rays is given in the publication of Schick et al.⁸³.

Raw data

At each detector position the detector returns a raw data image of how many photons have been recorded at each pixel during that exposure time. A graphic example of the observed raw data is given in Figure 2.8. The usage of an area detector is equivalent to doing many single pixel detections at different spatial positions at once. Conducting a scan where both sample angle ω and detector angle θ are increased so that the symmetric geometry is maintained corresponds to scanning along the q_z -direction in reciprocal space. This can directly be seen from the illustration shown in Figure 2.7 that shows a so called $\theta - 2\theta$ scan. This is the only type of scan used in this work but other types of scans of the reciprocal space are possible as the detector in the symmetric $\theta = \omega$ -geometry means that we detect the specular diffracted photons diffracted at an angle of 2ω in the center of the area detector. The additional area of the detector allows for the detection of photons also at different angles $\theta' = n\Delta\theta$ where n is the number of pixels away from the center at the same time and $\Delta\theta$ is the angular acceptance[§] of each detector pixel.

In the same way we have photons incident under different angles $\omega' \in [\omega - \frac{\Delta\omega}{2}, \omega + \frac{\Delta\omega}{2}]$ due to the angular convergence of the source of $\Delta\omega = 0.3^\circ$. Therefore it is possible to detect X-ray intensity from different peaks concurrently.

Transformation to reciprocal space

The concatenation of the measured intensity such as seen in the top of Figure 2.8 already shows maxima in the X-ray diffraction intensity in the direct $\omega - \theta$ space (see Figure 2.9). These maxima are related to the so called "Bragg - peaks" in reciprocal space but receive an undistorted image of the peaks a transformation between the angle axis ω, θ and the reciprocal space axis q_z, q_x has to be carried out, which is discussed in the following.

Each detector pixel in real space counts the photons in a volume element $dV = \Delta\omega\Delta\theta\Delta\phi$, where $\Delta\omega$ is given by the convergence of the incident beam and $\Delta\theta$ and $\Delta\phi$ are given by the finite pixel dimensions in real space. The newly appearing ϕ represents the diffraction angle relative to the plane defined by the source point and the surface normal of the sample. Dividing the number of detected photons by the sampled volume dV leads to a detected photon density $\rho(\omega, \theta, \phi)$ measured in $\frac{\text{photons}}{\text{srad}^3}$. The summation over vertical detector pixels discards the additional information from X-ray photons that are diffracted to away from the detector. In principle we could therefore use a line detector but the amount of detected photons would be significantly lower. The integration is carried out under the assumption that the sample is isotropic since so that measuring the intensity along the q_x -direction is sufficient. This approach simplifies the data routine. After the integration over the in-plane ϕ -components the signal shown in Figure 2.9 is proportional to the two dimensional photon density $\rho(\omega, \theta)$ with the units $\frac{\text{photons}}{\text{srad}^2}$.

[§]The angular acceptance $\Delta\theta$ angular acceptance of each detector pixel, depends on the detector distance l and pixel size $d = 0.172 \mu\text{m}$. It can be calculated by $\Delta\theta = \theta_{n+1} - \theta_n = \tan^{-1}\left(\frac{(n+1)d_{\text{px}}}{l}\right) - \tan^{-1}\left(\frac{nd_{\text{px}}}{l}\right) \approx \frac{d_{\text{px}}}{l} \approx 2.6 \cdot 10^{-7} \text{ rad}$.

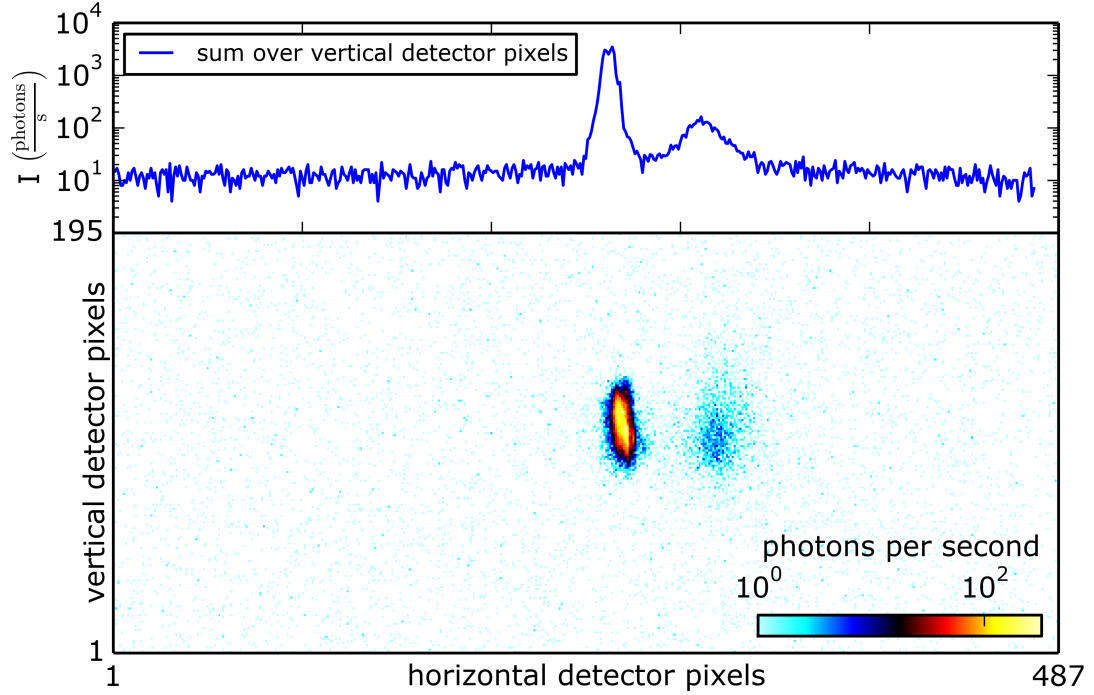


Figure 2.8. Raw data image: Visualization of the raw data obtained from the detector which stands at the beginning of the data evaluation routine. The displayed image is recorded at an angle of incidence of $\omega = 18.9^\circ$ with the detector placed symmetrically at an exit angle of $\theta = \omega$, which corresponds to the sapphire (11-20) - reflection seen close to the center. An additional reflection maximum is visible more to the right and it has its origin from photons diffracted from the (110) Niobium peak that is situated close in reciprocal space. While the horizontal axis corresponds to detection at different exit angles θ , the vertical axis corresponds to photons scattered out of the plane defined by source and surface normal of the sample where the center of the detector lies in that plane. Assuming that the in-plane dimension of our sample is isotropic one integrates over the vertical detector dimension resulting in one slice X-ray diffraction slice of the now 2D-reciprocal space. The obtained slice is displayed in the top of the graph. For each angle of incidence ω one such curve is recorded and then concatenation of all slices makes up the intensity map in angle space shown in Figure 2.9.

The nonlinear transformation

$$\vec{q} = \begin{pmatrix} q_x \\ q_z \end{pmatrix} = |\vec{k}| \begin{pmatrix} \sin(\omega) + \sin(\theta) \\ \cos(\theta) - \cos(\omega) \end{pmatrix} \quad (2.4)$$

maps the shown photon density from the $\omega - \theta$ -space to the reciprocal space of the sample⁸². It is defined using the definition of the reciprocal space coordinate system as it is shown in Figure 2.7 with the so far used convention for ω and θ depicted in Figure 2.3. The mapping from angular space to the reciprocal space allows for an integration over q_x , which considerably increases the signal to noise ratio of the relevant intensity versus q_z curve⁸³ (see also Figure 2.13 top).

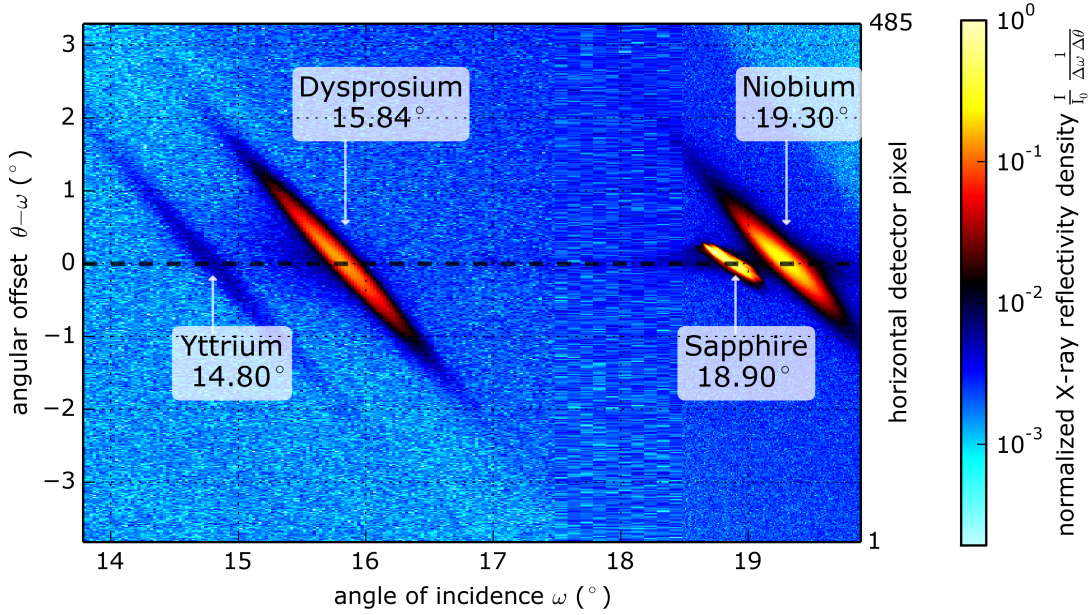


Figure 2.9. Diffraction intensity map in angle space: When the intensity slices obtained for each ω are concatenated one obtains this visualization of the reflected X-ray reflectivity in the angular space. It already shows diffraction maxima for certain $(\omega - \theta)$ -combinations, that can be attributed to the average lattice constant of the materials by Bragg's law $n\lambda = 2d \sin \theta$ for each material. The diffraction intensity is known to be highest where $\omega = \theta$, which defines the horizontal center pixel of our detector marked by a dashed line. From the angular acceptance $\Delta\theta$ of each pixel we can then convert the pixel number to a probed $\theta' = \omega + n\Delta\theta$. The different pixel sizes in this plot originates from the chosen inhomogeneous sampling along the ω axis, that has been conducted to save measurement time in areas where no significant X-ray intensity is known to occur.

The X-ray reflectivity density in Q-space under the nonlinear mapping 2.4 is shown in Figure 2.11. Since the area of each grid cell changes under the transformation it is necessary to rescale the photon density to the new area to conserve the total number of detected photons under the influence of this transformation. For that the density $\rho(\omega, \theta)$ of the old grid cells has to be divided by the Jacobian $J(\omega, \theta)$ of the transformation to obtain the density $\rho(q_x, q_z)$ in the new grid. The

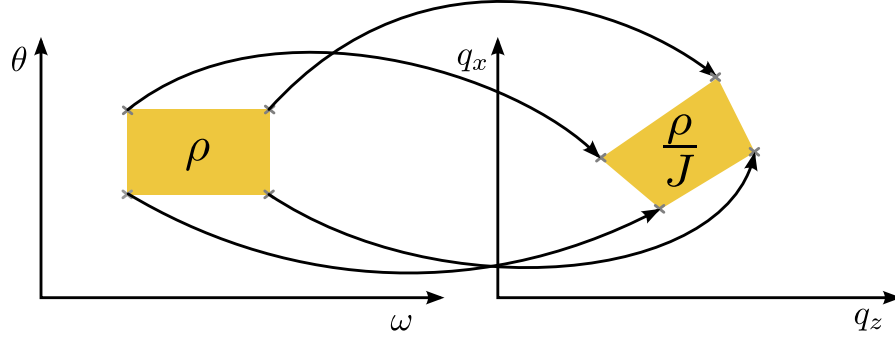


Figure 2.10. Transformation of one pixel from angle space to reciprocal space: The coordinates of the corners of each pixel in Figure 2.9 are separately transformed to the reciprocal space according to relation 2.4. The recorded photon in angle space ρ is divided by the Jacobian of the transformation J stated in relation 2.6 to conserve the number of detected photons. The result of the transformation applied to Figure 2.9 is shown in Figure 2.11.

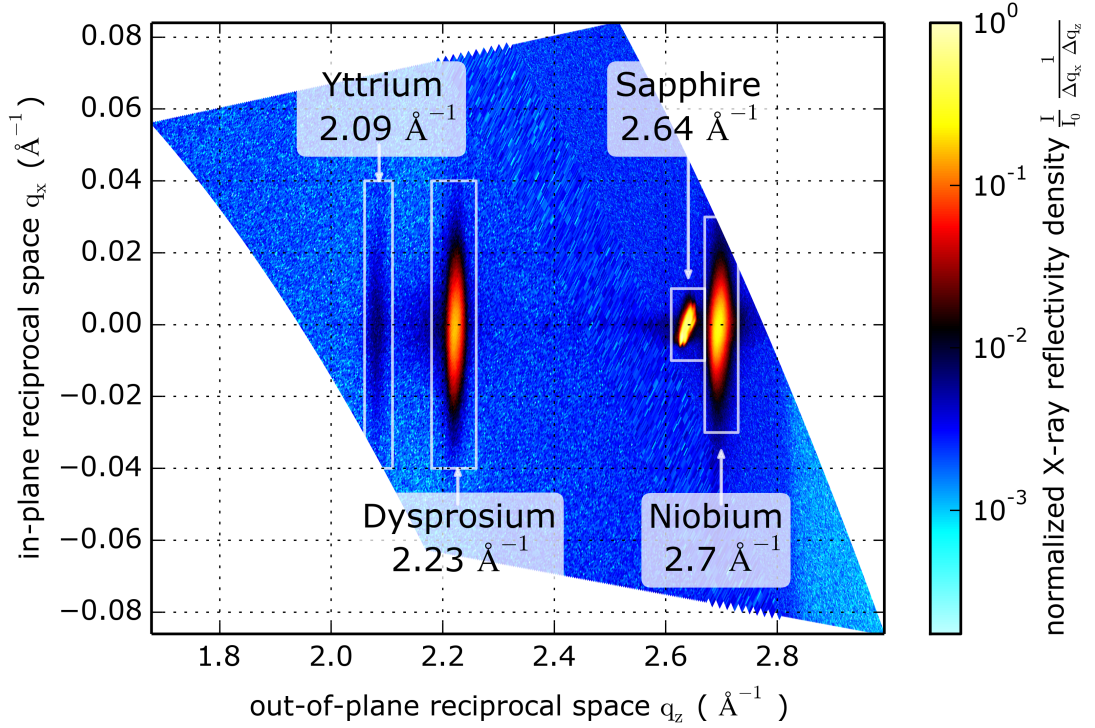


Figure 2.11. Intensity map in reciprocal space: Mapping the measurement grid from the $(\omega - \theta)$ -space via equation 2.4 to the reciprocal space yields the probed grid in the reciprocal $q_x - q_z$ -space of the sample. To conserve the number of photons detected in each grid cell the density from angle space is divided by the Jacobian of the mapping calculated according to relation (2.6). It is noteworthy that the shape of initially rectangular grid cell in angle space is an irregular tetragon after the transformation to reciprocal space. However the reflected photon density is known over the entire connected area patch that was sampled in the $(q_z - q_x)$ -plane.

Jacobian of transformation (2.4) is given by:

$$J(\omega, \theta) = \left| \begin{pmatrix} \frac{\partial q_x}{\partial \omega} & \frac{\partial q_x}{\partial \theta} \\ \frac{\partial q_z}{\partial \omega} & \frac{\partial q_z}{\partial \theta} \end{pmatrix} \right| = |\vec{k}|^2 \left| \begin{pmatrix} \sin(\omega) & -\sin(\theta) \\ \cos(\omega) & \cos(\theta) \end{pmatrix} \right| \quad (2.5)$$

$$= |\vec{k}|^2 (\sin(\omega) \cos(\theta) + \cos(\omega) \sin(\theta)) \quad (2.6)$$

and is determined at the center of each grid cell separately. A schematic sketch for the transformation procedure applied to one pixel is depicted in Figure 2.10.

In order to be able to numerically integrate in reciprocal space to obtain the reflected intensity as a one dimensional function of q_z it is necessary to sample it onto a rectangular grid. The chosen grid can in principle be arbitrarily fine. Its size is only limited by the increasing computational cost of the mapping. It should have at least as many grid cells as the irregular shaped grid shown in Figure 2.11 in order to not discard and distort too much of the measured photon density information. An example for the measured reciprocal spacemap is given in Figure 2.13.

Analysis of the obtained diffraction peaks

Which diffraction peak corresponds to which material can either be estimated from the relative peak intensity or calculated from literature values of the expected lattice constants in case it is not known from previous characterization measurements. The center point of the substrate peak has the highest reflectivity in q -space, to which the displayed intensity density maps shown in Figure 2.13 and Figure 2.11 are normalized here. Due to the large amount of unit cells in the substrate the reflectivity of the substrate peak can be approximated by a delta function in q -space. Therefore the substructure of the sapphire peak represents the instrument function of our setup.

The layer peaks of the Yttrium, Dysprosium and Niobium thin films are structurally broadened due to an epitaxial strain relaxation, a mosaic spread of grain size domains in the material and the finite number of scattering planes contributing to the peak. Their structure corresponds to the convolution of the instrument function with the reflectivity peak that has a finite width in reciprocal space. Their resulting peak shape observed in the measurement is dominated by the structural broadening and the instrument function is not appearing as a pronounced feature in the peaks. This is similar to what has been observed in the thin film measurements reported by Schick et al.^{87,83}.

The mapping from each of the detector pixels in direct $(\omega - \theta)$ -space (Figure 2.9) to the chosen grid in reciprocal space (Figure 2.13) including the calculation of the associated Jacobian element has to be done only once for a series of measurements under the same geometrical conditions. This data-analysis process is conducted for each dataset. The extracted peaks in q -space can then

be fitted by a Gaussian function of the type $Ae^{-\frac{(q_z - q_{z0})^2}{2\sigma^2}}$. The resulting center of the peak q_{z0} is a measure for the average lattice constant d of the materials in direct space via $d = \frac{2\pi n}{q_{z0}}$, where n is the order of the diffraction peak. The peak width is determined by the standard deviation σ . It is a measure for the distribution of lattice constants and thereby the strain of the thin film⁸⁸. A

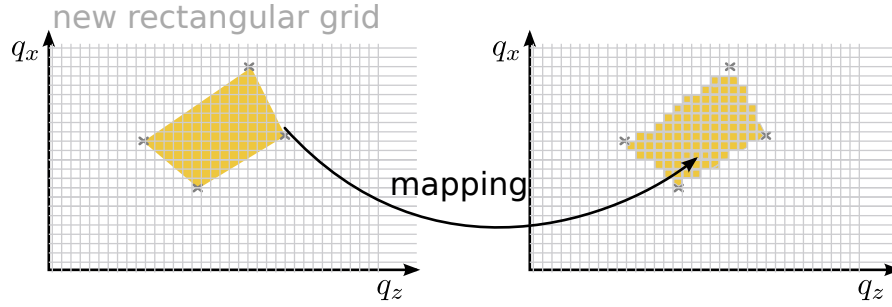


Figure 2.12. Mapping the density to a rectangular grid: For numerical integration in reciprocal space the irregular tetragon pixels (yellow) obtained after the transformation are mapped to a new finer rectangular grid (gray). To which irregular shaped patch the center of a gray grid cell belongs determines which intensity is assigned to it. The result obtained from mapping the density shown in Figure 2.11 to the new rectangular grid is shown in Figure 2.13.

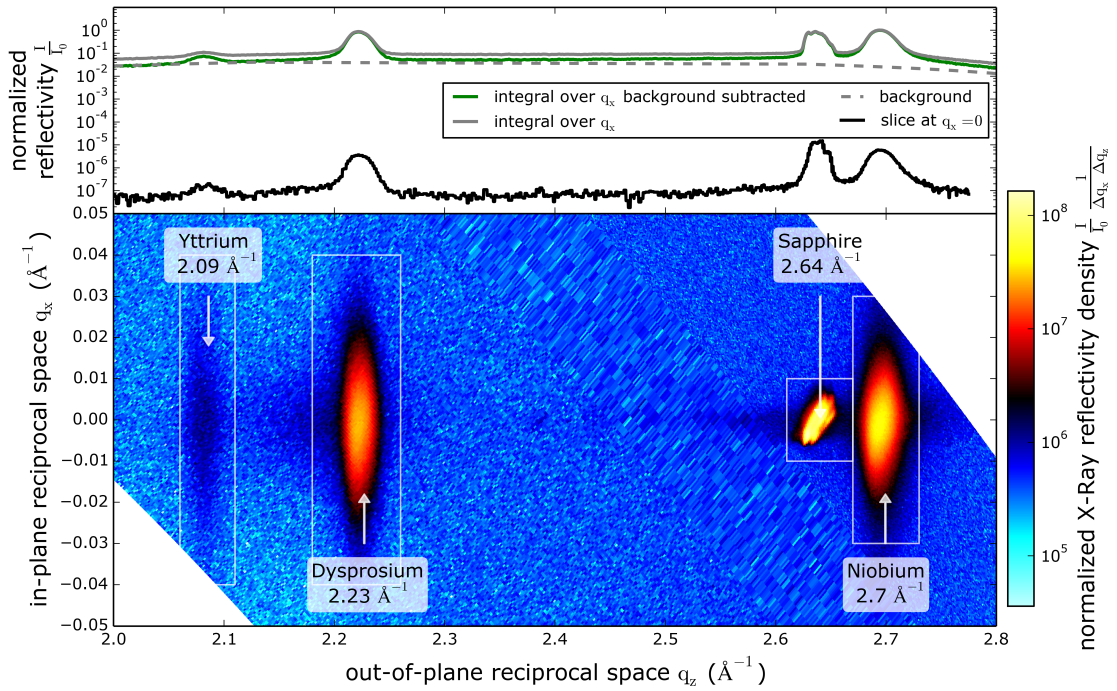


Figure 2.13. Intensity density mapped to a fine rectangular grid in reciprocal space: Reflectivity density from figure 2.9 mapped to a chosen fine rectangular grid in q -space. The distortions due to the tiling of the reciprocal space with the fine but rectangular grid are small, so that Figure 2.11 and 2.13 appear identical. From the fine new grid it is possible to directly select areas of the reciprocal space that correspond to the Bragg peaks of each material in order to analyze them as shown in Figure (2.14).

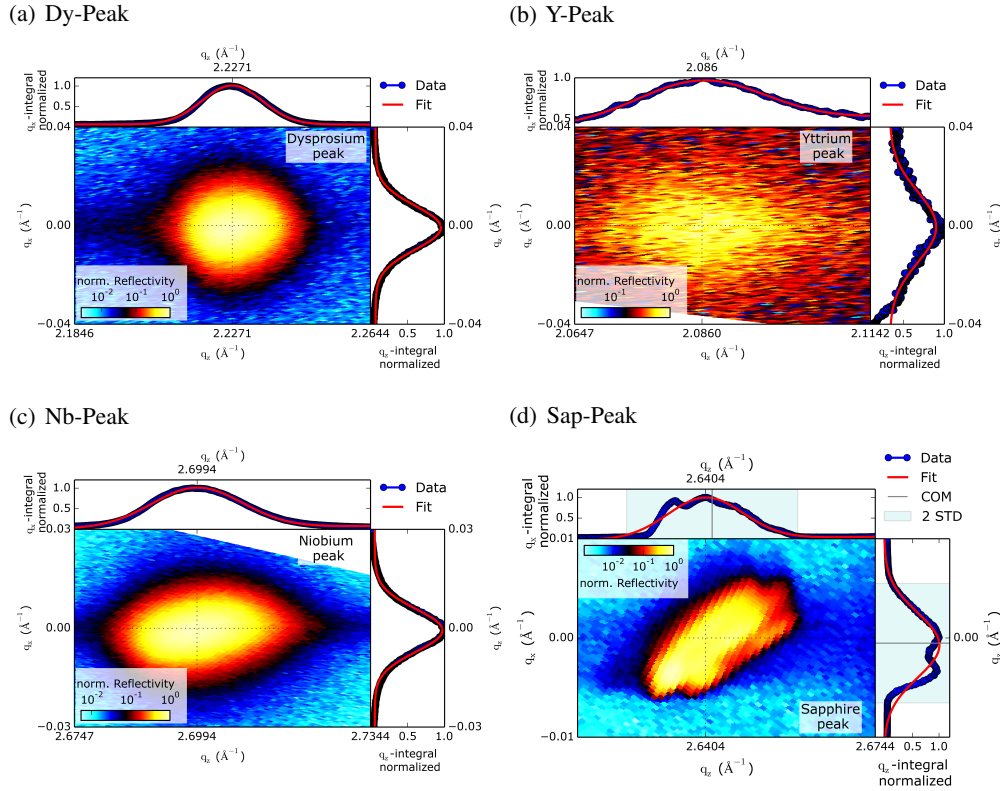


Figure 2.14. Overview and analysis of each diffraction peak: Top and side panel of each peak show the integrated intensity as a function of q_z and q_x respectively. They include a best fit of a Gaussian peak with a linear background. From such data I extract the peak center and peak width as FWHM of the Gaussian and evaluate their relative changes as a function of temperature in static characterization experiments or their change in time after the excitation with a femtosecond laser pulse. The shown extracts correspond to regions marked in the reciprocal space-map 2.13 by white boxes. Due to the substructure of the instrument function the Sapphire peak is not well approximated by a Gaussian fit. To report the peak center I thus use the model free parameters center of mass and to report its width the standard deviation derived from the variance of the distribution.

small width relates to a homogeneous material layer whereas a larger peak width corresponds to an inhomogeneously strained layer. In addition to fitting a Gaussian peak it is also possible to calculate the center of mass as a measure for the average interatomic distance according to:

$$\text{COM} : \bar{x} = \frac{\sum_{i=0}^n x_i I(x_i)}{\sum_{i=0}^n I(x_i)}. \quad (2.7)$$

The corresponding measure for the width of this distribution is the standard deviation. It is related to the second central moment, the variance as follows:

$$\text{STD} = \sqrt{\text{Variance}} = \sqrt{\frac{\sum_{i=0}^n (x_i - \bar{x})^2 I(x_i)}{\sum_{i=0}^n I(x_i)}}. \quad (2.8)$$

2.4 Static Measurements

For the static measurements the sample DyY24B containing the 10 nm thin Yttrium capping layer is mounted on its sample holder in the center of the goniometer. For these measurements the sample is under constant illumination of Cu-K α X-ray radiation from a microfocus X-ray tube that serves as a source of X-rays. At each temperature a so called $\theta - 2\theta$ scan is carried out. This means that the sample is rotated relative to the incoming X-rays and the detector is positioned at the same angle relative to the surface, which implies that in figure 2.3 $\omega = \theta$ is fulfilled for the center of the area detector. At each angle step the intensity of the X-rays is detected by the X-ray area detector. The recorded diffraction intensities are mapped to the part of the reciprocal space that is sampled by the scan as described in the previous section. Integration of the detected intensity over q_x yields the reflected X-ray intensity as a function of q_z . To obtain the center of the reflectivity peaks a Gaussian is fitted to the data or the center of mass of the peak can be calculated.

The results of the q_z scans for each material peak at different temperatures are displayed in Figure 2.15. All materials except Dysprosium exhibit a shift of the Bragg peak to smaller q_z . This behavior corresponds to an average lattice expansion. The Dysprosium peak on the other hand shifts to larger q_z , which corresponds to a lattice contraction with increasing temperature as can be seen from in Equation (2.3). This effect lasts up to the phase transition temperature of $T_N = 180\text{ K}$ after which the normal thermal expansion behavior is exhibited also in the Dysprosium layer.

An evaluation of the peak center to quantify the thermal expansion behavior of the lattice with temperature of each of the materials is shown in figure 6.5. One indeed observes clearly two distinct transitions in the Dysprosium lattice constant as a function of temperature shown in the top graph. Starting from room temperature Dysprosium contracts upon cooling up to $T \approx 180\text{ K}$. There the lattice starts to expand as the repulsive magnetostrictive force attributed to the onset of the magnetic ordering sets on. A second transition is seen at approximately 48 K upon cooling (at 61 K upon heating the sample). At these temperatures the lattice constant rapidly increases which is indicative of the first order antiferromagnetic to ferromagnetic phase transition that goes along with a crystal symmetry change from the hexagonal system to an orthorhombic unit cell⁴. I observe a clear hysteresis of the lattice constant in this ferromagnetic to antiferromagnetic phase

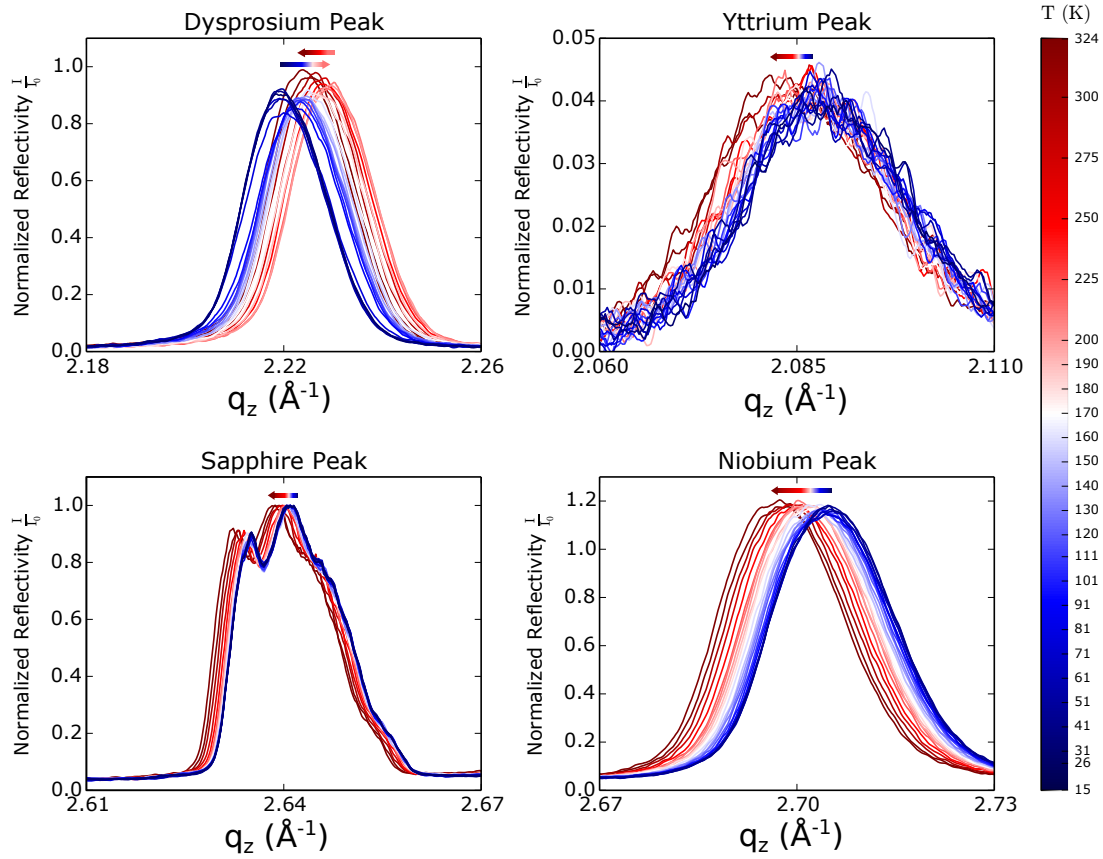


Figure 2.15. Temperature dependence of the diffraction maxima of the materials as function of q_z : The shown data originate from a series of $\theta - 2\theta$ -scans carried out at different temperatures of the sample. Increasing the temperature from 15 K to 325 K has the effect that the Yttrium, Niobium and Sapphire peak are shifting to lower q_z (indicated by arrows), which corresponds to an increase in their out-of-plane lattice distance. On the other hand the Dysprosium peak up to its Néel temperature $T_N = 180$ K shifts to larger q_z , which corresponds to a contraction. When Dysprosium is heated above its Néel temperature it resumes normal behavior and the peak shifts towards smaller q_z as it is the case for the other materials. From this data the center of the peak as well as the width of the peak is determined by Gaussian fits. The results are displayed in Figures 6.5 and 2.17 respectively.

transition. It is important to further note that the other materials in the sample do not show any particular features in their lattice constant as a function of temperature apart from the expected expansion by increasing the temperature.

The shift of the associated Curie temperature to lower temperatures as compared to the bulk values is known to occur when Dysprosium is grown onto Yttrium, which tends to stabilize the antiferromagnetic phase whereas Erbium stabilizes the ferromagnetic phase and increases T_C .⁹. One possible explanation for this behavior found by Dumesnil et al.⁹ is that the in-plane strain exerted by to the lattice mismatch of the in-plane lattice constants of Dysprosium ($a = 3.590 \text{ \AA}$), Yttrium ($a = 3.647 \text{ \AA}$) and Erbium ($a = 3.558 \text{ \AA}$) is the driving factor for the shift in the Curie temperature. This suggests that if the in-plane strain is contractive the ferromagnetic phase is stabilized as opposed to the case when the in-plane strain exerted by the adjacent layer is expansive that this thought to stabilize the antiferromagnetic phase. This finding shows once more the strong coupling between magnetism and the lattice in rare earth materials already from static measurements.

One more piece of information that can be inferred from the static q_z -scans is the evolution of the peak width as a function of temperature. The analysis results from a Gaussian FWHM and the standard deviation obtained by the second moment are shown in Figure 2.17 for each of the materials. A general trend that increases the peak width as a function of temperature is seen for all materials except the Dysprosium layer. There we see pronounced maxima in the peak width at the phase transition temperatures. I associate this increase of the peak width with inhomogenous strain present within the film⁸⁹. I interpret these maxima as to be indicative of domains of different magnetization states that are present in the thin film. Such domains have been proven to exist by the different reflection intensities of circular polarized resonant X-rays reflected from the Holmium thin films¹⁴ with different helicities. Lang et al. found the in-plane dimensions of the domains to be of the order of $50 \mu\text{m}$ for bulk Holmium.¹⁴. The existence of such domains has also been inferred by the observation of the speckle pattern the reflected coherent X-rays from a magnetic tau peak that occurs due to the additional periodicity of the spin spiral in the material¹⁵. These domains of different magnetization states would therefore have a different magnetostriction contribution which would lead to an averaging over a distribution of lattice constants, which leads to an effective broadening of the diffraction peak. Especially at the ferromagnetic to antiferromagnetic phase transition the broadening becomes very pronounced since the lattice undergoes a large change when switching from one phase to the other. Therefore the large peak width could be due a spatial averaging effect over domains in different magnetic phases by the X-ray probe beam that has effective footprint diameter of approximately $900 \mu\text{m}$.

In conclusion of this chapter I want to stress that the static diffraction data shown here evidence that the magnetostrictive contribution, which leads to the anomalous thermal expansion behavior reported for bulk Dysprosium^{4,90,41}, is also present as expected in the used thin film sample. The obtained reference curve of the lattice constant versus temperature is used to interpret the time-resolved experiments reported in the next section.

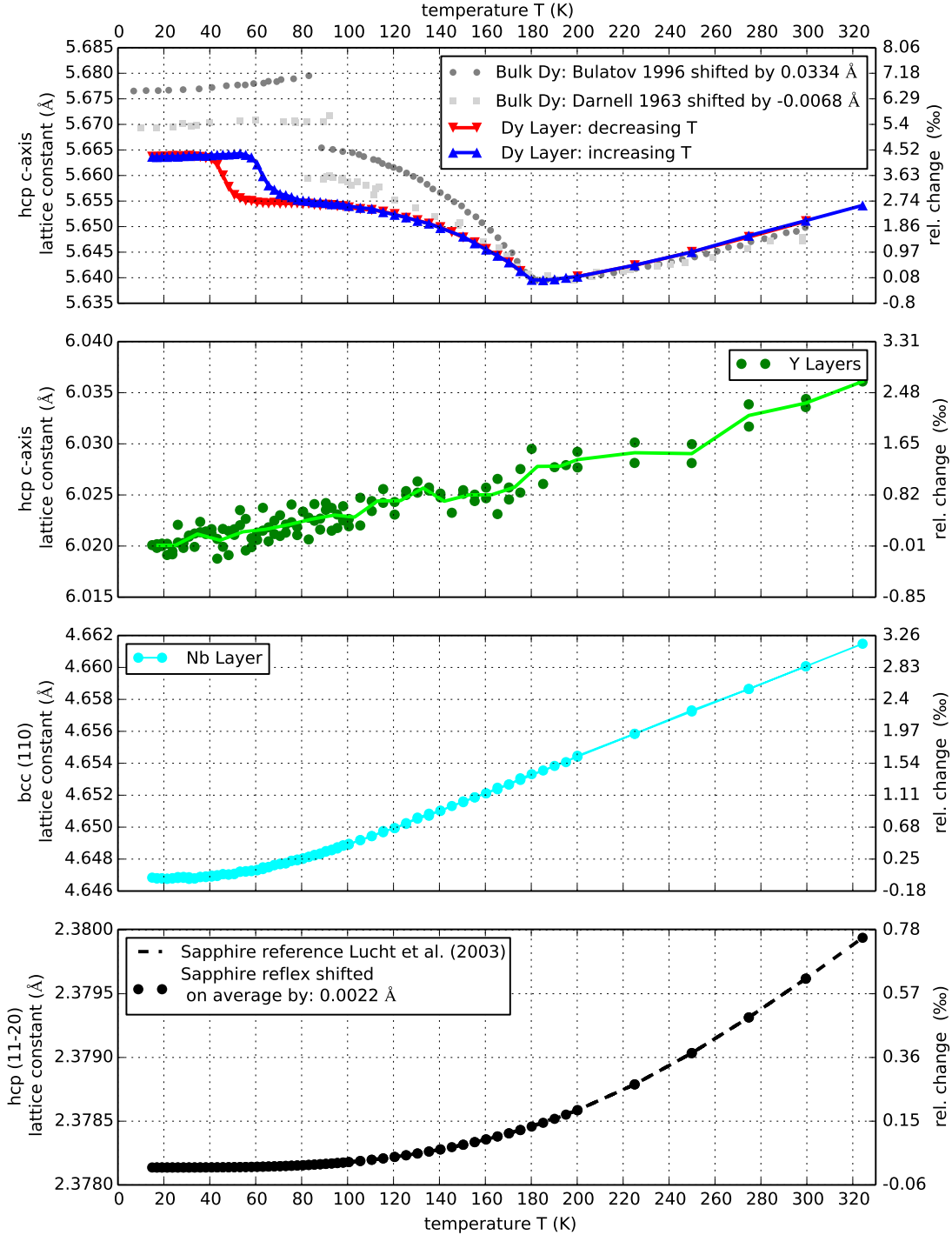


Figure 2.16. Characterization of the out-of-plane interatomic distances: The center of the Bragg peaks in q_z have been converted to the corresponding out of plane lattice constants of the materials shown in figure 2.15. The c-axis lattice constant of Dysprosium (a) displays a distinct phase transitions at $T \approx 180$ K, which is attributed to the second order paramagnetic - antiferromagnetic phase transition. The first order phase transition from the antiferromagnetic to the ferromagnetic state takes place at ≈ 48 K whereas it occurs at ≈ 61 K when Dysprosium is heated from the ferromagnetic state. Our thin film sample shows qualitatively similar behavior like bulk Dysprosium reported in the literature^{4,41}, where the shift of the first order phase transition might be due to in plane epitaxial strain effects from a small lattice mismatch between Yttrium and Dysprosium^{9,91}. Note that the Yttrium (b) and Niobium (c) buffer layers as well as the Sapphire substrate (d) do not display any transitions in the examined temperature range. The axis on the right denotes the change in the interatomic distance relative to smallest value of the corresponding measurement.

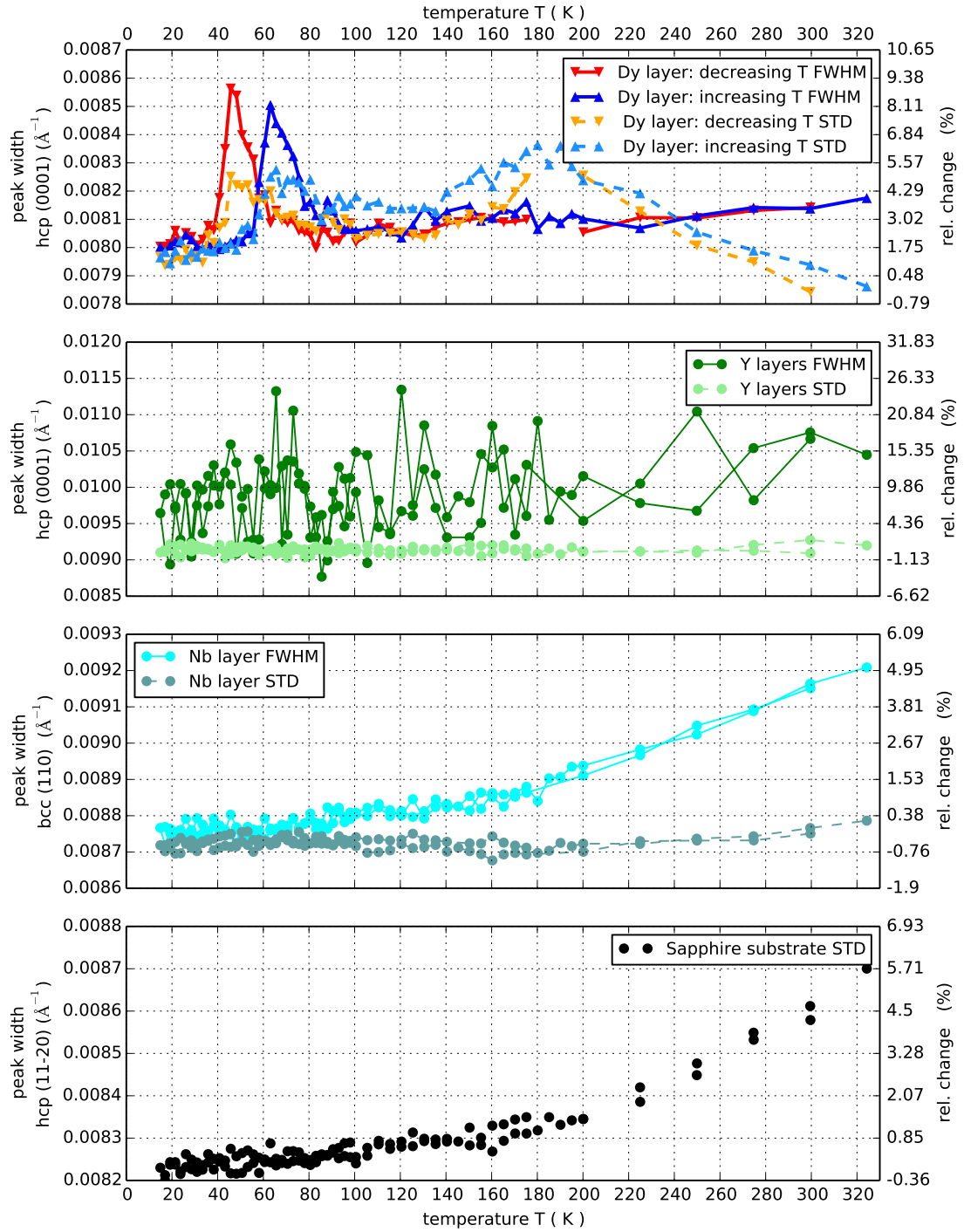


Figure 2.17. Peak width change: Shown here are the FWHM of a Gaussian fit (solid lines) as well as the standard deviation derived from the second moment of the intensity of the Bragg peaks in the selected regions of interest (dashed lines). It is remarkable that the peak width of the Dysprosium Bragg peak exhibits a maximum at both phase transition temperatures. An increased peak width indicates the existence of inhomogeneous lattice strain in the layer⁸⁸.

3 Time resolved measurements

This chapter contains the time-resolved experiments carried out in the framework of my thesis. After a brief introduction to the used pump-probe technique that allows for measuring time-resolved processes I will state how the necessary X-ray pulses with femtosecond duration are created. A brief overview over the entire setup is given in section 3.3. It is followed by the measurement principle that is used for the determination of the temporal and spatial overlap between the pump laser and the probing X-rays on a daily basis. The description of the relevant parts for the time-resolved measurements is followed by selected measurement results of time-resolved X-ray diffraction experiments. The mechanism of relativistic electron propagation in solid targets⁹² that leads to the X-ray emission and the technical aspects of the setup are not discussed in great detail in my work. Interested readers are referred to the literature mentioned in the course of the description. A more in-depth description of technicalities of the used setup is provided in the master thesis of my colleague Jan Pudell⁹³ (in German).

3.1 Principle of pump-probe experiments

The pump-probe technique is the mainly used experimental method to conduct time-resolved experiments of processes that occur on a timescale of few picoseconds and faster. In such experiments a short pump pulse triggers dynamics in the sample and a delayed short probe pulse detects changes in the sample. To record a full temporal evolution of the triggered process snapshots of the accessible properties have to be taken at various delays between excitation and detection. The total time resolution of this process is determined by the pulse length of the pump and probe pulses* and not by the speed of the detector.

Certain prerequisites are usually fulfilled to apply the pump-probe technique:

- **Reversible processes:** The dynamics induced by the pump pulses need to be repeatable, in the sense that the same process happens after each laser excitation. Therefore the studied processes have to be reversible.
- **Detection without impact:** The probe pulse merely detects the sample properties and does not induce dynamics in the sample by itself[†].
- **Adequate repetition rate:** The time period between the pump pulses should be long enough for the sample to recover its initial state before it is excited once more. High repetition rates are nevertheless desirable in the measurements for better statistics.

*A temporal jitter introduced by an instable synchronization of the pump and probe pulses also sets a limit to the temporal resolution of the method.

[†]Probe pulses provided by free electron laser sources are actually so intense that they often cause irreversible sample damage. As a consequence a fresh sample has to be used after each laser shot.

- **Synchronization and spatial overlap of pump and probe processes:** A temporal synchronization that stabilizes the pump pulses (excitation) with respect to the probe pulses (detection) in time needs to be available, as well as a method to create spatial overlap on the two pulses.
- **Sufficiently short pulses:** In order to resolve the fast dynamics it is crucial to use pump and probe pulses that are considerably shorter than the typical timescale of the process.

In my experiments the pump pulses are approximately 100fs long near infrared laser pulses with a center wavelength of approximately 800nm coming from a chirped pulse amplified Titanium-Sapphire laser. The probe pulses are approximately 250fs long bursts of Cu-K $_{\alpha}$ -radiation, that are used to detect the average out of plane distance between atoms in each of the sample materials by X-ray diffraction. A detailed discussion on the estimated pulse length is given in the context of the temporal overlap determination discussed in Section 3.4. A schematic sketch of the pump-probe geometry of the used sample is given in 3.1.

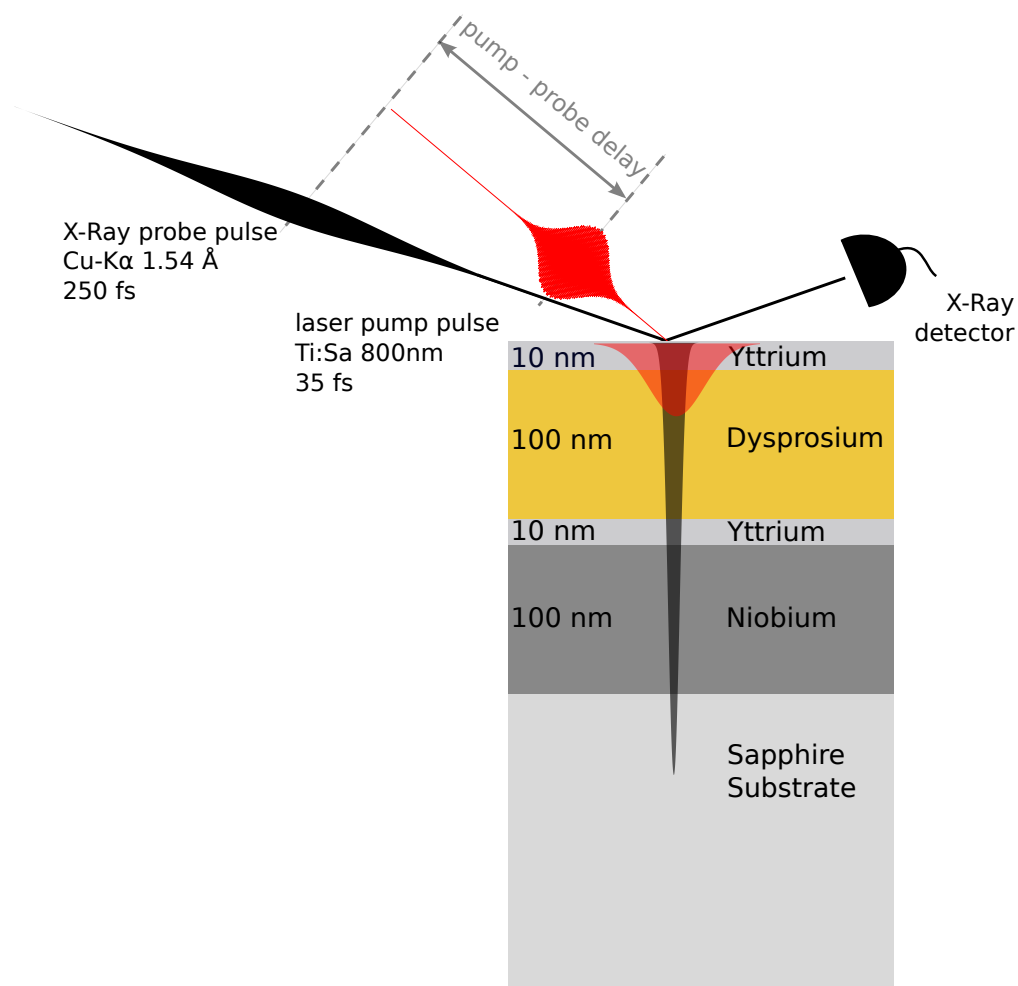


Figure 3.1. Schematic visualization of the pump-probe experiment: A fs-laser pump pulse excites dynamics in the sample and 250 fs X-ray pulse detects transient changes in the out-of-plane interatomic lattice spacing via X-ray diffraction. The optical penetration depth at the central wavelength of 800 nm has been estimated via ellipsometry to be 20 nm. The penetration depth of the hard Cu K α X-rays is on the order of micrometers.

3.2 Generation of short X-ray pulses

The plasma X-ray source (PXS) generates pulses of copper K_α radiation by focusing an intense laser pulse onto a $15\ \mu\text{m}$ or $20\ \mu\text{m}$ thin copper band^{2,94}. The rather complex process of X-ray generation by an intense laser field incident upon a metal surface with its details is an active area of research by its own right^{95,96,97}.

In a simplified picture the working principle of a plasma X-ray source can be viewed in an analogy to a classical X-ray tube. In an X-ray tube electrons are released by thermionic emission and then accelerated onto a metal anode in a static electric field. Upon collision with the target the decelerated electrons emit a broad bremsstrahlung background. This broad background is superimposed by material-specific sharp lines of high intensity. These characteristic lines correspond to the energy level differences in each of the electronic states in the anode. Instead of the dc-accelerating electric field between the cathode and the anode the electrons are accelerated in the oscillating laser field. Figure 3.2 schematically compares the geometry of the X-ray emission side by side.

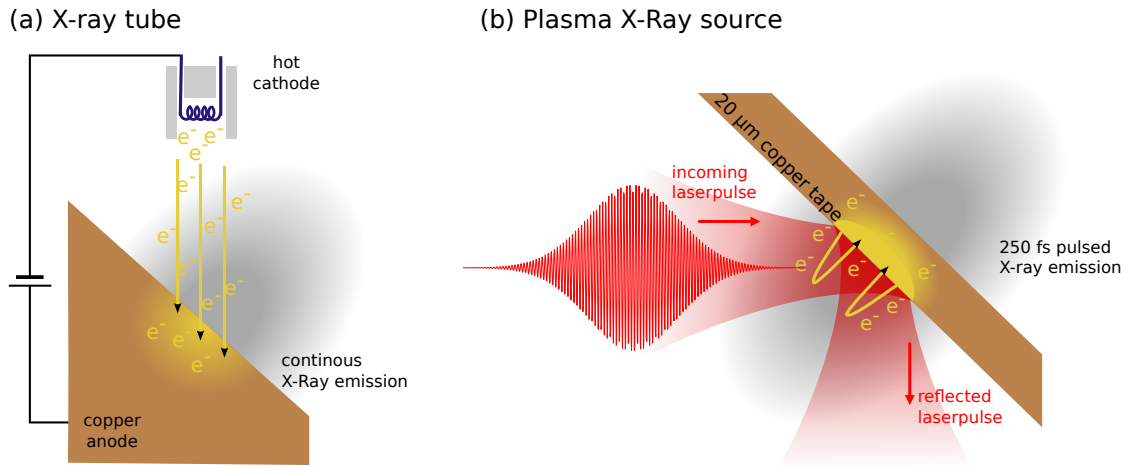


Figure 3.2. Schematic comparison between X-ray generation processes: (a) X-ray emission from a conventional X-ray tube where thermionically emitted electrons are accelerated in a dc field onto a solid copper target. The colliding electrons lead to the emission of X-rays with a continuous bremsstrahlung-spectrum that is superimposed by very sharp characteristic lines. (b) Geometry in the plasma X-ray source setup. The large electric field of the focused laser pulses is sufficient to free the valence electrons of the copper creating a plasma of free electrons at the metal surface. These free electrons are accelerated in the oscillating electric field of the laser pulse and upon recollision with the metal emit X-rays with a similar spectrum as the continuous wave X-ray tube. The advantage of the laser plasma source is that the emission processes is limited in time to the duration of the laser pulse and the ballistic propagation time of the electrons in the thin copper foil. The sketch of the laser plasma generation setup has been adapted from Weißhaupt et al.⁹⁵.

At first the intense electric field pulse of the laser creates a plasma of free electrons by stripping the weakly bound valence electrons from the copper either by tunneling or direct ionization. In the following the free electrons are accelerated first away from the sample and then back towards the

copper tape as the electric field of the pulse changes sign. The following X-ray emission process is then similar to the mechanism of the classical X-ray tube with the important difference that it is limited in time to approximately 250 fs duration. This is longer than the original 40 fs-laser pulses due to the ballistic excursion time of the accelerated electrons through the thin copper foil. The resulting emission of the X-ray fluorescence is in principle isotropic in a 4π -solid angle but it is shaped by the absorption of the copper band that runs at an angle of 45° relative to the incident laser beam. The copper band itself runs at a speed of approximately $60 \frac{\text{mm}}{\text{s}}$ and has a width of 2 cm a thickness of $20 \mu\text{m}$ and a length of approximately 360 m. A fresh tape usually lasts for 12 hours of continuous measurement time. A photograph of a used copper band held in front of a homogeneous white lamp is shown in Figure 3.4 in order to give a visual impression of the laser penetration into the metal band.

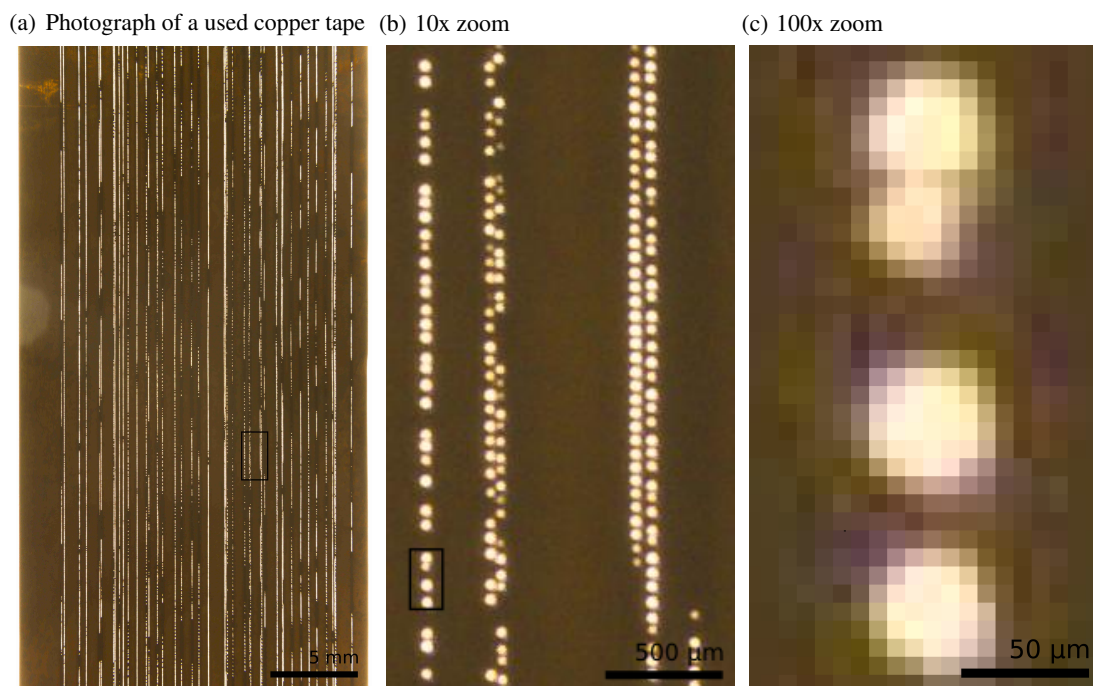


Figure 3.3. Copper tape after usage in the plasma X-ray source: Multiple lanes where the laser has penetrated the copper are visible in the section of the copper tape shown in (a). Graphics (b) and (c) show the selected area in (a) at a relative magnification of 10 and 100 respectively. Each hole is created by only one laser pulse. The hole diameter can be estimated by visual inspection of the image to be roughly $55 \pm 15 \mu\text{m}$ which corresponds to 8 ± 2 pixels. The image shown here was taken by Jan Pudell.

The emitted X-ray spectrum from the plasma X-ray generation process is depicted in Figure 3.4. A Monte-Carlo approach that simulates the electron path and their energy when they recollide with the target has been carried out by Brunel⁹⁸. Recently it has been shown by Weisshaupt et al. that the photon yield of a plasma X-ray source can be increased by a factor 25 when IR-radiation with a wavelength of $3.8 \mu\text{m}$ is used in the process due to the longer excursion time of the electrons in the accelerating electric field⁹⁹.

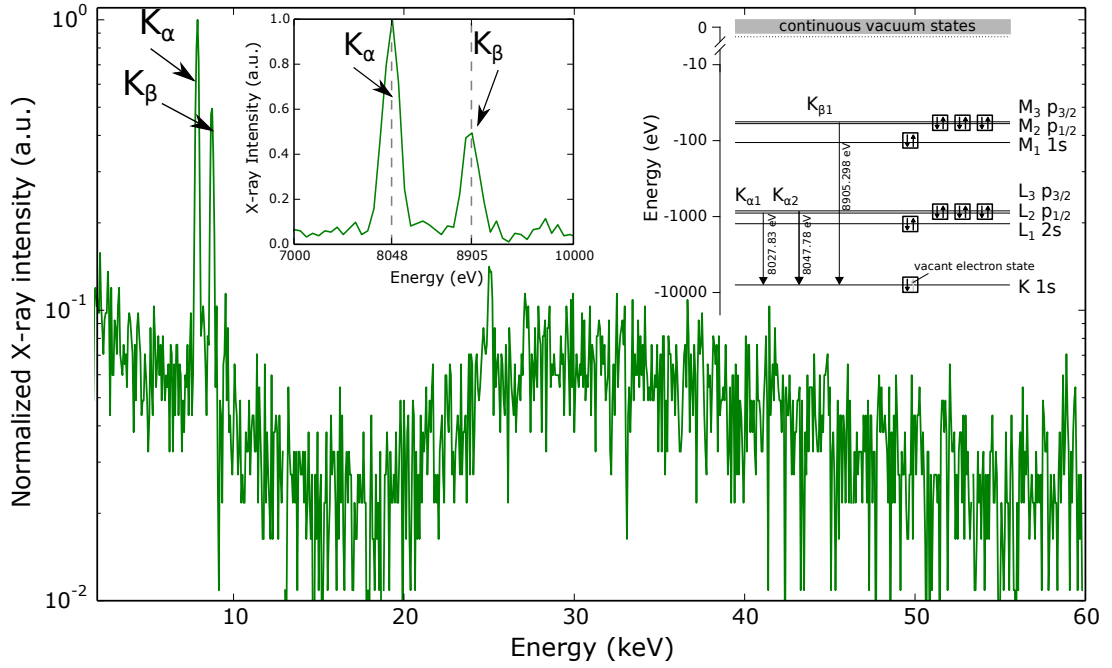


Figure 3.4. X-ray spectrum emitted by the plasma X-ray generation process from a copper tape: The green line depicts the X-ray fluorescence spectrum detected by an energy resolved X-ray detector that uses the electron generation in Silicon as detection process. Two sharp lines are observed at approximately 8 keV, which corresponds to the $Cu K_{\alpha 1}$ and $Cu K_{\alpha 2}$ transitions that are dominant above a bremsstrahlung background that has its maximum intensity at approximately 30 keV. The left inset depicts a zoom into the Copper K-edge energy region that shows that the K_{β} -emission peak is only half as intense as the $Cu K_{\alpha}$ peaks. The right schematic inset sketches the electronic transitions between the atomic levels of Copper that are involved in the generation of the observed characteristic lines. Values for the transition energies are taken from the X-ray data booklet⁸¹.

3.3 Experimental setup at the plasma X-ray source

We use a plasma X-ray source that was constructed in the year 2009 in a joint project of the Bargheer group the University of Potsdam and the Institute for Scientific Instruments in Berlin-Adlershof and put into operation in the course of the PhD thesis of Daniel Schick¹⁰⁰. The description of the prototype plasma X-ray source for this setup at the Max-Born institute has been given by Zamponi et al.⁹⁴. The publication by Schick et al.² that contains the specifications of the source also introduces the normalization scheme that enables us to monitor the unavoidable intensity fluctuations of the X-ray source.

Pioneering work on the development of the plasma X-ray source with femtosecond time resolution in the kHz regime was published in 2002 by Korn et al.¹⁰¹ and Jian et al.¹⁰². Their work was elaborated to point size sources by Zhavoronkov et al.^{103,104}, which eventually resulted in the design that is currently used. Although this type of source has matured to reliable day to day operation in laboratories where it can be run stable for hours its development has not stopped. In 2014 a new plasma source in Beijing was reported alongside with a modified normalization scheme¹⁰⁵ that operates with only one area detector. Recently it was shown theoretically as well as practically that the operation of a plasma X-ray source at driving laser fields in the mid IR ($\lambda = 3.9\mu\text{m}$) increases the peak X-ray photon yield by a factor of 25 despite a two orders of magnitude smaller laser field intensity, due to the longer excursion times of the electrons in the accelerating fields^{99,95}.

The first measurements using a plasma X-ray source setup studied the ultrafast melting of order in laser excited in Langmuir-Blodgett films¹⁰⁶ or GaAs semiconductors^{107,108}. After the PXS technology for ultrafast X-ray diffraction was established, even more intricate experiments where atomic motion was monitored non-destructively with femtosecond time resolution in Bismuth¹⁰⁹ and GaAs/AlAs superlattices¹¹⁰. An overview of the field was published in 2006 by Bargheer et al.⁸⁸ and most recent developments and perspectives for the field have been outlined in 2014 by Elsaesser and Woerner¹¹¹. The focus of the ultrafast dynamics group in Potsdam in the past have been time-resolved experiments on laser excited perovskite materials^{87,112,113,114}.

Figure 3.6 shows a schematic sketch of the setup. The fs-laser pulses are created in an oscillator laser that uses a Titanium doped sapphire crystal as active medium where mode-locking is achieved via the Kerr-lensing effect in a specially designed resonator^{115,116}. The oscillator emits femtosecond laser pulses at a repetition rate of 80 MHz with approximately 3 nJ of energy per pulse. Pulses selected at a rate of 1 ,kHz are amplified in a two stage regenerative amplifier laser. The amplification is based on the chirped pulse method¹¹⁷ where the pulses are first stretched in time via a grating setup, then amplified in an additional gain medium and finally compressed again in a grating compressor. The resulting laser pulses entering the setup have a repetition rate of 1 ,kHz, an energy per pulse of 7.5 mJ at a central wavelength of 800 nm and a pulse duration of approximately 40 fs. The emission spectra of the oscillator and the amplifier laser are shown in Figure 3.5.

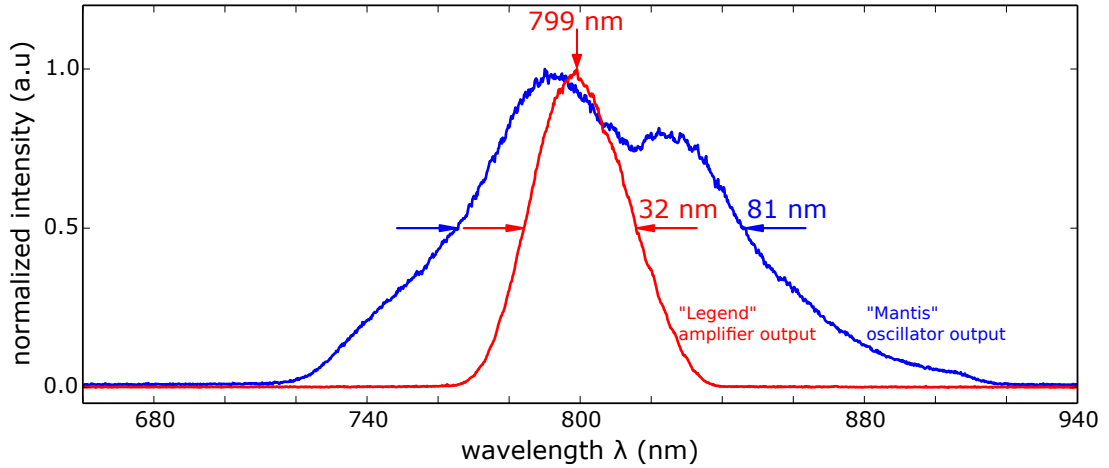


Figure 3.5. Spectra of the used laser pulses: Spectrally broad intensity profiles are necessary to generate short laser pulses. Using the frequently applied Gaussian approximation for the spectral profiles one obtains that bandwidth limited pulses from the oscillator laser would have a duration of 11.6 fs and the minimal pulse duration of the amplifier system would be 29.7 fs. Nonlinear chirp and deviations of the real spectra from the Gaussian approximation prolong the pulses in reality. Details of the short pulse generation process are for example given in the monographs by Rulliere¹¹⁸ or Diels and Rudolph¹¹⁹.

In the following the pulses are split so that 80% of the laser pulse energy is directed to the plasma X-ray source to generate the probe pulses and the remaining 20% are available as pump pulses. The pump pulses are directed over a mechanical delay stage that determines the relative timing between pump and probe pulses. Shortening the optical path of the pump pulses with respect to the beam path of the X-ray probe pulses corresponds to probing the sample dynamics at a later time after the excitation. The size of the beam profile of the pump pulses on the sample can be set by a telescope, which has an adjustable focal length. Once the size of the beam profile is set one can adjust the incident fluence of the pump laser pulses with an adjustable attenuation setup that uses the relative orientation of a $\frac{\lambda}{2}$ -waveplate and a polarizer. The polarizer is set to only transmit p-polarized light and any s-polarized components of the electric field that are introduced by the waveplate are attenuated. The beam position of the center of the pump beam is held stable within an accuracy of $30\,\mu\text{m}$ by an active beam stabilization. For that a very small part of the pump pulses is transmitted through the backside of a polished mirror and detected by a conventional CCD-camera. Its center position is monitored and deviations from a set value are corrected via an active steering mirror at a frequency of 2 Hz. This active beam stabilization ensures that the position of the excitation pulses does not deviate markedly from its set position in the course of the measurement day.

The probe pulses are generated by focusing the remaining 80% of the pulse energy on a $20\,\mu\text{m}$ thin copper foil as described in the previous section 3.2. The copper tape is constantly moving so that each laser pulse hits a fresh target. This is necessary since each laser pulse creates a small hole in the tape due to the large amount of energy deposited in the sample within a short amount of time,

which leads to the evaporation of the copper. As a consequence moving, transparent plastic bands are necessary to collect the debris from the resulting sputtering process in order to protect the entrance and exit windows of the plasma source from complete coverage by the evaporated copper.

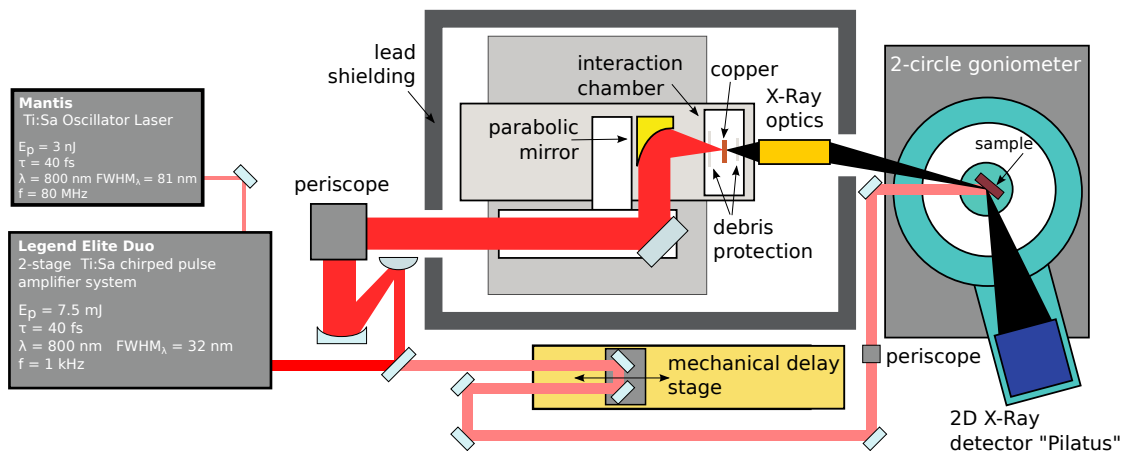
The emitted X-ray probe pulses are focused by a commercial Montel multilayer optic⁸⁴ onto the sample in order to increase the X-ray flux. The used optic is based on diffraction of X-rays from elliptically bent multilayers with a graded periodicity that is optimized to only reflect the $\text{Cu K}\alpha$ part of the created X-ray spectrum⁸⁵. This type of X-ray optic has been reviewed by Bargheer et al.⁸⁵ and Shymanovich et al.⁸⁶ and found to be suitable compromise between photon flux, time-smearing effects, convergence and spot size for ultrafast X-ray diffraction. A schematic sketch of the X-ray beampaths within the optics and the emitted intensity profile is given in Figure 3.7. Only X-ray photons that have been reflected twice are focused to a $\approx 300\text{ }\mu\text{m}$ large X-ray spot, which is incident on our sample. The beam of X-ray photons that goes directly through the X-ray optics is blocked. The intensity of the lower single reflected X-ray beam is monitored on a X-ray intensity detector to provide a reference for the incident photon flux on the sample² that fluctuates due to unavoidable mechanical instabilities originating from the uneven spooling of the copper tape within the plasma focus.

The X-ray photons incident on the sample under the angle ω are partially diffracted and then detected using an X-ray area at an angle detector θ that operates in single photon counting mode. For each of the $172\text{ }\mu\text{m} \times 172\text{ }\mu\text{m}$ large detector pixels it is registered whether or not an X-ray photon has been detected within this shot. The data evaluation that maps the detected X-ray intensity from the real space coordinates ω and θ to the reciprocal-space coordinates q_z, q_x is the same for the static measurements. The implementation of the ultrafast reciprocal- space mapping using a convergent X-ray beam is described in section 2.3 based on a publication by Schick et al.⁸³.

Table 3.1 lists and compares the properties of the pump and probe pulses at our plasma X-ray source that we used in day to day operation for the measurements on the Dysprosium thin film samples.

The advantage of this 6m by 1.5m tabletop setup in comparison to large scale synchrotron radiation or free electron laser facilities is the high time resolution paired with easier access to beam time and the much lower operational costs. The trade-offs are the low brightness that follows from the low X-ray flux, the lack of temporal and spatial coherence, the missing control over the X-ray polarization state and the very limited control over the used X-ray energies which can only be changed by changing the metal foil material. However many seminal experiments in ultrafast X-ray diffraction have been realized at plasma X-ray source setups^{106,107,108,110}.

(a) **Top view on the entire setup.** It includes both the laser and X-ray beampaths.



(b) **Side view on the plasma X-ray source:** Includes the X-rays generation and the relevant parts in the subsequent X-ray propagation. The laser beampath has been omitted for clarity.

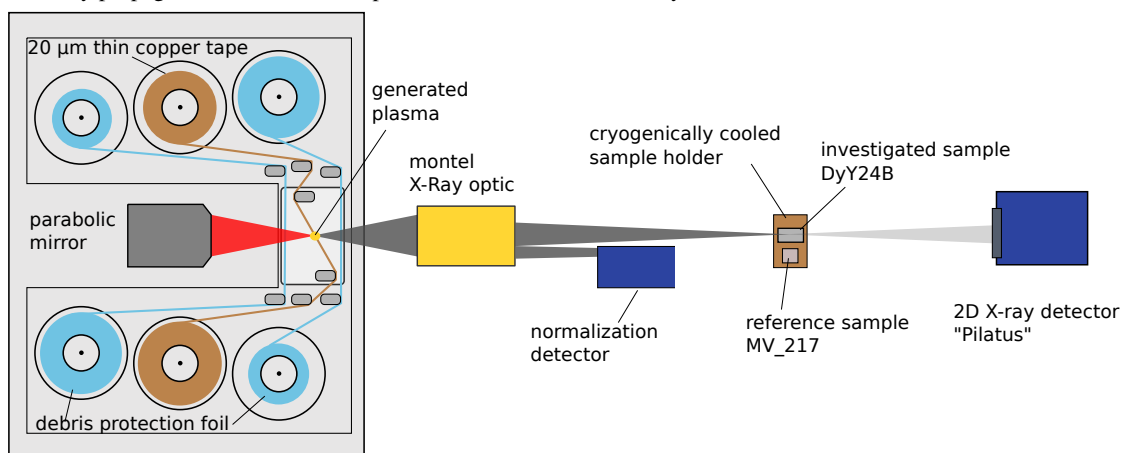


Figure 3.6. Schematic sketch of the tabletop plasma X-ray source: A Titanium sapphire chirped-pulse amplification setup creates 40fs laser pulses with a center wavelength of 800nm and a pulse energy of approximately 7.5mJ at a repetition rate of 1 ,kHz. Approximately 80% of the pulse energy is split off at a beam splitter and directed to the plasma X-ray source where the laser pulses are focused on a 20 μ m thin copper foil. The high intensity short pulses incident on the metal surface lead to X-ray emission from the created plasma at the copper surface. The resulting X-ray pulses are collected in transmission by a Montel multilayer optic that focuses the CuK α -part of the spectrum onto the sample. The sample is mounted in the center of the goniometer on a cryostatically cooled sample holder in a vacuum environment. The diffracted X-rays are collected by a two dimensional X-ray detector in the second circle of the goniometer. The remaining 20% of the laser pulse energy is directed over a delay stage that sets the relative timing between the arrival of the pump and probe pulses and it is then focused onto the sample as excitation where it triggers dynamics. The two sketches shown here are an adaptation from the originally published description of the setup by Schick et al.² and from the detailed description given in the master thesis of Pudell⁹³.

Table 3.1. Overview over typical pump and probe pulse properties: The following table contains some key specifications under which we operate the plasma X-ray source setup on a daily bases.

	laser pump pulses	X-ray probe pulses
energy per photon	1.55 eV	8048 eV ($\text{Cu K}_{\alpha 1}$)
wavelength	800 nm	1.54 Å
bandwidth FWHM	30 nm	FWHM $\text{Cu K}_{\alpha 1} = 2.2$ eV $\text{Cu K}_{\alpha 1} - \text{Cu K}_{\alpha 2} = 20$ eV
pulse duration	100 fs	250 fs
repetition rate	1 , kHz	1 , kHz
photons per pulse on sample	$4 \cdot 10^{14}$	$2 \cdot 10^5$
typical energy per pulse	0.1 mJ	260 pJ
typical angle θ rel. to surface	$28^\circ - 40^\circ$	$14^\circ - 20^\circ$
typical beam dimensions FWHM _x × FWHM _y	$1200 \mu\text{m} \times 1200 \mu\text{m}$	$300 \mu\text{m} \times 300 \mu\text{m}$
typical spot size on sample	$1.8 \cdot 10^{-2} \text{cm}^2$	$2 \cdot 10^{-3} \text{cm}^2$

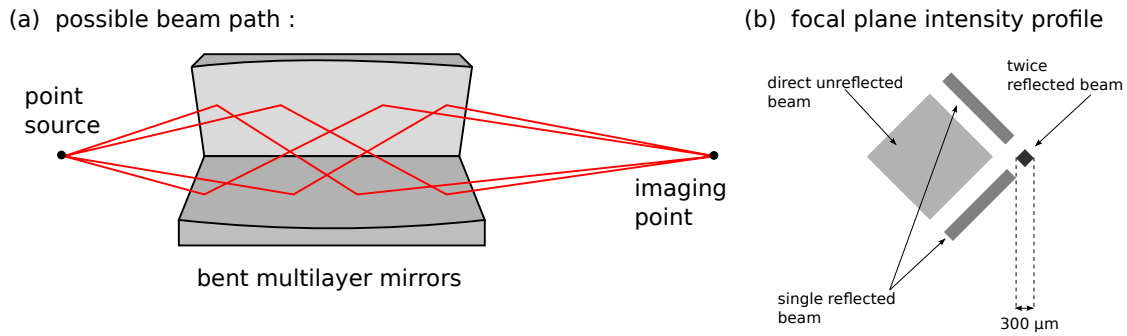


Figure 3.7. Schematic of the functioning principle of the used X-ray optics: The emitted X-rays from a point source are focused using the Kirkpatrick-Baez scheme¹²⁰. This sketch of the Montel optic is an adaptation of the sketch shown in the publication of Bargheer et al.⁸⁵ that compares the different X-ray optics for femtosecond X-ray diffraction and the Master Thesis of Pudell⁹³ that also holds a very detailed description of our setup.

3.4 Determination of the temporal overlap

For the time-resolved pump-probe experiments it is crucial to know the position of the delay stage at which the fs-optical pump laser pulses and the fs-X-ray-probe pulses arrive at the same time. This relative timing is called time zero, abbreviated as t_0 . Since our delay stage is part of the pump beam-path, it follows that shortening the optical beam path, while leaving the X-ray-path fixed, corresponds to probing the sample at later times after the excitation. Compared to optical experiments the photon flux of $10^5 \frac{\text{photons}}{\text{s}}$ of X-ray photons at the sample position is insufficient for the use of nonlinear effects as direct cross-correlation technique. The method we use to determine t_0 utilizes the nearly instantaneous onset of intensity oscillations of superlattice diffraction peaks from a metal-insulator superlattice after laser-excitation. It is based on the results published by Korff-Schmising et al.¹²¹ that have been elaborated and corroborated by the work of Bojahr et al.¹¹². In their work they carefully compare the t_0 obtained from the superlattice response to t_0 obtained by direct optical cross-correlation signals at the position of the sample between the pump laser pulses and the laser used to create the X-ray emission on the copper tape. They come to the conclusion that an accuracy of ± 100 fs can be achieved by using the superlattice oscillations^{121,112}.

A schematic sketch of the physical principles of X-ray diffraction from the used superlattice sample is provided in Figure 3.8. Our reference sample contains 30 thin crystalline films alternating between 13.7 nm transparent Barium-Strontium-Titanate (BST - $(\text{Ba}_{0.7}\text{Sr}_{0.3})\text{TiO}_3$) and 7.3 nm absorbing metal Lanthanum-Strontium-Manganate (LSMO - $(\text{La}_{0.7}\text{Sr}_{0.3})\text{MnO}_3$) on a transparent Strontium-Titanate substrate (STO - SrTiO_3). All of these materials crystallize in the perovskite structure shown in the top left of Figure 3.8 with very similar unit cell dimensions. This sample has been grown by Ionela Vrejoiu by Pulsed Laser Deposition (PLD)¹²².

The entire structure of the reference sample, depicted in the bottom left of Figure 3.8, leads to a static diffraction pattern shown the bottom right which can be simulated by dynamical X-ray diffraction using for example the UDKM1Dsim toolbox⁷. The simulated pattern agrees with the measured X-ray diffraction curve that is broadened by the instrument function of our plasma X-ray source. The diffraction pattern can be factorized into contributions from the superlattice periodicity of approximately 21 nm shown as the blue curve in the middle right panel and contributions from the single layer lattice plane periodicity shown in the top right of 3.823 Å and 4.0317 Å for LSMO (green curve) and BST (red curve) respectively. The periodic maxima in the X-ray diffraction signal are termed superlattice peaks and they are labeled according to a convention adapted from Bauer¹²³ that the zero order superlattice peak occurs in reciprocal space at $q_0 = n \frac{2\pi}{c_{\text{avg}}}$, where c_{avg} is the average interatomic distance in one double layer and n is the order of the investigated reflex. In our case $n = 2$ and $q_0 \approx 3.173 \text{ Å}^{-1}$. The amplitude of these superlattice peaks is determined by an envelope function $E(q)$ (not shown) that results from absolute value square of the complex sum of the scattering amplitudes of the single layer peaks as follows.

$$E = |A_{\text{LSMO}}(q) + A_{\text{BST}}(q)|^2 \quad (3.1)$$

The full details of the envelope formalism are described by Herzog et al.¹¹⁴. In the top right of

Figure 3.8 I show the simulated X-ray diffraction intensity of the single layers proportional to the scattering amplitudes of the isolated layers of LSMO $|A_{\text{LSMO}}(q)|^2$ (green curve) and BST $|A_{\text{BST}}(q)|^2$ (red curve), respectively.

An approximate[‡] formula modeling the observed X-ray diffraction intensity $I(q_z)$ is stated in equation (3.2). It is a sum of the superlattice peak intensity resulting from a product between the envelope and their intensity and the substrate diffraction intensity all convoluted with the instrument function F_{instr} of the plasma X-ray source:

$$I(q_z) = F_{\text{instr}} * (I_{\text{SL}}(q_z)E(q_z) + I_{\text{STO}}) \quad (3.2)$$

Having discussed the constituents of the X-ray diffraction contribution one can explain what happens upon laser excitation of this superlattice structure. Since only LSMO absorbs energy from the fs- laser pulses a periodical stress pattern that expands the LSMO layer from the BST-LSMO interfaces is generated. The LSMO expansion leads to a shift of the green curve to lower q_z and to a shift to higher q_z in the red curve. As long as heat expansion of the BST layer is negligible the superlattice periodicity remains unchanged in the process as only the LSMO-BST interface within the superlattice unit cell shifts. the total size of the LSMO-BST superlattice unit cell remains thus unchanged. The diffraction intensity of the superlattice peaks nevertheless starts to oscillate, since the the periodic strain pattern in the LSMO created by the fs-laser excitation shifts the constituents of the envelope function. The process can be compared to modulating the structure factor of the superlattice unit cell by displacing the elements of its basis. In our case we detect the X-ray diffraction intensity of the SL-1 peak that is strongly enhanced upon laser excitation. This is due to the increased constructive overlap of the diffraction amplitude of the BST and the LSMO layers as both envelopes shift towards each other. The resulting intensity oscillations of this superlattice peak are displayed in Figure 3.9.

In our experimental setup the reference sample is mounted right below the investigated sample. In the beginning of each measurement day it is translated up to the measurement position to determine t_0 of this day. For this we measure the oscillations in the intensity of X-rays diffracted by the SL-1 peak that occur as the relative timing of the laser pump pulses to the X-ray probe pulses is scanned by the delay stage, as exemplarily shown in Figure 3.9. For our purposes the onset of these large superlattice oscillations after laser excitation is regarded to be instantaneous as it has been shown for similar Strontium-Ruthenate (SRO - SrRuO_3) - STO superlattices under similar high fluence excitation¹¹². In Figure 3.9 I compare two methods that can be used to infer t_0 from the result. The first possibility is to fit a decaying cosine oscillation multiplied by a step function as stated in equation (3.3).

$$f(t) = \underbrace{\Theta(t - t_0)}_{\text{step at } t_0} \left(\underbrace{(m(t - t_0) + n)(\cos(\omega(t - t_0) + \pi) + 1)}_{\text{linearly decaying oscillations}} \right) \quad (3.3)$$

[‡]Strictly speaking one would need to discuss the superposition not of the Intensity but of the complex electric field amplitude to correctly predict the behavior of all superlattice intensities see Herzog et al.¹¹⁴.

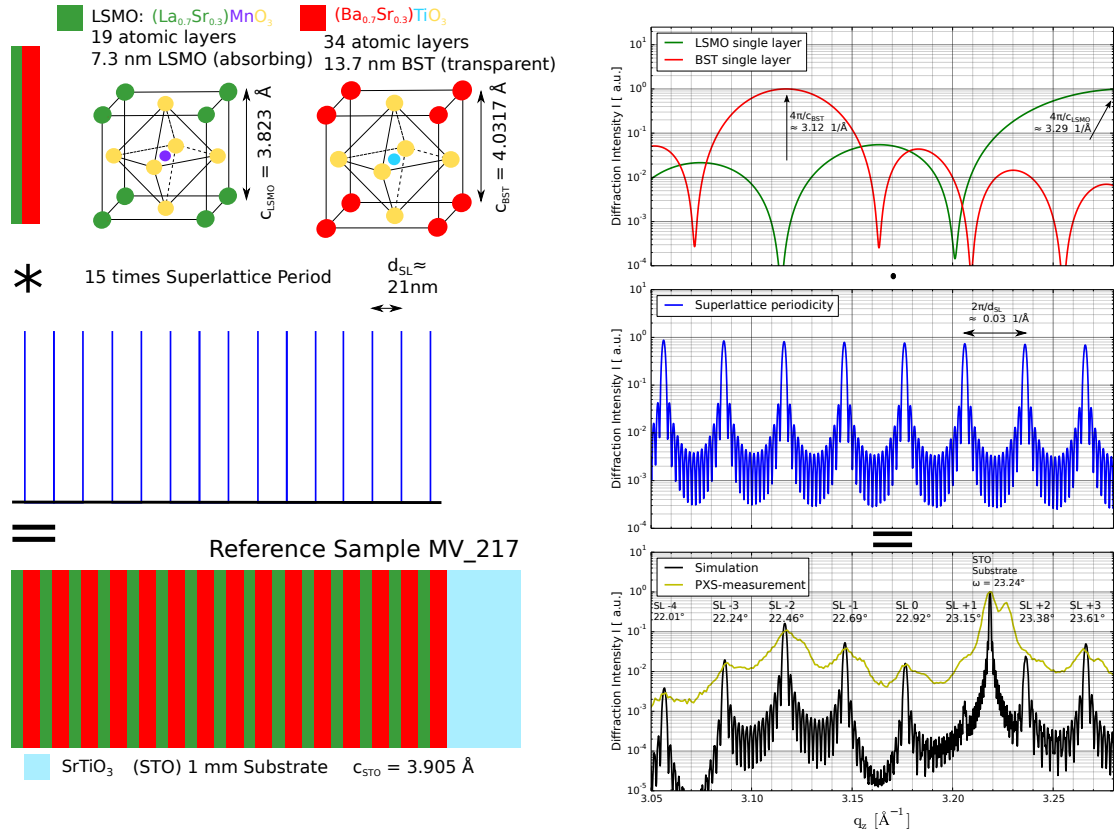


Figure 3.8. Physical principles of X-ray diffraction from a superlattice sample: Real space structures (left side) are directly compared to their reciprocal space equivalents (right side). In real space our sample (bottom left) consists of a 15 period superlattice (middle left) convoluted with a thin film double layer of the metal LSMO and the dielectric BST (top left) on top of a STO substrate. The perovskite unit cell of the two thin film materials are shown in the top left. The measured X-ray diffraction pattern (bottom right) follows the mathematical convolution theorem as it turns out to be the product of the diffraction intensities of the periodicity of the superlattice at $q_z = 2\pi/d_{SL}$ (middle right) with the diffraction from the sum of the single thin layers of the two materials in the superlattice (top right). Upon laser excitation only the metallic LSMO is heated and expands by compressing the adjacent BST layers. This leaves the superlattice periodicity d_{SL} unchanged but shifts the thin film envelopes (top right) to smaller q_z for the expanding LSMO and to larger q_z for BST. This increases the resulting X-ray diffraction intensity of the SL-1 peak due to an increased envelope function at this particular q-vector. As the generated periodic strain pattern travels through the superlattice an periodic modulation of the diffraction intensity of the superlattice peaks occurs. The large amplitude oscillations of the SL-1 peak that we use for the determination of t_0 are depicted in Figure 3.9. This sketch is based on a figure originally shown in an overview article by Bargheer¹²⁴ in 2007, but its elements have been adapted to our reference sample.

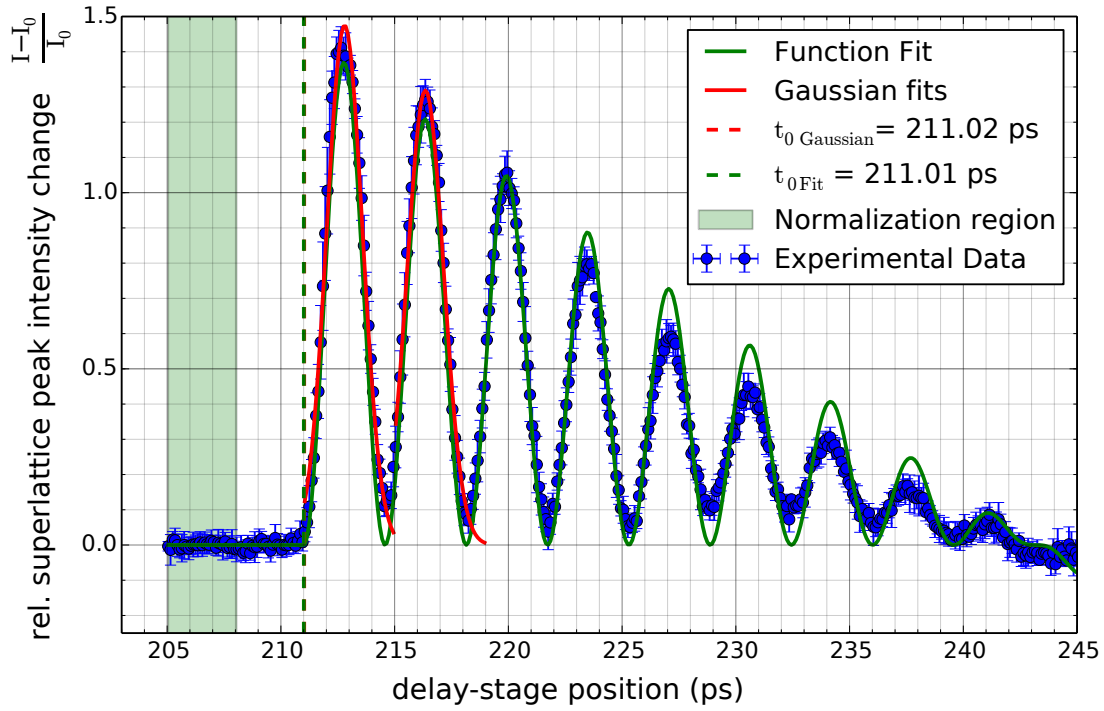


Figure 3.9. Determination of the temporal pump-probe overlap: The X-ray diffraction intensity oscillations of the superlattice Bragg-Peak SL-1 of our reference sample upon laser excitation using an incident laser fluence of 30 mJ/cm^2 . The shaded green region corresponds to the area over which the signal has been averaged to yield the unpumped diffraction intensity I_0 . The sharp onset of the oscillation of the peak intensity of the reference sample is used to determine the position of the delay stage where the relative delay of the pump laser pulses and the probing X-ray pulses in our experiments is zero. The function used to fit the data points are linearly decaying cosine oscillations with a step onset at t_0 as defined in equation (3.3). An equivalent way of determining the t_0 is the determination of the oscillation period fitting the two maxima using Gaussian functions and then subtracting half of the period from the first maximum. To find the optimal spatial overlap between pump and probe pulses the pump pulses are scanned laterally on the sample until the maximum amplitude of the oscillations is determined.

The Heaviside function $\Theta(t - t_0)$ represents an instantaneous onset of the oscillations at t_0 and the linear decay accounts for the propagation of the coherent phonon pulses into the substrate. t_0 is then returned from the fit shown as green curve in Figure 3.9. To be exact the fitting function would need to be convoluted in time with a Gaussian that represents the limited time resolution due to the length of the X-ray-pulses and the length of the laser pulses.

The second method is based on the timing of the first two maxima at t_1 and t_2 of the superlattice oscillations that are approximated here by the center of Gaussian fits. The oscillation period Δt is the difference $\Delta t = t_2 - t_1 \approx 3.55$ ps corresponding to an oscillation frequency of $f \approx 281.7$ GHz. By subtracting half the oscillation period $\Delta t/2$ from the first maximum we also obtain a value for time zero $t_0 = t_1 - \Delta t/2$ that is found to be very close to the results from the fit so that we consider both methods to be equivalent.

In addition to finding the temporal overlap via the timing of the oscillations they are also used to optimize the spatial overlap between the laser and the X-ray pulses. Using knife edge techniques we found that the laser profile has a spatial extension FWHM of $1200 \mu\text{m}$ and the X-rays have a spatial extension of approximately $300 \mu\text{m}$. The best spatial overlap is achieved when the oscillation amplitude is maximized as a function of the laser position on the reference sample.

The determination of the pulse length of the X-ray pulses at our plasma X-ray source is not straightforward. For a very similar setup at the Max-Born Institute an approximate pulse duration of 120 fs has been reported¹²⁵. It was inferred from measuring the instantaneous charge transfer in the ionic crystal Lithium-Borohydrid (LiBH_4) that is only present under the influence of the electric field of the used 35 fs laser pulse. The observed sharp transient polarization changes at t_0 have a temporal width of 120 fs which is attributed to the temporal cross-correlation function of the excitation and probe pulses¹²⁵. Returning to the superlattice oscillations shown in Figure 3.9 one can already see that the time resolution of our experiment is better than 1 ps. Under the assumption that the process that we observe is a pure displacive excitation mechanism as reported for GaAs – AlAs-superlattices¹¹⁰ the signal should modulate through zero relative change after one period. This is not the case and assuming that the major contribution to this effect originates from our limited time resolution I can estimate the time resolution. This can be done by a convolution of the ideal fit function with a Gaussian function in time with a variable width w as it is done in Figure 3.10. From there I see that the best agreement between data and theoretical function is achieved when the cosine oscillations are convoluted with a 250 fs or 300 fs- Gaussian function. I take this to be an upper limit estimate of the pulse duration of the X-ray pulses since it is theoretically not clear that the oscillations should modulate through to zero for the case of an LSMO – BST-superlattice, since the excitation mechanism for these materials does not necessarily need to be purely displacive. Moreover the full amplitude requires a perfect periodicity of the superlattice. Additionally the peak shift of the Bragg peaks might have an influence on the modulation amplitude. Having considered this information I assume that the pulse length is in the order of few hundreds of femtoseconds and most likely in the range between 160 – 300 fs, which is in the same order of magnitude of the 200 fs which Schick et al.^{126,83} assumed in previous publications for this setup.

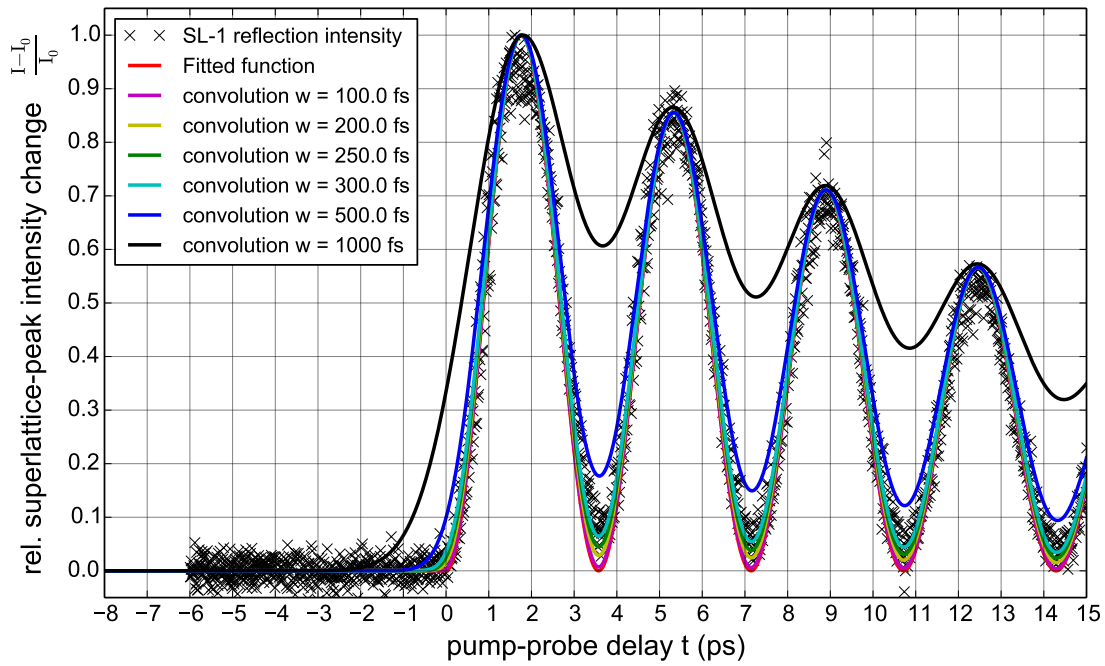


Figure 3.10. Estimation of the attained temporal resolution: Comparison of the measured data of the relative intensity change oscillations of the SL-1 peak and the ideal fit function convoluted with gaussian functions of different temporal widths. The convoluted functions are designed to represent different time resolutions of the experiment. The best agreement is obtained for the curves with 250 fs and 300 fs temporal resolution, which serves as an upper limit estimate of our pulse length.

The pulse length of the pump-laser pulses has been determined to be at best 35 fs using a commercial single shot autocorrelator. In daily operation when we tune the source for maximum X-ray output the grating compressor of the laser system is optimized so that the laser pulses are shortest in the plasma generating focus on the copper target. In this configuration the pump laser pulses close to the sample position are then found to be 100 fs long, which is still sufficient to trigger ultrafast dynamics, so that we refrain from further dedicated chirp optimization that would require an additional compressor setup.

3.5 Measurement results

In this section I present the main results of the time-resolved X-ray diffraction measurements carried out during my master thesis work. My observations are mainly depicted as average strain $\epsilon_{\text{Dy}}(t)$ in the Dysprosium thin film as a function of pump probe delay t . I use the term strain to indicate the relative change of the out-of-plane lattice constant that is mainly the c -axis change in the Dysprosium thin film compared to the unpumped state, where $t < 0$. The applied definition is as follows: 3.4

$$\epsilon_{\text{Dy}}(t) = \frac{c_{\text{Dy}}(t) - c_{\text{Dy}}(t < 0)}{c_{\text{Dy}}(t < 0)}. \quad (3.4)$$

Figure 3.11 provides an overview over the different observed strain responses of the Dysprosium layer upon laser excitation with a relatively large excitation laser fluence of approximately 10.5 mJ/cm^2 for different starting temperatures. Depending on this temperature one observes very different dynamics ranging from a pronounced expansion of the Dysprosium layer above 180 K to a contraction of the Dysprosium below 40 K. At intermediate temperatures, close to the AFM-PM phase transition temperature $T_{\text{Néel}} = 180 \text{ K}$, an initial expansion of the material that transitions into a delayed contraction is observed.

Starting from the overview results presented in Figure 3.11 I discuss the different observed responses by supplying selected fluence-resolved data. Making use of the large temperature range of the cryostat from 15 K – 300 K it is possible to explore the sample dynamics in the various magnetic phases of the Dysprosium thin film. In the following I will present selected measurement series where the start temperature T_{start} is kept fixed and the excitation is varied, to systematically obtain information on the laser driven ultrafast phase transition process.

3.5.1 Lattice response in the paramagnetic phase

The lattice response in the paramagnetic phase of Dysprosium is shown in Figure 3.12. The data shown there are taken at a base temperature of $T_{\text{start}} = 250 \text{ K}$, well above $T_{\text{N}} = 180 \text{ K}$, to omit contributions due to possible remaining short-range correlation effects in the magnetic order in the vicinity of the phase transitions.

In the data a large average expansion of the Dysprosium thin film is observed after laser excitation that has its maximum value 28 ps after excitation. Subsequently the lattice expansion relaxes towards its initial state with approximately 25% of the initial expansion remaining 3.8 ns after the excitation. This process is superimposed by an oscillation with a period of approximately 45 ps, corresponding to a frequency of 22 GHz, of which four to five periods are visible within the data.

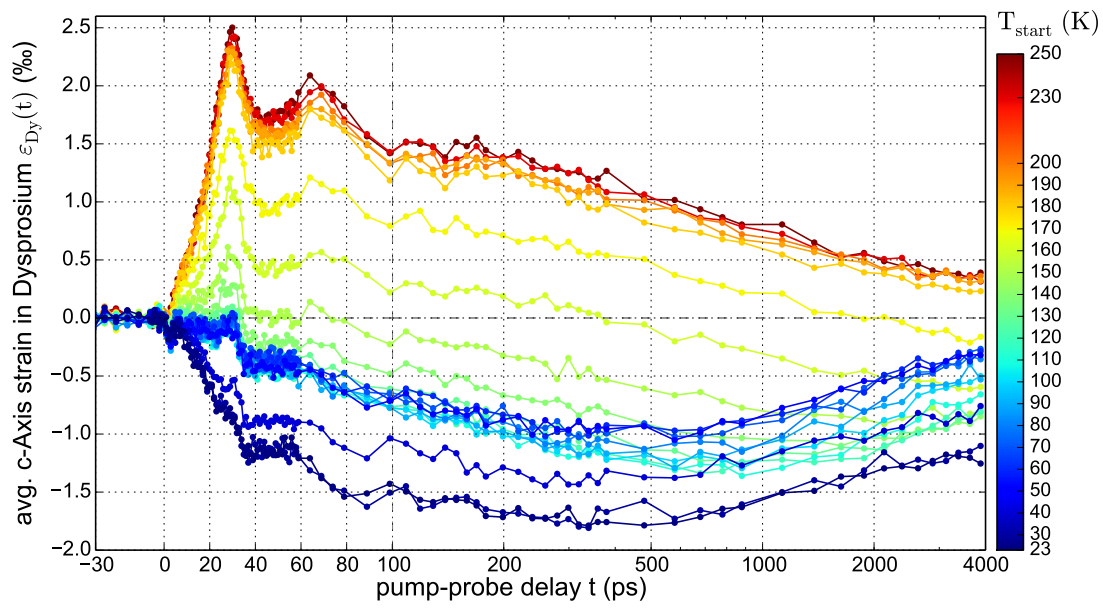
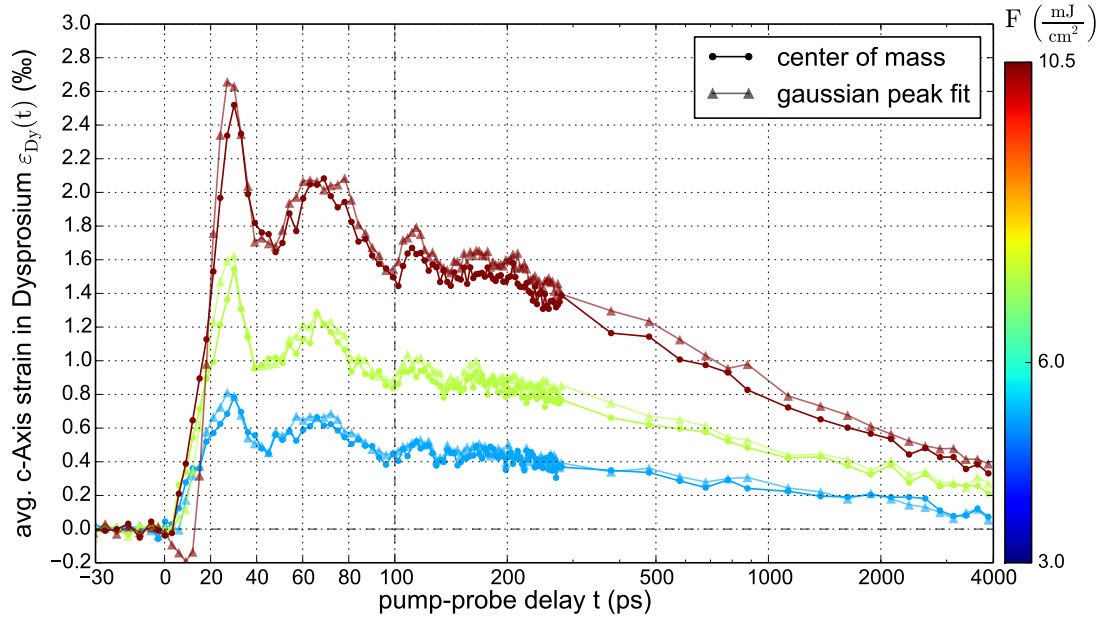


Figure 3.11. Temperature study of DyY24B with $F \approx 10.5 \text{ mJ/cm}^2$: time-resolved average strain of the Dysprosium layer for a fixed incident laser fluence of $F = 10.5 \text{ mJ/cm}^2$ at different bath temperatures. Note that the x-axis continues with a logarithmic scaling after 100 ps to include picosecond and nanosecond dynamics in one graph. One observes that the lattice dynamics strongly depends on the initial temperature. The average strain in the Dysprosium layer changes from almost entirely positive (expansion) above 180 K to almost entirely negative (contraction) below 130 K via an intermediate phase where an initial expansion is followed by a delayed contraction.

- (a) Paramagnetic phase at $T = 250$ K. The two different symbols compare the c-Axis response between the center of mass and the gaussian peak fit method. Deviations are most pronounced at early times where the Bragg peak becomes asymmetric due to coherent phonon effects.



- (b) Same data as in (a) normalized to the laser excitation fluence

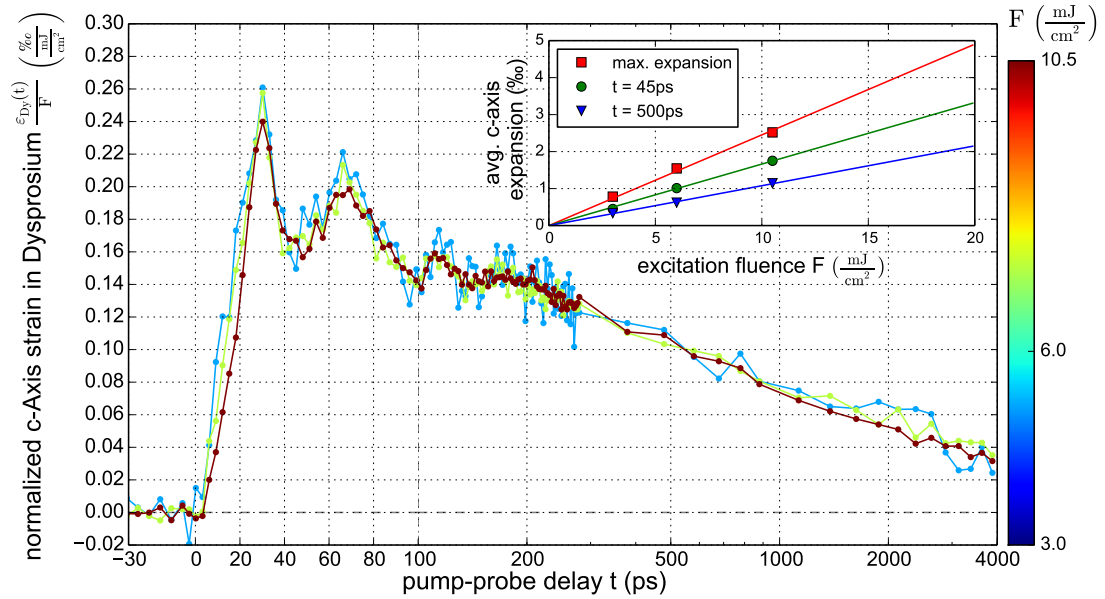


Figure 3.12. Fluence study of DyY24B in the paramagnetic phase at $T_{start} = 250$ K: The relative change in the interatomic distance of the Dysprosium in the paramagnetic phase at $T = 250$ K for three different excitation fluences is shown in (a). One observes a rapid expansion where the maximum average strain is attained at approximately 28 ps. The lattice subsequently relaxes towards its equilibrium position but the relaxation process is superimposed by oscillations with a period of approximately 45 ps that are visible within the first 250 ps.

The lattice dynamics in the paramagnetic phase can be viewed as ultrafast thermal expansion upon a temperature rise within the Dysprosium layer after laser excitation. The subsequent relaxation process shows how the heat is transported out of the Dysprosium layer. Similar dynamics observed by ultrafast X-ray diffraction are already reported in the literature for example for the case of the semiconductor Gallium-Arsenide GaAs¹⁰⁷ and the hexagonal lattice multiferroic Lutetium-Manganite LuMnO₃¹²⁷.

I attribute the superimposed oscillations to a strain wave starting mainly at the sample air interface, which propagates into the sample and gets partially reflected at material interfaces due to acoustic impedance mismatches. The coherent phonon dynamics is visible in my data within the first 300 ps. The generation and propagation of sound pulses using femtosecond lasers is known and studied intensively since the seminal work by Thomsen et al.¹²⁸ from 1986, but it is not the main focus of my work. I restrict myself here to use the coherent phonon dynamics in order to cross-check the sample structure by comparing it to simulations from a 1D masses-and-springs model provided by the UDKM1Dsim toolbox⁷. The results are reported in section 4.4. A detailed discussion of the lattice response of a thin metal film on a transparent substrate studied by ultrafast X-ray diffraction has recently been published by Schick et al.¹²⁹.

If the observed lattice expansion in the paramagnetic phase is normalized by the incident laser excitation fluence, the normalized c-axis change closely match as shown in Figure 3.12(b). This resulting linear relation between the lattice expansion and the laser excitation fluence can be used to cross - check the experimentally set laser fluence. The excitation fluence set by the incident laser power and pump-spot size is a quantity that is most prone to fluctuations on a day by day basis, when the laser is turned on and off in between the measurements. The uncertainty originates mainly from a varying spatial pump-probe overlap. However a comparison between the set fluence and the expansion of the sample in its paramagnetic phase allows for recalibration of the excitation fluence to a standardized scale determined by a fluence series on one set day. The inset of Figure 3.12 explicitly depicts this linear relation between the observed sample expansion and the incident laser fluence at three different times.

3.5.2 Lattice response in the antiferromagnetic phase

As the temperature is lowered below $T_N = 180\text{ K}$ the Dysprosium layer becomes magnetic, which adds an additional magnetostrictive component to the stress acting on the lattice. As it can already be seen from the overview temperature series shown in Figure 3.11 the observed lattice dynamics changes when the magnetostriction comes into play. The pure out-of-plane expansion in the paramagnetic phase changes to an early expansion which is followed by a contraction and as the temperature is lowered even more only a contraction is observed after the excitation.

In order to gain more insight into the change of dynamics I additionally carried out a series of measurements where the base temperature of the sample is kept fixed and the excitation fluence is increased after each run up to approximately 10.5 mJ/cm^2 . It was previously tested that the damage threshold of the sample where the Bragg peak intensity of the Dysprosium peak decreases over measurement time lies for our setup at an incident fluence of approximately 20 mJ/cm^2 .

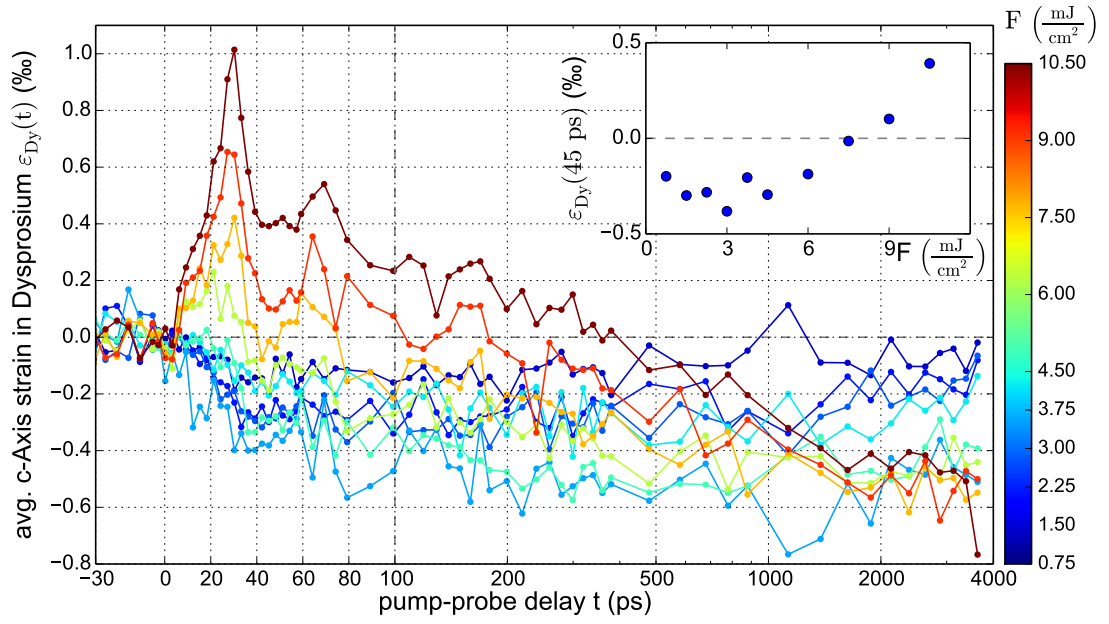


Figure 3.13. Fluence study of DyY24B at $T_{\text{start}} = 160 \text{ K}$ in the antiferromagnetic phase: Measurement series where the start temperature is set in the vicinity of the phase transition from the antiferromagnetic phase to the paramagnetic phase at $T_N = 180 \text{ K}$. Datapoints within 3 ps have been averaged to one point in order to increase readability. The strain at 45 ps shown in the inset depicts the transition from early contraction to expansion where the point of inflection is located at $F \approx 3 \text{ mJ/cm}^2$.

Figure 3.13 shows an overview over the measurement results of such a series of measurements with a starting temperature of 160 K. As opposed to the measurements in the paramagnetic phase an increase in fluence strongly alters the observed dynamics. From $0.75 - 3 \text{ mJ/cm}^2$ I observe a contraction of the c-Axis lattice that increases with increasing the laser fluence. The observed contraction has two components. One fast component that occurs within the first 40 ps and then a plateau in the contraction occurs up to 1 ns to 2 ns which is when the relative c-axis change starts to recover towards 0.

The saturation value of this contraction is found to be at a relative c-axis change of approximately -0.6% . For measurements with higher excitation fluences ranging from $3 - 10.5 \text{ mJ/cm}^2$ the initial response within the first 40 ps of the Dysprosium c-Axis changes gradually towards an expansion that increases with fluence. Following this initial response that can be either a contraction or an expansion a decrease of the lattice constant is observed. The slope of this contraction that occurs from $\approx 30 \text{ ps}$ onwards gradually increases with increasing fluence. The contraction continues up to the nanosecond timescale, when a recovery sets in. The observed general trend is: the higher the excitation fluence is, the later the remaining contraction recovers towards its equilibrium value again. For example at 3.5 mJ/cm^2 a change of slope can be seen at approximately 1.5 ns , at 6 mJ/cm^2 I observe it at 2.75 ns whereas for the largest excitation fluence of 10.5 mJ/cm^2 the lattice contraction has not stopped at the largest measured delay of approximately 3.8 ns .

The coherent phonon oscillations which were already mentioned in the discussion of the paramagnetic response are still visible within the data obtained in the antiferromagnetic phase. These oscillations superimpose the trends discussed here and they become more pronounced as for higher excitation fluence.

A second fluence series measured at a cryostat temperature of 130 K corroborates the findings from the 160 K measurement. Its results are shown in Figure 3.14. Up to a fluence of $2.5 - 3.2 \text{ mJ/cm}^2$ the initial lattice contraction occurs within the first 50 ps and it increases with excitation fluence to a relative change of -0.6% . When the excitation fluence is increased further, the initial lattice contraction is again weaker and gradually changes towards a lattice expansion. A striking difference between the measurement results of the 160 K and 130 K fluence series is that the amplitude of the relative c-Axis contraction that gets as large as 1.1% for an excitation fluence of 9 mJ/cm^2 . For laser excitation fluences above 4 mJ/cm^2 I observe in this dataset that the maximal contraction not only becomes larger with fluence but that the maximal contraction occurs at later pump-probe delays ranging from 500 ps to 1.8 ns for fluences from 4 mJ/cm^2 to 9 mJ/cm^2 respectively.

In general the out-of-plane lattice response in the antiferromagnetic phase of the Dysprosium thin film is different from the sample response in the paramagnetic phase and it is strongly dependent on the excitation fluence. For small excitation fluences well below the phase transition temperature, I measured only a contraction whereas for higher excitation fluences an initial expansion within the first 40 ps is followed by a contraction that continues beyond the equilibrium position before excitation to a maximum contraction. This maximum contraction amplitude

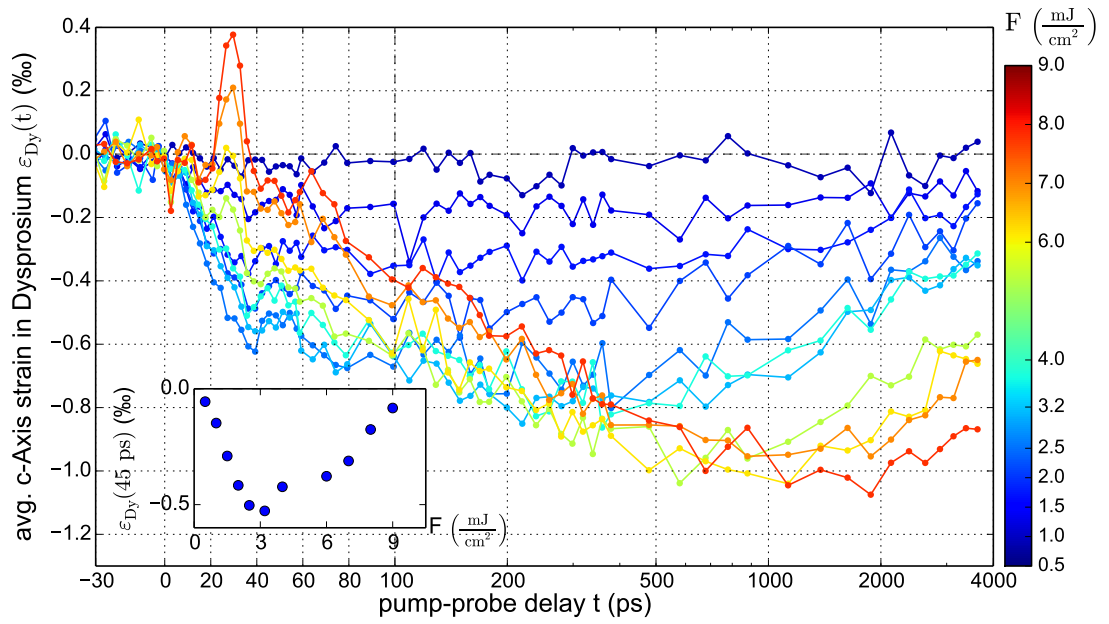


Figure 3.14. Fluence study of DyY24B at $T_{\text{start}} = 130\text{ K}$ in the antiferromagnetic phase: The starting temperature lies well in the antiferromagnetic phase. An initial contraction is observed except for the highest fluences used. As the excitation fluence is increased I observe an initial expansion followed by a delayed contraction. The contraction strain amplitude at 45 ps shown in the inset also depicts a point of inflection at $F \approx 3\text{ mJ/cm}^2$ where the early contraction saturates and starts to increase again.

increases with excitation fluence and also increases for temperatures further below T_N . The timing of the maximum contraction for the high fluence measurements is also fluence dependent and it shifts towards later times for higher fluences.

A more detailed discussion including an interpretation of the observed features of the measurements is deferred until chapter 4. In the following I continue to present the collected experimental evidence upon which I base my interpretations.

3.5.3 Lattice response in the ferromagnetic phase

Below the Curie temperature of $T_C = 85$ K bulk Dysprosium is known to become ferromagnetic⁵. This first order transition goes along with a steplike increase in the c-Axis distance and a symmetry change from a hexagonal phase to an orthorhombic unit cell which also significantly influences the in-plane lattice. In the case of our thin film Dysprosium sample a hysteresis of the interatomic c-Axis distance is observed upon cooling and heating the sample in the temperature region from 40 K up almost 100 K. This was seen in the static measurements shown in Figure 6.5 in section 2.4. In this first examination I restrict myself to measurements above and below the hysteresis region, because the initial lattice state towards which the sample relaxes after being excited with a short laser pulse might not be the same.

Figure 3.15 shows the out-of-plane lattice constant response upon ultrafast laser excitation. There I see that for small laser excitation fluences $F < 1.5 \text{ mJ/cm}^2$ a small positive strain in the out-of-plane lattice direction can be observed. For $F > 1.5 \text{ mJ/cm}^2$ one observes a lattice contraction that increases up to approximately -1.75 ‰ for an excitation fluence of 10 mJ/cm^2 . Similar to the measurements in the antiferromagnetic phase I observe two components in the lattice response on different timescales. One fast lattice contraction within the first 40 ps and then a slower contraction from 40 ps to the maximal contraction. The amplitude of the fast contraction saturates at an incident laser fluence of 6 mJ/cm^2 . As opposed to measurements in the AFM-phase the timing of the contraction minimum does not shift to later delays with increasing fluence and it occurs between 500 ps and 1 ns. Subsequently the lattice relaxes back towards its initial equilibrium position. I observe the positive slope of the recovery to be larger for higher fluences.

Having considered the sample response in the paramagnetic, antiferromagnetic and ferromagnetic response of the Dysprosium lattice after femtosecond laser excitation the aim of the following measurements was to study the influence of other boundary parameters such as sample geometry and external magnetic fields on our measurement results.

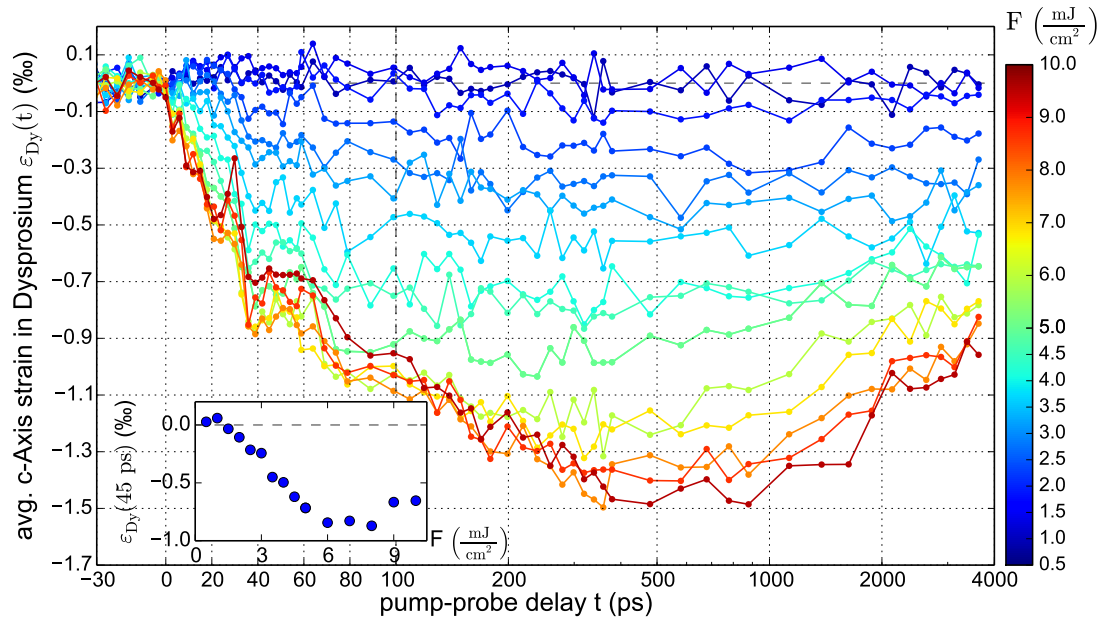


Figure 3.15. Fluence study DyY24B at $T_{\text{start}} = 40\text{K}$ in the ferromagnetic phase: A large lattice contraction is observed within the first 40ps. It is followed by a second decay which occurs on a timescale of hundreds of picoseconds leading towards the maximal contraction that occurs within 0.5 – 1 ns after excitation. The subsequent recovery of the lattice takes place on a nanosecond timescale and occurs faster for higher fluences but is not complete at 3.8ns after the excitation. The contraction strain amplitude at 45ps shown in the inset emphasizes the saturation of the fast contraction response at an excitation fluence of 6‰.

3.6 Dynamics in an external magnetic field

Bulk Dysprosium is known not only to undergo spontaneous magnetostriction⁴ but also forced magnetostriction³ where the application of an external magnetic field changes the interatomic lattice constant of up to 4%. The possibility to manipulate the lattice dynamics is a desired property for technological applications. Therefore it is relevant to see if and how an external magnetic field affects the lattice response in the magnetic phases. Apart from the layer thicknesses, the starting temperature and the excitation fluence, an external magnetic field provides a way that possibly enables the control of the lattice dynamics. To my knowledge it is so far unknown how the application of an external magnetic field affects the ultrafast demagnetization or remagnetization dynamics of Dysprosium in either of its two magnetic phases. Therefore such a study might also be of fundamental interest.

As a first step we proved that the application of an external magnetic field shows a measurable effect on the out-of-plane lattice constant in a static measurement. Similar results have already been reported in the literature^{24,130}, Figure 3.17 shows the influence of a moderate external magnetic field applied on the interatomic distance as a function of temperature. Since the plateau of a large lattice constant preceding a hysteresis is a feature indicative for the ferromagnetic phase it shows the external B-field stabilizes the ferromagnetic phase thereby shifting the observed hysteresis loop to higher temperatures.

The magnetic easy axis of Dysprosium are the hexagonal in-plane a-axis and the magnetic hard axis is the out-of-plane c-axis³. The external magnetic field was applied by attaching the sample onto a small cubic magnet that has a field strength of approximately 0.4 T on its surface as measured with a commercial hall effect sensor. For the application of an in-plane field the magnet was turned so that the large sample surface was aligned parallel to the field lines. The in-plane magnetic field of this static construction was only 0.1 T, and thus four times smaller than the out-of-plane magnetic field.

A temperature series with a fixed laser fluence of 18 mJ/cm² was carried out in one measurement run. The used excitation fluence was accidentally set to a too large value which can be seen by the lattice expansion in the paramagnetic phase that is approximately 3.6‰ as compared to the 2.1‰, which are expected for the intended fluence of 10.5 mJ/cm².

Having the very large excitation fluence in mind it can be said that the general nature of the lattice dynamics upon laser excitation did not change notably as a consequence of the applied external B-Field. The observed response can be described very similarly to the features observed in the temperature series shown initially in Figure 3.11 where no external magnetic field is present. The amplitude and sign of the initial lattice response within the first 40 ps depends on the starting temperature. Regardless of the starting temperature the initial response is followed by a second decrease in the out-of-plane interatomic lattice distance. It is worth mentioning that the curves decrease very parallel with the same slope after the initial dynamics up to the point where they reach their maximum contraction. A delay in the maximum contraction is visible for starting temperatures higher than 90 K.

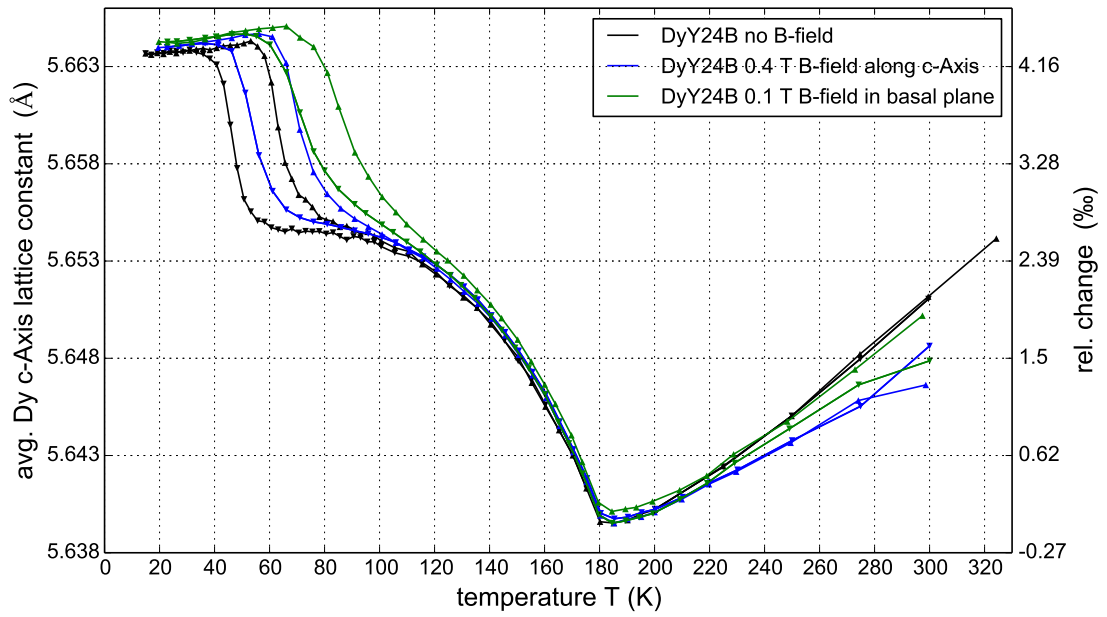


Figure 3.16. Characterization of DyY24B sample in an external magnetic-field: The static external magnetic field of approximately 0.4 T has been applied using a fixed bar magnet right below the sample. We observe that the application of an external magnetic field tends to stabilize the ferromagnetic phase which is seen by shifting the hysteresis loop in the magnetization to higher temperatures. The curves with applied field have been shifted vertically so that the smallest lattice expansion overlap in space. The hysteresis behavior is indicated by the triangles on the data points that indicate how the temperature was varied.

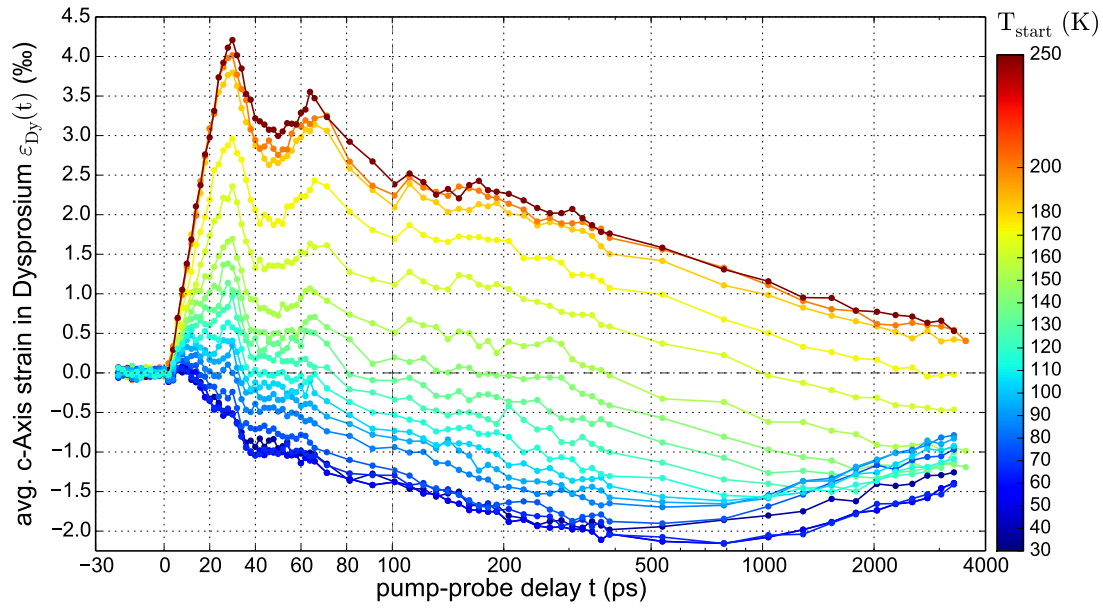


Figure 3.17. Study of DyY24B with $F \approx 18 \text{ mJ/cm}^2$ with in-plane external B-field of 0.1 T: The observed lattice dynamics is found to be similar to the initially reported measurements from figure 3.11 without an applied magnetic field except for the increased signal amplitude that can be accounted for by the higher excitation density. Note that after the initial response in the first 40 ps the measured curves evolve parallel up to the delays when some of the dynamics reach their maximum contraction while in measurements with a higher starting temperature the contraction continues for longer times. A very large signal to noise ratio, which can be seen from the large lattice response compared to the small fluctuation before time zero was achieved in this measurement.

For one additional measurement that was carried out I can directly compare the lattice response in the antiferromagnetic phase under the application of an external magnetic field. Figure 3.18(a) shows the lattice response of the two different datasets in the paramagnetic phase, to underline the comparability of the two different sample responses. Figure 3.18(b) directly compares the sample responses with and without an applied magnetic field in the antiferromagnetic phase at 160 K. From these first measurements I conclude that the in-plane application of a relatively small static external B-Field has no pronounced effect on the timescale of the lattice dynamics in the antiferromagnetic phase. Only a careful systematic study can resolve the fine differences.

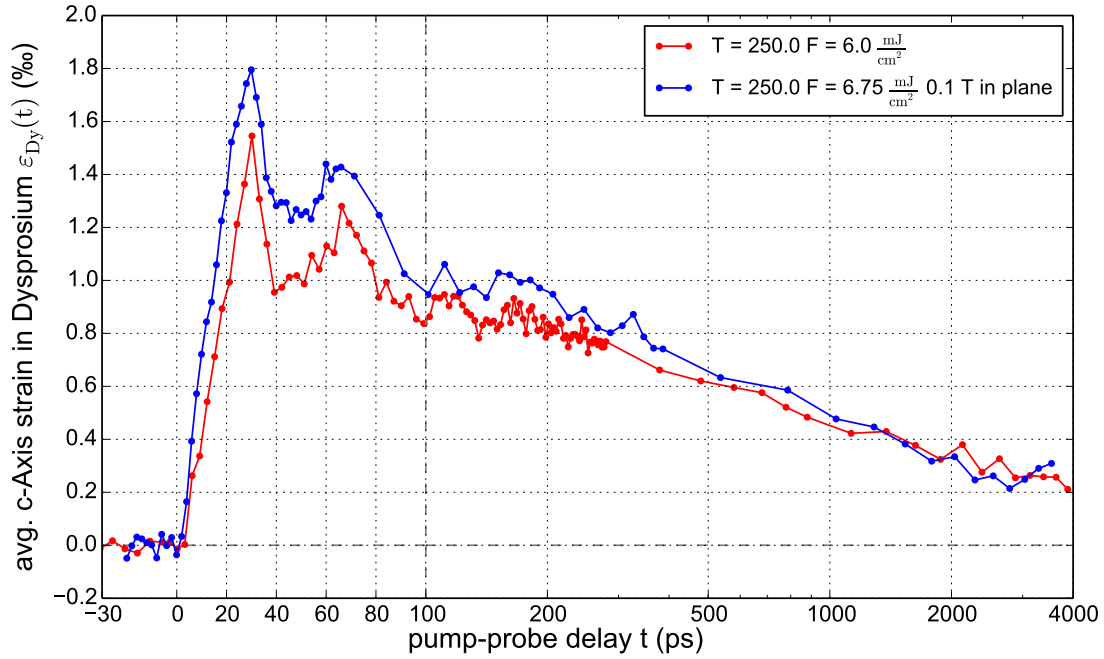
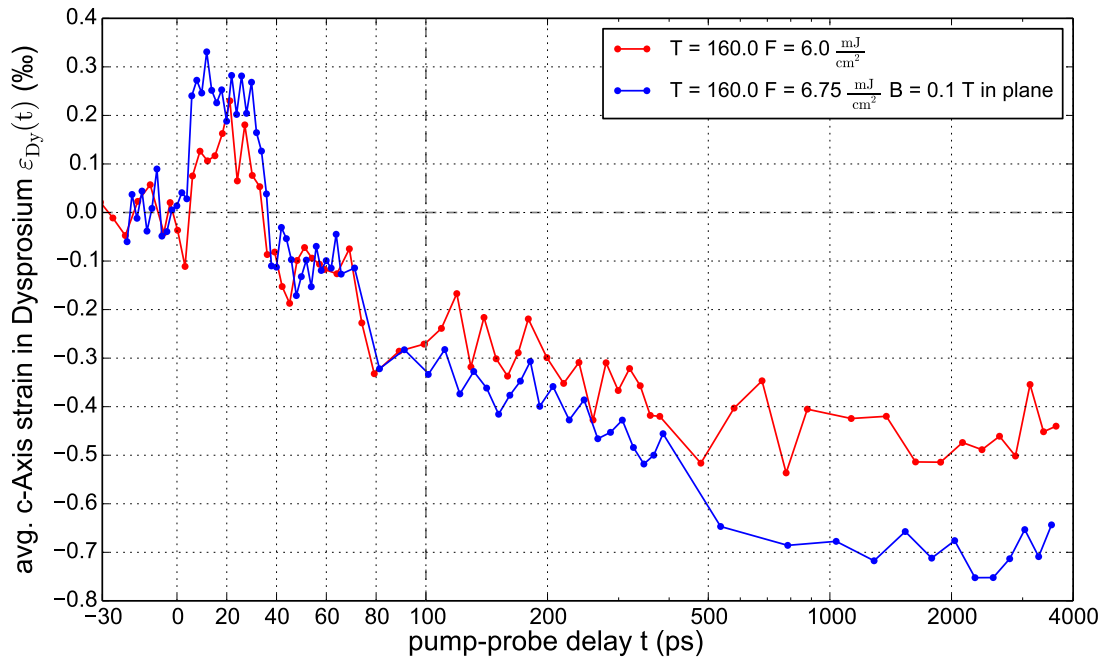
(a) Comparison paramagnetic phase at $T_{\text{start}} = 250\text{ K}$ (b) Comparison in the antiferromagnetic phase at $T_{\text{start}} = 160\text{ K}$ 

Figure 3.18. Lattice dynamics of DyY24B with and without $B = 0.1\text{ T}$ in the basal plane: The top graph (a) shows the similar responses in the paramagnetic phase that indicate the comparability of the used excitation fluences. Comparing the general lattice response in the antiferromagnetic phase in the bottom graph (b) no general changes of the lattice response are observed.

3.7 Indirect excitation of the Dysprosium layer

In the so far discussed sample geometry of the sample DyY24B the Dysprosium layer is directly excited, since the laser penetration depth is approximately 20 nm at the excitation wavelength of 800 nm and the Yttrium capping layer has a thickness of 10 nm. According to Lambert-Beers law 60.65% of the incident laser fluence reaches the top of the Dysprosium layer and is used to directly excite the electronic system in Dysprosium.

To cross check whether the excitation process has a significant influence on the lattice dynamics we conducted a measurement series in a different sample geometry of the sample labeled DyY26DI that has a 50 nm thick Yttrium capping and bottom layer. The full sample geometry that is otherwise identical to the DyY24B sample is shown in Figure 3.19. Assuming the same penetration depth only approximately 9% of the incident laser fluence is transmitted through the capping layer so that only a small fraction of the Dysprosium is directly excited.

50 nm	Yttrium
100 nm	Dysprosium
50 nm	Yttrium
100 nm	Niobium
0.5 mm	Sapphire Substrate
DyY26DI	

Figure 3.19. Sample geometry of DyY26I: In this sample the Dysprosium layer is situated between two 50 nm thick Yttrium layers as opposed to the smaller 10 nm thin Yttrium capping layers used so far. Otherwise the sample geometry is the same as for the mainly studied DyY24B sample. Due to the limited optical penetration depth of 24 nm at the wavelength of 800 nm I can assume that the buried Dysprosium layer is not directly excited by the used laser pulses.

The resulting c-Axis response of the 100 nm thick Dysprosium layer upon indirect excitation at different starting temperatures and comparable excitation fluences is displayed in Figure 3.20. I observe pronounced differences as compared to the previously shown experiments on DyY24B where the Dysprosium layer is to a large extent directly excited. Regardless of start temperature a strong compression followed by an expansion is taking place within the first 100 ps, which I attribute to the strain wave launched into the Dysprosium due to the expansion of the adjacent Yttrium. This initial dynamics is either followed by an expansion in the paramagnetic phase or by a contraction at temperatures in the magnetic phases. However the lattice expansion maximum in the paramagnetic phase is considerably delayed as compared to the sample with the thin Yttrium capping layer it occurs at approximately 500 ps. In a similar way also the contraction response within the magnetic phase is delayed as compared to the direct excitation results measured in the 10 nm Yttrium capping layer geometry.

Systematic studies of the ultrafast out-of-plane lattice response upon changing the excitation fluence in this sample geometry are shown for the two starting temperatures $T = 165$ K and $T = 20$ K in Figure 3.21 and 3.22 respectively.

In the fluence series at 165 K I observe that the amplitude of the strain pulse due to the excitation

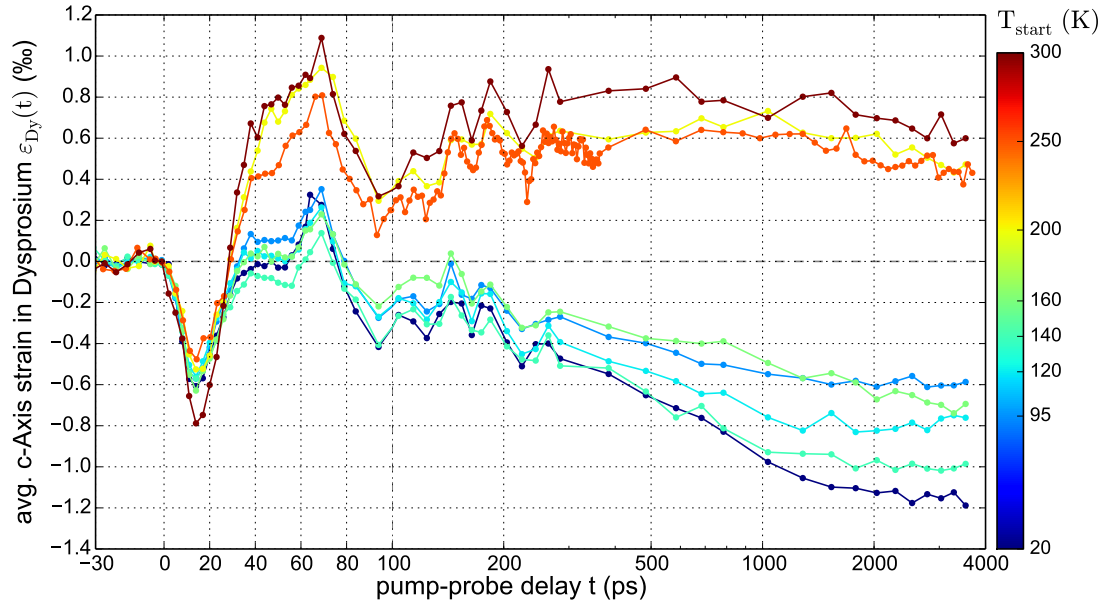


Figure 3.20. Temperature study of DyY26DI with $F = 7.5 \pm 0.5 \text{ mJ/cm}^2$: Measurement series of the time-resolved Dysprosium c-Axis change as a function of pump-probe delay for a sample geometry where the Dysprosium layer is only marginally excited and the main part of the laser energy is deposited in the Yttrium capping layer. The measurements shown here were conducted at different starting temperatures under comparable excitation fluence conditions with $F = 7.5 \pm 0.5 \text{ mJ/cm}^2$. The effect of the initial strain wave is much more pronounced for this sample geometry. The subsequent lattice dynamics nevertheless strongly depend on the starting temperature. A lattice expansion is observed in the paramagnetic phase whereas an out-of-plane lattice contraction takes place in the antiferromagnetic and ferromagnetic phase of the Dysprosium thin film.

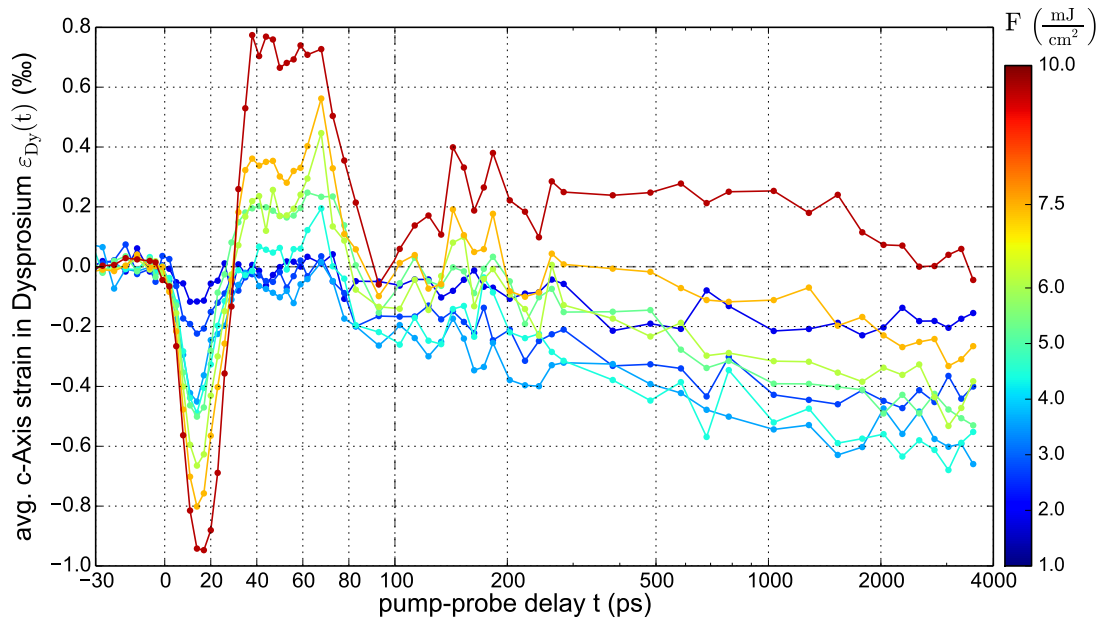


Figure 3.21. Fluence study DyY26DI at $T_{\text{start}} = 165 \text{ K}$: The compression and expansion amplitude of the pronounced strain pulse within the first 100ps increases with increasing excitation fluence. The subsequent dynamics depends on the excitation fluence. For $F \leq 5 \text{ mJ/cm}^2$ I observe a lattice contraction whereas for larger fluences the lattice initially expands and then contracts on a larger timescale.

of the coherent phonons in the adjacent Yttrium layer increases with increasing laser excitation fluence. The subsequent lattice response at later times $t > 100$ ps depends however on the excitation fluence. For low fluences below 6 mJ/cm^2 we observed a contraction of the out-of-plane lattice constant that has its largest amplitude for a fluence of 3 mJ/cm^2 . As the excitation fluence is increased the Dysprosium lattice dynamics changes towards an out-of-plane expansion, which at long delays turns into a lattice contraction on the few nanosecond timescale.

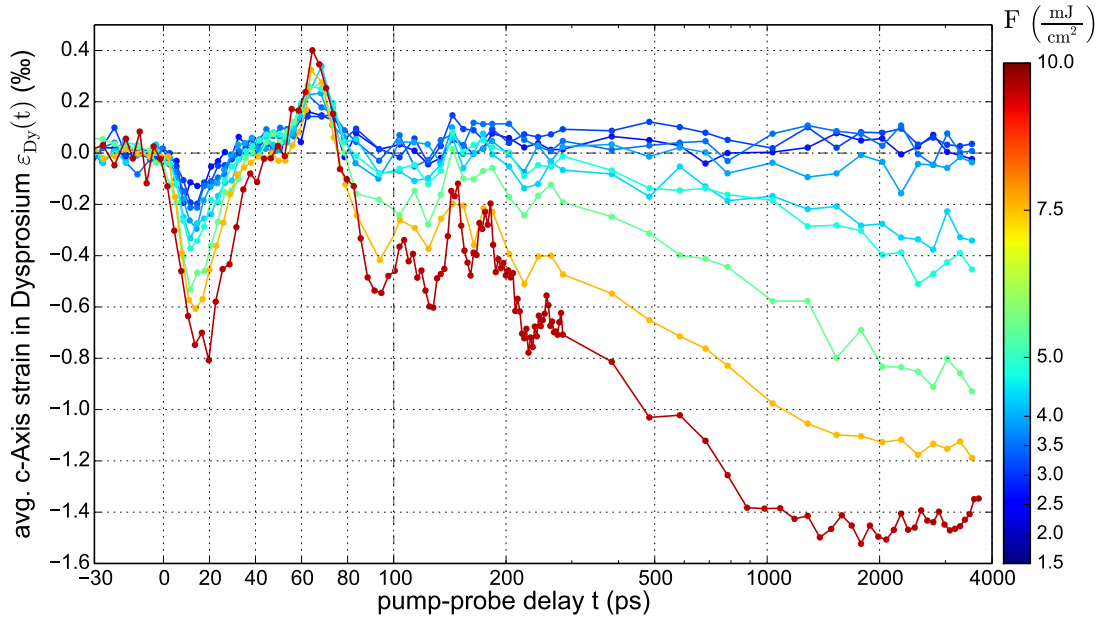


Figure 3.22. Fluence study of DyY26DI at $T_{\text{start}} = 25 \text{ K}$: The compression amplitude of the pronounced strain pulse within the first 100 ps increases with increasing excitation fluence. However the expansive part of the strain wave is similar for all excitation fluences. The timing and amplitude of the contraction increases with increasing fluence.

The lattice dynamics observed in a fluence study at a fixed starting temperature of 25 K exhibits a somewhat different behavior as compared to the fluence study at 165 K. In the early dynamics only the compressive part of the strain wave increases with fluence but the amplitude of the expansive part remains nearly constant regardless of excitation fluence. The subsequent response seems to obey a threshold behavior. If the excitation fluence is $\leq 3.0 \text{ mJ/cm}^2$ the amplitude of the lattice response is very small and on the edge of the signal to noise resolution of the measurement. For larger fluences a significant increase in the lattice contraction at delay times larger than 200 ps is observed.

The fact that Dysprosium is not directly excited together with the much larger timescale of the observed dynamics, leads to the conclusion that the heat transport is a dominant mechanism for this sample geometry where mainly the large capping layer is excited. In order to be able to adequately model the sample response it is thus necessary to simulate also the heat diffusion in

addition to the initial energy distribution in the sample.

4 Discussion and interpretation of the results

In this chapter I interpret the experimental findings that were reported in the previous chapter. At first I will summarize the general trends that I find in my data and supplement them by direct comparison of selected datasets and as well as representative quantities automatically extracted from all measurements. Especially the very early dynamics, are addressed to some detail.

In a second step I will discuss the first intuitive analysis approach, which I call the equilibrium model, that assumes that the electronic, phononic and magnetic system rapidly reach their thermal equilibrium so that temperature is a unique and well-defined quantity within the sample. The analysis contains a simple model where the deposited energy and its flux is calibrated once by a measurement in the paramagnetic phase and then applied in the magnetic phases. This model is supplemented by heat simulations from the UDKM1DSim Toolkit⁷ that have a higher level of detail since a spatial resolution of the temperature profile within the sample is achieved. However the simulations are still in the equilibrium model framework where one unique temperature determines the state of the system at each point of the sample.

The observed deviations of this first equilibrium approach from the data call for a more in depth analysis of the energy balance within the Dysprosium layer. Particularly the assumption of a fast thermal equilibration process between the phonon and magnon system is relaxed. For that I developed an experimental solution of a two temperature model for the phonon and magnon temperature within the Dysprosium layer. It explicitly allows for two separate temperatures for these systems. Based on simple arguments a non-equilibrium between the phonon and magnon temperature is found to exist up to nanoseconds after the excitation. Within my analysis I am comparing the strain measured in static experiments with the transient strain observed in ultrafast experiments. The required estimation of the in-plane clamping effect on the out-of-plane response that occurs on ultrafast timescales is given in this context.

I conclude this section by a synthesis of the identified different subprocesses of energy transport within the sample, to a self-consistent picture.

4.1 General Trends

Upon contemplating on the obtained data presented in the previous chapter several systematic trends occur to me. I state them here supplemented by an automatized meta analysis which aims

at quantifying and visualizing the trends.

I analyze the data in terms of the absolute value of the maximal expansion and contraction as well as the time at which they occur with the help of computer script. To decrease the influence of noise I reject all found extrema that deviate from zero by not more than two standard deviations of the data scatter recorded before t_0 . Figure 4.1 provides an example where the extrema are explicitly marked within the measurement series. It is a striking feature that the maximum expansion occurs always at early times $t \lesssim 30$ ps whereas the maximum contraction that is observed in the low temperature phase only occurs at delays $t > 200$ ps. The resulting overviews of the extracted extrema from the temperature and fluence measurement series are shown in Figure 4.2 and 4.3 respectively.

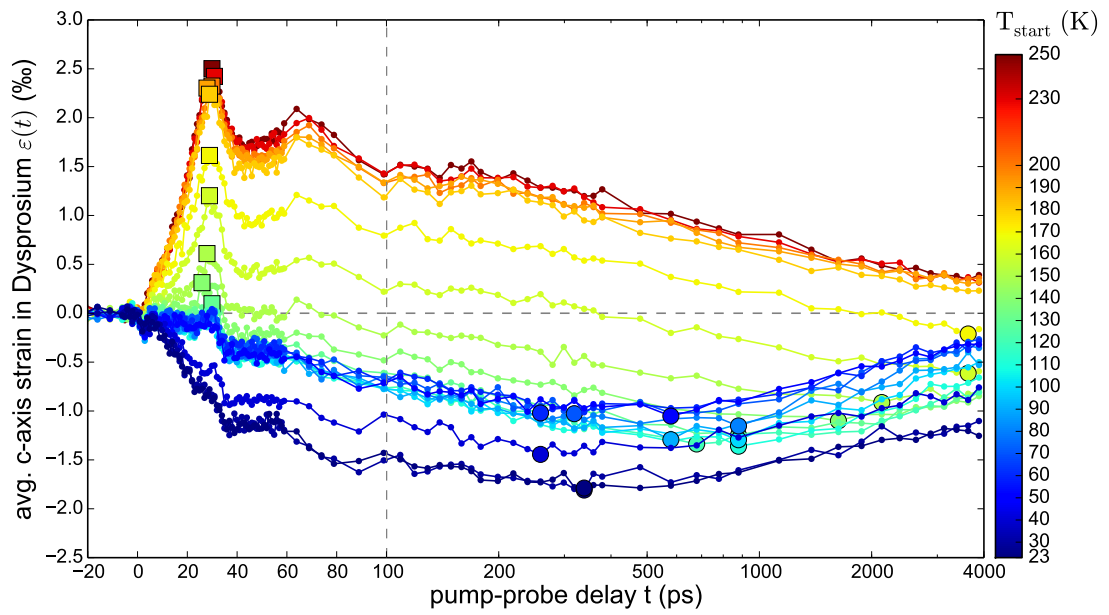


Figure 4.1. Extracted extrema: Example for the extracted extrema that are marked with squares for maximal expansion and circles for maximal contraction. The maximum expansion in the Dysprosium layer occurs at approximately 28 ps after excitation regardless of start temperature whereas its amplitude is temperature dependent. The observed maximum contraction in the low temperature phase occurs at considerably larger delays $t > 200$ ps where amplitude and timing vary with T_{start} .

Since Dysprosium undergoes two magnetic phase transitions upon varying its temperature the question arises to what extent the changes of the static properties affect the dynamics in the sample. The observed changes from the high temperature paramagnetic phase compared to the low temperature antiferromagnetic phase or the ferromagnetic phase can be attributed to the magnetostrictive interaction. This interaction only exists due to the magnetic orderings in the low temperature phases. The results from the measurement series where the excitation fluence F is fixed and start temperature T_{start} is varied are shown in Figure 4.2. They exhibit the following trends:

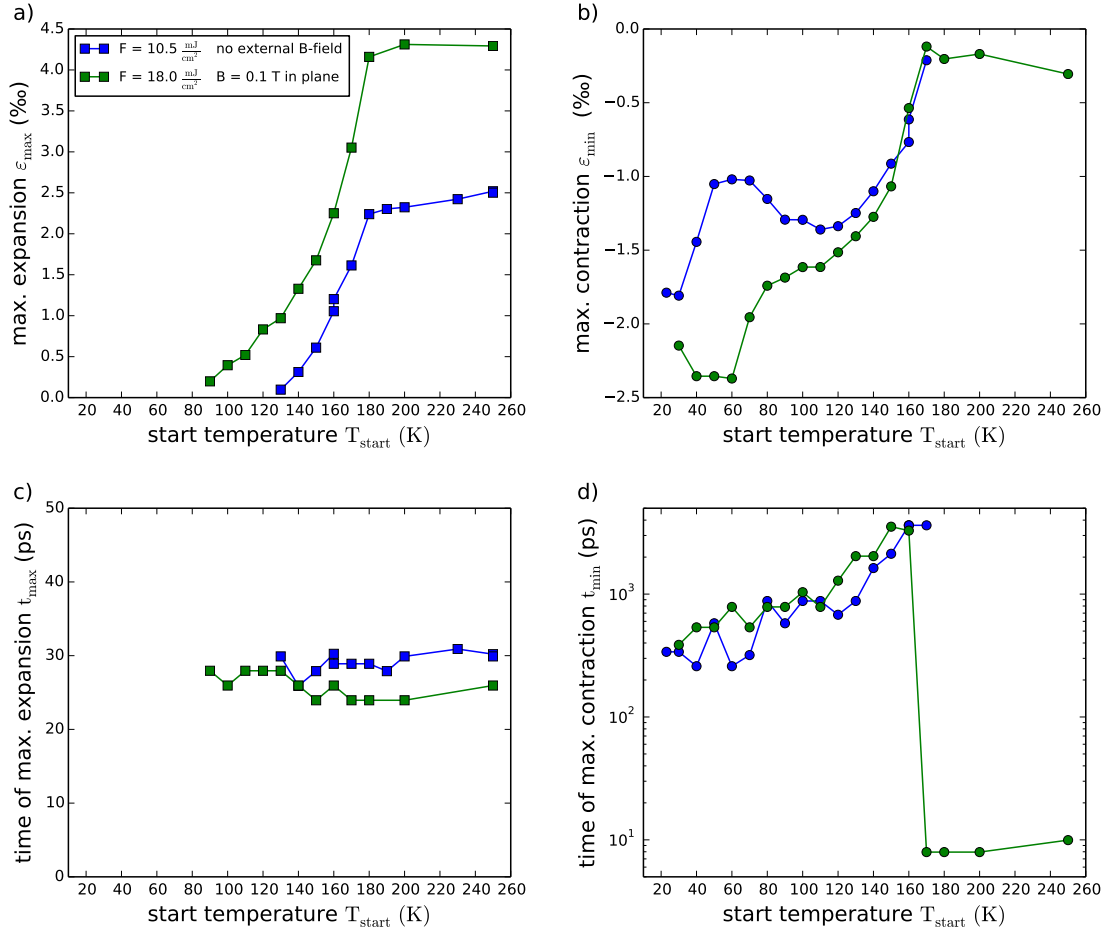


Figure 4.2. Analysis of the temperature series measured on DyY24B: Results of the transient strain observed in experiments where the excitation fluence is kept fixed and the start temperature T_{start} is systematically varied. It is observed that the maximum expansion shown in a) displays a threshold behavior and increases up to its saturation value attained in the paramagnetic phase. The timing of the maximum expansion of the Dysprosium layer shown in c) is relatively constant for all starting temperatures. On the contrary the amplitude of the maximum contraction in the Dysprosium thin film shown in b) increases as the temperature is lowered. The deviation in the blue and green curve has its origin in the shift of T_C to higher origin due to the applied in-plane B-field. The timing of the maximum contraction displayed in d) changes by one order of magnitude as the temperature is increased close to the phase transition.

- There exists a threshold temperature that depends on the excitation fluence at which no considerable expansion is seen. For 10.5 mJ/cm^2 this threshold temperature is 130 K. Above this threshold temperature the expansion increases with T_{start} up to a saturation that sets in at $T_N = 180 \text{ K}$.
- The timing of the early expansion is independent of starting temperature and it occurs approximately 24 – 28 ps after excitation.
- The maximal observed contraction varies also strongly with the start temperature. Both phase transitions can be seen in the maximal contraction. In the paramagnetic phase no contraction is seen apart from an early compression at approximately $t < 10 \text{ ps}$ that I attribute partially to the expansion of the adjacent Yttrium layer. Below the phase transition the observed maximum contraction increases up to $T_{\text{start}} = 110 \text{ K}$. Lowering the start temperature below the Curie temperature T_C adds an additional increase to the maximum contraction.
- The timing of the maximum contraction undergoes strong changes within the temperature series. For bath temperatures close but below $T_{\text{Néel}}$ the maximum contraction occurs on a timescale of a few nanoseconds. As the temperature is lowered the maximum contraction shifts to smaller delays but it occurs not earlier than 300 ps.

To supplement the findings from the temperature series I consider now the fluence dependence of the extrema in the observed transient strain. This is expected to yield relevant information because the incident laser fluence determines how much energy is delivered to the sample. In thermal equilibrium the supplied energy sets the limit whether or not a phase transition is possible. Therefore the supplied energy will also play a crucial role on ultrafast timescales, even though thermal equilibrium between all subsystems is not guaranteed. The measured fluence series have been subjected to the same meta analysis as for the temperature series and the results are displayed in Figure 4.3.

The general trends observed from the extrema are:

- The maximum expansion occurs only at temperature close to or above T_N at a delay between 26 – 30 ps and its amplitude depends linearly on the excitation fluence F .
- A threshold fluence exists below which no expansion is observed. At 160 K this fluence is approximately 4.5 mJ/cm^2 .
- The observed maximum contraction increases with excitation fluence but this starts to saturate after a threshold fluence is reached. The saturation value is approximately 3 mJ/cm^2 for the 160 K fluence series.
- A delayed maximum contraction is observed for increasing the fluence close to the second order AFM-PM phase transition. This is not the case for the 40 K data set measured in the ferromagnetic phase.

One omnipresent feature in the recorded data is the subsequent contraction of the Dysprosium thin film after the initial dynamics has occurred within the first 100 ps. It is most strikingly seen in the temperature series data where between 100 – 400 ps all curves exhibit the same trend.

In a semi-logarithmic plot I observe a linear decay that is defined only by the two parameters the slope a and an offset b : 4.1.

$$\epsilon(t) = a \log(t) + b. \quad (4.1)$$

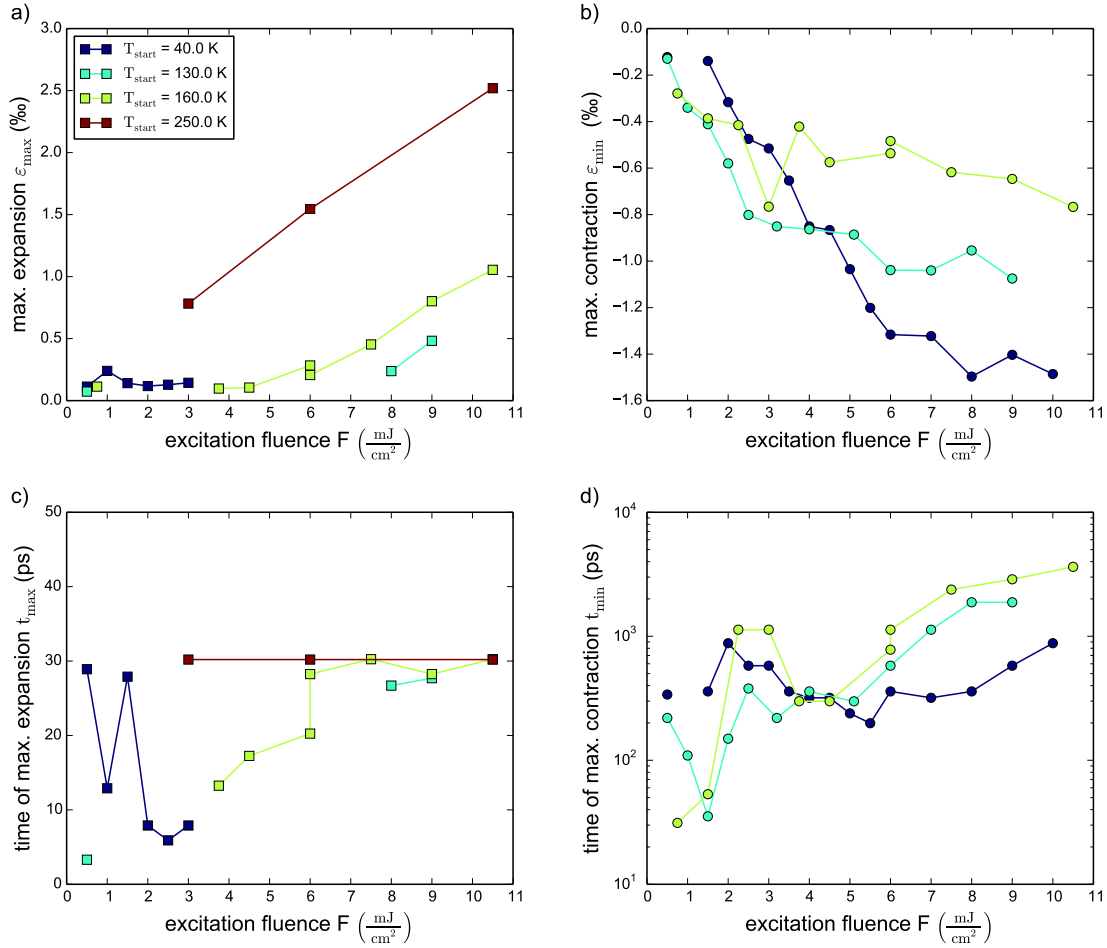


Figure 4.3. Analysis of the fluence series: Results of the measurement series where the start temperature T_{start} is kept fixed and the laser fluence F is successively increased. A linear rise of the maximum expansion in a) with excitation fluence is confirmed in the paramagnetic case and the maximum expansion time shown in c) is again constant within the time interval of 25 – 30 ps. In the antiferromagnetic case one observes a saturation of the lattice contraction with excitation fluence after a strong increase for low fluences shown in b). Underpinning the findings from the temperature series the timing of the maximum contraction displayed in d) is found to increase dramatically when the excitation fluence of the incident laser is increased.

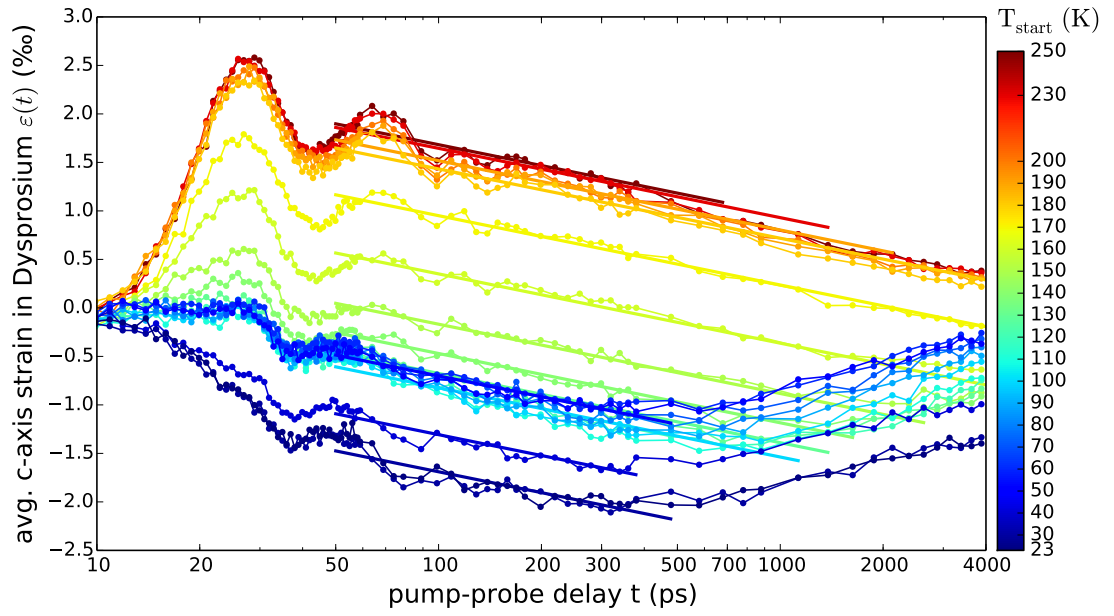


Figure 4.4. Phonon cooling: One striking feature in the temperature series is the common contraction slope that exists within 100ps – 400ps regardless of starting temperature. It is illustrated by lines with identical slope in the semi-logarithmic depiction that are only shifted by a different offset. The common behavior of the material suggests a common physical mechanism, which I identify as cooling of the phonons to the substrate.

The straight lines that have been added as a guide to the eye in Figure 4.4 all have the same slope $a \approx -0.31 \frac{\%}{\log(\text{ps})}$ and only the offset b has been used as fit parameter. In spite of this strong restriction a good agreement between the measured data and the fit is observed. The drawn lines start at 50 ps and end when the datapoints deviate by more than 0.175 % from the fit. Some lines have been omitted for clarity but a reasonable agreement can be achieved for all datasets with the same laser fluence on the timescale between 100 – 400 ps. In addition I observe that the closer T_{start} is to T_N the longer does this trend continue.

I attribute this feature to the cooling of the phonon system to the substrate, because this is the only mechanism on that timescale present that is present in all three magnetic phases of the Dysprosium layer. Supporting this claim is that the timescale and behavior is confirmed by standard heat transport theory simulated using the UDKM1Dsim toolkit as will be discussed in section 4.3. Its presence in the paramagnetic phase assures me that this feature of the lattice response can be attributed to dynamics within the magnetic system.

The time at which the observed signal deviates markedly from the linear slope coincides with the point of inflection that marks the maximum contraction. I interpret this as the time when the influence of the recovering magnetic order starts to dominantly act on the Dysprosium lattice constant. That is the time when the contraction due to the cooling of the phonon system is less strong than the expansion due to the recovering magnetostriction. Since the mechanism of magnetostriction can only act when magnetic order is present, the lattice dynamics also provide an upper limit for the time scale of the recovery of magnetic order within the Dysprosium thin film. The obtained data show that this magnetic recovery is strongly dependent on the starting temperature and deposited energy. This indicates the importance of energy transport processes within the sample that are discussed to some more detail in section 4.3 within an equilibrium point of view and in section 4.5 in a non equilibrium approach.

4.2 Initial dynamics

From the perspective of research in ultrafast dynamics a driving question for research is in many occasions: "What are the timescales of the involved processes and what physical mechanism determine the speed limitations?". Insights into these problems are often closely related to the observed sample response directly after the excitation, which I consider in the following paragraph.

4.2.1 Speed limit of Magnetostriction

In the following I consider the question "How fast is the magnetostriction mechanism in rare earth materials?". It is of fundamental interest and one of the main motivating factors of my investigations. Based on my data it is possible to give an approximate upper boundary for the mechanism in Dysprosium. For that I compare in Figure 4.5 data of the average Dysprosium c-axis strain measured within the first 20 ps after excitation with an excitation fluence of 5 mJ/cm²

for all three magnetic phases.

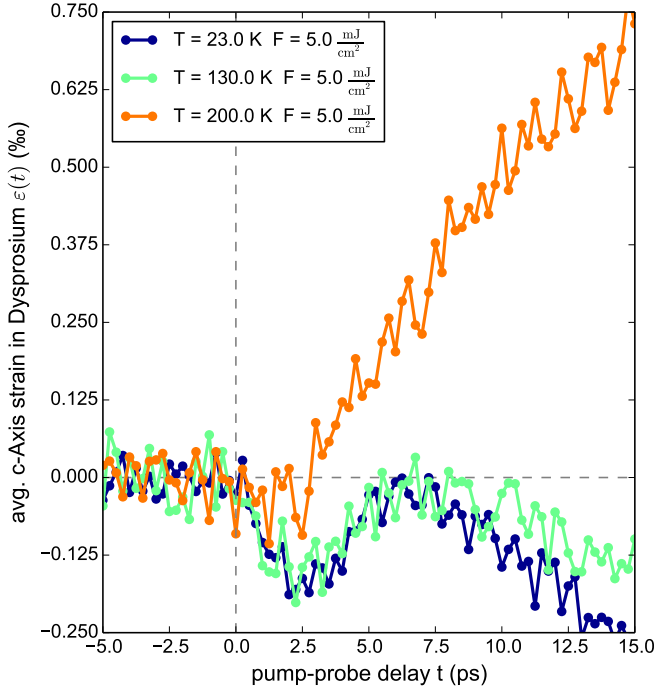


Figure 4.5. Initial dynamics: Comparison of three datasets acquired with a high point density of 250fs within the first 20ps averaged over ten delay loops. The blue and green datasets acquired in the magnetic phase visually deviate from the orange data acquired in the paramagnetic phase at approximately 1.25ps. I consider this relative pump-probe delay as an upper limit to the onset of the contractive magnetostriction stress subsequent to a loss of magnetic order.

The data for the ultrafast dynamics shown in Figure 4.5 have been obtained with a stepsize of 250fs in time which corresponds approximately to the temporal resolution of our setup. Each point represents the averaged value of the data obtained within ten subsequent delay loops. In all three magnetic phases I observe a negative average strain in the Dysprosium layer, that is maximal at approximately 2.5ps after the excitation. I attribute that to the expansion of the 10nm Yttrium top layer, which must be larger than for the Dysprosium layer. This top layer is excited with a higher energy density due to the exponentially decaying excitation profile with a penetration depth of ≈ 24 nm. The imbalance of the expansion forces due to the exponential penetration depth manifests itself via a compression of the adjacent Dysprosium layer. This small compression is superseded when the large expansion pulse from the air-Yttrium interface enters the Dysprosium layer. Unfortunately this early expansion of the Yttrium capping layer happens on the same timescale and thus superimposes the effect of magnetostriction at very early delays.

As an estimation of the upper speed limit for the onset of magnetostriction I can therefore state that it takes less than 1.25ps to act. This is the time I read from Figure 4.5 when the orange curve measured in the paramagnetic phase at 200K starts to deviate considerably from the temporal evolution of the green curve measured in the antiferromagnetic phase at 130K. Korff-Schmising et al.⁷⁵ reported a magnetostriction strain rise time of 500fs in the material Strontium-Ruthenate, which is a metallic itinerant ferromagnet with a Perovskite lattice structure. This timescale is somewhat faster than the upper limit I can read from my data but there is no disagreement in the

order of magnitude of the timescale of the magnetostriction process.

A combined study of the demagnetization and the lattice response on the same rare earth sample structure is desirable because it will provide a deeper insight into the subprocesses and identify whether there exists a delay between demagnetization and lattice response in either the demagnetization or the remagnetization process. If no delay between the magnetization and the lattice response is found then it might be more convenient to probe the lattice dynamics for some experimental questions, because it relaxes the requirement of resonant X-rays as probe pulses.

Selective probing of the Dysprosium magnetization in the ferromagnetic phase after femtosecond laser excitation is possible with time-resolved X-ray-Magnetic-Dichroism measurements that probe the magnetic ordering. Such measurements have already been successfully carried out on the rare earth metals Gadolinium and Terbium^{69,71} providing insights into a two step demagnetization process. Probing the magnetic order in a helical antiferromagnet has been demonstrated using time-resolved resonant X-ray diffraction from the magnetic side peaks that occur due to the additional periodicity of the spin helix in the rare earth material Holmium⁷³. An extended study that combines probing the magnetization dynamics in the antiferromagnetic and ferromagnetic phase of Dysprosium has been carried out at the FemtospeX facility at BESSY II synchrotron by Thielemann-Kühn et al. in the group of Prof. Föhlisch. The data are still in the evaluation phase. Preliminary results discussed in a private communication confirm a two step decrease of the magnetic ordering in the antiferromagnetic phase where the first step occurs on the order of 150 fs and a second slower demagnetization dynamics which has a time-constant in the order of 30 ps. These so far unpublished results are not in disagreement with our observed lattice dynamics in the sense that the observed lattice response occurs on longer time scales.

Current limits for the direct comparison of the magnetic response and the lattice response are given by the different thicknesses of the probed Dysprosium layer combined with the different X-ray penetration depths in the two separate setups. The used resonant techniques at the femtoslicing beamline use radiation resonant to the M_5 -edge of Dysprosium in the soft X-ray regime at 1295 eV where the X-ray penetration depth is on the order of 10 nm and therefore these techniques are much more surface sensitive²². In comparison the hard $\text{Cu K}\alpha$ radiation has an extinction length of a few micrometers into our sample, which also provides information on the buried layers. Thus the results reported here probe the full Dysprosium layer. For details on the energy resolved penetration depths see Figure 6.8 in the appendix. Furthermore it is important to note that any stress induced by the laser excitation can only fully manifest itself as measurable lattice strain on the timescale that it takes to propagate a sound wave through the magnetic layer. Thus the lattice response is to some extent limited by the finite speed of sound, which in the case of Dysprosium is $3.1 \frac{\text{nm}}{\text{ps}}$ as calculated from the elastic constants reported by Palmer and Lee¹³¹.

In order to answer the question of the speed of magnetostriction in rare earth Materials I believe it is necessary to change the sample geometry. One way would be a thin film sample without the Yttrium capping layer, where all energy is absorbed within the Dysprosium layer, and the ambiguity due to the coherent strain pulse launched from the capping layer could be avoided. The difference of transient strain in the paramagnetic phase and the antiferromagnetic phase for

the same excitation fluence could then be directly attributed to the magnetostriction due to the loss of magnetic order. Such a sample geometry has been proven to work²² for Dy/W(110) but only under maintained ultrahigh vacuum conditions where the thin sample films are prepared and measured within the same vacuum chamber so that the oxidation of the Dysprosium thin film is suppressed.

4.2.2 Compensation effect in the fast dynamics

Considering the coherent dynamics within the first 50 ps I observe a peculiar lattice response of the Dysprosium layer that exhibits nearly no strain in the first 30 ps of the antiferromagnetic phase for starting temperatures between 50 – 120 K at an excitation fluence of approximately 10.5 mJ/cm². The corresponding strain measurements are shown in Figure 4.6(a). It includes also the transient strain observed at other T_{start} as a comparison, where a significant expansion almost instantly after the excitation can be seen. After 30 ps a step-like fast contraction of approximately -0.5% occurs within 5 ps. The coincidence of the lattice contraction in the low temperature phase at 30 ps with

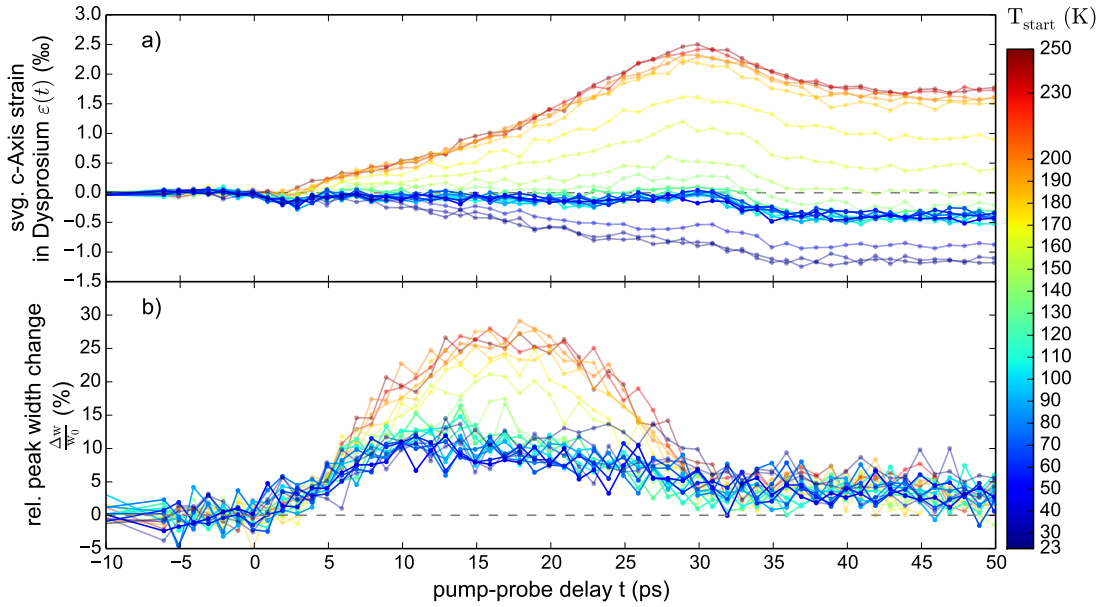


Figure 4.6. Initial lattice dynamics: Relative change of (a) the Center of Mass (COM) and (b) the standard deviation (STD) of the Dysprosium peak that are model independent quantities for the center and width of the Bragg peaks. Shown here are data for an excitation fluence of 10.5 mJ/cm² for T_{start} in all magnetic phases. The saturation of colors emphasizes the peculiar lattice response observed for $50 \leq T_{\text{start}} \leq 120$ K where almost no lattice strain is observed within the first 30 ps although the peak width increases much earlier. This is evidence for a spatial compensation effect of compressive and contractive strain components as discussed in this section.

the negative slope due to the coherent phonon oscillation in the high temperature phase already suggests the involvement of the coherent strain wave starting at the air Yttrium interface in this process. The decisive quantity for the interpretation is the relative peak width change shown in

4.6(b) that is not delayed with respect to the transient peak width change of the measurements at other T_{start} . The increase of the transient peak width of the Dysprosium Bragg peak indicates an inhomogeneous strain within the thin layer⁸⁸. The only possible way for the average strain to remain zero while the layer becomes inhomogeneously strained is that there exist positive and negative strain components that compensate each other, but have a different spatial profile. For an exact cancellation of strain throughout the layer also the change of the peakwidth would have to be zero.

In Figure 4.6 I display the relative change of the Center of Mass (COM) μ and the standard deviation (STD) σ as the first and second moment of the Bragg peak intensity distribution of the Dysprosium Bragg peak in the reciprocal space area $2.2 \text{ \AA}^{-1} \leq q_z \leq 2.25 \text{ \AA}^{-1}$. The COM and the STD are model free quantities that can be calculated for any distribution and are calculated according to relation 4.2 and 4.3 respectively:

$$\mu = \frac{\sum_i^N x_i y_i}{\sum_i^N y_i} \quad \text{Center of Mass} \quad (4.2)$$

$$\sigma = \sqrt{\frac{\sum_i^N (x_i)^2 (y_i - \mu)^2}{(y_i)^2}} \quad \text{Standard Deviation} \quad (4.3)$$

On purpose I do not use the center of a fitted Gaussian as it is much less sensitive to small asymmetric changes in the peak profile since the fit function is inherently symmetric. Such asymmetries however occur on ultrafast timescales when strain pulses enter the layer so that it is only partially expanded. As a consequence the COM shows a faster response for the average strain in the Dysprosium layer than the fitted Center of the Peak. For large timescales times both quantities show very comparable dynamics as shown in Figure 3.12(a).

One compensation mechanism that would explain the zero net strain within the first 30 ps, followed by a steplike contraction are spatially different magnetic and phonon excitation profiles. Such spatially inhomogeneous stress profiles would be capable of generating compensating strain effects. To clarify this idea, I carried out two separate simulations of the coherent phonon waves using the UDKM1Dsim-toolkit⁷: one for a generic expansive phonon stress profile shown in Figure 4.7 and one for a contractive magnetic stress profile shown in Figure 4.8. The main finding is that strain waves are launched at gradients within the stress profile. For the exponentially decaying stress profile the largest gradient exists at the air sample interface leading to the expansive strain wave that propagates at the speed of sound into the sample and gets reflected at sample interfaces. The average strain in the Dysprosium layer of the simulation shown in Figure 4.7 matches approximately the measured average strain from our paramagnetic experiments. For an assumed flat magnetic excitation profile within the Dysprosium thin film from Figure 4.8 one obtains contractive strain waves propagating into the Dysprosium layer from both of its interfaces with Yttrium. At long timescales a contraction remains in the rare earth thin film.

In the experiment phonon expansion and magnetostrictive contraction act concurrently and superimpose each other, which could then lead to the observed compensation effect. One strong evidence for spatially inhomogeneous strain profiles is the increase of the peak width after

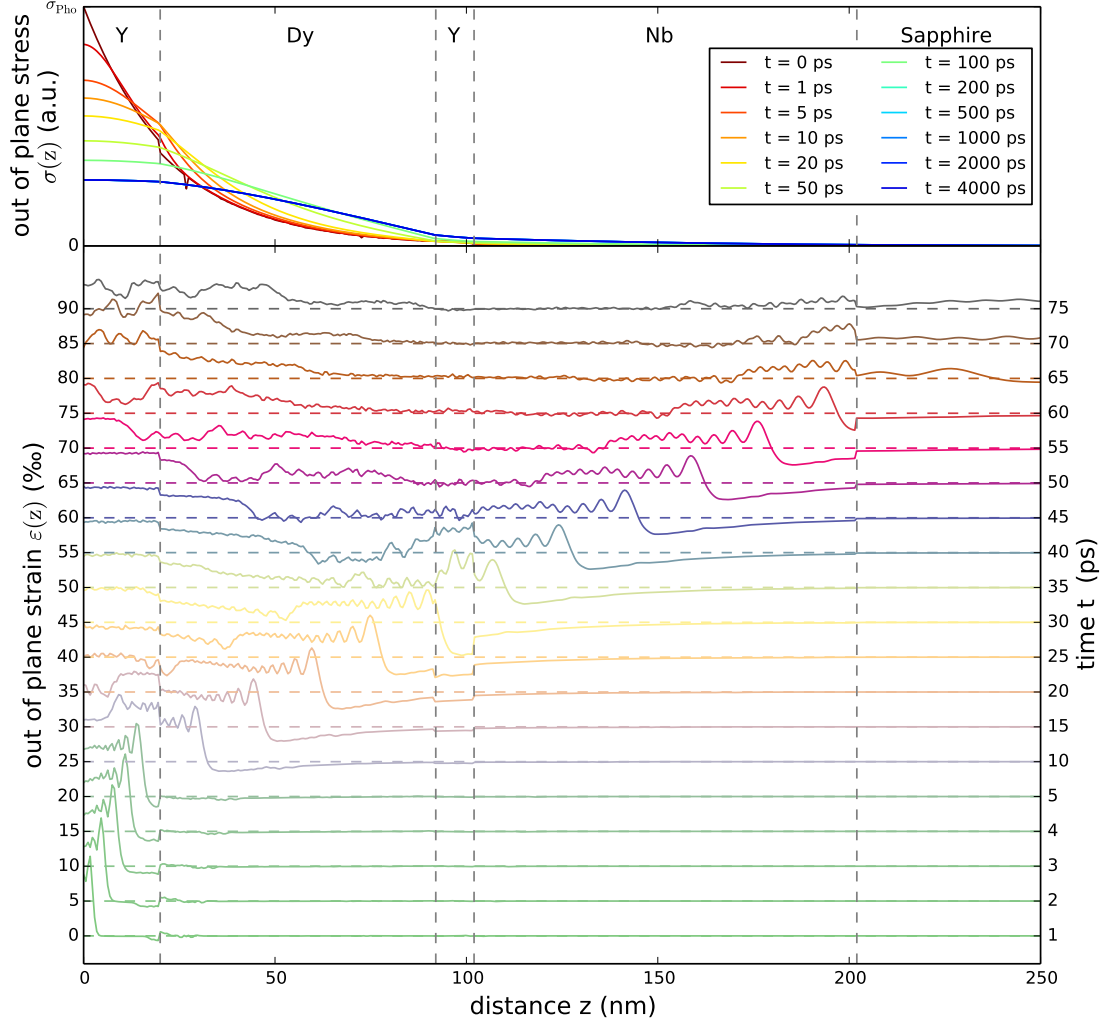


Figure 4.7. Strain pattern due to heat expansion: Spatially resolved stress (top) and resulting strain (bottom) for an expansive stress that models the excitation of the phonon system in the paramagnetic phase. A large amplitude strain wave starts at the air-sample interface and propagates through the sample at the speed of sound. It gets partially reflected at each interface resulting in the coherent phonon oscillations observed within the first 200 ps of my measurements that only resolve the average strain in the Dysprosium thin film. The thin film dimensions shown here have been adjusted slightly from their value entered in the growth process so that the coherent phonon oscillations match the measurement results. The spatial strain profiles are offset by 5% for each timestep for better visibility.

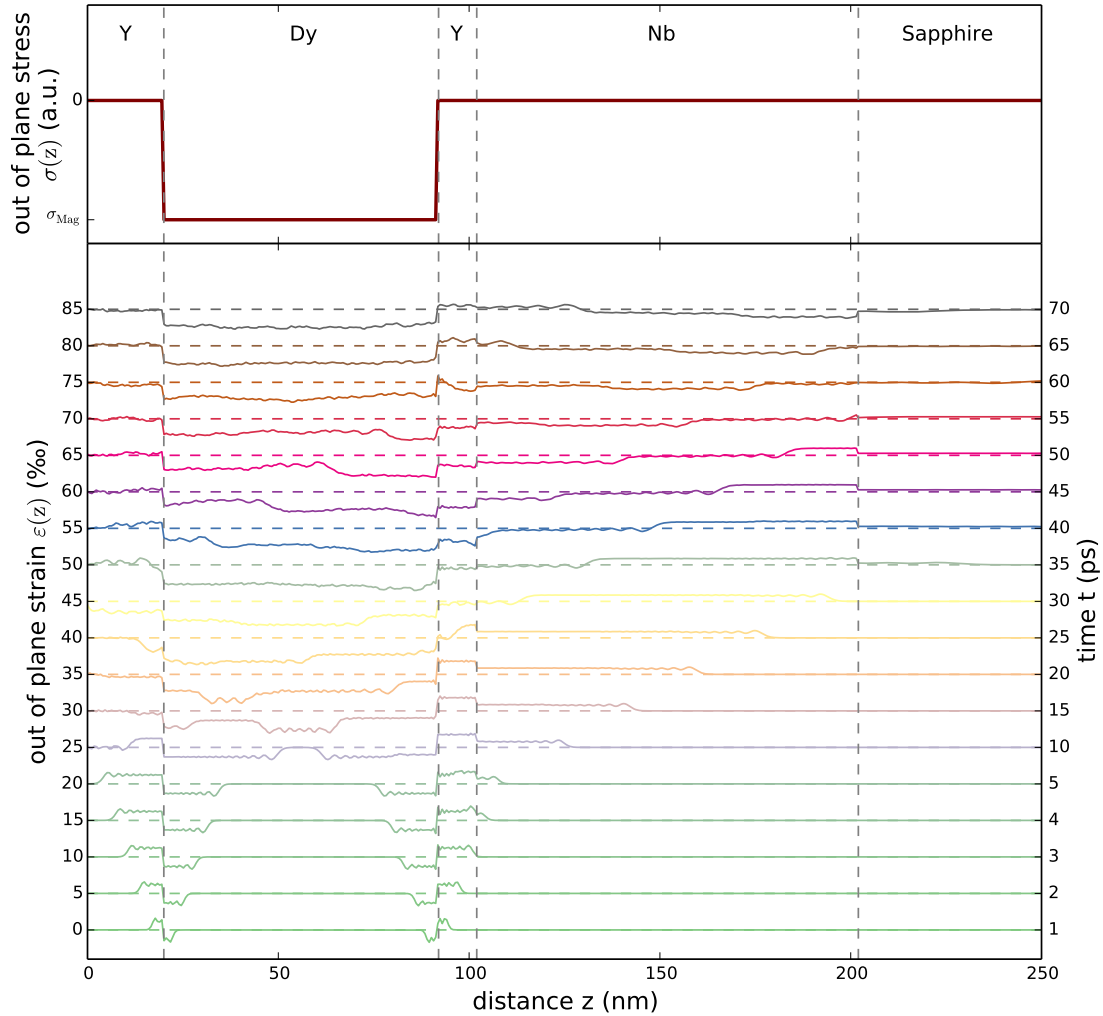


Figure 4.8. Strain pattern from a simplified model for the magnetic-stress profile: The assumption of a fast spatially uniform demagnetization leads to a stress profile shown in the top, which is only present within the Dysprosium film. The resulting contractive strain waves shown at the bottom emerge at the Yttrium-Dysprosium interfaces and propagate into the rare earth layer. I consider this as the most probable mechanism that could counterbalance the large expansive strain wave from the phonon system that emerges at the sample-air interface.

excitation shown in Figure 4.6(b), that exhibits no delay after excitation. The step-like decay at 30 ps coincides with the moment when the large expansive strain wave from the sample surface leaves the Dysprosium layer. The partial reflection at Yttrium interface that has a lower acoustic impedance Z than the Dysprosium thin film leads to a phase shift in the reflected wave that then reaches the Dysprosium layer as a contraction. A spatially homogeneous stress profile that would not create any net lattice strain could only be zero within the entire layer, which is contradicted by the peak width increase. As a consequence I conclude that the spatial profiles for magnetic stress and phonon stress have to be different.

Admittedly the premise of a flat stress profile for the contractive magnetic force is a makeshift assumption that originates from the lack of more precise knowledge on the propagation of magnetic disorder within my sample. It is motivated with the idea of hot ballistic electrons in mind. They could propagate from the excitation volume into the sample with near Fermi velocity. Such an injection of hot electrons into the conduction band would most likely distort the RKKY-coupling mechanism and lead to a partial demagnetization, within the injection volume. The existence of ballistic electrons upon laser irradiation has been demonstrated by Brorson et al.¹³² for thin gold films and the ballistic electrons in Gold are known to have a mean free path of approximately 100 nm within the first 100 fs¹³³. However it is established that the phonon coupling in Gold is particularly weak as compared to other less noble metals¹³⁴. With the current sample geometry at hand I see no direct way to detect the existence of these hot electron currents. In a sample geometry where the capping layer of Yttrium is very thin compared to the bottom layer of Yttrium and the Dysprosium is much thicker than the optical penetration depth one could monitor the timing of the peak shift of the thick Yttrium detection layer. If it expands right after excitation it can only be due to the contraction of the adjacent Dysprosium resulting from ballistic electrons distorting the magnetic ordering.

A first study of the temporal stress pattern in the rare earth magnetic film has been carried out in the Master Thesis of my colleague Jan Pudell⁹³. He finds that a magnetic stress profile that resembles a diffusion process where a negative stress enters the magnetic layer increases over time, best describes the observed lattice response obtained on the Holmium thin film sample. He found that a negative Gaussian function that extends into the layer and becomes broader over time at a diffusion rate of $4.3 \frac{\text{nm}}{\sqrt{\text{ps}}}$ described the initial lattice dynamics within the first 70 ps. For me it is an interesting question how fast and by what mechanism a disturbance in the magnetic system on the one end of the rare earth thin film propagates through the sample but at the moment this question lies out of the scope of this work.

4.3 Equilibrium Model approach

In this section I present the first crude but intuitive approach to the interpretation of our time resolved measurements which are presented in section 3.5. This so called equilibrium model treats the Dysprosium layer as a zero dimensional system that is in thermal equilibrium at all times after the laser excitation. The schematic visualization in Figure 4.9 stresses the equilibrium mindset of the model that assumes that all subsystems of the laser excited material remain in thermal equilibrium with each other. One consequence is that one temperature used to describe the status of the sample. The simple equilibrium approach does not resolve any inhomogeneous stress or temperature profiles within the Dysprosium layer. It is intended as an estimation of the temperature change after the laser excitation. For that it is assumed that Dysprosium exhibits the same temperature dependence of the heat capacity as reported in the literature for bulk material⁴⁶ and that the lattice constant behaves as a function of temperature as it was determined in the static characterization measurements. The time resolved process is then modeled by the assumption that the laser pulse deposits energy into the material, which leads to a rise in the temperature. The rise in temperature is defined by the deposited energy in relation to the heat capacity. It is numerically determined by integrating the heat capacity $C_p(T)$ from T_{start} to the end temperature T_{end} at which the deposited energy Q equals the integral value as stated in relation (4.4):

$$Q_{\text{deposited}} \stackrel{!}{=} \int_{T_{\text{start}}}^{T_{\text{end}}} C_p(T) dT \quad (4.4)$$

In order to apply this method it is therefore necessary to calibrate the amount of deposited energy Q by the laser pulse. This quantity is inferred from the initial lattice expansion in the paramagnetic phase where the magnetic contribution to the lattice response is negligible. In the paramagnetic phase one observes a fast out-of-plane lattice expansion along the c-axis of Dysprosium due to the thermoeleastic response of the material. This expansive strain has for an excitation fluence of $F = 10.5 \text{ mJ/cm}^2$ an amplitude of approximately 2‰ at 45 ps as can be seen in Figure 3.12. In the determination of this expansion I take into account that the coherent excitation of phonons mainly at the air sample interface creates strain pulse effects that superimpose the thermal expansion and can be seen as oscillations in the signal. The thermal expansion contribution can be extracted intuitively by eye or by applying a running average smoothing routine where the average is taken over the period of the oscillations.

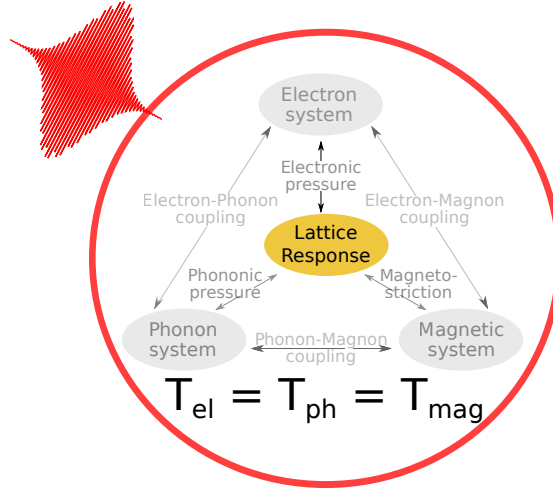
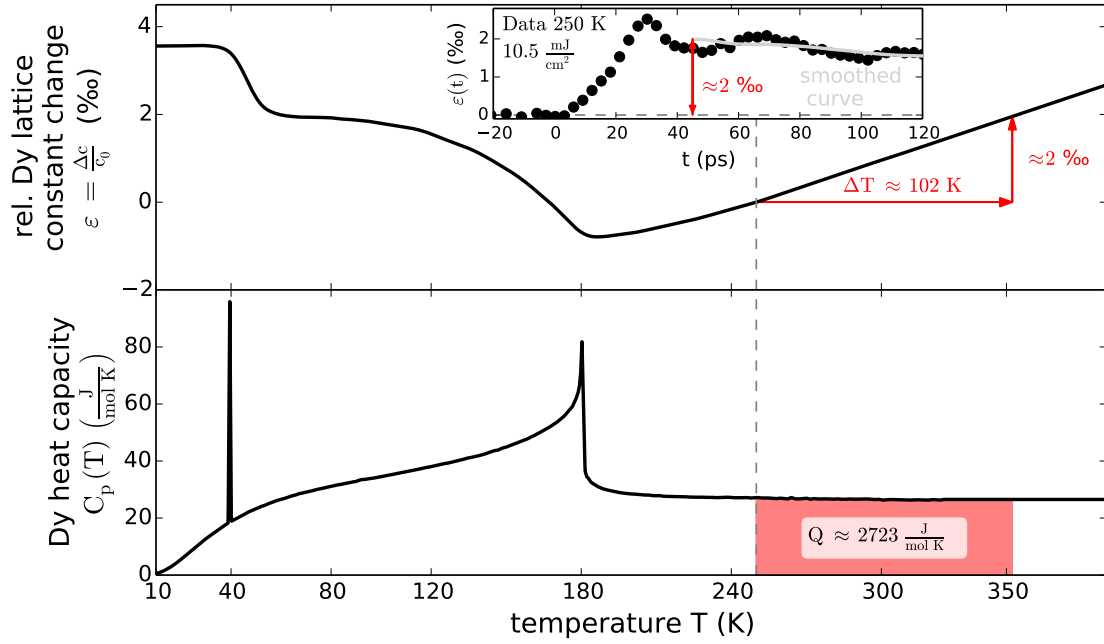


Figure 4.9. Equilibrium approach: Energy is deposited in the sample but instantly redistributed in such a way that all subsystems are in thermal equilibrium. No subprocesses are resolved.

- (a) **Example for the Calibration at $t = 45$ ps:** The deposited energy $Q(t)$ is inferred from the lattice strain $\varepsilon(t) = 2\%$ expansion after laser excitation



- (b) **Resulting Application:** Depositing the calibrated amount of energy $Q(t)$ in the antiferromagnetic-phase of the material

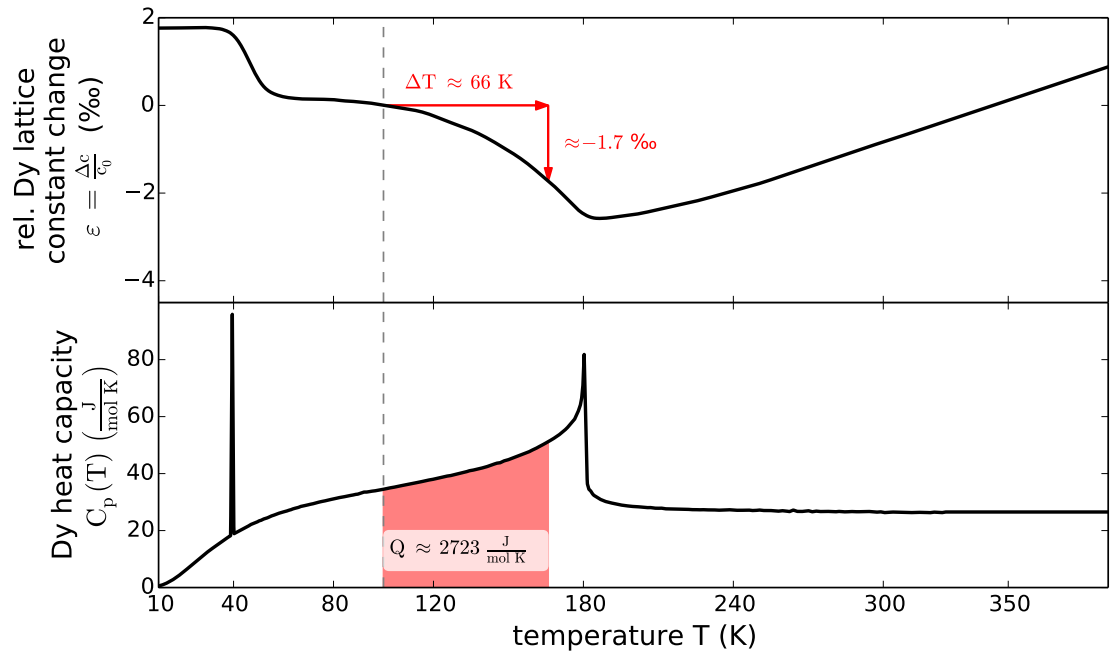


Figure 4.10. Principle of the Equilibrium Model approach: In a first step shown in (a) the deposited amount of energy in the Dysprosium layer Q is calibrated in the paramagnetic phase by calculating the associated temperature step that corresponds to the observed initial lattice expansion of 2 ‰ with a laser excitation fluence $F = 10.5 \frac{\text{mJ}}{\text{cm}^2}$. In the second step depicted in (b) the calibrated energy is used to predict the temperature step ΔT via the heat capacity of Dysprosium. From the temperature change one can then extract the expected strain within the thin film. Under the assumption that the heat conduction process is similar in the paramagnetic and the magnetic phase this analysis can be carried out for each recorded timestep. The implicit assumption of this model is that all degrees of freedom in the material rapidly reach their thermal equilibrium after the excitation. Since this model does not provide any spatial resolution and assumes a constant temperature throughout the layer. The results of this reasoning are shown in 4.11 in comparison to the measured data.

The extracted expansive strain of 2‰ starting from the equilibrium lattice constant at 250 K corresponds to a temperature increase of $\Delta T = 102$ K, which can be extracted from the c-axis versus temperature characterization measurement. Integrating the heat capacity of Dysprosium from $T_{\text{start}} = 250$ K to $T_{\text{end}} = 352$ K I obtain that the deposited energy amounts to $2.723 \frac{\text{kJ}}{\text{mol}}$. The calibration process for the deposited amount of energy is visualized in Figure 4.10(a).

With a brief characterization measurement I assured myself that the ratio of the relative reflected laser power $\frac{P_{\text{reflected}} - P_{\text{incident}}}{P_{\text{incident}}}$ does not change as a function of the temperature of the sample within my measurement resolution of approximately $\pm 5\%$, that is given by fluctuations in the laser intensity. This indicates that the amount of surface-transmitted fluence remains nearly constant for our measurements regardless of T_{start} . Having no other indications I thus assume that the amount of absorbed energy stays the same if the amount of the incident laser fluence is kept fixed.

Knowing the amount of deposited energy from the calibration at 250 K, permits a first estimation for the temperature step and thus the expected lattice strain as shown exemplarily for the case of $T_{\text{start}} = 100$ K in Figure 4.10(b) where the model predicts an initial relative contraction of $\frac{\Delta c}{c_0} = -1.7\%$. This analysis can be carried out for every time-step of the measurement. More explicit: At each timestep t_x I calibrate the energy $Q(t_x)$ that is present in the Dysprosium layer from the observed lattice expansion $\varepsilon^{\text{PM}}(t_x)$ in the paramagnetic phase at 250 K at t_x , which corresponds to 4.10(a). In the next step I integrate the heat capacity from T_{start} to the point when $Q(t_x)$ is in the system from which I obtain the equilibrium temperature estimate $T(t_x)$. Via the equilibrium calibration curve of lattice constant versus temperature I can obtain the predicted $c(T)$ lattice strain $\varepsilon(T(t_x))$ which corresponds to Figure 4.10(b). In Figure 4.11 I compare a representative selection of datasets at a fixed fluence of 10.5 mJ/cm^2 with the prediction of the equilibrium model.

The agreement between the data and the equilibrium model prediction in the paramagnetic phase at $T_{\text{start}} = 250$ K results from the calibration of the model at that temperature. However as the temperature is lowered below T_N the equilibrium model predictions strongly deviate from the measured strain. Three possible reasons for this deviation are possible. Firstly the spatial inhomogeneity of the temperature profile, combined with the non-linear $c(T)$ lattice constant versus temperature behavior leads to deviation, that can not be resolved in this zero dimensional model. The influence of the inhomogeneous strain profile will be estimated by spatially resolved equilibrium model simulations shown in the next section. Secondly the instantaneous equilibration between the electron-, phonon- and magnon system might not be achieved on the considered timescales. An experimental approach that investigates the possible non-equilibrium state between phonons and magnons in Dysprosium is carried out in section 4.5*. As a last possibility it could be that the used calibration curves namely the conversion between temperature and strain as well as the used bulk Dysprosium heat capacity are not valid for ultrafast excitation conditions of our thin film sample. An estimation of the in-plane clamping effect of the excited thin film samples

*The equilibration between phonon and electron system is expected to be on the timescale of one picosecond¹³⁵ therefore it is sufficient to consider a two temperature model between the magnon and the phonon system in Dysprosium.

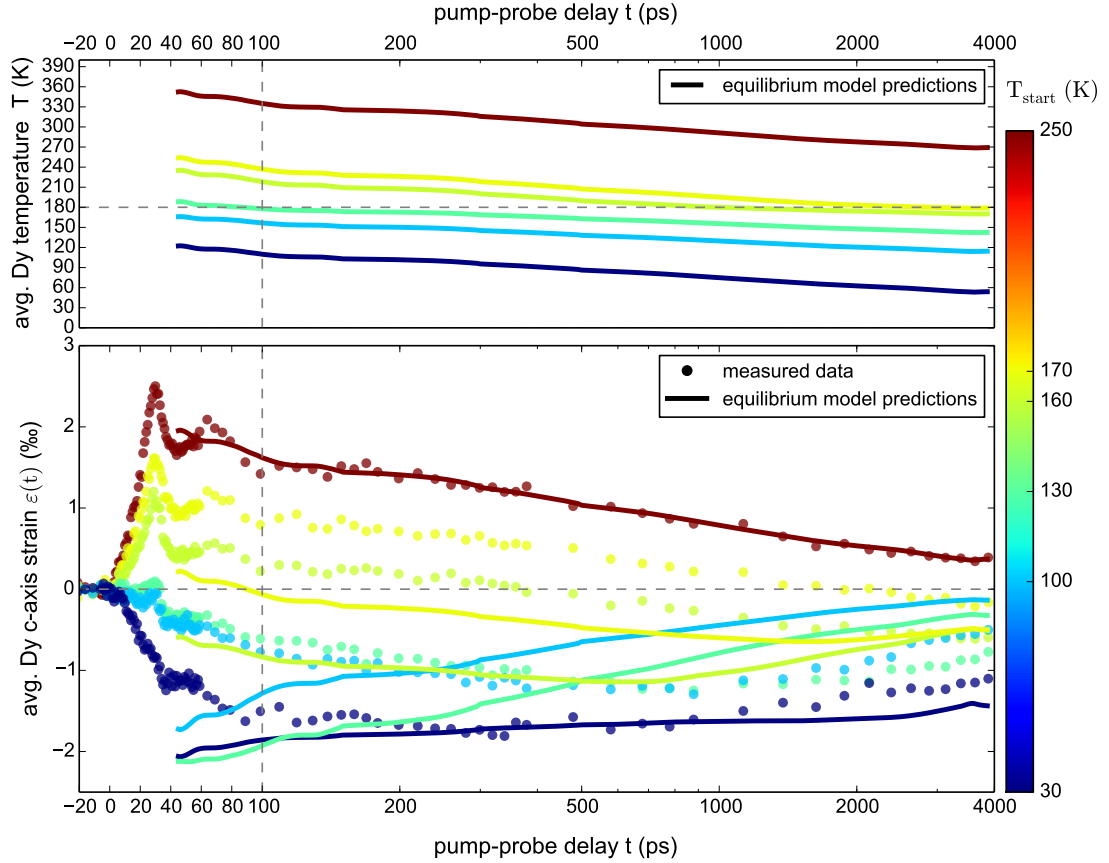


Figure 4.11. Equilibrium Model perspective: Using the calibration method for the deposited energy illustrated in figure 4.10 one obtains an order of magnitude estimation of the average temperature after the laser excitation shown in the top graph. The predicted strain of the equilibrium approach shown in (b) however strongly deviates from measured data except for paramagnetic phase, where the equilibrium model was calibrated. This sparked a more in depth analysis that takes into account the spatial inhomogeneities of the temperature profile carried out in section 4.4. Another route that relaxes the condition of one unique temperature in the system is pursued in section 4.5.

on ultrafast timescales has been carried out in Section 6.1. As of now I am not aware of a method that would help to extract the heat capacity of our thin film sample upon ultrafast excitation in order to use more exact values than the bulk measurements of Pecharsky et al.⁴⁶, which are in good agreement with other reports^{45,136,47,48,49}.

4.4 Spatially resolved Equilibrium Model simulation

One potential reason for the deviations of the equilibrium model from the actual measurements is the effect of a spatially inhomogeneous temperature profile that has not been taken into account. The tool at hand to extend the previous zero dimensional equilibrium model to a one dimensional model is a numerical simulation for the deposition of heat and its subsequent transport within in the sample in a one temperature model.

The following estimation motivates that it is sufficient to simulate the heat transport in the laser excited thin films only in the out-of-plane dimension. This simplification strongly reduces the computational costs of the model. The main argument is the large excited in-plane sample area as compared to the limited speed of heat propagation. Because even if I overestimate the velocity at which the heat flows and assume that it propagates ballistically with the speed of sound in Dysprosium of $3.1 \frac{\text{nm}}{\text{ps}}$ it takes approximately 190 ns to propagate $600 \mu\text{m}$ from the center of the laser excitation profile outwards to the point when the laser intensity is only half of its maximal value. This crude overestimation of the heat propagation still yields an approximately 50-fold larger time for the in-plane heat transport by phonons as for the out-of-plane heat transport. Therefore it is a justified assumption that the heat transport in the first four nanoseconds takes place perpendicular to the sample surface. In that direction the temperature gradient is much steeper since the laser extinction depth into the sample determined by ellipsometry measurements is only 24 nm^\dagger . Another way to look at it is that the temperature gradient, which drives the heat transport is out of plane much larger as the temperature gradient in plane. For a temperature change of 100 K upon laser excitation I obtain:

$$\frac{dT}{dz} \approx \frac{100 \text{ K}}{100 \text{ nm}} \ll \frac{100 \text{ K}}{600 \mu\text{m}} = \frac{dT}{dx} \quad (4.5)$$

An open source simulation toolbox which is tailored to model the one-dimensional lattice response of laser excited thin film samples with unit-cell spatial resolution on the femtosecond to the nanosecond timescale has been developed in the ultrafast dynamics group and its details have been published by Schick et al.⁷. This so called udkm1Dsim-toolbox is a program library written in the frequently used scripting language MATLAB and it is based on a one dimensional linear chain model of atoms. The elaborate program code provides the possibility to model not only the heat propagation within the sample but also the resulting lattice strain due to thermal stress after laser excitation including coherent phonon effects. The toolbox has

[†]Ellipsometry measurements from the IR to the near UV yielded the real and imaginary part of the pseudo-dielectric function of the layer ϵ_1 and ϵ_2 . From this information the optical penetration depth α has been determined at $\lambda = 800 \text{ nm}$ according to the relations stated in Kuzmany¹³⁷. For more details on this method see the appendix of the thesis of Pudell⁹³

already been applied in numerous contexts such as modeling the heat transport in nanoscale structures¹³⁸, predicting the strain response ferroelectric thin film samples⁸⁷, modeling the sample response upon the application of different stress profiles in the multiferroic BiFeO₃¹²⁶ as well as in the unified description of the response of a photo-excited thin film on a transparent substrate¹²⁹.

Here I apply this `udkm1Dsim-toolbox` to model the temperature and strain profiles within my sample, which provides a spatially resolved equilibrium model. Relevant physical simulation parameters have been taken from the literature and they are provided in Table 4.1 for $T_{\text{start}} = 300\text{ K}$. The temperature dependencies of the relevant parameters, which I obtained from the literature, and the static calibration measurements are shown as a reference in section 6.2 of the appendix together with the currently used parametrization in the simulations. It is relevant to note that the simulation itself does not explicitly calculate the magnetic dynamics but implicitly includes contributions of the magnetic system due to the parametrization of the linear thermal expansion, heat capacity and heat conductivity as a function of temperature.

The idea in the interpretation of the simulation is once more to make use of the possibility to compare the lattice dynamics of the Dysprosium thin film in the magnetic and non-magnetic phases. Observed differences will be related to the presence and influence of the spin system on the lattice dynamics. The paramagnetic phase is used to calibrate the absorbed fluence and thicknesses of the thin films by adjusting the simulation parameters so that the simulation matches the data, which should in principle be possible since no magnetic contribution is present. At the point when an acceptable agreement between data and simulation has been achieved these bounding parameters are kept fixed and the simulation is run in the low temperature magnetic phase. Under the assumption that the used temperature dependencies of the simulation parameters are sufficiently accurate the deviations of the data from the simulations then indicate the limitation of the equilibrium approach. A comparison between the data and the current status of the simulations is shown in Figure 4.12.

The comparison of the data in the paramagnetic phase with the simulation yields that the timing and shape of the coherent phonon oscillations as well as the amplitude of the initial lattice expansion is well represented. Some discrepancy currently remains between the data and the measurement from 80 – 500 ps. Within this time the simulated strain and the measured data deviate at by approximately 25%. Further improvements of the simulations need to address this issue which might be related to an insufficient model for the heat transport within the layers but time restrictions of the project currently set a limit to the achieved accuracy of the simulations. Since many temperature dependent parameters are taken into account and approximately 21 000 unit cells of material are simulated, one run takes approximately five hours, which inhibits a swift optimization process.

Despite the mentioned imperfection of the simulation of the lattice dynamics in the paramagnetic phase I regard the achieved degree of accuracy to be sufficient to qualitatively discuss the relation between simulation and experiment also in the magnetic phases at low temperatures. A first striking feature is that the amplitudes of the initial strain response are not well reproduced even

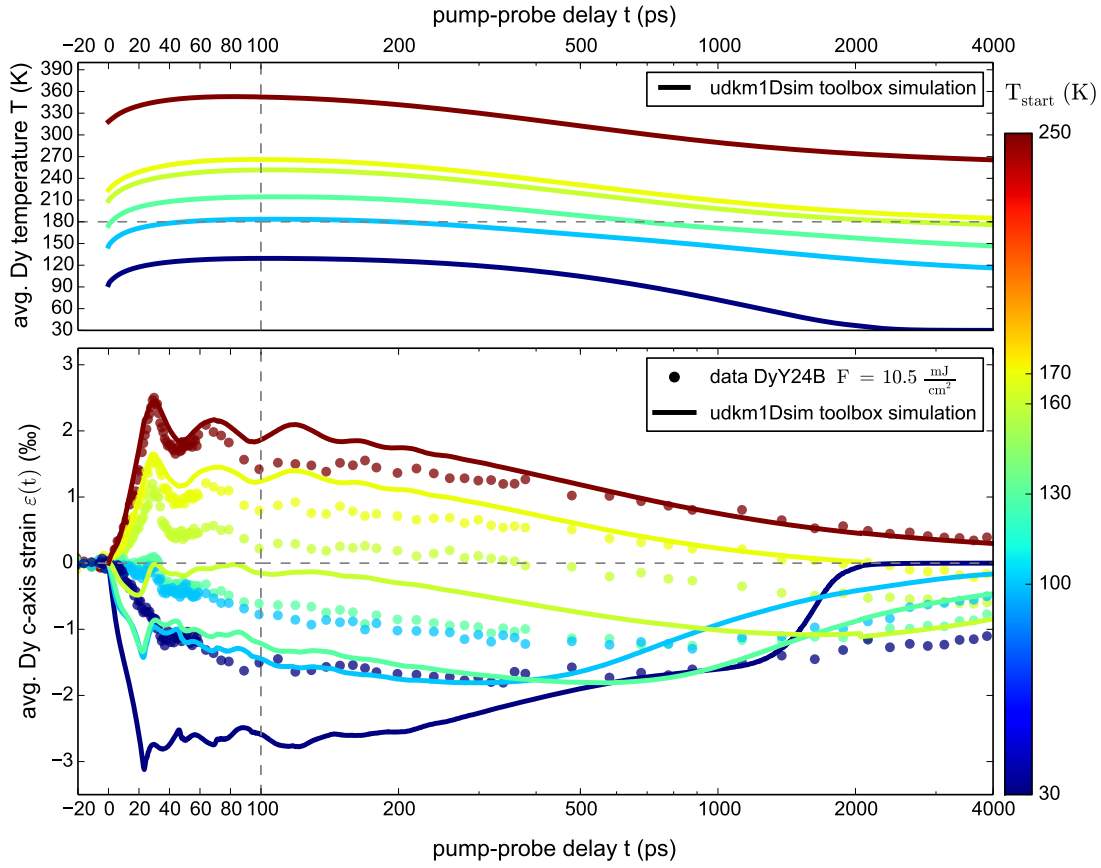
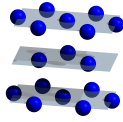
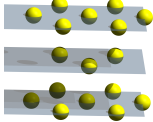
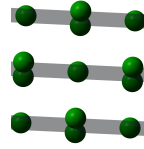
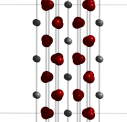


Figure 4.12. 1D-Equilibrium Model simulation results: Simulation of the one-dimensional lattice dynamics after laser excitation using the `udkm1Dsim-toolbox`¹²⁶. The top graph shows the average temperature in the Dysprosium layer and the bottom graph shows the average lattice strain in this layer. Only a representative selection of data and simulations is shown for clarity. Fair agreement has been achieved in the simulation of the signal in the paramagnetic phase at $T_{\text{start}} = 250$ K. Especially the timing of the coherent phonon oscillations within the first 200 ps and the initial lattice expansion match, which determines the thickness of the thin films and the absorbed laser fluence respectively. Lowering the start temperature, while keeping the laser fluence and sample geometry fixed, yields a prediction of the Dysprosium strain response in the magnetic phase from an equilibrium point of view. The resulting simulations at low temperatures deviate considerably from the corresponding data. The dark blue curve at $T_{\text{start}} = 30$ K deviates most, evidencing the large expected contraction in an equilibrium model. The simulation returns an expected fast contraction at 1.5 ns for this curve since it uses the bulk heat conductivity of sapphire and niobium which in theory drastically increases at such low temperatures but in practice this is not the case in our experiment. I take the deviations of the simulations from the measurements as indication for the limitations of the equilibrium model approach, that assumes that one temperature is sufficient to describe the state of the system. An analysis of the energy distribution between phonons and magnons that removes the requirement of thermal equilibrium is carried out in the next chapter.

Table 4.1. Relevant material properties used in the udkm1Dsim toolbox simulations: The values given here are reported near room temperature at $T = 300\text{ K}$. Properties marked with a star vary considerably with temperature and their temperature dependence as it is used in the simulations is provided in section 6.2 of the appendix. Sources to the literature values are provided wherever possible. The linear expansion coefficients are derived from the static characterization measurements reported in section 2.4. The extinction length for the laser light is taken to be the effective penetration depth of 24 nm determined in ellipsometry measurements.

	Dysprosium Dy 	Yttrium Y 	Niobium Nb 	Sapphire Al₂O₃ 
sketch of the unit cell crystal structure oriented as grown				
growth orientation in the used samples	hcp (0001)	hcp (0001)	bcc (110)	hcp (11 $\bar{2}$ 0)
out of plane lattice constants (Å)	5.6475 ²⁹	5.7306 ²⁹	4.667 ¹³⁹	4.758
in plane lattice constant (Å)	3.5903 ²⁹ hcp a-axis	3.6474 ²⁹ hcp a-axis	4.667 ¹³⁹ a-axis 3.30 ¹³⁹ b-axis	8.214 a-axis 12.804 b-axis
molar mass (g/mol)	162.5 ¹⁴⁰	88.91 ¹⁴⁰	92.91 ¹⁴⁰	101.96 ¹⁴⁰
density ρ (g/cm ³)	8.551 ¹⁴⁰	4.469 ¹⁴⁰	8.57 ¹⁴⁰	4.05 ¹⁴¹
out-of-plane linear thermal expansion coefficient* α ($10^{-6} \cdot 1/\text{K}$)	18.27	11.9	7.6	6.6 ¹⁴²
sound velocity* c_{sound} (nm/ps)	3.1 ¹³¹	4.148 ¹⁴³	5.083 ¹⁴⁴	11.075 ¹⁴⁵
acoustic impedance $Z = \rho c_{\text{sound}}$ (g/cm ³ · nm/ps)	26.508	18.537	43.56	44.853
heat capacity* C_p (J/kg K)	162.3 ⁴⁶	298.39 ¹⁴⁰	264.77 ¹⁴⁰	7783 ¹⁴⁶
heat conductivity* κ (W/mK)	11.7 ¹⁴⁷	24.6 ¹⁴⁷	58.7 ¹⁴⁷	40.43 ¹⁴¹
light intensity extinction length at 800 nm δ_p (nm)	24	24	24	infinity

though they match in the paramagnetic phase. In general a much larger contraction of the lattice is predicted in the magnetic phase compared to what is shown in the data. This conclusion from the zero dimensional equilibrium model is therefore still valid when a detailed spatial strain profile of the temperature is taken into account.

The observed instantaneous response is followed by the nearly parallel temporal evolution of the strain up to the turning point that is different for each curve. The turning point of the simulation occurs when the average temperature of the layer passes the $T = 180\text{K}$ point. If the average temperature after excitation is below 180K then the maximum contraction occurs in the instant when the maximum temperature has been reached.

Another characteristic that the simulation currently fails to reproduce is the compensation effect of the strain within the first 30ps. This feature is observed over the large temperature range from $50 - 120\text{K}$ that is discussed in section 4.2.2, but is not observed in any of the simulations. This indication is in support of the spatially different excitation profile for magnons and phonons that are introduced in the aforementioned section, that would need to be added to the simulations.

The obvious advantage of the simulation over the 0D-equilibrium model introduced in the previous section is that it provides a spatial resolution of the strain and temperature within the thin films and thus is able to account for coherent phonon dynamics that occur due to gradients in the stress profiles. These stress profiles result from varying spatial temperature profiles within the sample. The evolution of one of those spatial temperature profiles at different times after the excitation is shown in Figure 4.13. The dynamics of the heat transport goes along temperature gradients, however the general shape and progression of the temperature is similar among all simulations, nearly independent of the absolute start temperature T_{start} . Since only details of the amplitude and speed of the heat flow gradually vary I choose to display only one exemplary case.

From the simulated temperature profiles one can extract the average temperature in the each layer and thereby follow the propagation of the heat through the sample. The results have been shown in Figure 4.14. The shown simulated transient average temperatures can be confirmed by measurements of the dynamics of all four Bragg peaks. Especially the shift of the Niobium Bragg peak is expected to yield direct access to the temperature in that thin film layer, whereas the Yttrium Bragg peak dynamics will show a superposition of the mixed dynamics of the two symmetric layers in the sample. Previous experiments in our group have already demonstrated that time-resolved X-ray diffraction is a suitable method to monitor transient temperature changes in nanoscopic layers on the timescale of picoseconds to nanoseconds with a high degree of accuracy^{148,138}. A study that is able to follow the heat transport in a magnetic system and compare the heat transport between the paramagnetic and antiferromagnetic phase might be able to monitor if and how the presence of magnetic order influences the heat flow.

The `udkm1Dsim` toolbox offers the possibility to extend the one temperature simulations to a coupled n-temperature model to allow for more than one temperature field to be present within the sample. A three temperature model for electrons, lattice and spins has already been proposed in the data interpretation of the seminal work for ultrafast demagnetization by Beaurepaire et al.¹.

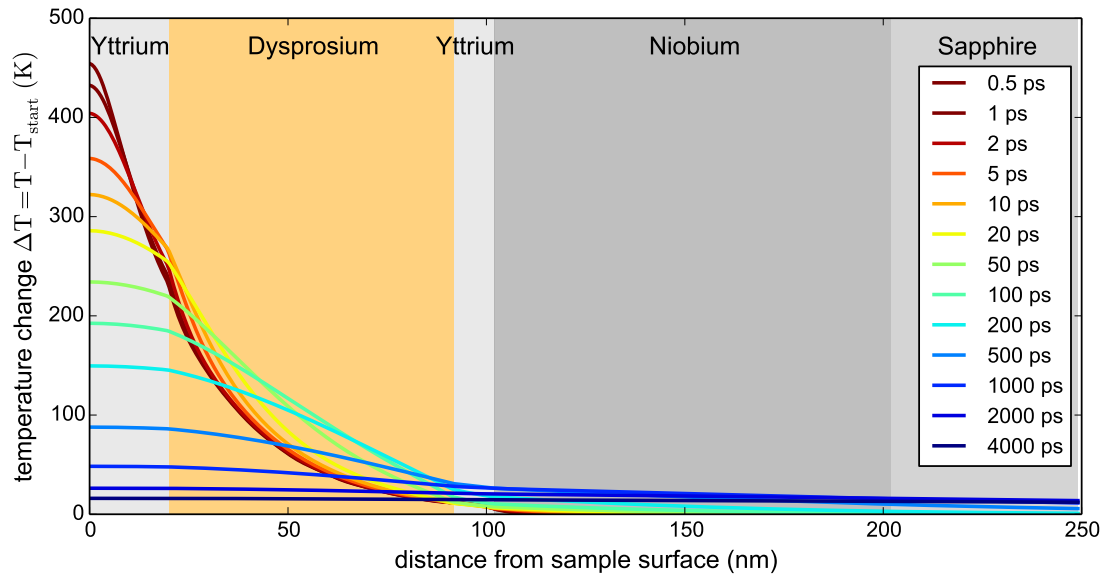


Figure 4.13. Evolution of the temperature profile after laser excitation. Shown here is the evolution of the temperature within the DyY24B sample using the example of a start $T_{\text{start}} = 250$ K in the paramagnetic phase. The general shape and temporal progression of the shown temperature profile is similar for the different simulations. First the heat is deposited within an exponential penetration depth. The initially steep profile levels out as time progresses while heat flows into the substrate and the temperature within the thin films gradually equilibrates. The average temperatures in each thin film layer are shown in Figure 4.14. The background colors indicate the layer thicknesses that are used in the current simulations. This graph shows that a strong temperature gradient within in the Dysprosium with a temperature difference of up to 250 K between the front and the back of the Dysprosium thin film is predicted to occur.

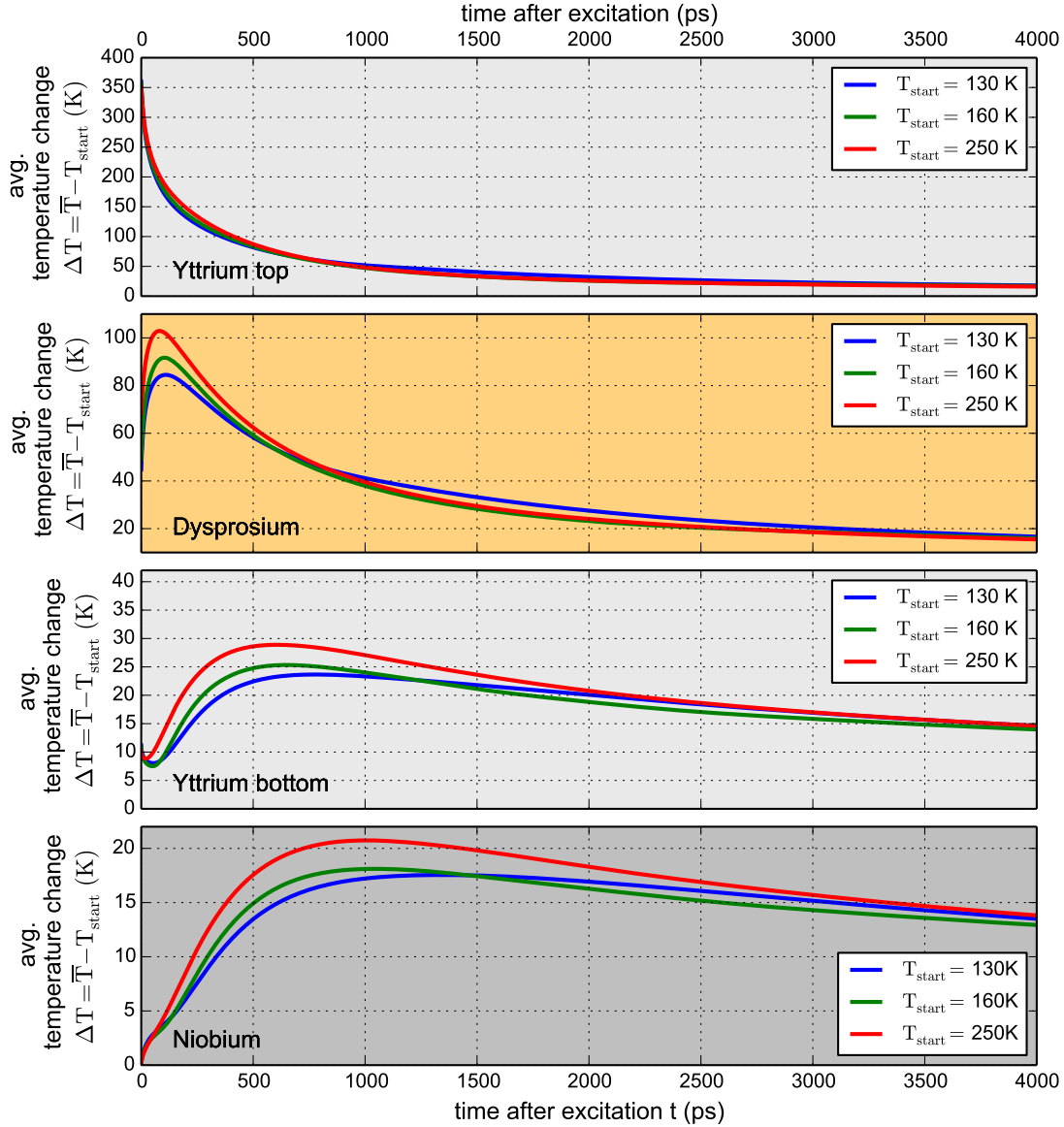


Figure 4.14. Average simulated temperature in each thin film layer: Compared here is the relative temperature change after excitation averaged for each thin film. This is intended to provide an estimation of magnitude of the temperature change and the speed at which the heat flows through the thin film.

The coupled differential equations of such a three temperature model for the electron temperature T_e , the phonon temperature T_p and the spin temperature T_s as functions of time t and one spatial coordinate z are stated in equations (4.6) - (4.8).

$$C_e \frac{\partial T_e(z,t)}{\partial t} = -G_{ep}(T_e - T_p) - G_{es}(T_e - T_s) - \kappa_e \frac{dT_e}{dz} + \underbrace{P(t)}_{\text{source term}} \quad (4.6)$$

$$C_p \frac{\partial T_p(z,t)}{\partial t} = -G_{ep}(T_p - T_e) - G_{ps}(T_p - T_s) - \kappa_p \frac{dT_p}{dz} \quad (4.7)$$

$$C_s \frac{\partial T_s(z,t)}{\partial t} = -G_{es}(T_s - T_e) - G_{ps}(T_s - T_p) - \kappa_s \frac{dT_s}{dz} \quad (4.8)$$

Looking at this model it becomes obvious that the augmented degree of freedom of the model leads to an increased amount of parameters in the calculations. Not only the specific heats C_e, C_p, C_s and thermal conductivities $\kappa_e, \kappa_p, \kappa_s$ have to be known but also the coupling constants between phonons and spins G_{ps} , spins and electrons G_{se} and electrons and phonons G_{ep} are required by the model. Especially the values and temperature dependencies of the material specific coupling constants and the thermal conductivities are frequently unknown and therefore used as fitting parameters to match simulation results to the obtained data. In the experiments conducted here the experimental observable is the out-of-plane lattice constant and in order to compare the obtained results to the output of a three temperature model it would be necessary to determine additionally the three thermal expansion coefficients which translate for each system how an increase in temperature influences the lattice constant.

In the following section I present an approach to interpret my data in a two temperature model based on the collected experimental data but without any assumptions on the spin-phonon coupling. It is a zero dimensional model in the sense that it determines the average temperature and energy for the two systems and the average energy density as a function of time after the excitation. This spatial limitation is due to the fact that the measured strains that enter the analysis are already averages over the Dysprosium layer.

4.5 Non-Equilibrium data analysis

As a consequence of the remaining deviations of the so far discussed equilibrium approach from the measured data I developed an analysis of the experimental data that relaxes the assumption that all subsystems attain the same temperature after the initial laser excitation. By allowing for a non equilibrium energy distribution within the phonon and spin system it is possible to gain insights into the energy transport and coupling strengths between them. This contrast is symbolized in the schematic Figure 4.15 where the laser pulse excites the electron system which is then coupled to the spin and phonon system. Thus the energy initially deposited in the electron system will be distributed to the phonon and spin system.

Within the following argumentation I regard the electron and phonon system as in thermal equilibrium since the electron-phonon coupling time in rare earth materials is expected to be on the order of few picoseconds¹³⁵. In this section I only analyze dynamics later than 45 ps after the excitation so that the assumption of electron-phonon equilibrium should be well satisfied. The reason for the exclusion of the very fast dynamics is the finite time it takes to transform the initial stress generated upon excitation of the sample into strain. Since neighboring atoms, which are excited nearly equally, can not move due to the counterbalancing stresses, the main strain relaxation process starts at the surface air interface and then travels into the material at the speed of sound.

To separate the strain contribution of the phononic pressure from the magnetostriction contribution resulting from excitation in the spin system within time resolved

results it is necessary to develop a model for the lattice strain response upon selective excitation of each system. As a first guess I have chosen in my model is a superposition of magnetostrictive and phononic stresses so that they can act concurrently without influencing each other. A linear chain model approach of masses and springs shown in Figure 4.16 schematically visualizes the underlying principle. In the paramagnetic phase well above $T_{\text{Néel}}$ the main part of the energy will be deposited in the excitation of incoherent lattice vibrations, which exert an expansive stress on the lattice. In the picture of a linear chain model this stress, which originates from the repulsive RKKY interaction, can be modeled via the insertion of rigid spacer sticks into the linear chain, which results in an increase of the equilibrium lattice constant¹⁴⁹. As the heat flows out of the sample the length of the spacer sticks is reduced and eventually the atoms retain their equilibrium position. This approach is also used to model the lattice dynamics in the udkm1Dsim simulation

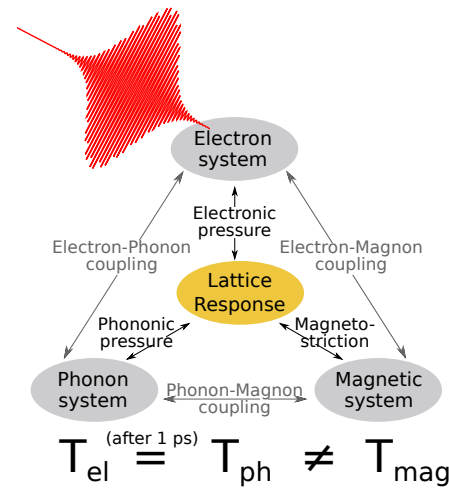


Figure 4.15. Non equilibrium approach: Energy is deposited in the electronic system and distributed from there into phonon and magnon excitations. The resulting phonon T_{pho} and magnon temperature T_{mag} do not need to be equal.

toolbox⁷.

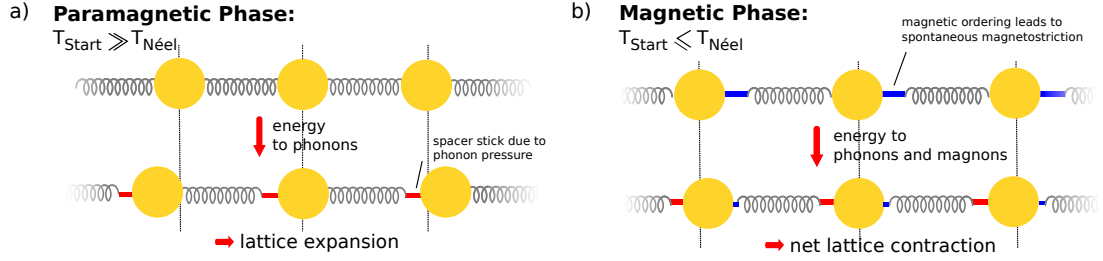


Figure 4.16. Schematic separation of the thermoelastic and magnetostrictive stress on the lattice.

In the paramagnetic phase shown in a) the energy of the laser pulse is mainly taken up by the excitation of incoherent phonons which leads to an expansive stress on the lattice due to the anharmonicity of the lattice potential. This thermoelastic stress is expansive and modeled via the introduction of the rigid red spacer sticks into the linear chain model that increase the equilibrium lattice constant. On the other hand in the magnetic phase shown in b) a magnetostrictive interaction that shifts the equilibrium lattice constant is already present due to the magnetic ordering and modeled by the blue spacer sticks. The action of the laser pulse is then twofold. The deposition of energy to the phonon system introduces again the expansive stress modeled by the red spacer sticks. The energy deposited into the spin system will introduce a certain degree of disorder, which reduces the sublattice magnetization and therefore shortens the blue spacer sticks that represent the magnetostrictive repulsion. The net stress is then a superposition of the expansive phonon stress and reduced magnetostrictive stress which can be positive or negative depending on the start temperature and used laser fluence. In the following it will be necessary to quantify the relation between the observed lattice strain and deposited energy separately for the excitation of phonons and magnons.

A similar approach can be pursued in the modeling of the magnetostrictive contribution to the lattice dynamics. In the low temperature magnetic phase the presence of the magnetic order exerts a repulsive stress on the atoms. This is symbolized by a blue spacer stick that shifts the equilibrium lattice configuration already in the absence of the laser excitation simply due to the ordering of the magnetic system. As the thin film is excited two processes are assumed to happen concurrently. Energy deposited in the phonon system leads to the appearance of the red rigid spacer sticks that exert an expansive stress. The deposited energy in the spin system will diminish the sublattice magnetization in each lattice plane by introducing disorder in the spin system, which effectively decreases the length of the blue magnetostrictive spacer sticks. The transient lattice equilibrium position is then a superposition of the strain due to the expansive thermoelastic phonon stress as well as the contractive stress that originates from the partial removal of the magnetic order.

In a theoretical study Kittel has derived an implicit relation for magnetostrictive contribution to the lattice constant in thermal equilibrium conditions, which I represented by the blue spacer sticks in Figure 4.16(b). This relation is stated in equation (4.9) for the equilibrium deviation of the lattice constant $c(T)$ from the pure phonon lattice that is not subjected to magnetic forces. It has been shown by the experiments of Darnell^{4,43} that this functional dependence can be used

to match the observed lattice constant of the heavy rare earth metals:

$$c(T) = c_0 - \frac{c^2}{Y} \frac{\partial \beta}{\partial c} M^2 \cos(\psi) \quad (4.9)$$

In this relation c_0 is the lattice constant of the material without any magnetic forces, β is the magnetic molecular field constant, Y is the elastic constant, M is the sublattice magnetization and ψ is the interlayer turn angle of the magnetization vector within the helical spin arrangement. It is particular noteworthy that the lattice strain is proportional to the square of the sublattice magnetization, which explains the decrease of this additional contribution with temperature.

In order to apply this so far theoretical decomposition of the phonon contribution and the magnetic contribution to the lattice strain I need to extract the functional relation between deposited energy in a system and the resulting lattice strain separately for each system. The dissection of the heat capacity and the lattice strain is carried out in the next section that discusses the concrete setup of the model.

4.5.1 Setup of the model

In order to know how much energy it takes to increase the temperature of the spin or phonon subsystem I analyze the literature heat capacity of Dysprosium. Figure 4.17 displays the result of the scheme I used to extract the contributions for each of the subsystems to the total heat capacity of Dysprosium. The phonon system contribution has been taken from the heat capacity of the non-magnetic rare earth Lutetium, which has been rescaled to the Debye temperature of Dysprosium as proposed in the publication of by Jennings et al.¹⁵⁰. This is justified by the fact that Lutetium and Dysprosium exhibit the same crystal lattice and bonding parameters due to the similar trivalent electron structure. The main difference is that Lutetium has a completely filled 4f electron shell and thus is only weakly paramagnetic¹⁴⁰ ($\chi > 0$). The resulting lattice heat capacity depicted in red matches very well the shape of a Debye model heat capacity, which shows that the electronic contribution depicted in green is very small in the considered temperature range. The electronic heat capacity is modeled by a Drude-Sommerfeld model that linearly increases with temperature. Details of the Debye and Drude-Sommerfeld models are discussed in standard solid state textbooks^{151,26}. I attribute the part of the heat capacity that remains after the phonon and electron contribution have been subtracted to the magnetic system (depicted in blue). Similar separation approaches have also been reported in the literature^{152,49}.

The other necessary element for the non-equilibrium model is a separation of the contribution of the magnetic system and the phonon system to the lattice constant. Figure 4.18 shows the separation of the equilibrium lattice strain into the two contributions as a function of temperature (a) as well as a function of deposited energy (b) exemplified for $T_{\text{start}} = 100$ K. The thermal expansion response due to the excitation of incoherent phonons is extracted from the observed linear thermal expansion in the paramagnetic phase. This linear thermal expansion is then extrapolated to lower temperatures via the assumption of a constant Grüneisen coefficient for the lattice expansion. I use a macroscopic definition of the Grüneisen coefficient that relates the deposited energy to the amount of the observed lattice strain as stated in relation 4.10. In

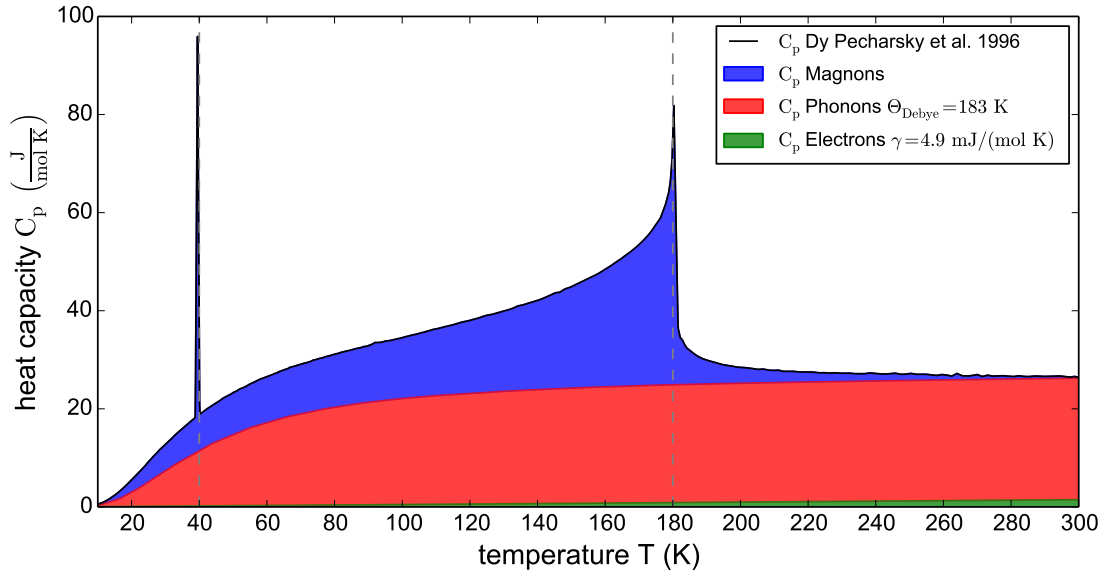


Figure 4.17. Heat capacity separation of Dysprosium: The heat capacity of Dysprosium⁴⁶ is separated into its magnetic and non-magnetic contributions. The nonmagnetic contribution shown here is derived from the heat capacity of Lutetium which is an equivalent non-magnetic rare earth¹⁵³ rescaled to the Debye temperature of Dysprosium $\Theta_{\text{Deb}} = 183 \text{ K}$ according to the method described by Jennings et al.¹⁵⁰. As a visualization for the smallness of the electronic contribution C_{el} I added its approximated value from a Sommerfeld model with the proportionality constant $\gamma = 4.9 \frac{\text{mJ}}{\text{mol K}}$ ¹⁴⁰. Similar separation approaches are found in the literature^{152,49}. The latent heat contribution from the first order ferromagnetic to antiferromagnetic phase transition has been shifted to 40 K, which is used as the temperature where the phase transition takes place in our strained thin film. The non-vanishing magnetic contributions above the phase transition to the paramagnetic phase is attributed to a remaining short range order within the spin system⁴⁹. This separation provides a naive way to convert the deposited energy in one of the systems to an effective system temperature by filling the area under the respective heat capacity curve up the point when the integral matches the deposited energy.

this relation Γ is the Grüneisen coefficient of the considered system, ε is the lattice strain, T represents the temperature C is the specific heat capacity of each system and $\kappa = 40.5 \text{ GPa}$ the bulk modulus of Dysprosium.

$$\Gamma_{\text{pho,mag}} = \frac{d\varepsilon_{\text{pho,mag}}}{dT} \frac{\kappa}{C_{\text{pho,mag}}} \quad (4.10)$$

From the respective Grüneisen constant Γ one can determine the resulting strain per deposited energy via integration over temperature and the result is shown in Equation 4.11.

$$\varepsilon_{\text{pho,mag}} = \kappa \Gamma_{\text{pho,mag}} \Delta Q_{\text{pho,mag}} \quad (4.11)$$

The necessary translation $Q(T)$ between the temperature axis used in Figure 4.18(a) and deposited energy axis used in Figure 4.18(b) for each subsystem is done via integration of the corresponding heat capacity $C_P(T)$ from T_{start} to T . The dashed lines in this figure indicate a corrected version of the strain versus temperature (or energy) relation, which takes into account that the lattice dynamics on ultrafast timescales of ps can only occur out-of-plane but not in-plane due to the large size of the excitation spot. I estimated that this in-plane clamping effect, which via Poisson's-ratio also affects the out of plane dimension, increases the observed out-of-plane lattice expansion on ultrafast timescales by 9% whereas it diminishes an out-of-plane contraction by 13% as compared to the lattice expansion that would be observed if the material had time to also relax in-plane. The detailed calculations for this estimation are provided in the appendix in section 6.1. At this point the dashed lines in Figure 4.18 provide the translation between deposited energy and observed lattice strain, which are used in the non-equilibrium data analysis.

4.5.2 Application and results of the Non-Equilibrium model

In this section I derive the distribution of the deposited energy between the phonon and the spin system after the excitation based on the measured data. I limit myself for the analysis of measurements carried out on the DyY24B sample with the thin Yttrium capping layer although the analysis could in principle also be carried out using the data obtained from the DyY26DI sample with the 50 nm Yttrium capping layer. The non-equilibrium analysis, which is carried out at each timestep is based on the two physical arguments that are summarized as follows:

$$Q_{\text{tot}} = Q_{\text{pho}} + Q_{\text{mag}} \quad \text{energy balance} \quad (4.12)$$

$$\varepsilon_{\text{exp}} = \varepsilon_{\text{pho}}(Q_{\text{pho}}) + \varepsilon_{\text{mag}}(Q_{\text{mag}}) \quad \text{superposition of strains} \quad (4.13)$$

Relation (4.12) states that the total amount of energy that is deposited into Dysprosium has to be distributed between the phonon system and the magnetic system, because the electron system contribution is relatively small and we expect the electrons to be in thermal equilibrium with the phonons within a few picoseconds. The total amount of deposited energy Q_{tot} at each timestep is calibrated by the lattice expansion in the paramagnetic phase in the same way as in the equilibrium model presented in Section 4.3. The second argument summarized in Equation (4.13) is that the lattice strain ε_{exp} that we experimentally observe has to be a superposition of the expansive thermoelastic response ε_{pho} resulting from the deposition of energy into incoherent phonons and

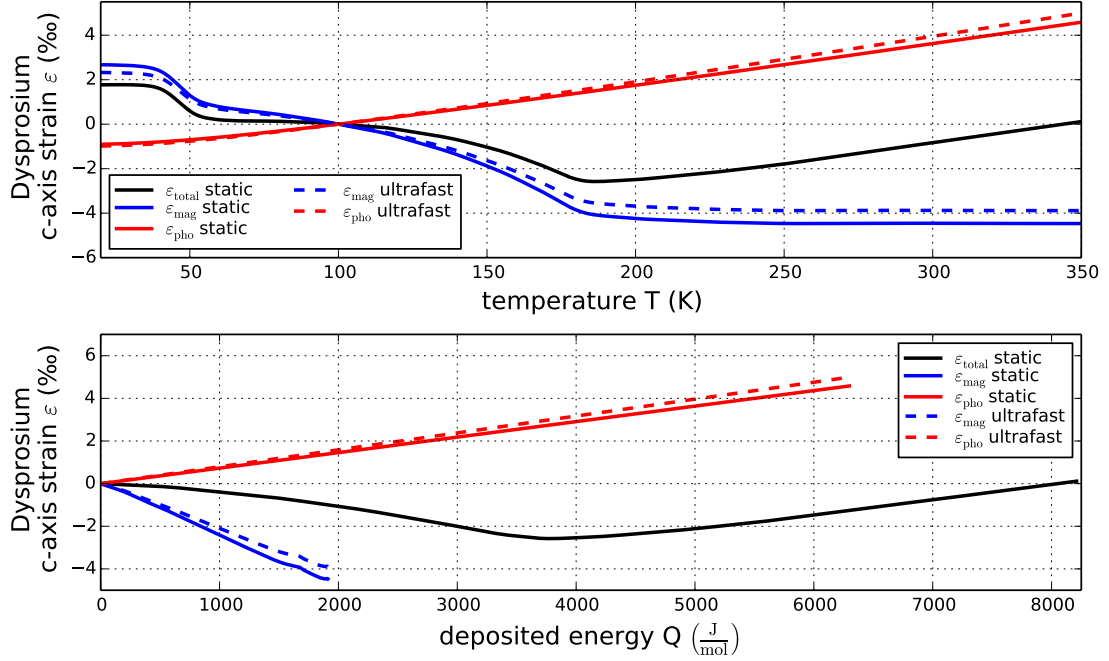


Figure 4.18. Separation of the lattice strain contributions at $T_{\text{start}} = 100\text{ K}$: The top graph exemplifies the separation method of the lattice strain as a function of temperature. The black line corresponds to the static c-axis strain measured in Dysprosium. It is separated into the thermoeleastic expansion contribution (solid red curve) which is extracted by a linear fit in the paramagnetic phase and the magnetostrictive contribution (solid blue curve) that remains when the thermoeleastic contribution is subtracted. Dashed lines show the corrected curves that are expected in an ultrafast experiment where the in-plane clamping enhances the out-of-plane expansion by 9% and reduces an out-of-plane contraction by 13% (see section 6.1 for details). The bottom graph shows the same strain separation but as a function of energy where the transformation has been done according to the heat capacity separation shown in Figure 4.17. Note that the linear slope in the magnetic curve is approximately three times steeper than the thermal expansion slope which underlines again the strong influence of the magnetic system on the lattice. The blue line breaks off because the energy that can be deposited into the spin system is limited. The nearly linear dependence $\epsilon_{\text{pho,mag}} \propto \Delta Q_{\text{pho,mag}}$ justifies the Grüneisen-assumption in Equation (4.10).

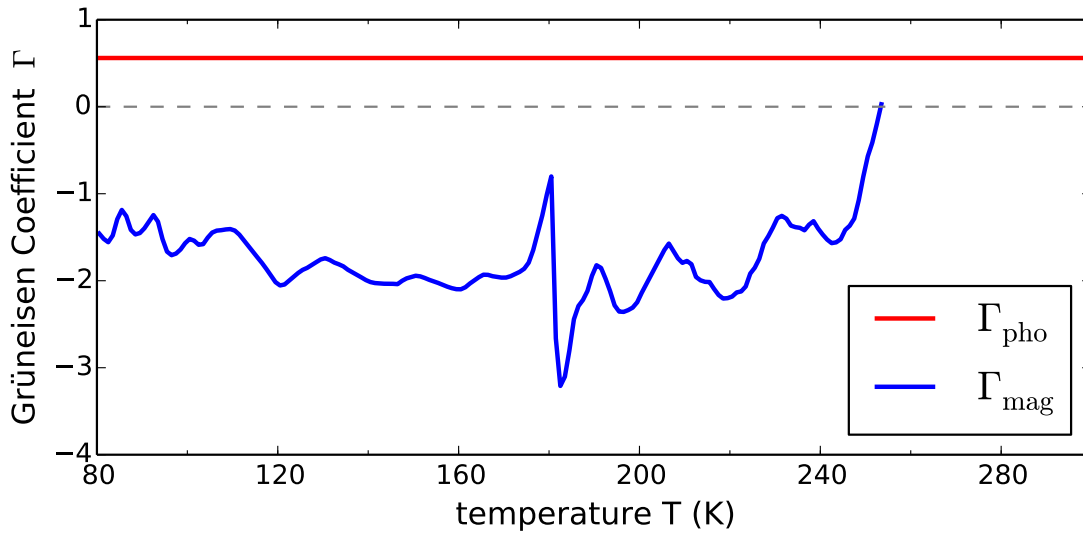


Figure 4.19. Comparison of the Grüneisen parameter for the phonon and magnon system: Shown here is the Grüneisen parameter of the phonon and magnon system as defined in relation 4.10 separately for the phonon and the magnon system. The Grüneisen parameter is the proportionality constant between the observed strain and the deposited energy. Note that the absolute value of the negative magnetic Grüneisen constant is approximately three times as large as the positive phonon Grüneisen constant. Γ_{mag} is in addition nearly constant over a large temperature region. The large fluctuation at the phase transition temperature $T_N = 180$ K is due to a slight mismatch of the phase transition temperature in the used heat capacity (see Figure 4.17) that is slightly smaller than the point of inflection of the c-axis versus temperature measurements (see Figure 4.17).

the contractive strain ϵ_{mag} originating from the deposition of energy into the magnetic system. I so far regard the introduced phonon temperature and magnon temperature in the model as auxiliary quantities, since we have not conducted any experiment that could separately access them. The main intention of the non-equilibrium model is to determine the energy distribution between the systems, however the associated temperatures provide a certain intuition for the state of the subsystems. Nevertheless I want to emphasize that the used subsystems themselves do not necessarily need to be thermalized for my analysis, since their Grüneisen constants shown in 4.19 are nearly constant over the relevant temperature region.

The term temperature of a subsystem has to be used with care in the context of a system that is initially driven out of equilibrium. From Figure 4.13 I know that the system has a considerable temperature gradient throughout the observed dynamics. In addition, locally the magnons and phonons may not be well described by a temperature. Magnons and phonons are bosons and their occupation probability is therefore described by a Bose-distribution that is associated with a temperature T . By assigning a temperature to a subsystem I implicitly use the assumption that the occupation probability of the excited system has recovered to a thermalized Bose distribution and that their heat capacity on ultrafast timescales is similar to their equilibrium heat capacity. Nonetheless the analysis strictly relies on the proportionality of energy ΔQ and strain ϵ , which is not affected by these cautionary remarks, unless one would expect strongly mode -dependent Grüneisen coefficients.

Figure 4.20 compares examples of the results of this analysis carried out on the datasets with $F = 10.5 \text{ mJ/cm}^2$ in the paramagnetic phase and in the antiferromagnetic phase for three selected timesteps. In the paramagnetic phase (top row $T_S = 250 \text{ K}$) the energy is assumed to be deposited exclusively into the phonon system, which leads to the calibrated lattice expansion. In this case the magnetic summands in the system of equations (4.12-4.13) are zero. Since we measure the strain in the lattice we can thus infer the deposited energy as it was already used in the equilibrium model in section 4.3. The observed strain relaxation from the experiment then shows how the energy flows out of the Dysprosium layer as indicated by the shrinking red area below heat capacity curve.

The results in the antiferromagnetic phase at $T_{\text{start}} = 100 \text{ K}$ are shown in the bottom row of Figure 4.20. They originate from the solution of the system of equations (4.12 - 4.13) at the delays indicated at the top of each plot. In the top graphs I marked the strain exerted by the spin and phonon system separately as points on their strain versus temperature curves derived in the previous section. The deposited energy in each system has been indicated by the filled area under the heat capacity curves. From the analysis of these selected delays one observes a feature that I frequently encountered in the non-equilibrium analysis at relatively large excitation fluences: Initially at 45 ps the energy in the phonon system corresponds to a temperature that is larger than the corresponding temperature attained in the magnetic system. For larger delays one observes a reversal of the situation, which indicates that energy flows out of the phonon system at a rate considerably faster than out of the magnetic system.

Once the deposited energy is calibrated by the observed lattice strain in the paramagnetic phase

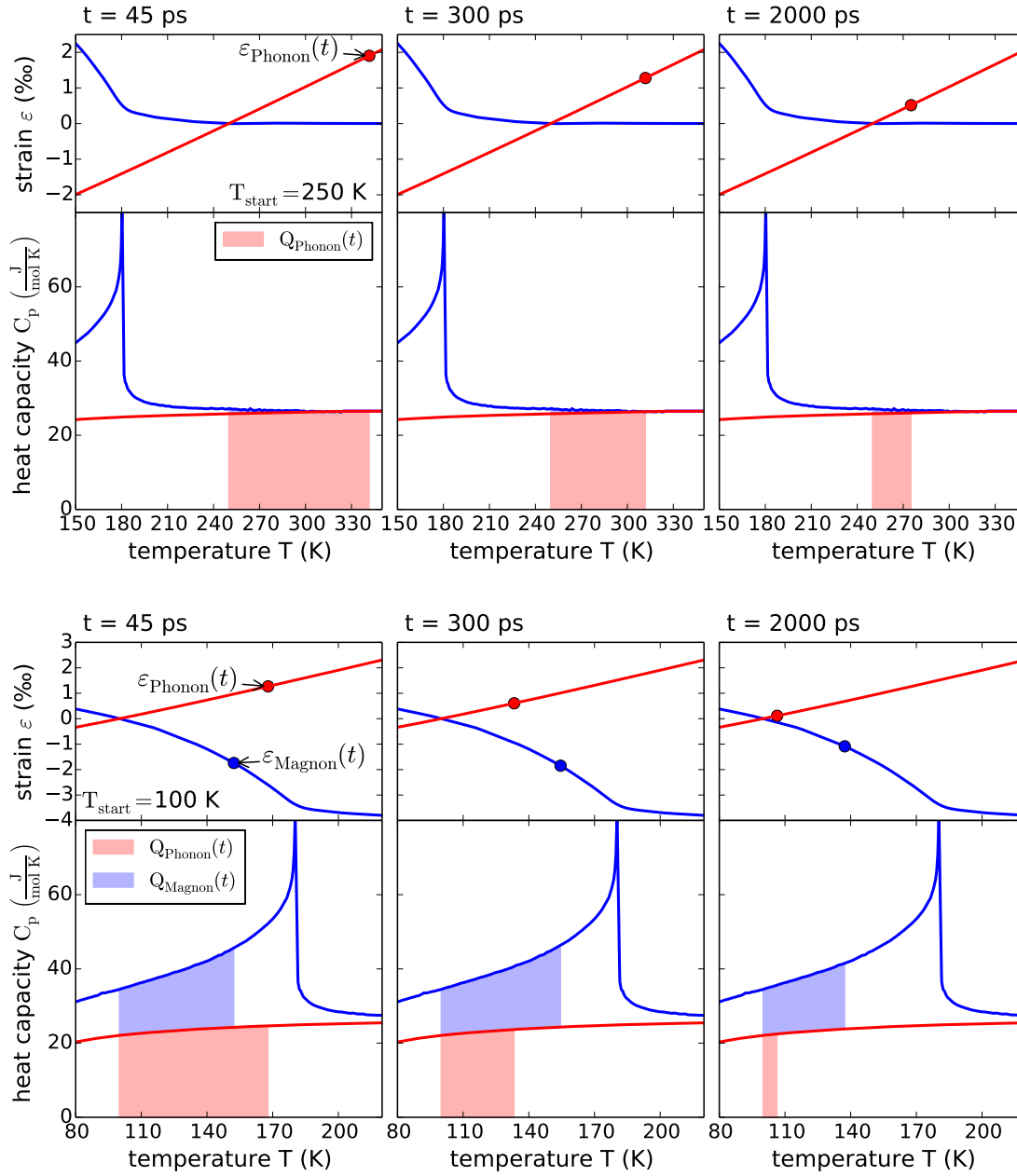


Figure 4.20. Non-Equilibrium model results at selected delays: The top row depicts selected results of the strain model in the paramagnetic phase where the energy is almost entirely deposited in the excitation of incoherent phonons, which leads to heat expansion. Since our experiments monitor the strain as a function of delay we can follow how the heat flows out of the sample. Since the heat capacity of the spin system above 250 K is nearly zero I refrain from assigning a spin temperature in this case. The bottom row depicts the distribution of energy and the associated strain in the antiferromagnetic phase for $T_{\text{start}} = 100$ K. The temperature associated with the phonon system is initially larger than the temperature of the magnetic system. However the phonon system cools whereas the energy in the spin system is found to stay in the spin system for a much longer time. This behavior is prototypical for the analysis results of the non-equilibrium model in the antiferromagnetic phase. An overview over the energy and temperature evolution of the non-equilibrium data for the temperature series at $F = 10.5 \text{ mJ/cm}^2$ is provided in figure 4.21.

one can carry out the calculation of the energy in the phonon and the magnon system from the observed lattice strain for all measurements in the antiferromagnetic phase. A non-equilibrium model analysis of the lattice response in the ferromagnetic phase has been omitted due to the lack of the appropriate heat capacity data for a thin film sample, which also exhibits an extended hysteresis in the first order ferromagnetic to antiferromagnetic phase transition.

Figure 4.20 shows the results of this analysis for five representative datasets selected from a temperature series where the incident laser fluence $F = 10.5 \text{ mJ/cm}^2$ was kept fixed. In Figure 4.21(a) I depicted the energy deposited in the phonon and the magnon system. It quantifies that for this large excitation fluence initially more energy is deposited in the phonon system as compared to the magnon system. At later times after the excitation the energy of the phonons is found to flow out of the Dysprosium layer, whereas the energy in the magnetic phase remains nearly unchanged. Inset (b) shows the initial energy distribution between the phonon and the magnon system at the earliest data analysis point. It shows that at temperatures sufficiently below T_N the energy is distributed to approximately 35% into the spin system and to 65% into the phonon system. This relation subsequently shifts towards a larger portion of the energy deposited in the phonon system as the temperature is increased close to and above the phase transition temperature T_N . Interestingly the associated temperatures of each of the systems shown in (c) are found to develop as if there was only a very weak coupling between phonons and magnons. This is seen from the fact that the initial temperature of the phonons decreases continuously whereas the temperature of the magnon system remains stable over a long time after the excitation. The energy flow between the phonon system and the spin system appears to be small as compared to the energy flow out of the phonon system into other parts of the sample.

For each dataset I plotted an uncertainty range in energy and temperature which originates from the uncertainty in the heat transport and the possibility of trapping energy in the magnetic system. For lower starting temperatures where the energy can also be deposited into the magnetic system the attained average temperature in the Dysprosium layer will not be as large as for the case where this additional contribution to the heat capacity is absent. This will decrease the temperature gradient in the phonon system to the adjacent layers and it is thus expected to diminish the flow of energy. This can be seen in the one dimensional case of the heat transport equation stated in 4.14.

$$\Delta Q = -k \frac{\partial T}{\partial z} \quad (4.14)$$

This relation is often referred to as Fourier's law¹⁵⁴ and it relates the energy transported across a unit sample cross-section ΔQ to the material specific heat conductivity constant k and the gradient of temperature. Additionally the energy that is deposited into the spin system can not be transported out of the Dysprosium layer via magnetic excitation since the adjacent layers are non-magnetic. Therefore it needs to be converted back to energy in the phonon system to flow out of the thin film. This might lead to a temporal trapping effect of energy in the magnetic system. Both effects will modify the heat flow out of the sample as compared to the paramagnetic phase where the magnetic system has a vanishing heat capacity contribution. As a rough estimation of the magnitude of this effect I solved the non-equilibrium analysis a second time with the assumption that the energy initially deposited in the magnetic system remains within the Dysprosium layer.

The energy initially deposited in the phonon system flows out of the layer at the same rate as it was the calibrated energy for the energy rate in the paramagnetic phase. This is stated in relation 4.15.

$$Q'_{\text{tot}}(t) = Q_{\text{mag}}(t = 45 \text{ ps}) + Q_{\text{pho}}(t = 45 \text{ ps}) \frac{Q_{\text{tot}}(t)}{Q_{\text{tot}}(t = 45 \text{ ps})} \quad (4.15)$$

In this relation $Q'_{\text{tot}}(t)$ is the maximal energy, which is assumed to be in the Dysprosium layer at each timestep, $Q_{\text{pho}}(t = 45 \text{ ps})$ and $Q_{\text{mag}}(t = 45 \text{ ps})$ are the energies initially deposited into the phonon and magnon system respectively. $Q_{\text{tot}}(t)$ is the currently used value for the deposited energy derived from the lattice strain in the paramagnetic phase, which as discussed will overestimate the energy transport out of the thin film and thereby underestimate the stored energy in the layer. Solving the non-equilibrium two temperature model with this new estimation of the deposited energy Q' leads to the upper boundary estimation of the energy and temperature whereas using the calibrated energy Q directly from the lattice response in the paramagnetic phase leads to the lower curves since by design $Q' \geq Q$ is fulfilled for all t .

Since the deposited energy is assumed to scale linearly with the incident laser fluence I can apply the same two-temperature analysis routine also on the data of the fluence series measurements by rescaling the energy within the Dysprosium layer according to $Q(F) = Q_{\text{calib}} \frac{F}{F_{\text{calib}}}$. This allows me to monitor the flow of the deposited energy as a function of the incident laser fluence F for a fixed start temperature T_{start} . The results for $T_{\text{start}} = 130 \text{ K}$ and $T_{\text{start}} = 160 \text{ K}$ are shown in Figure 4.22(a) and (b) respectively. They display the energy and associated temperature in the phonon and spin system in a similar fashion as in Figure 4.21 which allows for direct comparison.

The trends observed in the data are as follows: The attained temperature change within the Dysprosium layer is smaller for lower excitation fluences. This is the case both for the phonon and the magnon temperature. The initial energy distribution at $t = 45 \text{ ps}$ changes from an almost equal distribution, which is associated with a higher spin temperature than phonon temperature, towards the deposition of more energy into the phonon system than into the magnon system as the laser fluence is increased. The energy deposited in the magnetic system saturates with increasing fluence, and this effect is more pronounced closer to the phase transition at 160 K than at 130 K . It appears that the recovery of the magnetic system occurs faster for the lower fluences than for higher fluences. This trend was seen in the timing of the maximal contraction reported in Figure 4.3(d) which would agree with the findings of Kazantseva et al.¹⁵⁵ that reported a slower recovery of the magnetic ordering for a ferromagnet if the initial demagnetization was larger.

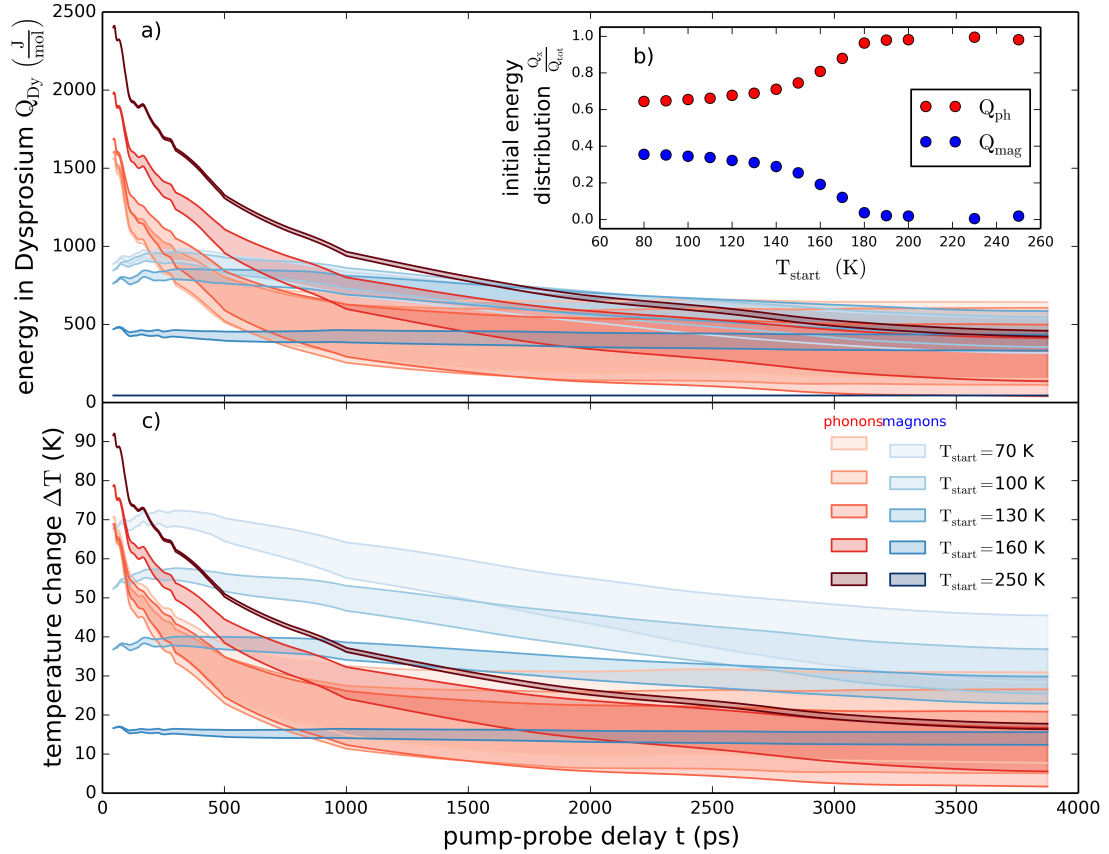


Figure 4.21. Non-equilibrium model analysis for a temperature series at $F = 10.5 \text{ mJ/cm}^2$: a) Energy in the phonon and spin system derived from the data according to the non-equilibrium model described in the text. Inset b) shows the resulting initial energy distribution between phonons and magnons, yielding that approximately 35% or less of the incident energy is deposited in the magnetic system upon laser excitation. For each selected dataset a range is given as follows: The upper curve overestimates the energy in the layer by assuming that the energy initially deposited in the magnetic system can not flow out of the layer, whereas the lower curve underestimates the energy by assuming the same flow of energy out of the sample as in the paramagnetic phase where the maximum temperature difference is realized. Translating the deposited energy to a change in temperature via the heat-capacity one obtains the relative temperature changes shown in c). The resulting temperatures indicate a long-lasting non-equilibrium between phonon and magnon systems.

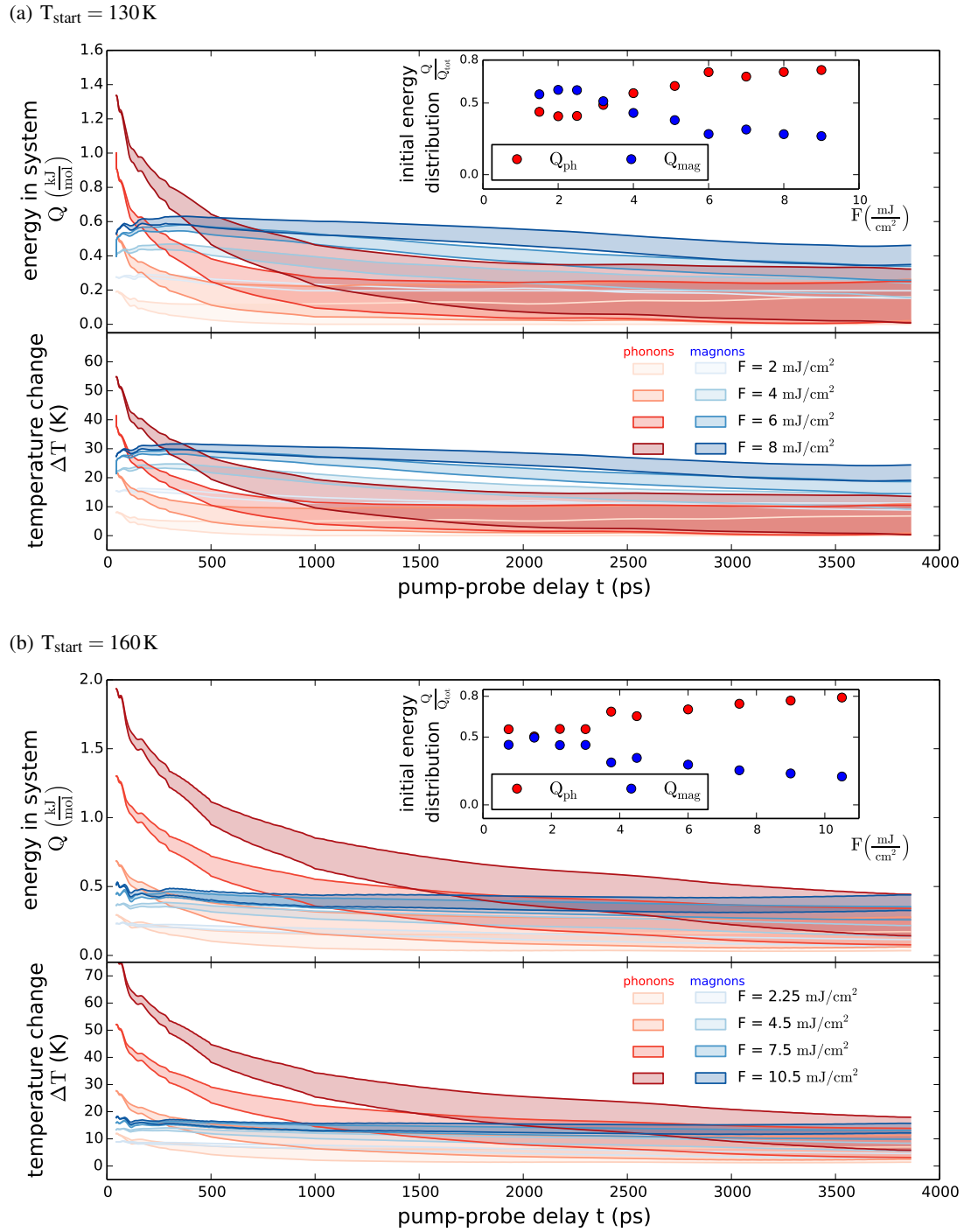


Figure 4.22. Non-equilibrium data analysis for two different fluence series: The shown quantities are arranged in a similar fashion as for the previously shown results of a temperature series in Figure 4.21. As it is expected the average temperature changes in the magnetic and the phononic system increase with the increasing laser fluence as more energy is delivered to the sample. However a saturation of the temperature change in the spin system occurs for large fluences and this trend is more pronounced for the 160 K data than for the 130 K data. The initial energy distribution between phonons and magnons determined at 45 ps is found to shift from approximately equal distribution at low fluences towards a dominant deposition of energy into phonons. The onset of the cooling of the magnon system, which is marked by a downward bend of the magnetic temperature occurs earlier for lower fluences and it is more pronounced in the 130 K data sets shown in (a) as in the 160 K datasets shown in (b). These datasets essentially corroborate the hypothesis of a long lasting non-equilibrium energy distribution between the phonon and the spin system that was conjectured from the analysis of the temperature series data.

Combining the experimentally solved two temperature model results for both temperature and fluence, the following features of the dynamics are robust against modifications of the model: For large excitation fluences the phonon temperature is initially higher than the temperature of the magnetic system. At low excitation fluences this situation reverses. The phonons cool rapidly at a rate much faster than the magnetic system. It is interesting to note that some of the dynamic changes of the two temperatures are consistent with equilibrium expectations: At short time delays the temperature of the magnetic system increases slightly, since it is coupled to the hotter phonon system. However, it is not true that the heat flow reverses its sign as soon as $T_{\text{mag}} > T_{\text{pho}}$. For all temperatures, the phonon cooling is faster than the heat dissipation for the magnetic system. Apparently there exists a limiting process in the heat flow from the magnetic excitation to the phonons. In particular, close to T_N there is nearly no heat flow from the lattice to the spins over the observed time range, despite the large temperature difference.

4.6 Synthesis of the interpretation steps

In this section I put the observed sample dynamics into the context of the sample geometry. The aim is to use the insights gained from the previously discussed two temperature data analysis to link the physically possible processes within the sample to the observed features in the obtained data.

A schematic sketch of the sample as it is mounted on the cryostat is shown in Figure 4.23. The different sample layers are indicated by the same color code as in the original sample sketch shown in Figure 2.1. In this graphic I overlaid the different subsystems according to their spatial extent. Lattice vibrations are sustained by all materials so that the phonon system is present throughout the sample. It is seen as the main way to transport energy from the excited thin films to the cold cryostat which I consider has heat sink. A system of delocalized electrons is expected to be present within all metallic thin films that are grown on top of the dielectric nonconducting Sapphire substrate. Magnetic excitations will only be sustained in the magnetic Dysprosium layer[‡]. As a consequence there is no direct channel for the transport of energy from the excited spin systems in the form of magnons to the cryostat. The energy has to be converted first from the magnons to the coupled electron-phonon system.

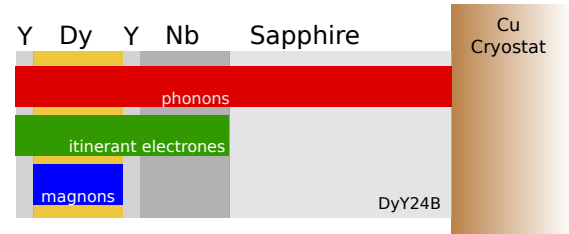


Figure 4.23. Subsystems dimension across the sample: Colors signify the spatial extent of the phonon system (red), the itinerant conduction band electrons (green) and magnons (blue). Phonons can propagate through the entire sample, whereas the itinerant electrons are confined to the conductive metals. Magnons will mainly be confined to the spin system of the magnetic Dysprosium layer.

[‡] Although there is evidence that the adjacent Yttrium layer stabilizes and to some extent also sustains magnetic ordering in a Dysprosium-Yttrium superlattice⁷⁹ the effect is thought to be small since the reported Yttrium layer thickness is only 4 nm and no such behavior is known for the adjacent Niobium.

Figures 4.24 and 4.25 exemplify the different processes that I identified using the Non-equilibrium data analysis in the previous section alongside with their signatures in the data. As discussed in section 4.2 the laser pulse deposits energy to the 5d6s conduction band electron system[§].

The disturbance of the valence electron system is evidently sufficient to reduce the repulsive RKKY interaction since I observe already at 1.25 ps after the excitation a change of the strain response in the Dysprosium layer in the antiferromagnetic phase in comparison to the strain response in the paramagnetic phase (see Section 4.2). The initial strain response highlighted in Figure 4.24(a), can be expansive or contractive depending on the distribution of energy between the phonon and the magnon system. For low fluences the non-equilibrium two temperature analysis yields a nearly equiproportional distribution of energy between the two systems. As the fluence is increased progressively more energy is deposited to the phonon system. This is in accordance with the change of the initial lattice dynamics from contractive strain to expansive strain, which is most pronounced in the fluence series obtained at 160 K (see Figure 3.13). The full strain amplitude caused by the initial excitation is only seen after the coherent strain wave from the sample surface has passed the Dysprosium layer and thus released the out-of-plane clamping exerted by the balancing stress of the neighboring atoms (see Section 4.2.2).

The initial sample response is always followed by a transient decrease of the lattice constant. The associated mechanism that I identify to cause this behavior is the flow of energy from the phonon system to the substrate, which continuously removes expansive thermal stress. This is schematically depicted in Figure 4.24(b). Evidence for this process has been found in the data analysis in Section 4.1 (see Figure 4.4). This qualitative analysis is further supported by the findings of the non-equilibrium data analysis where the phonon system is found to cool at a much faster rate than the magnetic system.

This phonon cooling process lasts until the recovery of the magnetic order in the Dysprosium thin film starts to act on the lattice again. In order for this to happen energy has to be removed from the spin system. The only possible mechanism to transport the excess energy from the Dysprosium layer through the substrate to the heat sink is a transfer of energy into the phonon system. This is depicted in Figure 4.24(c). This transfer of energy however seems to be rather slow since the point of the maximal contraction that marks the recovery of the repulsive magnetostriction is on a timescale of hundreds of picoseconds or even nanoseconds. A comparison of all data shows that the delay of the maximum contraction increases with excitation fluence and the start temperature (see Figures 4.2 and 4.3). The relative timing of the maximal contraction is from my point of view determined by two factors: As long as the phonon system is hotter than the magnetic system I do not expect a substantial cooling of the magnetic system. The effect of heat transfer from phonons to the magnon system seen in the non-equilibrium data analysis is small, but one nevertheless observes some flow of energy from the lattice into the magnetic system. A second process that might set a limit to the magnetic recovery has been reported in the literature by Kazantseva et al.¹⁵⁵, who find that the speed of the recovery of the magnetic

[§]The 1.55 eV of energy of the incident photons is insufficient to directly excite the lower lying 4f-electrons as it is evident from the electronic density of states of Dysprosium depicted in Figure 1.7

order in a ferromagnet depends to some extent on the initially introduced disorder. Both effects are a possible explanation for the delayed onset in the recovery of the lattice from a negative strain.

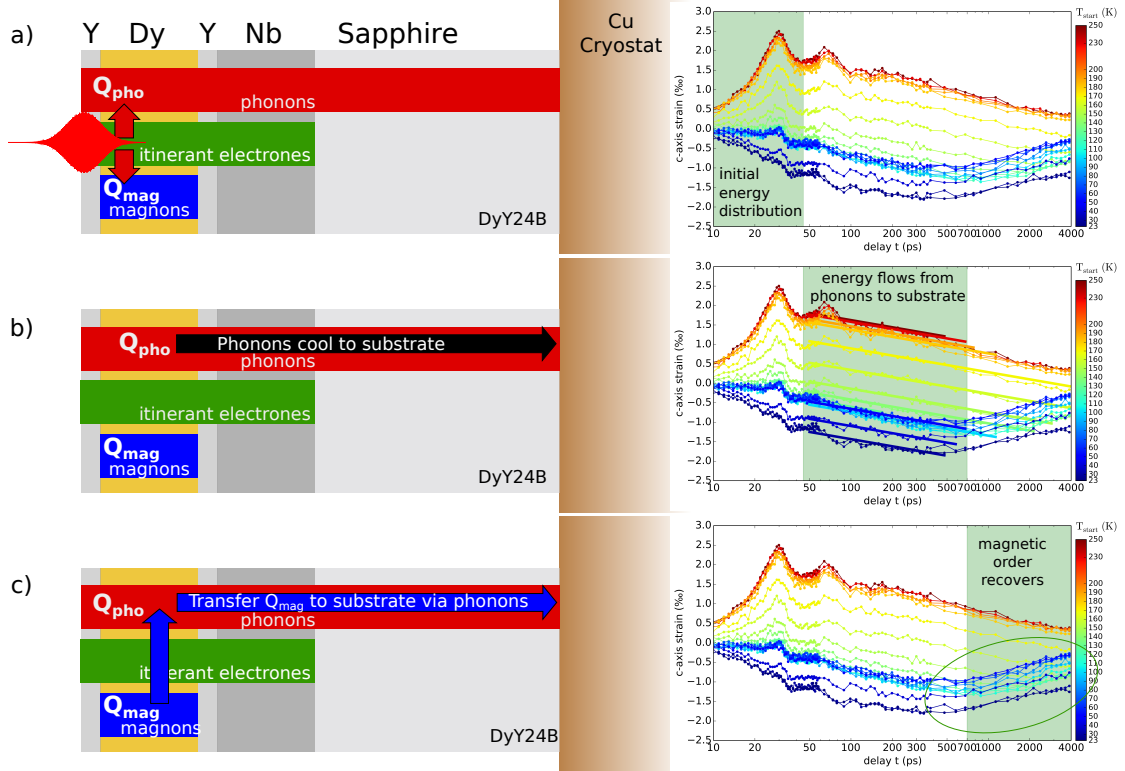


Figure 4.24. Synthesis of data and interpretation: Shown here are the different physical processes that are observed in the lattice dynamics in Dysprosium studied via ultrafast X-ray diffraction. The physical processes depicted on the left side are shown alongside their signature in the data on the right. The used data are the same as in Figure 4.1 where they are shown in full scale. The first process shown in a) is that the laser pulse deposits energy into the conduction band electrons which then distribute it to the phonon and magnon systems. This relative distribution determines the amplitude and sign of the lattice response. After the initial dynamics, a relative lattice contraction is observed which I attribute to the transfer of energy from the phonon system to the substrate, as schematically depicted in b). This process lasts until the recovery of the magnetic order starts to act on the lattice again. A prerequisite for this is a process that transfers energy from the spin system to the phonons as depicted in c). The timing of the recovery is on the order of hundreds of picoseconds or larger, but it strongly depends on the laser fluence F and T_{start} .

The last process which has so far not been discussed extensively is the indirect demagnetization of the Dysprosium layer in the sample geometry of the DyY26DI sample with a large 50nm thick Yttrium capping layer. Despite the comparatively small laser penetration depth of 24nm one observes a lattice contraction. One possible explanation for the contractive magnetostrictive strain is a heat assisted demagnetization process that I schematically depict in Figure 4.25. In this process energy flows from the phonon system to the magnetic system. Due to the limited penetration depth of the laser light the Dysprosium layer is only excited by a very small fraction

of 9% of the incident laser energy. From the response in the paramagnetic phase one observes that the maximal thermal expansion[¶] occurs at approximately 800 ps which marks the timescale of net heat transport into the Dysprosium layer within this sample. In the antiferromagnetic and ferromagnetic phase the lattice constant decreases on the same timescale which motivates the assumption of energy transfer from the propagating heat in the phonon system to the spin system.

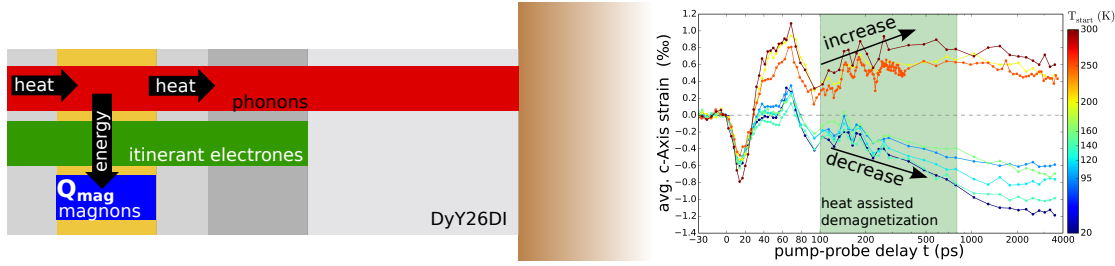


Figure 4.25. Heat assisted demagnetization observed in DyY26DI: The lattice response of the DyY26DI sample shows that a mechanism exists that transports energy into the magnetic system of the initially unexcited Dysprosium layer. Heat assisted demagnetization that uses a transport of energy from the phonon system to the spin system seems to me the most likely cause, since the magnetic contraction increases while thermal energy is known to flow into the Dysprosium layer as seen in the paramagnetic phase where the lattice constant increases up to approximately 800 ps. The data shown on the right originate from a temperature series measured at an excitation fluence of $F = 7.5 \pm 0.5 \text{ mJ/cm}^2$ (for full scale depiction see Figure 3.20).

The observed lattice dynamics upon ultrafast laser excitation of the rare earth Dysprosium turned out to be very rich. The analysis of the experiments is a still ongoing process and in this chapter I have tried to capture the current status of the discussions and the models I have developed in the course of the work on my thesis. The next chapter summarizes the main findings.

[¶]This disregards the maximum layer expansion due to the large amplitude coherent phonon observed at approximately 80 ps.

5 Summary

The ultrafast X-ray diffraction experiments on the rare earth Dysprosium carried out in this thesis have disclosed very rich lattice dynamics that strongly depend on the initial magnetic phase of the Dysprosium thin film, as well as the laser excitation fluence.

I have found that the influence of the magnetostrictive strain is detectable as early as 1.25 ps after the excitation if one compares the sample response in the paramagnetic and antiferromagnetic phase as it is done in Section 4.2.1. The stress-component, which originates from the loss of magnetic order that precedes the generated strain has thus to be present even within the first picosecond.

In addition I obtained strong indications for different spatial stress profiles of the expansive thermoelastic stress generated by the excitation of incoherent phonons and the contractive stress that is caused by the release of the repulsive magnetostriction force. This is evident from a zero average strain in the Dysprosium layer within the first 30 ps, which is concomitant to an increased peak width seen over a large temperature region from 50 K - 120 K for an excitation fluence of $F = 10.5 \text{ mJ/cm}^2$ as discussed in Section 4.2.2.

The main finding of my work is that equilibrium approaches that aim to describe the observed lattice dynamics using the same temperature for the phonon, electron and spin system are found to be unsuccessful. Based on simple arguments I developed an experimental solution for a two temperature model for the phonon and the spin system, which I evaluated based on my measurements without assumptions on their coupling parameters. From that I obtain that the excitation energy is distributed between the phonon system and the spin system in such a way that their attained temperatures correspond to a pronounced non-equilibrium, if a temperature can be defined at all. My two-temperature data analysis yields that a non-equilibrium between the phonon and the spin systems lasts up to the nanosecond timescale.

A general behavior that I extract from my measurements is that the energy initially deposited in the phonon system flows out at a faster rate than the energy initially deposited in the magnetic system, which remains almost constant up to the nanosecond timescale. The most probable explanation for this behavior is a weak coupling between the phonon and spin system. The initial distribution of energy between the phonon and the magnon system depends on the starting temperature and excitation fluence. For high excitation fluences the energy is distributed as such that 35% of the energy is deposited into the magnetic system whereas 65% of the energy is deposited in the phonon system. I found that the higher the excitation energy and the closer the starting temperature to T_N the more energy is initially deposited into the phonon system.

In conclusion I find that monitoring the lattice response on ultrafast timescales in a magnetic sample with a strong magnetostrictive coupling can indeed provide insights into the dynamics of the magnetic system. Especially the flow of energy between different degrees of freedom, which is usually not addressed by methods that probe the magnetization state, is a relevant piece of information that can be inferred from ultrafast X-ray diffraction measurements. The heat flow represents one aspect of a complete theory for the correlated dynamics between electrons, phonons and spins, which has to be considered in addition to the treatment of angular momentum and entropy transfer in the sample systems.

Bibliography

- [1] E. Beaurepaire, J. C. Merle, A. Daunois, and J. Y. Bigot, “Ultrafast Spin Dynamics in Ferromagnetic Nickel,” *Phys. Rev. Lett.*, vol. 76, pp. 4250–4253, May 1996.
- [2] D. Schick, A. Bojahr, M. Herzog, C. von Korff Schmising, R. Shayduk, W. Leitenberger, P. Gaal, and M. Bargheer, “Normalization schemes for ultrafast x-ray diffraction using a table-top laser-driven plasma source,” *Rev. Sci. Instrum.*, vol. 83, no. 2, p. 025104, 2012.
- [3] S. Legvold, J. Alstad, and J. Rhyne, “Giant Magnetostriction in Dysprosium and Holmium Single Crystals,” *Phys. Rev. Lett.*, vol. 10, pp. 509–511, Jun 1963.
- [4] F. J. Darnell and E. P. Moore, “Crystal Structure of Dysprosium at Low Temperatures,” *Journal of Applied Physics*, vol. 34, no. 4, pp. 1337–1338, 1963.
- [5] W. C. Koehler, “Magnetic Properties of Rare Earth Metals and Alloys,” *Journal of Applied Physics*, vol. 36, no. 3, pp. 1078–1087, 1965.
- [6] W. Eerenstein, N. D. Mathur, and J. F. Scott, “Multiferroic and magnetoelectric materials,” *Nature*, vol. 442, pp. 759–765, aug 2006. 10.1038/nature05023.
- [7] D. Schick, A. Bojahr, M. Herzog, C. von Korff Schmising, R. Shayduk, and M. Bargheer, “udkm1Dsim - A Simulation Toolkit for 1D Ultrafast Dynamics in Condensed Matter,” *Comput. Phys. Commun.*, vol. 185, no. 2, pp. 651–660, 2014.
- [8] J. Yu, P. R. LeClair, G. J. Mankey, J. L. Robertson, M. L. Crow, and W. Tian, “Exploring the magnetic phase diagram of dysprosium with neutron diffraction,” *Phys. Rev. B*, vol. 91, p. 014404, Jan 2015.
- [9] K. Dumesnil, C. Dufour, P. Mangin, G. Marchal, and M. Hennion, “Magnetoelastic and Exchange Contributions to the Helical-Ferromagnetic Transition in Dysprosium Epitaxial Films,” *EPL (Europhysics Letters)*, vol. 31, no. 1, p. 43, 1995.
- [10] V. Leiner, D. Laberge, R. Siebrecht, C. Sutter, and H. Zabel, “Investigation of the magnetism in thin single Ho(00.1) films via neutron reflectivity measurements,” *Physica B: Condensed Matter*, vol. 283, no. 1–3, pp. 167–170, 2000.
- [11] V. Leiner, K. Westerholt, B. Hjörvarsson, and H. Zabel, “Tunability of the interlayer exchange coupling,” *Journal of Physics D: Applied Physics*, vol. 35, no. 19, p. 2377, 2002.
- [12] K. Dumesnil, A. Stunault, P. Mangin, C. Vettier, D. Wermeille, N. Bernhoeft, S. Langridge, C. Dufour, and G. Marchal, “Resonant magnetic x-ray studies of magnetic ordering in dysprosium layers,” *Phys. Rev. B*, vol. 58, pp. 3172–3179, Aug 1998.

- [13] H. Ott, C. Schüßler-Langeheine, E. Schierle, A. Y. Grigoriev, V. Leiner, H. Zabel, G. Kaindl, and E. Weschke, “Magnetic x-ray scattering at the M_5 absorption edge of Ho,” *Phys. Rev. B*, vol. 74, p. 094412, Sep 2006.
- [14] J. C. Lang, D. R. Lee, D. Haskel, and G. Srajer, “Imaging spiral magnetic domains in Ho metal using circularly polarized Bragg diffraction,” *Journal of Applied Physics*, vol. 95, no. 11, pp. 6537–6539, 2004.
- [15] S. W. Chen, H. Guo, K. A. Seu, K. Dumesnil, S. Roy, and S. K. Sinha, “Jamming Behavior of Domains in a Spiral Antiferromagnetic System,” *Phys. Rev. Lett.*, vol. 110, p. 217201, May 2013.
- [16] E. Weschke, H. Ott, E. Schierle, C. Schüßler-Langeheine, D. V. Vyalikh, G. Kaindl, V. Leiner, M. Ay, T. Schmitte, H. Zabel, and P. J. Jensen, “Finite-Size Effect on Magnetic Ordering Temperatures in Long-Period Antiferromagnets: Holmium Thin Films,” *Phys. Rev. Lett.*, vol. 93, p. 157204, Oct 2004.
- [17] B. Coqblin, *The electronic structure of rare-earth metals and alloys: the magnetic heavy rare-earths*. Academic Press., 1977.
- [18] I. Hughes, M. Däne, A. Ernst, W. Hergert, M. Lüders, J. Poulter, J. Staunton, A. Svane, Z. Szotek, and W. Temmerman, “Lanthanide contraction and magnetism in the heavy rare earth elements,” *Nature*, vol. 446, no. 7136, pp. 650–653, 2007.
- [19] R. Elliott, *Magnetic properties of rare earth metals*. Springer Science & Business Media, 1972.
- [20] J. Jensen and A. R. Mackintosh, *Rare Earth Magnetism - Structures and Excitations*. Clarendon Press, 1991.
- [21] B. Coqblin, *The electronic structure of rare-earth metals and alloys: the magnetic heavy rare-earths*. Academic Press., 1977.
- [22] H. Ott, *Magnetic Structures and Phase Transitions in Thin and Ultrathin Films of Heavy Lanthanide Metals Investigated by Resonant Magnetic X-Ray Scattering*. PhD thesis, Freie Universität Berlin, May 2004.
- [23] D. R. Behrendt, S. Legvold, and F. H. Spedding, “Magnetic Properties of Dysprosium Single Crystals,” *Phys. Rev.*, vol. 109, pp. 1544–1547, Mar 1958.
- [24] A. E. Clark, B. F. DeSavage, and R. Bozorth, “Anomalous Thermal Expansion and Magnetostriction of Single-Crystal Dysprosium,” *Phys. Rev.*, vol. 138, pp. A216–A224, Apr 1965.
- [25] A. J. Freeman and R. E. Watson, “Theoretical Investigation of Some Magnetic and Spectroscopic Properties of Rare-Earth Ions,” *Phys. Rev.*, vol. 127, pp. 2058–2075, Sep 1962.
- [26] C. Kittel, *Introduction to solid state physics*. New York [u.a.]: Wiley, 7th ed., 1996.

- [27] R. Gross and A. Marx, *Festkörperphysik*. Oldenbourg Wissenschaftsverlag, 2012.
- [28] J. K. Lang, Y. Baer, and P. A. Cox, “Study of the 4f and valence band density of states in rare-earth metals. II. Experiment and results,” *Journal of Physics F: Metal Physics*, vol. 11, no. 1, p. 121, 1981.
- [29] F. H. Spedding, A. H. Daane, and K. W. Herrmann, “The crystal structures and lattice parameters of high-purity scandium, yttrium and the rare earth metals,” *Acta Crystallographica*, vol. 9, pp. 559–563, Jul 1956.
- [30] M. A. Ruderman and C. Kittel, “Indirect Exchange Coupling of Nuclear Magnetic Moments by Conduction Electrons,” *Phys. Rev.*, vol. 96, pp. 99–102, Oct 1954.
- [31] T. Kasuya, “A Theory of Metallic Ferro- and Antiferromagnetism on Zener’s Model,” *Progress of theoretical physics*, vol. 16, pp. 45–57, jul 1956.
- [32] K. Yosida, “Magnetic Properties of Cu-Mn Alloys,” *Phys. Rev.*, vol. 106, pp. 893–898, Jun 1957.
- [33] W. Nolting and A. Ramakanth, *Quantum theory of magnetism*. Springer Science & Business Media, 2009.
- [34] B. Frietsch, J. Bowlan, R. Carley, M. Teichmann, S. Wienholdt, D. Hinzke, U. Nowak, K. Carva, P. Oppeneer, and M. Weinelt, “Disparate ultrafast dynamics of itinerant and localized magnetic moments in gadolinium metal,” *Nature communications*, vol. 6, 2015.
- [35] M. Doerr, M. Rotter, and A. Lindbaum, “Magnetostriction in rare-earth based antiferromagnets,” *Advances in Physics*, vol. 54, no. 1, pp. 1–66, 2005.
- [36] M. K. Wilkinson, W. C. Koehler, E. O. Wollan, and J. W. Cable, “Neutron Diffraction Investigation of Magnetic Ordering in Dysprosium,” *Journal of Applied Physics*, vol. 32, no. 3, pp. S48–S49, 1961.
- [37] K. M. Döbrich, A. Bostwick, J. L. McChesney, K. Rossnagel, E. Rotenberg, and G. Kaindl, “Fermi-Surface Topology and Helical Antiferromagnetism in Heavy Lanthanide Metals,” *Phys. Rev. Lett.*, vol. 104, p. 246401, Jun 2010.
- [38] W. E. Evenson and S. H. Liu, “Theory of Magnetic Ordering in the Heavy Rare Earths,” *Phys. Rev.*, vol. 178, pp. 783–794, Feb 1969.
- [39] J. Joule, “On a new class of magnetic forces,” *Ann. Electr. Magn. Chem*, vol. 8, no. 1842, pp. 219–224, 1842.
- [40] J. P. Joule, “On the effects of magnetism upon the dimensions of iron and steel bars,” *Philosophical Magazine Series 3*, vol. 30, no. 199, pp. 76–87, 1847.
- [41] A. S. Bulatov, V. F. Dolzenko, and A. V. Kornietz, “Temperature dependences of thermal expansion and exchange magnetostriction of holmium and dysprosium single crystals,” *Czechoslovak Journal of Physics*, vol. 46, no. 4, pp. 2119–2120, 1996.

- [42] J. M. D. Coey, *Magnetism and Magnetic Materials*. Cambridge University Press, 2012.
- [43] F. J. Darnell, “Temperature Dependence of Lattice Parameters for Gd, Dy, and Ho,” *Phys. Rev.*, vol. 130, pp. 1825–1828, Jun 1963.
- [44] J. R. Banister, S. Legvold, and F. H. Spedding, “Structure of Gd, Dy, and Er at Low Temperatures,” *Phys. Rev.*, vol. 94, pp. 1140–1142, Jun 1954.
- [45] M. Griffel, R. E. Skochdopole, and F. H. Spedding, “Heat Capacity of Dysprosium from 15 to 300 K,” *The Journal of Chemical Physics*, vol. 25, no. 1, pp. 75–79, 1956.
- [46] V. K. Pecharsky, K. A. G. Jr, and D. Fort, “Superheating and other unusual observations regarding the first order phase transition in Dy,” *Scripta Materialia*, vol. 35, no. 7, pp. 843–848, 1996.
- [47] E. B. Amitin, W. G. Bessergenev, Y. A. Kovalevskaya, and I. E. Paukov, “Thermodynamic properties of dysprosium from 7 to 300 K,” *The Journal of Chemical Thermodynamics*, vol. 15, no. 2, pp. 181–188, 1983.
- [48] K. D. Jayasuriya, S. J. Campbell, and A. M. Stewart, “Magnetic transitions in dysprosium: A specific-heat study,” *Phys. Rev. B*, vol. 31, pp. 6032–6046, May 1985.
- [49] S. A. Nikitin, A. M. Tishin, S. F. Savchenkova, Y. I. Spichkin, O. D. Chistykov, S. V. Red’ko, and Y. A. Nesterov, “Magnetic part of specific heat in high-purity Dy single crystal,” *Journal of Magnetism and Magnetic Materials*, vol. 96, pp. 26–28, jun 1991.
- [50] M. Agranat, S. Ashitkov, A. Granovsky, and G. Rukman, “Interaction between Picosecond Laser-Pulses with the Electron, Spin and Phonon Subsystems of Nickel,” *Zhurnal Eksperimentalnoi Teor. Fiz.*, vol. 86, no. 4, pp. 1376–1379, 1984.
- [51] A. Vaterlaus, D. Guarisco, M. Lutz, M. Aeschlimann, M. Stampanoni, and F. Meier, “Different spin and lattice temperatures observed by spinpolarized photoemission with picosecond laser pulses,” *Journal of Applied Physics*, vol. 67, no. 9, pp. 5661–5663, 1990.
- [52] A. Vaterlaus, T. Beutler, and F. Meier, “Spin-lattice relaxation time of ferromagnetic gadolinium determined with time-resolved spin-polarized photoemission,” *Phys. Rev. Lett.*, vol. 67, pp. 3314–3317, Dec 1991.
- [53] A. Vaterlaus, T. Beutler, D. Guarisco, M. Lutz, and F. Meier, “Spin-lattice relaxation in ferromagnets studied by time-resolved spin-polarized photoemission,” *Phys. Rev. B*, vol. 46, pp. 5280–5286, Sep 1992.
- [54] R. J. Elliott, “Theory of the Effect of Spin-Orbit Coupling on Magnetic Resonance in Some Semiconductors,” *Phys. Rev.*, vol. 96, pp. 266–279, Oct 1954.
- [55] B. Koopmans, G. Malinowski, F. Dalla Longa, D. Steiauf, M. Fahnle, T. Roth, M. Cinchetti, and M. Aeschlimann, “Explaining the paradoxical diversity of ultrafast laser-induced demagnetization,” *Nature Materials*, vol. 9, no. 3, pp. 259–265, 2010. 10.1038/nmat2593.

- [56] M. Battiato, K. Carva, and P. M. Oppeneer, “Superdiffusive Spin Transport as a Mechanism of Ultrafast Demagnetization,” *Phys. Rev. Lett.*, vol. 105, p. 027203, Jul 2010.
- [57] A. J. Schellekens, W. Verhoeven, T. N. Vader, and B. Koopmans, “Investigating the contribution of superdiffusive transport to ultrafast demagnetization of ferromagnetic thin films,” *Applied Physics Letters*, vol. 102, no. 25, pp. –, 2013.
- [58] B. Koopmans, H. H. J. E. Kicken, M. van Kampen, and W. J. M. de Jonge, “Microscopic model for femtosecond magnetization dynamics,” *Journal of Magnetism and Magnetic Materials*, vol. 286, pp. 271–275, 2005. Proceedings of the 5th International Symposium on Metallic Multilayers.
- [59] B. Koopmans, J. J. M. Ruigrok, F. D. Longa, and W. J. M. de Jonge, “Unifying Ultrafast Magnetization Dynamics,” *Phys. Rev. Lett.*, vol. 95, p. 267207, Dec 2005.
- [60] C. von Korff Schmising, M. Giovannella, D. Weder, S. Schaffert, J. L. Webb, and S. Eisebitt, “Nonlocal ultrafast demagnetization dynamics of Co/Pt multilayers by optical field enhancement,” *New Journal of Physics*, vol. 17, no. 3, p. 033047, 2015.
- [61] A. Melnikov, I. Razdolski, T. O. Wehling, E. T. Papaioannou, V. Roddatis, P. Fumagalli, O. Aktsipetrov, A. I. Lichtenstein, and U. Bovensiepen, “Ultrafast Transport of Laser-Excited Spin-Polarized Carriers in Au/Fe/MgO(001),” *Phys. Rev. Lett.*, vol. 107, p. 076601, Aug 2011.
- [62] A. Eschenlohr, M. Battiato, Maldonado P., N. Pontius, T. Kachel, K. Holldack, R. Mitzner, A. Föhlisch, P. M. Oppeneer, and C. Stamm, “Ultrafast spin transport as key to femtosecond demagnetization,” *Nat Mater*, vol. 12, pp. 332–336, apr 2013. 10.1038/nmat3546.
- [63] E. Turgut, C. La-o vorakiat, J. M. Shaw, P. Grychtol, H. T. Nembach, D. Rudolf, R. Adam, M. Aeschlimann, C. M. Schneider, T. J. Silva, M. M. Murnane, H. C. Kapteyn, and S. Mathias, “Controlling the Competition between Optically Induced Ultrafast Spin-Flip Scattering and Spin Transport in Magnetic Multilayers,” *Phys. Rev. Lett.*, vol. 110, p. 197201, May 2013.
- [64] B. Y. Mueller and B. Rethfeld, “Thermodynamic μ T model of ultrafast magnetization dynamics,” *Phys. Rev. B*, vol. 90, p. 144420, Oct 2014.
- [65] P. Zhang G., W. Hubner, G. Lefkidis, B. Yihua, and G. Thomas, “Paradigm of the time-resolved magneto-optical Kerr effect for femtosecond magnetism,” *Nat Phys*, vol. 5, pp. 499–502, jul 2009. 10.1038/nphys1315.
- [66] J.-Y. Bigot, M. Vomir, and E. Beaurepaire, “Coherent ultrafast magnetism induced by femtosecond laser pulses,” *Nat Phys*, vol. 5, pp. 515–520, jul 2009. 10.1038/nphys1285.
- [67] Munzenberg Markus G., “Magnetization dynamics: Ferromagnets stirred up,” *Nat Mater*, vol. 9, pp. 184–185, mar 2010. 10.1038/nmat2706.

- [68] M. Wietstruk, Ultraschnelle Magnetisierungsdynamik in itineranten und Heisenberg-Ferromagneten. PhD thesis, Technische Universität Berlin, 2010.
- [69] M. Wietstruk, A. Melnikov, C. Stamm, T. Kachel, N. Pontius, M. Sultan, C. Gahl, M. Weinelt, H. A. Dürr, and U. Bovensiepen, “Hot-Electron-Driven Enhancement of Spin-Lattice Coupling in Gd and Tb 4f Ferromagnets Observed by Femtosecond X-Ray Magnetic Circular Dichroism,” *Phys. Rev. Lett.*, vol. 106, p. 127401, Mar 2011.
- [70] A. Eschenlohr, Element-resolved Ultrafast Magnetization Dynamics in Ferromagnetic Alloys and Multilayers. PhD thesis, Universität Potsdam, 2012.
- [71] A. Eschenlohr, M. Sultan, A. Melnikov, N. Bergéard, J. Wieczorek, T. Kachel, C. Stamm, and U. Bovensiepen, “Role of spin-lattice coupling in the ultrafast demagnetization of $\text{Gd}_{1-x}\text{Tb}_x$ alloys,” *Phys. Rev. B*, vol. 89, p. 214423, Jun 2014.
- [72] S. Muhammad, Ultrafast magnetization dynamics of lanthanide metals and alloys. PhD thesis, Freie Universität Berlin, 2012.
- [73] C. Trabant, Ultrafast photoinduced phase transitions in complex materials probed by time-resolved resonant soft x-ray diffraction. PhD thesis, Universität Potsdam, Aug. 2014.
- [74] D. Schick, “private communication.” private communication, Jan. 2015.
- [75] C. von Korff Schmising, A. Harpoeth, N. Zhavoronkov, Z. Ansari, C. Aku-Leh, M. Woerner, T. Elsaesser, M. Bargheer, M. Schmidbauer, I. Vrejoiu, D. Hesse, and M. Alexe, “Ultrafast magnetostriction and phonon-mediated stress in a photoexcited ferromagnet,” *Phys. Rev. B*, vol. 78, no. 6, p. 060404, 2008.
- [76] M. Woerner, C. v. Korff Schmising, M. Bargheer, N. Zhavoronkov, I. Vrejoiu, D. Hesse, M. Alexe, and T. Elsaesser, “Ultrafast structural dynamics of perovskite superlattices,” *Applied Physics A*, vol. 96, no. 1, pp. 83–90, 2009.
- [77] O. Kovalenko, T. Pezeril, and V. V. Temnov, “New Concept for Magnetization Switching by Ultrafast Acoustic Pulses,” *Phys. Rev. Lett.*, vol. 110, p. 266602, Jun 2013.
- [78] J.-W. Kim, M. Vomir, and J.-Y. Bigot, “Ultrafast Magnetoacoustics in Nickel Films,” *Phys. Rev. Lett.*, vol. 109, p. 166601, Oct 2012.
- [79] J. J. Rhyne, R. W. Erwin, M. B. Salamon, S. Sinha, J. Borchers, J. E. Cunningham, and C. P. Flynn, “Long-range incommensurate magnetic order in Dy-Y multilayers,” *Journal of the Less Common Metals*, vol. 126, no. 0, pp. 53–62, 1986. Proceedings of the Seventeenth Rare Earth Research Conference - Part 1.
- [80] W. Friedrich, P. Knipping, and M. Laue, “Interferenzerscheinungen bei Röntgenstrahlen,” *Annalen der Physik*, vol. 346, no. 10, pp. 971–988, 1913.
- [81] “X-ray data booklet,” Jan. 2001.

- [82] V. Holy, U. Pietsch, and T. Baumbach, *High-resolution X-ray Scattering from Thin Films and Multilayers*. Springer Tracts in Modern Physics, Springer, 1st ed., 1999.
- [83] D. Schick, R. Shayduk, A. Bojahr, M. Herzog, C. von Korff Schmising, P. Gaal, and M. Bargheer, “Ultrafast reciprocal-space mapping with a convergent beam,” *Journal of Applied Crystallography*, vol. 46, pp. 1372–1377, Oct 2013.
- [84] M. Montel, “Aberrations du Premier Ordre des Systèmes Catoptriques Asymétriques Application au Microscope X à Réflexion Totale,” *Optica Acta: International Journal of Optics*, vol. 1, no. 3, pp. 117–126, 1954.
- [85] M. Bargheer, N. Zhavoronkov, R. Bruch, H. Legall, H. Stiel, M. Woerner, and T. Elsaesser, “Comparison of focusing optics for femtosecond X-ray diffraction,” *Applied Physics B: Lasers and Optics*, vol. 80, pp. 715–719, may 2005.
- [86] U. Shymanovich, M. Nicoul, K. Sokolowski-Tinten, A. Tarasevitch, C. Michaelsen, and D. von der Linde, “Characterization and comparison of X-ray focusing optics for ultrafast X-ray diffraction experiments,” *Applied Physics B: Lasers and Optics*, vol. 92, pp. 493–499, 2008. 10.1007/s00340-008-3138-8.
- [87] D. Schick, A. Bojahr, M. Herzog, P. Gaal, I. Vrejoiu, and M. Bargheer, “Following Strain-Induced Mosaicity Changes of Ferroelectric Thin Films by Ultrafast Reciprocal Space Mapping,” *Phys. Rev. Lett.*, vol. 110, p. 095502, Feb 2013.
- [88] M. Bargheer, N. Zhavoronkov, M. Woerner, and T. Elsaesser, “Recent Progress in Ultrafast X-ray Diffraction,” *ChemPhysChem*, vol. 7, no. 4, pp. 783–792, 2006.
- [89] M. Bargheer, J. C. Woo, N. Zhavoronkov, D. S. Kim, M. Woerner, and T. Elsaesser, “Excitation mechanisms of coherent phonons unravelled by femtosecond X-ray diffraction,” *phys. stat. sol. (b)*, vol. 243, no. 10, pp. 2389–2396, 2006.
- [90] E. B. Amitin, V. G. Bessergenev, and Y. A. Kovalevskaya, “Thermal expansion anomalies in dysprosium,” *Journal of Physics F: Metal Physics*, vol. 14, no. 12, p. 2935, 1984.
- [91] F. Tsui and C. P. Flynn, “Magnetic phase diagram of epitaxial dysprosium,” *Phys. Rev. Lett.*, vol. 71, pp. 1462–1465, Aug 1993.
- [92] F. Zamponi, *Electron propagation in solid matter as a result of relativistic laser plasma interactions*. PhD thesis, Friedrich-Schiller-Universität Jena, 2007.
- [93] J. E. Pudell, “Ultraschnelle Magnetostriktion von antiferromagnetischem Holmium,” *masterarbeit*, Universität Potsdam, 2015.
- [94] F. Zamponi, Z. Ansari, C. von Korff Schmising, P. Rothhardt, N. Zhavoronkov, M. Woerner, T. Elsaesser, M. Bargheer, T. Trobitzsch-Ryll, and M. Haschke, “Femtosecond hard X-ray plasma sources with a kilohertz repetition rate,” *Appl. Phys. A*, vol. 96, pp. 51–58, July 2009.

- [95] J. Weisshaupt, V. Juvé, M. Holtz, M. Woerner, and T. Elsaesser, “Theoretical analysis of hard x-ray generation by nonperturbative interaction of ultrashort light pulses with a metal,” *Structural Dynamics*, vol. 2, no. 2, pp. –, 2015.
- [96] W. Lu, M. Nicoul, U. Shymanovich, A. Tarasevitch, P. Zhou, K. Sokolowski-Tinten, D. von der Linde, M. Mašek, P. Gibbon, and U. Teubner, “Optimized $K\alpha$ x-ray flashes from femtosecond-laser-irradiated foils,” *Phys. Rev. E*, vol. 80, p. 026404, Aug 2009.
- [97] L. Wei, Ultrafast time-resolved X-ray diffraction using an optimized laser-plasma based X-ray source. PhD thesis, Universität Duisburg-Essen, 2013.
- [98] F. Brunel, “Not-so-resonant, resonant absorption,” *Phys. Rev. Lett.*, vol. 59, pp. 52–55, Jul 1987.
- [99] W. Jannick, V. Juvé, M. Holtz, K. ShinAn, M. Woerner, T. Elsaesser, A. Skrimantas, P. Audrius, and A. Baltuska, “High-brightness table-top hard X-ray source driven by sub-100-femtosecond mid-infrared pulses,” *Nat Photon*, vol. 8, pp. 927–930, dec 2014.
- [100] D. Schick, Ultrafast Lattice Dynamics in Photoexcited Nanostructures. PhD thesis, Universität Potsdam, Oct. 2013.
- [101] G. Korn, A. Thoss, H. Stiel, U. Vogt, M. Richardson, T. Elsaesser, and M. Faubel, “Ultrashort 1-kHz laser plasma hard x-ray source,” *Opt. Lett.*, vol. 27, pp. 866–868, May 2002.
- [102] Y. Jiang, T. Lee, W. Li, G. Ketwaroo, and C. G. Rose-Petruck, “High-average-power 2-kHz laser for generation of ultrashort x-ray pulses,” *Opt. Lett.*, vol. 27, pp. 963–965, Jun 2002.
- [103] N. Zhavoronkov, Y. Gritsai, M. Bargheer, M. Woerner, and T. Elsaesser, “Generation of ultrashort K-alpha radiation from quasipoint interaction area of femtosecond pulses with thin foils,” *Applied Physics Letters*, vol. 86, no. 24, p. 244107, 2005.
- [104] N. Zhavoronkov, Y. Gritsai, M. Bargheer, M. Woerner, T. Elsaesser, F. Zamponi, I. Uschmann, and E. Forster, “Ultrafast Optics - Microfocus Cu Ka source for femtosecond x-ray science,” *Optics Letters*, vol. 30, pp. 1737–1739, July 2005.
- [105] B. B. Zhang, S. S. Sun, D. R. Sun, and Y. Tao, “Note: A novel normalization scheme for laser-based plasma x-ray sources,” *Review of Scientific Instruments*, vol. 85, no. 9, pp. –, 2014.
- [106] C. Rischel, A. Rousse, I. Uschmann, P.-A. Albouy, J.-P. Geindre, P. Audebert, J.-C. Gauthier, E. Froster, J.-L. Martin, and A. Antonetti, “Femtosecond time-resolved X-ray diffraction from laser-heated organic films,” *Nature*, vol. 390, pp. 490–492, dec 1997. 10.1038/37317.
- [107] C. Rose-Petruck, R. Jimenez, T. Guo, A. Cavalieri, C. W. Siders, F. Rksi, J. A. Squier, B. C. Walker, K. R. Wilson, and C. P. J. Barty, “Picosecond-milliangstrom lattice dynamics measured by ultrafast X-ray diffraction,” *Nature*, vol. 398, pp. 310–312, mar 1999. 10.1038/18631.

- [108] K. Sokolowski-Tinten, C. Blome, C. Dietrich, A. Tarasevitch, M. Horn von Hoegen, D. von der Linde, A. Cavalieri, J. Squier, and M. Kammler, “Femtosecond X-Ray Measurement of Ultrafast Melting and Large Acoustic Transients,” *Phys. Rev. Lett.*, vol. 87, p. 225701, Nov 2001.
- [109] K. Sokolowski-Tinten, C. Blome, J. Blums, A. Cavalieri, C. Dietrich, A. Tarasevitch, I. Uschmann, E. Forster, M. Kammler, M. Horn-von Hoegen, and D. von der Linde, “Femtosecond X-ray measurement of coherent lattice vibrations near the Lindemann stability limit,” *Nature*, vol. 422, pp. 287–289, mar 2003. 10.1038/nature01490.
- [110] M. Bargheer, N. Zhavoronkov, Y. Gritsai, J. C. Woo, D. S. Kim, M. Woerner, and T. Elsaesser, “Coherent Atomic Motions in a Nanostructure Studied by Femtosecond X-ray Diffraction,” *Science*, vol. 306, no. 5702, pp. 1771–1773, 2004.
- [111] T. Elsaesser and M. Woerner, “Perspective: Structural dynamics in condensed matter mapped by femtosecond x-ray diffraction,” *The Journal of Chemical Physics*, vol. 140, no. 2, pp. –, 2014.
- [112] A. Bojahr, D. Schick, L. Maerten, M. Herzog, I. Vrejoiu, C. von Korff Schmising, C. J. Milne, S. L. Johnson, and M. Bargheer, “Comparing the oscillation phase in optical pump-probe spectra to ultrafast x-ray diffraction in the metal-dielectric SrRuO₃/SrTiO₃ superlattice,” *Phys. Rev. B*, vol. 85, p. 224302, Jun 2012.
- [113] L. Maerten, A. Bojahr, M. Gohlke, M. Rössle, and M. Bargheer, “Coupling of GHz Phonons to Ferroelastic Domain Walls in SrTiO₃,” *Phys. Rev. Lett.*, vol. 114, p. 047401, Jan 2015.
- [114] M. Herzog, D. Schick, W. Leitenberger, R. Shayduk, R. M. van der Veen, C. J. Milne, S. L. Johnson, I. Vrejoiu, and M. Bargheer, “Tailoring interference and nonlinear manipulation of femtosecond x-rays,” *New J. Phys.*, vol. 14, no. 1, p. 013004, 2012.
- [115] T. Brabec, C. Spielmann, P. F. Curley, and F. Krausz, “Kerr lens mode locking,” *Opt. Lett.*, vol. 17, pp. 1292–1294, Sep 1992.
- [116] G. Cerullo, S. D. Silvestri, V. Magni, and L. Pallaro, “Resonators for Kerr-lens mode-locked femtosecond Ti:sapphire lasers,” *Opt. Lett.*, vol. 19, pp. 807–809, Jun 1994.
- [117] D. Strickland and G. Mourou, “Compression of amplified chirped optical pulses,” *Optics Communications*, vol. 55, no. 6, pp. 447–449, 1985.
- [118] C. H. . Rullière, ed., *Femtosecond laser pulses : principles and experiments*. New York;[Heidelberg]: Springer, 2. ed., 2005.
- [119] J.-C. . R. W. Diels, *Ultrashort laser pulse phenomena : fundamentals, techniques and applications on a femtosecond time scale*. Amsterdam, Heidelberg [u.a.]: Academic Press, 2. ed., 2006.

- [120] P. Kirkpatrick and A. V. Baez, "Formation of optical images by X-rays," *JOSA*, vol. 38, no. 9, pp. 766–773, 1948.
- [121] C. von Korff Schmising, M. Bargheer, M. Kiel, N. Zhavoronkov, M. Woerner, T. Elsaesser, I. Vrejoiu, D. Hesse, and M. Alexe, "Accurate time delay determination for femtosecond X-ray diffraction experiments," *Appl. Phys. B*, vol. 88, no. 1, pp. 1–4, 2007.
- [122] I. Vrejoiu, M. Alexe, D. Hesse, and U. Gösele, "Functional Perovskites – From Epitaxial Films to Nanostructured Arrays," *Adv. Funct. Mater.*, vol. 18, no. 24, pp. 3892–3906, 2008.
- [123] G. Bauer, *Optical characterization of epitaxial semiconductor layers*. Berlin: Springer, 1996.
- [124] M. Bargheer, "Atombewegung im Röntgenkino - Die Femtosekunden-Röntgenbeugung entschlüsselt ultraschnelle Gitterdynamik.," *Physik Journal*, vol. 6, no. 8/9, pp. 1–6, 2007.
- [125] J. Stingl, F. Zamponi, B. Freyer, M. Woerner, T. Elsaesser, and A. Borgschulte, "Electron Transfer in a Virtual Quantum State of LiBH_4 Induced by Strong Optical Fields and Mapped by Femtosecond X-Ray Diffraction," *Phys. Rev. Lett.*, vol. 109, p. 147402, Oct 2012.
- [126] D. Schick, M. Herzog, H. Wen, P. Chen, C. Adamo, P. Gaal, D. G. Schlom, P. G. Evans, Y. Li, and M. Bargheer, "Localized excited charge carriers generate ultrafast inhomogeneous strain in the multiferroic BiFeO_3 ," *Phys. Rev. Lett.*, vol. 112, p. 097602, Mar. 2014.
- [127] H. J. Lee, J. Workman, J. S. Wark, R. D. Averitt, A. J. Taylor, J. Roberts, Q. McCulloch, D. E. Hof, N. Hur, S.-W. Cheong, and D. J. Funk, "Optically induced lattice dynamics probed with ultrafast x-ray diffraction," *Phys. Rev. B*, vol. 77, p. 132301, Apr 2008.
- [128] C. Thomsen, H. T. Grahn, H. J. Maris, and J. Tauc, "Surface generation and detection of phonons by picosecond light pulses," *Phys. Rev. B*, vol. 34, pp. 4129–4138, Sep 1986.
- [129] D. Schick, M. Herzog, A. Bojahr, W. Leitenberger, A. Hertwig, R. Shayduk, and M. Bargheer, "Ultrafast lattice response of photoexcited thin films studied by X-ray diffraction," *Structural Dynamics*, vol. 1, Nov. 2014.
- [130] A. S. Chernyshov, A. O. Tsokol, A. M. Tishin, K. A. Gschneidner, and V. K. Pecharsky, "Magnetic and magnetocaloric properties and the magnetic phase diagram of single-crystal dysprosium," *Phys. Rev. B*, vol. 71, p. 184410, May 2005.
- [131] S. B. Palmer and E. W. Lee, "The Elastic Constants of Dysprosium and Holmium," *Proceedings of the Royal Society of London. A. Mathematical and Physical Sciences*, vol. 327, no. 1571, pp. 519–543, 1972.
- [132] S. D. Brorson, J. G. Fujimoto, and E. P. Ippen, "Femtosecond electronic heat-transport dynamics in thin gold films," *Phys. Rev. Lett.*, vol. 59, pp. 1962–1965, Oct 1987.

- [133] J. Hohlfeld, J. Müller, S.-S. Wellershoff, and E. Matthias, "Time-resolved thermorefectivity of thin gold films and its dependence on film thickness," *Applied Physics B*, vol. 64, no. 3, pp. 387–390, 1997.
- [134] M. Bonn, D. N. Denzler, S. Funk, M. Wolf, S. S. Wellershoff, and J. Hohlfeld, "Ultrafast electron dynamics at metal surfaces: Competition between electron-phonon coupling and hot-electron transport," *Phys. Rev. B*, vol. 61, pp. 1101–1105, Jan 2000.
- [135] U. Bovensiepen, "Coherent and incoherent excitations of the Gd(0001) surface on ultrafast timescales," *Journal of Physics: Condensed Matter*, vol. 19, no. 8, p. 083201, 2007.
- [136] T. J. McKenna, S. J. Campbell, D. H. Chaplin, and G. V. H. Wilson, "A.C. specific heat of terbium and dysprosium," *Solid State Communications*, vol. 40, no. 2, pp. 177–181, 1981.
- [137] H. Kuzmany, *Solid-state spectroscopy - an introduction*. Berlin: Springer Verlag, 2nd. ed., 2009.
- [138] H. A. Navirian, D. Schick, P. Gaal, W. Leitenberger, R. Shayduk, and M. Bargheer, "Thermoelastic study of nanolayered structures using time-resolved x-ray diffraction at high repetition rate," *Appl. Phys. Lett.*, vol. 104, no. 2, p. 021906, 2014.
- [139] M. E. Straumanis and S. Zysczynski, "Lattice parameters, thermal expansion coefficients and densities of Nb, and of solid solutions Nb–O and Nb–N–O and their defect structure," *Journal of Applied Crystallography*, vol. 3, pp. 1–6, Feb 1970.
- [140] W. M. Haynes, *CRC Handbook of Chemistry and Physics*, 93rd Edition. CRC Handbook of Chemistry and Physics, Taylor & Francis, 2012.
- [141] E. Dobrovinskaya, L. Lytvynov, and V. Pishchik, "Properties of Sapphire," in *Sapphire, Micro- and Opto-Electronic Materials, Structures, and Systems*, pp. 55–176, Springer US, 2009.
- [142] M. Lucht, M. Lerche, H. C. Wille, Y. V. Shvyd'ko, H. D. Rüter, E. Gerdau, and P. Becker, "Precise measurement of the lattice parameters of α -Al₂O₃ in the temperature range 4.5–250K using the Mössbauer wavelength standard," *Journal of Applied Crystallography*, vol. 36, pp. 1075–1081, Aug 2003.
- [143] J. Smith and J. Gjevre, "Elastic Constants of Yttrium Single Crystals in the Temperature Range 4.2–400 K," *Journal of Applied Physics*, vol. 31, no. 4, pp. 645–647, 1960.
- [144] K. J. Carroll, "Elastic Constants of Niobium from 4.2 to 300 K," *Journal of Applied Physics*, vol. 36, no. 11, pp. 3689–3690, 1965.
- [145] J. Wachtman, W. Tefft, D. Lam, and R. Stinchfield, "Elastic Constants of Synthetic Single-Crystal Corundum at Room Temperature," *Journal Of The American Ceramic Society*, vol. 43, no. 6, pp. 334–334, 1960.
- [146] D. C. Ginnings and G. T. Furukawa, "Heat Capacity Standards for the Range 14 to 1200° K.," *Journal of the American Chemical Society*, vol. 75, no. 3, pp. 522–527, 1953.

- [147] C. Y. Ho, R. W. Powell, and P. E. Liley, "Thermal Conductivity of the Elements," *Journal of Physical and Chemical Reference Data*, vol. 1, no. 2, pp. 279–421, 1972.
- [148] R. Shayduk, H. A. Navirian, W. Leitenberger, J. Goldshteyn, I. Vrejoiu, M. Weinelt, P. Gaal, M. Herzog, C. von Korff Schmising, and M. Bargheer, "Nanoscale heat transport studied by high-resolution time-resolved x-ray diffraction," *New J. Phys.*, vol. 13, p. 093032, Sept. 2011.
- [149] M. Herzog, D. Schick, P. Gaal, R. Shayduk, C. von Korff Schmising, and M. Bargheer, "Analysis of ultrafast X-ray diffraction data in a linear-chain model of the lattice dynamics," *Appl. Phys. A*, vol. 106, pp. 489–499, Feb. 2012.
- [150] L. D. Jennings, R. E. Miller, and F. H. Spedding, "Lattice Heat Capacity of the Rare Earths. Heat Capacities of Yttrium and Lutetium from 15–350°K," *The Journal of Chemical Physics*, vol. 33, no. 6, pp. 1849–1852, 1960.
- [151] N. D. Ashcroft and N. W. Mermin, *Solid state physics*. Fort Worth: Saunders College, 1st ed., 1976.
- [152] R. M. Nicklow, N. Wakabayashi, and P. R. Vijayaraghavan, "Lattice Dynamics of Holmium," *Phys. Rev. B*, vol. 3, pp. 1229–1234, Feb 1971.
- [153] B. C. Gerstein, W. A. Taylor, W. D. Shickell, and F. H. Spedding, "Heat Capacity of Lutetium from 6 to 300°K," *The Journal of Chemical Physics*, vol. 51, no. 7, pp. 2924–2928, 1969.
- [154] J. R. Cannon, *The one-dimensional heat equation*, vol. 23 of *Encyclopedia of Mathematics and Its Applications*. Addison-Wesley Publishing Company, 1984.
- [155] N. Kazantseva, U. Nowak, R. W. Chantrell, J. Hohlfeld, and A. Rebei, "Slow recovery of the magnetisation after a sub-picosecond heat pulse," *EPL (Europhysics Letters)*, vol. 81, no. 2, p. 27004, 2008.
- [156] D. Royer and E. Dieulesaint, *Elastic Waves in Solids I, Free and Guided Propagation*. Heidelberg: Springer, 2000.
- [157] P. C. Landry, "Variation of the Helicomagnetic Turn Angle in Dysprosium," *Phys. Rev.*, vol. 156, pp. 578–583, Apr 1967.
- [158] W. E. Tefft, "Elastic constants of synthetic single crystal corundum," *Elastic*, vol. 70, no. 4, 1966.
- [159] T. Goto, O. L. Anderson, I. Ohno, and S. Yamamoto, "Elastic constants of corundum up to 1825 K," *Journal of Geophysical Research: Solid Earth*, vol. 94, no. B6, pp. 7588–7602, 1989.
- [160] B. L. Henke, E. M. Gullikson, and J. C. Davis, "X-ray interactions: photoabsorption, scattering, transmission, and reflection at E=50-30000 eV, Z=1-92," *Atomic Data and Nuclear Data Tables*, vol. 54, pp. 181–342, July 1993.

6 Appendix

This chapter is intended as reference where I summarize frequently used calculations, relevant details of my work or overview figures that would otherwise impair the reading flow of the main text.

6.1 Influence of the inhibited in-plane expansion

In my data analysis I am comparing the lattice strain of time resolved experiments on a timescale of few nanoseconds and less with the lattice strain measured in an equilibrium heating process that takes place on the timescale of minutes. In the quasi-static heating case the energy is deposited via thermal contact between the tempered cryostat and the sample. The following comparison of the two situations points out that probing the strain on different timescales after the thermal stress is exerted leads to different outcomes.

The corresponding thought experiments for the different strain responses after ultrafast heating and equilibrium heating progress as follows: Suppose that the same excitation energy density or temperature is provided into the sample by two different ways:

- Ultrafast heating by the deposition of energy using a femtosecond laser pulse. In this case the strain is subsequently probed on a timescale smaller than few nanoseconds after the excitation.
- Slow heating of the sample using a thermalization process with the adjacent cryostat. In this static experiment the strain is probed approximately five minutes after thermal equilibrium is reached.

In both cases heating the sample creates a stress in all crystal directions. On ultrafast timescales the in-plane stresses are not converted to strains since stresses from adjacent unit cells are balancing each other. This in-plane clamping leads to a change in the observed out of plane expansion. The following calculations provide an estimate of the magnitude of this effect. Since the observed strain ε is on the order of few per mil. of the interatomic distances I neglect any effects that are of the order ε^2 .

The general linear relation between stress σ and strain ε from linear elastic theory is tensor like and is stated in equation 6.1 with the help of the stiffness tensor C_{ijkl} . A review of the relevant quantities is provided for example in the book by Royer and Dieulesaint¹⁵⁶.

$$\sigma_{ij} = \sum_{kl} C_{ijkl} \varepsilon_{kl} \quad (6.1)$$

Using the symmetry properties of a hexagonal system and applying the compressed Voigt notation (1 = 11, 2 = 22, 3 = 33, 4 = 23, 5 = 31, 6 = 12) equation (6.1) can be simplified to the six relations (6.2) with the five independent material parameters $C_{11}, C_{33}, C_{12}, C_{13}$ and C_{44} ($C_{66} = 0.5(C_{11} - C_{12})$).

$$\underbrace{\begin{pmatrix} \sigma_1 \\ \sigma_2 \\ \sigma_3 \\ \sigma_4 \\ \sigma_5 \\ \sigma_6 \end{pmatrix}}_{\text{stress}} = \underbrace{\begin{pmatrix} C_{11} & C_{12} & C_{13} & 0 & 0 & 0 \\ C_{12} & C_{11} & C_{13} & 0 & 0 & 0 \\ C_{13} & C_{13} & C_{33} & 0 & 0 & 0 \\ 0 & 0 & 0 & C_{44} & 0 & 0 \\ 0 & 0 & 0 & 0 & C_{44} & 0 \\ 0 & 0 & 0 & 0 & 0 & C_{66} \end{pmatrix}}_{\text{stiffness tensor } C} \underbrace{\begin{pmatrix} \varepsilon_1 \\ \varepsilon_2 \\ \varepsilon_3 \\ \varepsilon_4 \\ \varepsilon_5 \\ \varepsilon_6 \end{pmatrix}}_{\text{strain}} \quad (6.2)$$

In the experiments presented here I neglect any shear strain effects because their occurrence would require stresses coplanar with the materials surface. Neither heat expansion, nor magnetostriction nor epitaxial bounding effects are expected to act in that way. For the further analysis I only take the first three equations from relation (6.2) into consideration that are shown separately in (6.3). When the elastic constants of Dysprosium are known it is straightforward to calculate the resulting strains when the applied stresses are known and vice versa.

$$\begin{pmatrix} \sigma_1 \\ \sigma_2 \\ \sigma_3 \end{pmatrix} = \begin{pmatrix} C_{11} & C_{12} & C_{13} \\ C_{12} & C_{11} & C_{13} \\ C_{13} & C_{13} & C_{33} \end{pmatrix} \begin{pmatrix} \varepsilon_1 \\ \varepsilon_2 \\ \varepsilon_3 \end{pmatrix} \quad (6.3)$$

The elastic constants C_{ij} for bulk Dysprosium have been determined by Palmer and Lee¹³¹ by measuring the sound velocity of sound and shear waves propagating along different directions of single crystalline Dysprosium. The values I used for my calculations are listed in Table 6.1 and they correspond to the stiffness values at the highest available temperature of 300 K. I used them because far above $T_N = 180$ K the magnetic contributions to the elasticity constants are expected to be negligibly small.

Table 6.1. Elements of the stiffness tensor in in of bulk Dysprosium measured at 300 K as reported by Palmer and Lee¹³¹.

C_{11} [GPa]	C_{33} [GPa]	C_{12} [GPa]	C_{13} [GPa]	C_{44} [GPa]	C_{66} [GPa]
73.1	78.1	25.3	22.3	24.0	23.9

In the case of the slow heating process there is sufficient time for all stresses to equilibrate to zero, resulting in the thermal strains $\varepsilon_1, \varepsilon_2, \varepsilon_3$ in the a, b, c directions of the crystal respectively. The thermal strain is related to the change in temperature ΔT via the linear thermal expansion coefficients $\alpha_1, \alpha_2, \alpha_3$ in the respective direction according to equation 6.4.

$$\varepsilon_i = \alpha_i \Delta T \quad i \in \{1, 2, 3\} \quad (6.4)$$

The used linear thermal expansion coefficients have been extracted from the data measured by Bulatov et al.⁴¹ by linear fits of the a and c -axis in the temperature range 250 – 300 K and they

Table 6.2. Linear thermal expansion coefficients in the paramagnetic phase determined from the measurements by Bulatov et al.⁴¹

$\alpha_1 \left(\frac{10^{-6}}{K} \right)$	$\alpha_2 \left(\frac{10^{-6}}{K} \right)$	$\alpha_3 \left(\frac{10^{-6}}{K} \right)$
3.1337	3.1337	20.836

are listed in Table 6.2. On ultrafast timescales the in-plane strain that develops in a thin film is relatively small. In the idealized situation that a thin film is excited with a homogeneous energy density all crystal unit cells develop an expansive stress in all directions. The fact that the stresses from adjacent unit cells compensate each other leads to a delayed development of the strain which can only occur via a relaxation process from the interface between excited and unexcited parts of the sample. Therefore a strain wave travels in towards the center of the material and the development of the strain is thus limited by the speed of sound in the material. A detailed discussion of strain effects within thin films on a transparent substrate including simulations and measurements of the lattice dynamics has been given recently by Schick et al.¹²⁹.

Since the spatial extent of the laser pulse with $\approx 1200 \mu\text{m}$ FWHM is large compared to the thickness of the thin films, which is on the order of few hundred nanometers ($\approx 200 \text{ nm}$), it takes a much longer time ($\frac{1200 \mu\text{m}}{2v_{\text{sound}}} \approx 200 \text{ ns}$) until the in-plane strain can develop as compared to the out of plane strain $\frac{110 \text{ nm}}{2v_{\text{sound}}} \approx 13.7 \text{ ps}$. So for timescales larger than 30 ps but smaller than 200 ns I assume that the position of the thin film material atoms are fixed in plane but are free to move out of plane. This in plane clamping effect will change the observed out of plane strain due to the nonzero coupling term C_{13} in the stiffness matrix.

Poisson's ratio ν is defined as the negative ratio between the in-plane contraction relative to the out of plane expansion under uniaxial stress. It can be deduced for the hexagonal system from solving the system of equations stated in equation 6.5

$$\begin{pmatrix} 0 \\ 0 \\ \sigma \end{pmatrix} = \begin{pmatrix} C_{11} & C_{12} & C_{13} \\ C_{12} & C_{11} & C_{13} \\ C_{13} & C_{13} & C_{33} \end{pmatrix} \begin{pmatrix} \varepsilon_1 \\ \varepsilon_2 \\ \varepsilon_3 \end{pmatrix} \quad (6.5)$$

It follows that the Poisson ratio for the hexagonal system is a given by equation (6.6), which merely contains certain elements of the stiffness tensor C . Inserting the numerical values for Dysprosium at 300 K amounts to $\nu \approx 0.266$.

$$\nu = -\frac{\varepsilon_1}{\varepsilon_3} = \frac{C_{13}}{C_{12} + C_{11}} \approx 0.226 \quad (6.6)$$

If ν would be zero then there is no effect by the in-plane clamping in the ultrafast experiment. However its nonvanishing value leads to a necessary correction between the out of plane strain observed on ultrafast timescales ε^u and the out of plane strain observed on very long timescales ε^h by heating. In the following I am going to compute the ratio $\varepsilon^u / \varepsilon^h$ using a two step Gedanken-experiment schematically depicted in Figure 6.1.

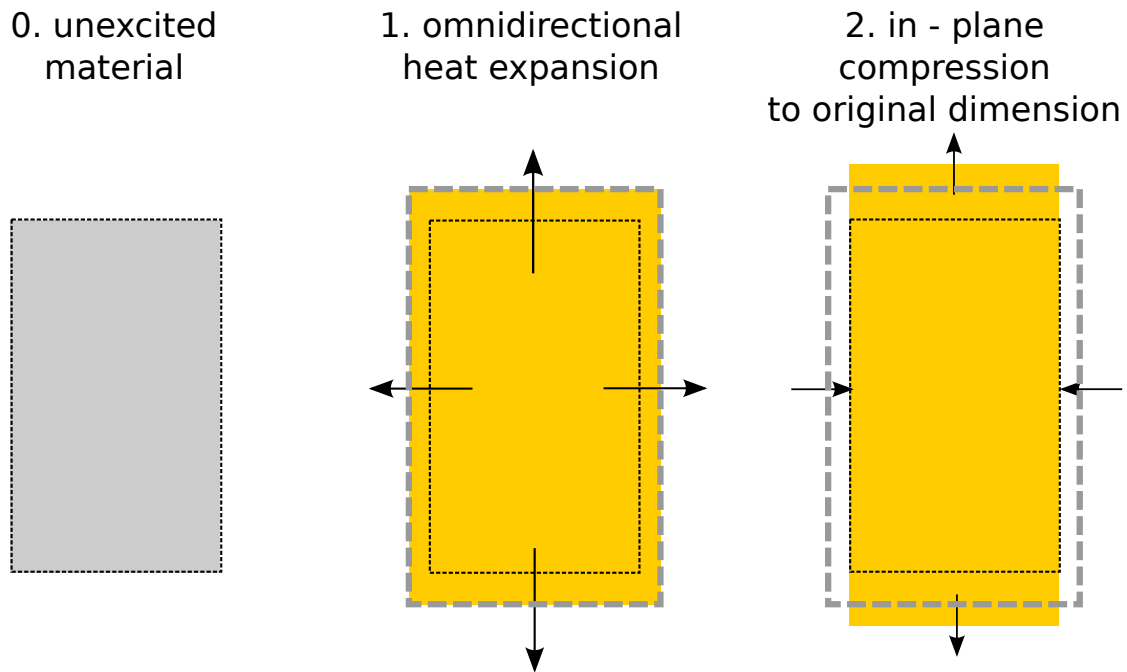


Figure 6.1. Schematic visualization of the two step process applied to quantify the effect of the in-plane clamping on ultrafast timescales. In a first step the sample expands due to heating, which results in the thermal strain according to the linear expansion coefficient. In the second step the sample is again compressed in plane to its original dimension. Stresses are indicated by arrows. The required additional in plane stress leads to an additional expansion out of plane. The out of plane lattice strain observed on the ultrafast timescales is modeled as the sum of the out of plane heat expansion and the additional out of plane strain resulting from the in plane clamping, whereas on long timescales only the out of plane strain due to heating is observable.

In the first step the sample is expanding in all directions due to the change in temperature as given by the linear thermal expansion law. Then the sample volume is compressed by in plane stresses that originate from the adjacent unit cells. As a first approximation the stress is taken to be so large that no in-plane lattice change can occur. This results in the set of 3 linear equations with the three unknowns σ'_1 , σ'_2 and ϵ'_3 stated in equation (6.7).

$$\begin{pmatrix} \sigma'_1 \\ \sigma'_2 \\ 0 \end{pmatrix} = \begin{pmatrix} C_{11} & C_{12} & C_{13} \\ C_{12} & C_{11} & C_{13} \\ C_{13} & C_{13} & C_{33} \end{pmatrix} \begin{pmatrix} \epsilon'_1 \\ \epsilon'_2 \\ \epsilon'_3 \end{pmatrix} \quad (6.7)$$

Solving relation (6.7) for ϵ'_3 leads to :

$$\epsilon'_3 = -\frac{C_{13}}{C_{33}}(\epsilon'_1 + \epsilon'_2) \quad (6.8)$$

$$= \frac{C_{13}}{C_{33}}(\alpha_1 \Delta T + \alpha_2 \Delta T) \quad (6.9)$$

and thus the ratio of the expansion that is observed in the ultrafast experiment ϵ'' and the slow heating experiment ϵ^h can be estimated according to relation (6.11):

$$\frac{\epsilon''_3}{\epsilon^h_3} = \frac{\epsilon^h_3 + \epsilon'_3}{\epsilon^h_3} \quad (6.10)$$

$$= 1 + \underbrace{\frac{C_{13}}{C_{33}}}_{\approx 0.28} \underbrace{\frac{\alpha_1 + \alpha_2}{\alpha_3}}_{0.334} \quad (6.11)$$

$$\approx 1.09 \quad (6.12)$$

Thus I conclude that the c-axis expansion observed in the ultrafast heating experiment will be approximately 9% larger as compared to the expansion probed at very late times, given that no heat would flow out of the sample layer.

A similar estimation is necessary for the strain due to magnetostriction. The magnetostrictive stress is to a first approximation uniaxial along the c-axis¹⁵⁷. However such a uniaxial out of plane stress leads not only to an out of plane strain but also to an in plane strain. This in plane strain is generated via the Poisson relation from equation (6.6). The in plane stress can in a similar way not manifest itself on the ultrafast timescales due to the adjacent unit cells. Therefore the strain observed in an ultrafast experiment will not be the same as the strain when probing the material after the time it takes for the in plane stress to relax. A similar two step scheme for the calculation of the in plane clamping effect for this case is given in Figure 6.2.

In the first step the uniaxial magnetostrictive stress results in an in-plane contraction and an out-of-plane expansion assuming that there would not exist any clamping effect. In the second step a pressure is applied to compensate for the in plane expansion which in reality originates from the adjacent unit cells. For the case of an uniaxial contraction I expect the observed contraction in an ultrafast experiment to be less than the contraction that occurs when the in-plane clamping

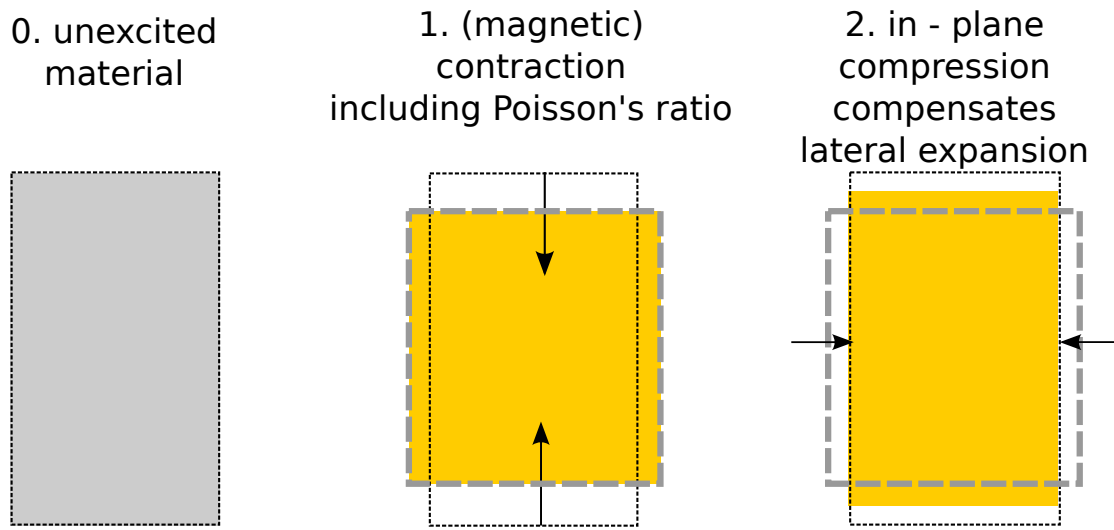


Figure 6.2. Schematic visualization of the two step process applied to quantify the effect of the in-plane clamping on the observed out of plane contraction under the effect of a uniaxial stress. In the first step the sample contracts out of plane due to the removal of the magnetostrictive stress, which results via the Poisson ratio to an in plane expansion. In the second step the sample is again compressed to its original in-plane dimension. The required additional in plane stress leads to an additional expansion out of plane. The out of plane lattice strain observed on the ultrafast timescales is modeled as the out of plane lattice contraction due directly to the stress less the expansion that occurs out of plane by forcing the unit cell to its original in-plane dimension. As opposed to the case for heat expansion the observed contraction in the ultrafast experiment is an underestimation for the contraction that would be observed at times when the in plane stress is relaxed.

is released. Explicitly this effect can be calculated by substituting $\varepsilon'_1 = \varepsilon'_2 = -\nu\varepsilon_3$ into equation (6.9) where ν is the Poisson ratio derived in relation (6.6).

$$\frac{\varepsilon''}{\varepsilon^s} = \frac{\varepsilon_3^s + \varepsilon'_3}{\varepsilon_3^s} \quad (6.13)$$

$$= 1 - 2\nu \frac{C_{13}}{C_{33}} \quad (6.14)$$

$$\approx 0.87 \quad (6.15)$$

Inserting the elastic constants known for Dysprosium¹³¹ into relation (6.15) leads to estimate that approximately 13% less contraction is observed when the sample is clamped in plane as compared to the unclamped situation.

6.2 Reference Values of Material Properties

The achievable accuracy of the simulations of the lattice dynamics depends to some extent on the amount of information known about the material properties. The simulation results can only approximate the reality if relevant input parameters are known. My samples contain the four different materials Dysprosium, Yttrium, Niobium and Sapphire for which I reproduce here the relevant quantities, heat capacity C_p , thermal conductivity λ , linear thermal expansion coefficient α and speed of sound v_{sound} as a function of temperature. Dashed lines indicate the constant values that are used as approximations in some cases when a full temperature dependent description is not expected to be necessary.

The quality of the available data varies greatly and I acknowledge that a refinement of these parameters is needed in the development of the lattice simulations. As of now this collection of material properties for the four materials is intended as a report on the current state and providing references for further improvements.

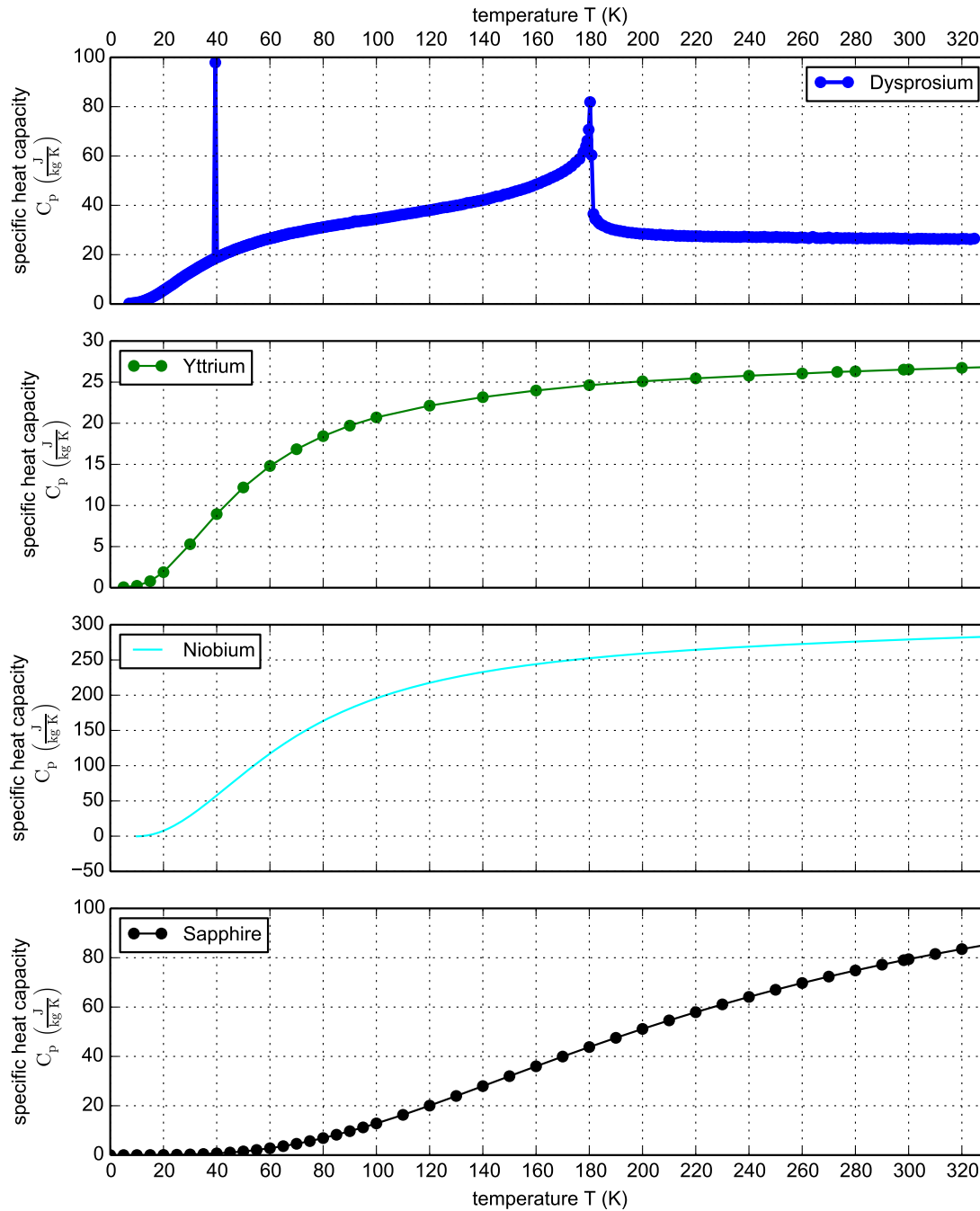


Figure 6.3. Specific heat capacity C_p for each of the sample constituent materials. Dysprosium taken from Pecharsky et al.⁴⁶, Yttrium taken from Jennings et al.¹⁵⁰, Niobium approximated by a Debye function that fits the known high temperature value¹⁴⁰ and Sapphire known from Ginnings et al.¹⁴⁶. Accurate measurements of the heat capacity values for Niobium in the relevant temperature range from 15 – 350 K have so far remained elusive to me.

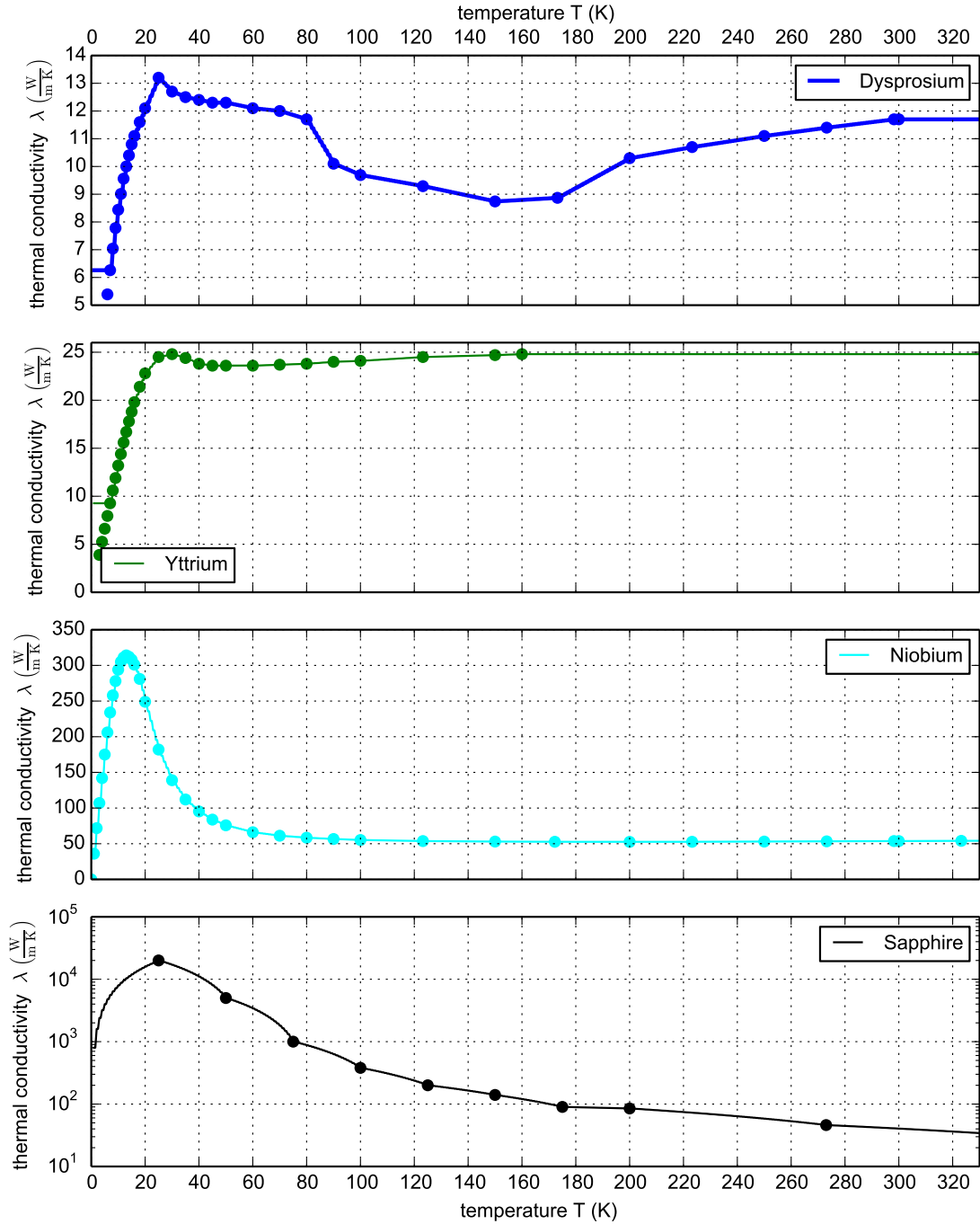


Figure 6.4. Thermal conductivity λ for each of the sample constituent materials. The values for the heat conductivity of the elements Dysprosium, Yttrium and Niobium are reproduced from the compendium of Ho et al.¹⁴⁷ and the values for Sapphire are taken from the book of Dobrovinskaya¹⁴¹. I suspect that the pronounced low temperature maximum in the thermal conductivity of Niobium and Sapphire lead to a fast cooling effect in the simulation at 40 K and below that are present in the measurements. A more detailed research of the validity of these bulk values for thin film samples needs to be undertaken in order to adequately simulate the simulation of the lattice dynamics in the Ferromagnetic phase at temperatures of 50 K and below.

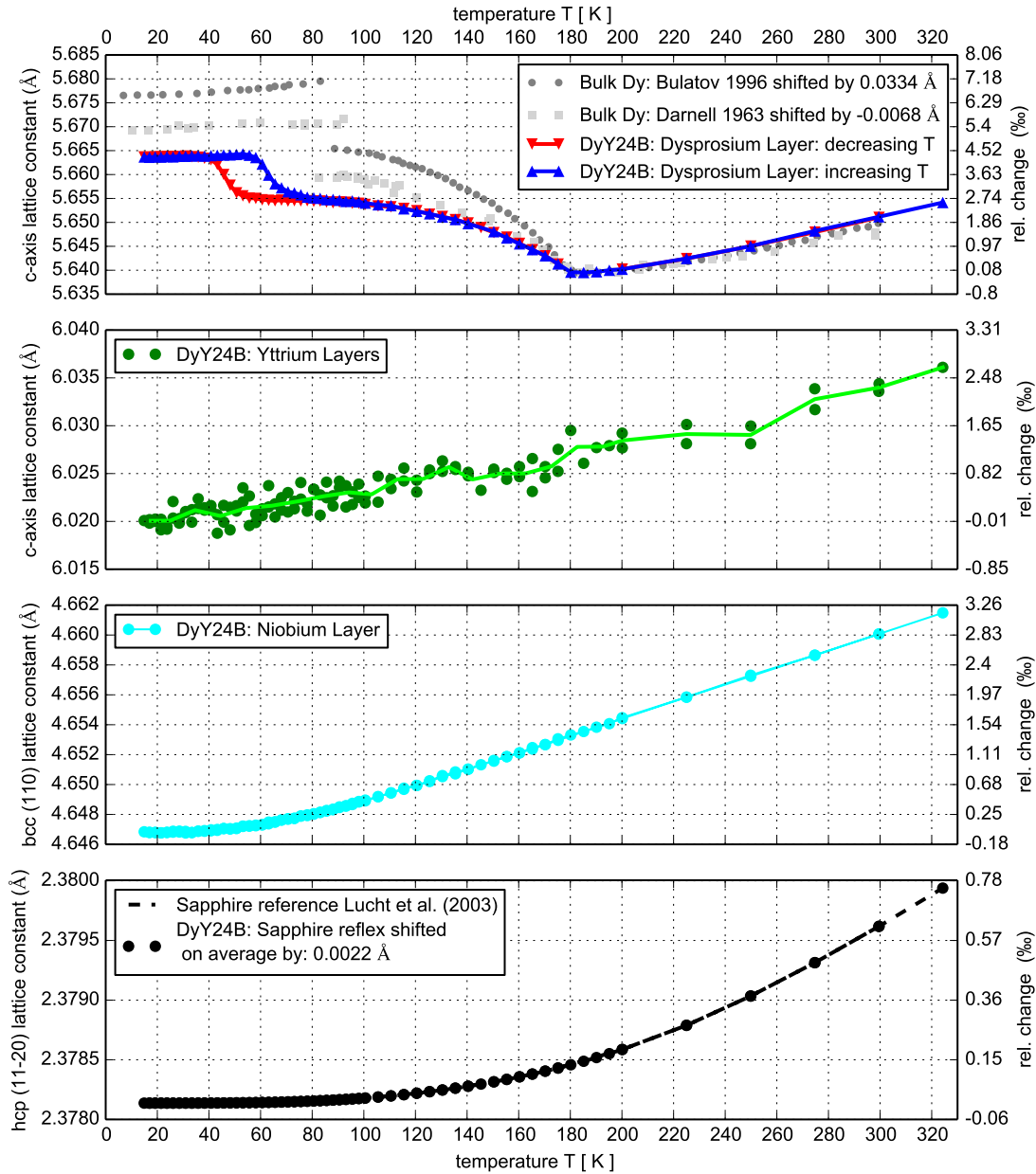


Figure 6.5. Out of plane lattice constant for each of the materials as determined from static X-Ray diffraction using the microfocus X-Ray tube. The Sapphire interatomic distance has been used as a reference according to the values given by Lucht et al.¹⁴². Other values than that are then determined by our measurements. For Dysprosium I added the bulk values reported by Darnell⁴ and Bulatov et al.⁴¹ as a reference. One possible explanation for the deviations are explained by epitaxial strain due to the growth on Yttrium which has a 1.6% larger in plane lattice constant²⁹ and thereby shifting T_{Curie} to lower temperatures^{9,91}.

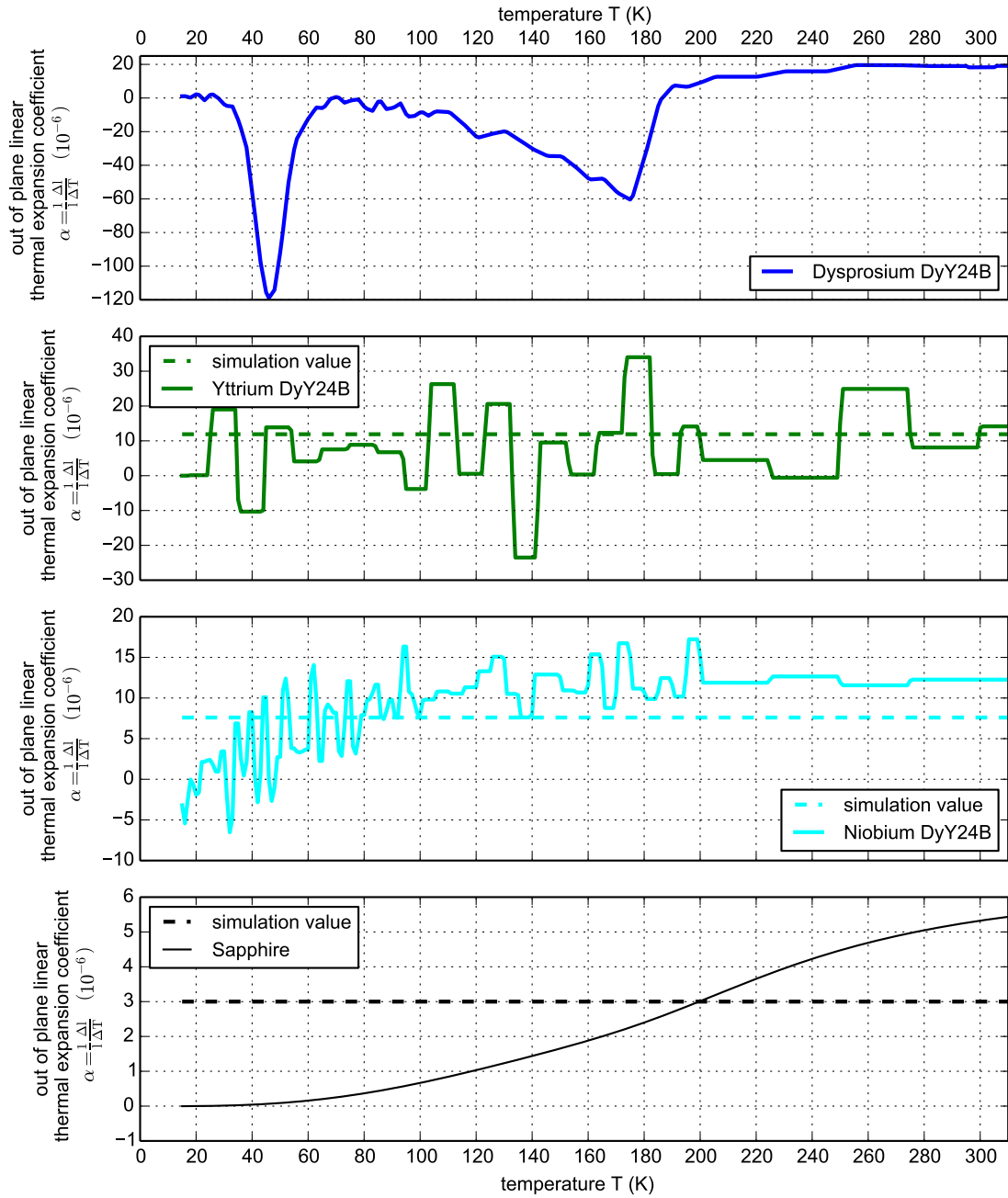


Figure 6.6. Linear thermal expansion coefficients α : Resulting linear thermal expansion coefficients derived from our measurements shown in the previous Figure 6.5 using the discrete approximation for the derivative in the formula $\alpha = \frac{1}{l} \frac{\Delta l}{\Delta T}$. The dashed lines indicate constant values that have been used in the simulations as a first approximation to the temperature behavior. Especially the the used thermal expansion for sapphire is currently too high but it is of little importance due to the negligible temperature change in the sapphire substrate.

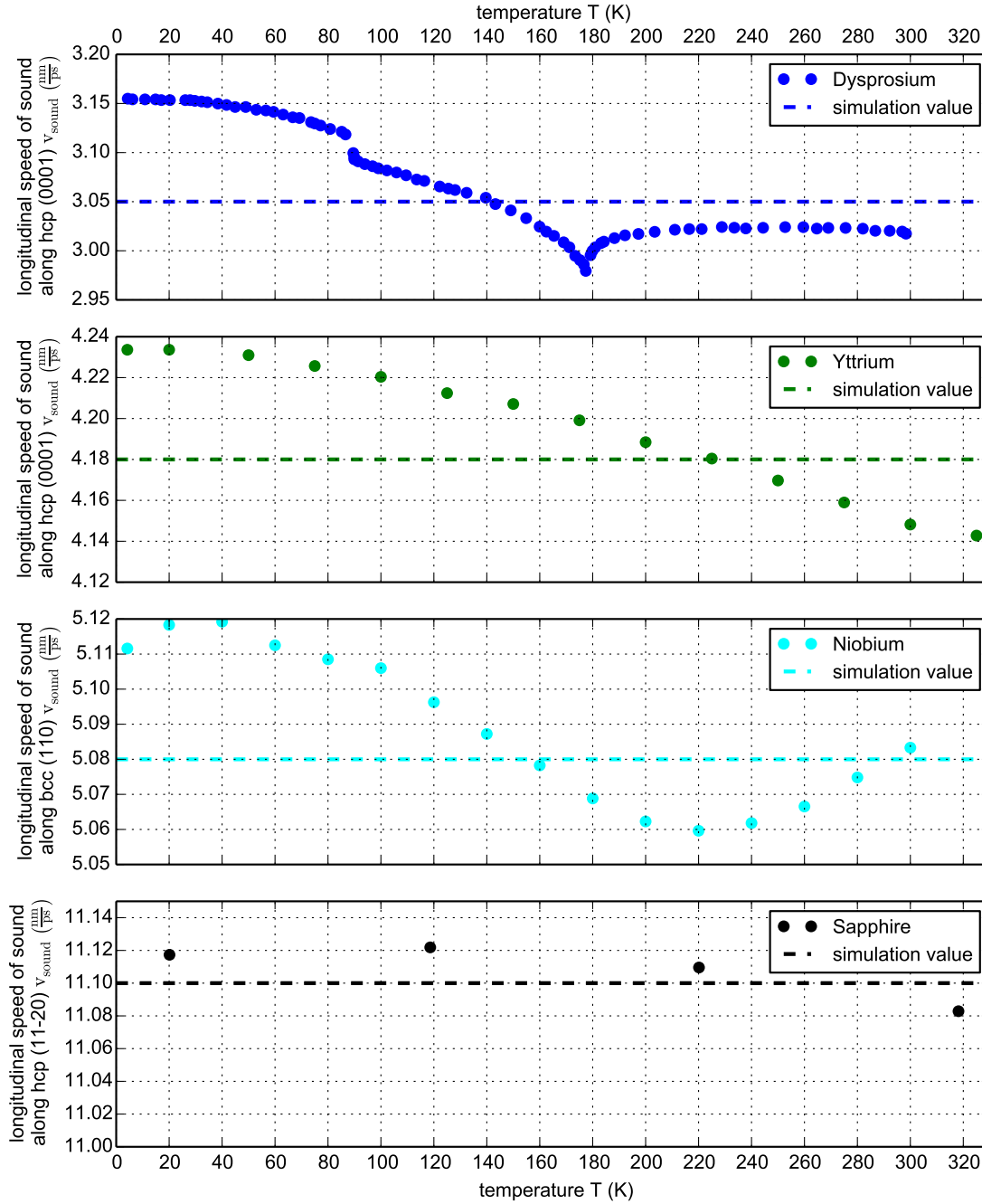


Figure 6.7. Out of plane longitudinal sound velocities v_{sound} : The propagation speed of the coherent longitudinal strain waves in relation to the thin film thicknesses is decisive for the modeling of the strain rise time and the subsequent strain oscillations observed within the first 200 ps. Due to the relatively small temperature dependence of less than 10% over the relevant temperature range I set the sound velocity to a constant value to reduce the computational costs. Elastic constants from which the values have been derived were published by Palmer and Lee for Dysprosium¹³¹, by Carroll for Niobium¹⁴⁴, by Smith and Gjevre for Yttrium¹⁴³ and by Tefft and Wayne^{158,159} for Sapphire. The relevant relations between the sound velocity, material density and elastic constants are for example stated in the book of Royer and Dieulesaint¹⁵⁶.

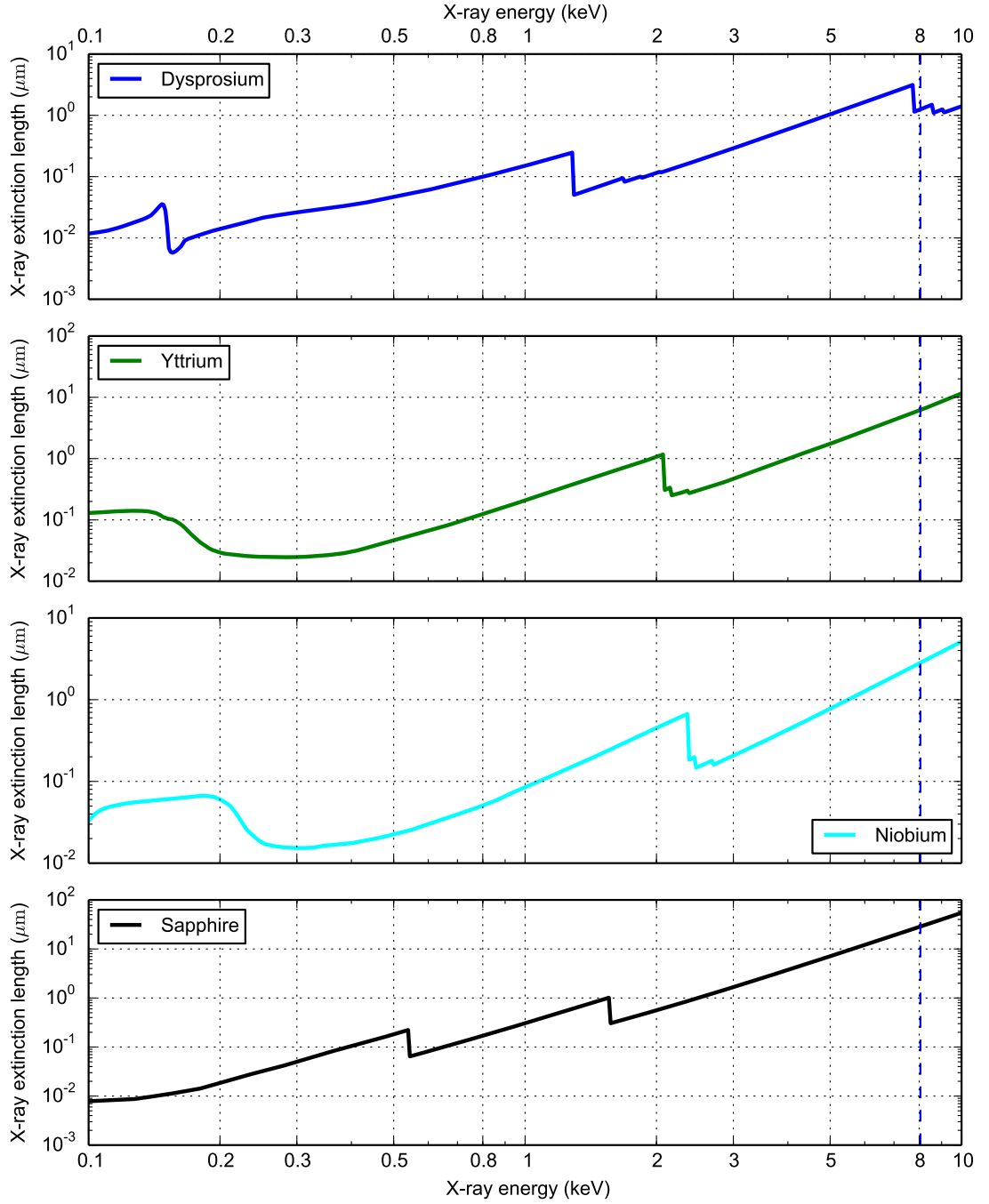
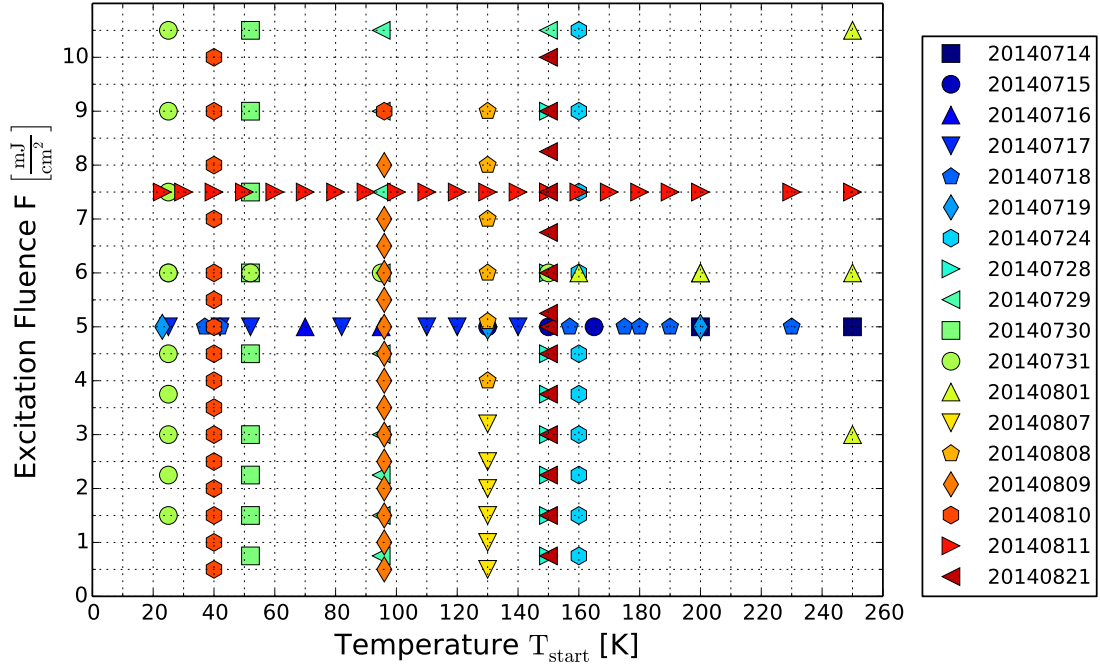


Figure 6.8. X-Ray extinction length: Shown here is the X-ray extinction length as a function of energy for a typical angle of incidence $\omega = 20^\circ$. The values have been taken from the reference publication by Henke et al.¹⁶⁰. Absorption edges where the X-ray penetration suddenly drops can be clearly seen in the data for each of the materials. The blue dashed line indicates the $\text{Cu K}\alpha$ energy available at our plasma X-ray source.

6.3 Listing of measurements

Not all data that was obtained on the ultrafast lattice response of Dysprosium after laser excitation could be discussed within the framework of this thesis. In the following I provide graphics that displays an overview over the carried out measurements along with their measurement dates for future reference.

(a) Overview over measurements on DyY24B where the excitation fluence is taken as determined by the beam profile and incident power



(b) Same data as in (a) but the excitation fluence is rescaled to a common scale determined by the expansion in the paramagnetic phase at 250 K measured on at 20140801. Measurements where the excitation fluence is uncertain are plotted in a lighter shade.

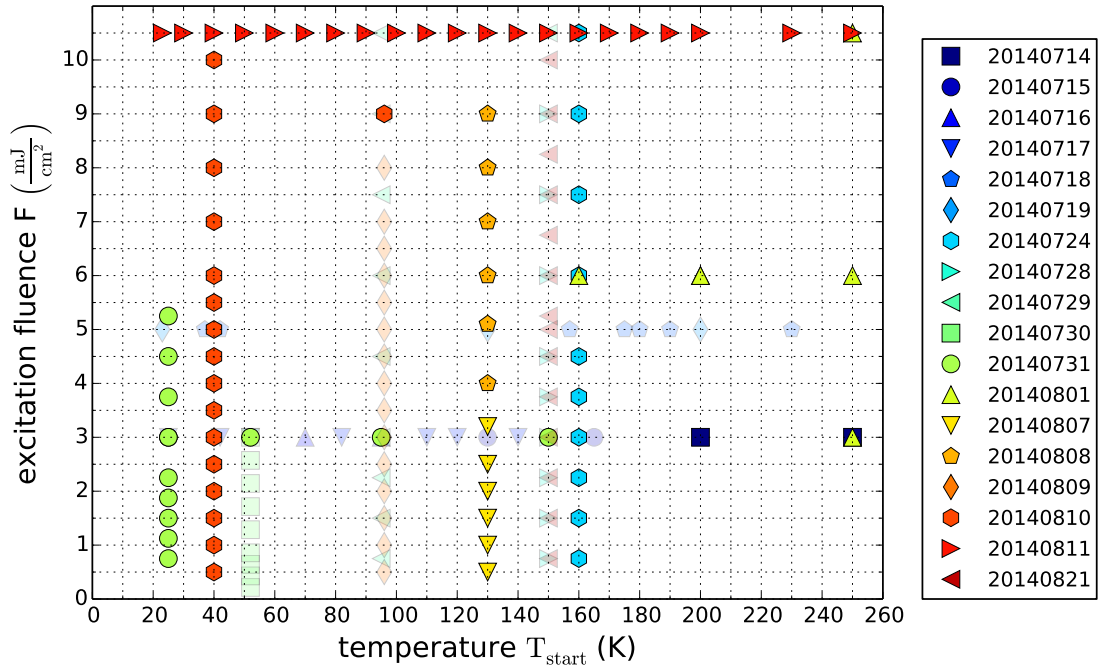
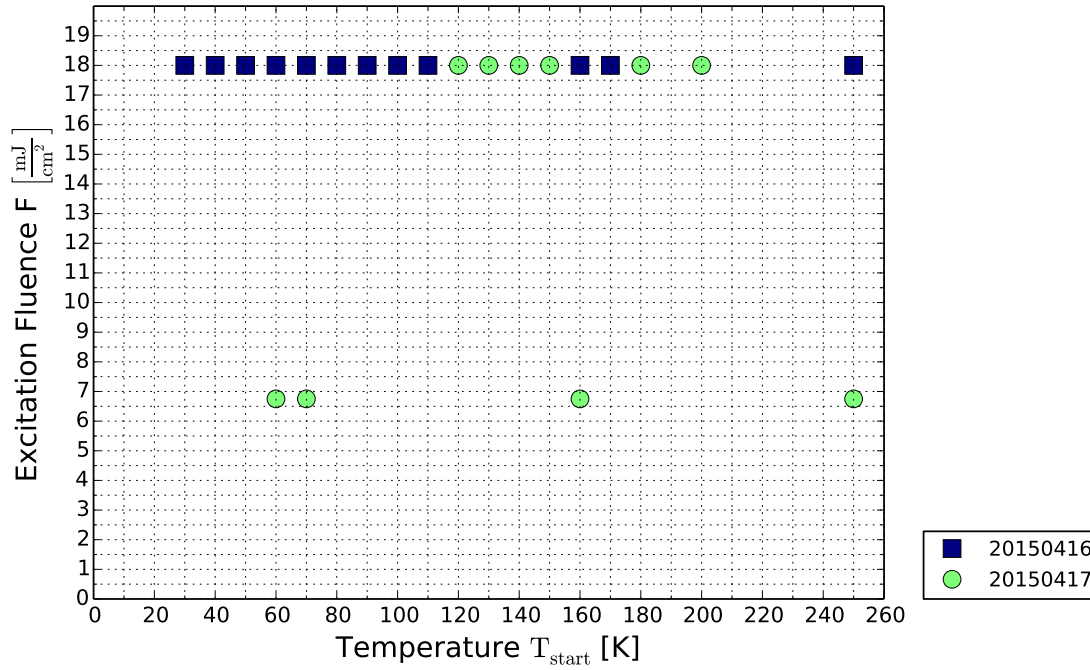


Figure 6.9. Fixed angle DyY24B: Overview over measurements carried out on DyY24B. (a) Displays the excitation fluence as it was determined from the beam profile and incident power. Subplot (b) shows the excitation fluence where it was possible to recalibrate the expansion in the paramagnetic phase at 250 K that scales linearly with excitation fluence. Measurements where a recalibration is so far uncertain are plotted in a lighter shade in (b). Measurements of the same day can readily be compared among each other to obtain trends. Comparisons of measurements between different days should only be carried out if their fluence is verified against the standard calibration scale established from the measurement series in the paramagnetic phase on 20140801.

(a) Measurements with a B-Field of approximately 0.1 T applied in plane.



(b) Measurements on DyY24B where a full reciprocal spacemap has been recorded for each delay.

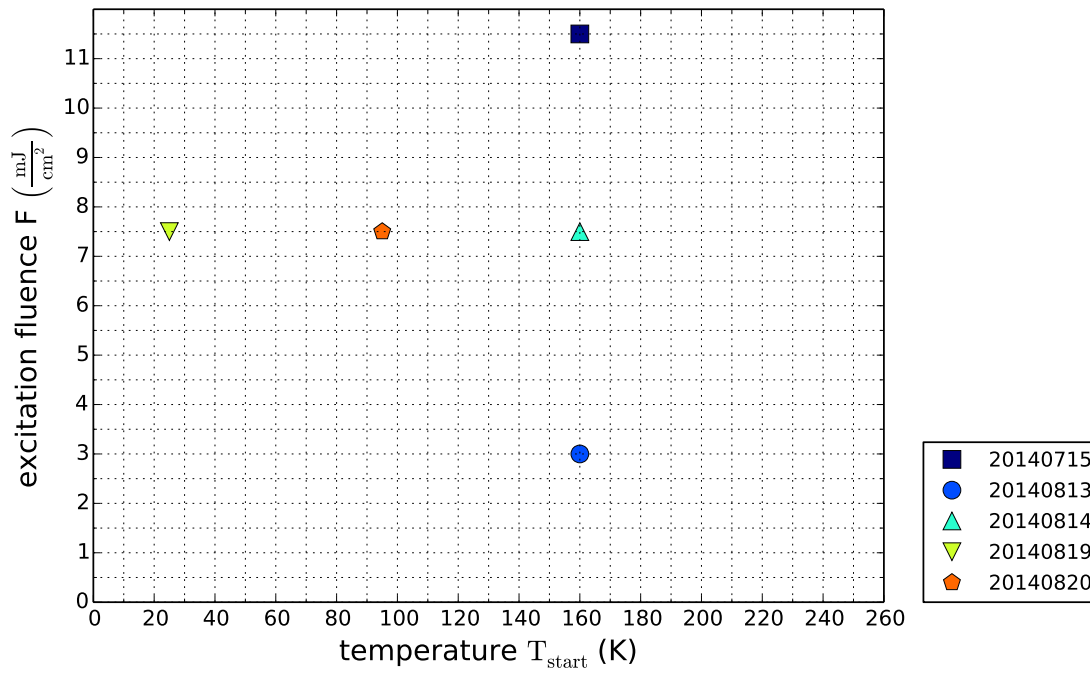


Figure 6.10. Special measurements on DyY24B: (a) Measurements with an applied magnetic field in plane and (b) measurements where a full reciprocal-space-map has been recorded for each delay.

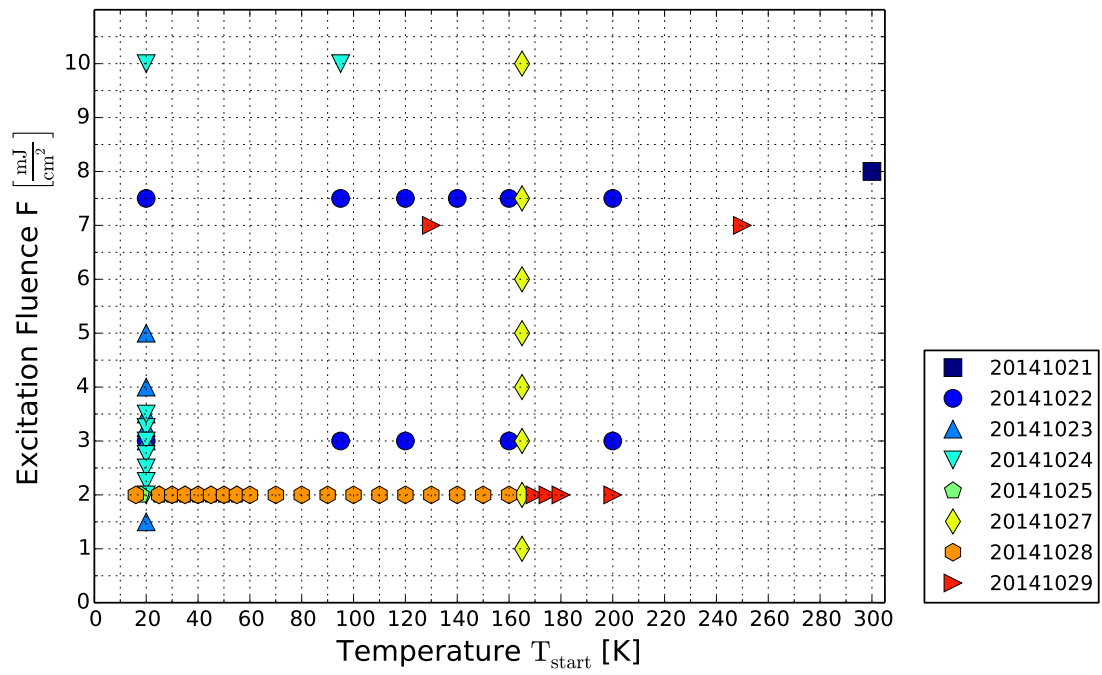


Figure 6.11. DyY26DI fixed angle measurements: Measurements carried out on the sample with the thick 50nm Yttrium capping layer.

Statement of authorship

I hereby certify that this master thesis was written independently and without assistance from third parties. Other than the stated sources and aids were not used. Parts of the sources that have been used verbatim or in substance are identified as such. This master thesis has not been presented in the same or similar form to any audit authority and was not published.

Hiermit versichere ich, dass die vorliegende Masterarbeit selbstständig und ohne Hilfe Dritter verfasst habe. Andere als die angegebenen Quellen und Hilfsmittel wurden nicht verwendet. Die den benutzten Quellen wörtlich oder inhaltlich entnommenen Abschnitte sind als solche kenntlich gemacht. Diese Masterarbeit hat in gleicher oder ähnlicher Form noch keiner Prüfungsbehörde vorgelegen und wurde auch nicht veröffentlicht.

Potsdam, 30.9.2015

(Alexander von Reppert)